# PLANE SHOCK WAVES IN GRANULAR GASES AND REGULARIZED MOMENT EQUATIONS

A Thesis
Submitted for the Degree of
Doctor of Philosophy

by

M. H. Lakshminarayana Reddy


Engineering Mechanics Unit
Jawaharlal Nehru Centre for Advanced Scientific Research
(A Deemed University)
Bangalore – 560 064

SEPTEMBER 2016

*my sir* **V.K.Ranga Reddy,**

*for his encouragement and financial assistance*

*my wife* **Usha,**

*for her constant love and support*

*my daughter* **Jaswita Reddy** *and my lovely* **parents.**

# DECLARATION

I hereby declare that the matter embodied in the thesis entitled "**PLANE SHOCK WAVES IN GRANULAR GASES AND REGULARIZED MOMENT EQUATIONS**" is the result of investigations carried out by me at the Engineering Mechanics Unit, Jawaharlal Nehru Centre for Advanced Scientific Research, Bangalore, India under the supervision of **Prof. Meheboob Alam** and that it has not been submitted elsewhere for the award of any degree or diploma.

In keeping with the general practice in reporting scientific observations, due acknowledgment has been made whenever the work described is based on the findings of other investigators.

**M. H. Lakshminarayana Reddy**

# CERTIFICATE

I hereby certify that the matter embodied in this thesis entitled "**PLANE SHOCK WAVES IN GRANULAR GASES AND REGULARIZED MOMENT EQUATIONS**" has been carried out by **Mr. M. H. Lakshminarayana Reddy** at the Engineering Mechanics Unit, Jawaharlal Nehru Centre for Advanced Scientific Research, Bangalore, India under my supervision and that it has not been submitted elsewhere for the award of any degree or diploma.

**Prof. Meheboob Alam**
(Research Supervisor)

# Acknowledgements

I am deeply indebted to all those who made this thesis possible, which is personally an amazing experience for me. First and foremost, I express my deepest sense of gratitude to my Ph.D. thesis advisor, Prof. Meheboob Alam, for his constant encouragement and support throughout the course of the study and the thesis. Without his systematic guidance, insightful comments, vast knowledge and immense patience, this thesis would not have been a reality. His dedication towards work is a quality that I hope to emulate in my academic life.

I would like to sincerely thank Prof. Santosh Ansumali for his guidance in moment closure methods, and more importantly, his support in implementing numerical methods which helped me to complete this work.

I would also like to thank all the other faculty members of Engineering Mechanics Unit [ Prof. K. R. Sreenivas, Prof. S. M. Deshpande, Prof. Ganesh Subramanian and Prof. Roddam Narasimha], Prof. Rama Govindarajan, Prof. Kavita Jain, Prof. Umesh V. Waghmare and Prof. C. N. R. Rao for their valuable teachings and inspiration. I gratefully thank all my professors at Pondicherry University [Prof. M. Subbiah, Prof. V. Indumathi, Prof. A. M. S. Ramasamy, Prof. K. M. Tamizhmani, Prof. T. Duraivel, Prof. V. Muruganandam] and all my teachers for teaching those courses which formed the basis for my research work.

I owe my deepest gratitude to Sri. V. K. Ranga Reddy and his family, for their encouragement and financial assistance during my under graduation and post graduation which enabled me to pursue higher education, and thereby made this endeavor possible.

I am grateful to my friends who shared their experiences and supported me in the times of need. I offer my very sincere and special thanks to K. Siddharth, for his support while I was learning and writing numerical codes. I would like to thank my fellow labmates: Dr. Nandu Gopan, Sunil, Achal, Saikat, R.K, Ronak, Prateek, and all other EMUites for their valuable advice, immeasurable help and the friendly working environment in the lab and the department.

I also thank my fellow batchmates: Ramana Reddy, Rajdeep Singh Payal, Venky, Gangaiah, Loukya and all other JNC friends. I really enjoyed my life in JNC which was particularly memorable because of playing football (sometimes in rain too). I offer my special regards to all of those who played football with me. I would also like to express my sincere thanks to my senior researchers: Dr. Priyanka Shukla, Dr. Vinay Kumar Gupta, Dr. Ujjayan Paul, Deepthi, Dr. Anubhab Roy, Dr. Harish N Dixit, Dr. Sumesh P.T, Dr. Dhiraj V. Patil, Dr. Ratul Dasgupta, Dr.Gayathri, Dr. Rakshith, Dr. Ponnu Lakshmi, Dr. Dhiraj Kumar Singh, Dr. Shiwani Singh, Dr. Shailendra Kumar Singh and Dr. Srikanth.

I would like to gratefully acknowledge my friends: V. K. Rakesh, V. K. Bhupesh, Gideon Suman Dadpogu, Kalesh Itlapuram, K. Ramamohan Reddy, Dr. Damodar Reddy, Raghunath Reddy, Lokanath Reddy, Mahesh Gowd, N. Narendra Reddy, Dileep, Balam Pradeeep, Ravi,

Dr. Ramakrishna Reddy Vemula, Raghu Hatkari, N. Srinivas and all other my classmates for their valuable help and advice. I would also like to acknowledge few people who helped me and my child hood friends from my village: B. Srinivas Reddy, Venkat Rami Reddy (Geetha Hotel), M. H. Harinath Reddy, Amaresh, Mahesh, Adishesha, Shiva, Chinnapa Reddy, Ramu, Kumar, Simha, Narapa Reddy and all other cricketing friends and swimming mates of my village.

I would like to thank my colleagues who worked with me at Nalla Malla Reddy Engineering College (Hyderabad) for my wonderful experiences there. I offer my sincere thanks to Sailu sir, Raghavendra Kulkarni sir, D. Sreenivas sir, G. Venkat Reddy sir, Suman sir, Anantha Reddy sir, Vishnuvardhana Reddy sir, Durga Srinivas sir and all other faculty colleagues for their inspiration and valuable advice.

I thank our A.O sir A N Jayachandra, admin staff and academic staff for their invaluable support from time to time. I thank all other members (especially the Dhanvantari staff, security staff, cleaning staff and the mess staff) of JNC community who made my life possible at JNC. I thank JNCASR and DST for providing me with timely financial assistance (which helped me to attend conferences) and infrastructural support for my research. I am very grateful to Prof. Meheboob Alam and Prof. Santosh Ansumali for their partial funding during my Ph.D. studies.

Finally, I take this opportunity to express my deeply profound gratitude to my beloved parents, my siblings, grandparents, my uncle O. Sunki Reddy, and his family members for their love and continuous support. Words can not express how grateful I am to my father-in-law and mother-in-law for all the sacrifices that they have made on my behalf.

I would like to thank my beloved wife Usha, for her love, affection, immense patience and support that helped me overcome some of the most challenging suituations and difficult times. Lastly, to my beloved daughter Jaswita Reddy, I would like to express my thanks for being such a good girl and always cheering me up.

# Synopsis

This thesis starts with a brief introduction about granular materials and their importance as described in Chapter 1. The background literature on shock waves in both molecular and granular gases as well as the objective and motivation of present research work are presented later in this chapter. The primary goals of this thesis are to (i) study the well-known Riemann problem of plane shock waves propagating in a granular gas using hydrodynamic-like equations (Chapters 3 and 4), (ii) develop numerical schemes to solve the related inhomogeneous PDEs (Chapter 3), (iii) analyse and identify the unique characteristics of granular shock-waves in comparison to their molecular counterparts (Chapter 4), (iv) a comparative analysis between the predictions of the Euler- and Navier-Stokes-order hydrodynamic equations and the "extended" (beyond Navier-Stokes-order) hydrodynamic models (Chapter 6), (v) analyse the characteristics and the well-posedness of extended granular hydrodynamic models (Chapter 5) and finally (vi) suggest ways to 'regularize' the extended moment models for a granular gas (Chapter 7) so as to obtain smooth solutions at any Mach number.

Chapter 2 provides a brief overview of the kinetic theory of a dilute granular gas starting with the derivation of basic inelastic Boltzmann equation and discusses the properties of the inelastic collision integral. The well-known closure problem and its solution via moment closure methods, namely, the Chapman-Enskog method, Grad's moment method and the maximum entropy method, are discussed. The Grad's moment method has been used to obtain the extended sets of hydrodynamic equations, namely, 10-moment, 13-moment and 14-moment equations for a dilute granular gas, and the respective constitutive relations are taken from the work of Kremer & Marques Jr (2011). Chapter 3 to 7 contain new contributions of the present work.

The theory of normal shocks in molecular/granular gases and the formulation of Euler and Navier-Stokes-order hydrodynamic equations for plane shock waves are described in Chapter 3. The resulting one-dimensional PDEs have been solved by two relaxation-type numerical schemes: (i) PDE-splitting technique following Jin & Xin (1995) and (ii) the numerical scheme of Delis & Katsaounis (2003). Both numerical schemes produce shock-profiles accurately, and the shock thickness results extracted from both schemes have been compared with the data of Torrilhon & Struchtrup (2004) [who used a different numerical method], which further confirms the accuracy of both numerical schemes. The relative performance of two numerical schemes has been evaluated, and it is shown that the PDE-splitting technique is faster than the method of Delis & Katsaounis.

A detailed analysis of the Riemann problem for granular shock waves is presented in Chapter 4 by numerically solving the Euler and Navier-Stokes-Fourier (NSF) equations. The numerical results reveal that the density and temperature profiles are asymmetric, with an 'overshoot' of

the density occurring within the shock-layer; moreover, this density-peak travels with a constant speed at late times, i.e., the shock travels with a steady speed in the asymptotic limit. The above findings constitute two distinguishing features of the "granular" Riemann problem compared to its ideal-gas counterpart. The fundamental difference of the granular shock problem from its ideal-gas counterpart can be tied to 'inelastic dissipation' since this makes the upstream and downstream states of a granular shock to live in non-equilibrium 'decaying' states [similar to the 'homogeneous cooling state' (HCS)]. The origin of asymmetric density profiles, leading to the continual build-up of density inside the shock, seems to be tied to a pressure instability in granular gases. It is shown that the granular energy equation must be regularized (Reddy & Alam 2015) in order to arrest the maximum density.

Chapter 5 provides a detailed analysis of the extended hydrodynamic equations with reference to the plane shock wave problem. A detailed analysis on the characteristics of extended hydrodynamic models is presented and this analysis confirms that the largest characteristic speed in extended hydrodynamic equations depends on the number of moments retained in hydrodynamic equations. Moreover, the largest characteristic speed increases if the number of moments is increased: $s_{\max} = \sqrt{3\theta}$, $\sqrt{4.54\theta}$ and $\sqrt{5.18\theta}$ (where $\theta$ is the dimensionless granular temperature) for 10, 13 and 14-moment models, respectively. An analysis of the 10-moment model for a granular gas for plane shock waves reveals that the density gradient can blow up if the upstream Mach number exceeds a critical value; it is shown that this critical Mach number is not influenced by the restitution coefficient ($\alpha$) and the critical Mach number is increased when the number of moments increases in extended hydrodynamic models. Lastly, a derivation of Haff's law is presented by assuming a spatially homogeneous solution for the 14-moment model.

Chapter 6 presents numerical solutions of plane shock waves in both molecular and granular gases for extended hydrodynamic equations, and the results from extended hydrodynamic models are compared with the numerical solutions of Navier-Stokes-Fourier model. For shock waves in a molecular gas it is found that the agreement for the shock solutions of the 13- and 14-moment equations is better than those predicted by the NSF equations since the results from moment models show a quantitative agreement with the data from DSMC simulations for Mach numbers up to Ma $\approx$ 2.0. More specifically, for Mach numbers Ma $\leq$ 1.3 the shock width described by the NS, 13-moment and 14-moment equations are within the DSMC computational scatter and for Mach numbers Ma $>$ 1.3 the 13-moment and 14-moment predictions are more accurate as compared to NS-model predictions, whereas the shock width described by the 10-moment equations is in poor agreement with DSMC data as well as other models for all $Ma$. From the results on shock waves in a granular gas, a density overshoot is found, which is not present in the case of shocks in a molecular gas, which is predicted by every moment model as well as the standard hydrodynamic models (as discussed in Chapter-4); among all models presented here, the 14-moment model predicts a lesser density overshoot. Interestingly, all models predict the same asymptotic value for the normalized shock speed and the maximum temperature within the shock-layer follows the Haff's law up to a critical time and the decay is much slower thereafter, indicating quasi-invariant shock profiles. Different moment models do not seem to have noticeable effect on the magnitude of this critical time for given control parameters.

Appendix-A has been added as a supplement to Chapter-6 in which the numerical results for blast waves are presented using four variants of hydrodynamic equations: Euler, 10-moment, NSF and 14-moment models. Blast waves are a special class of shock waves that are caused by the rapid and localized release of a large amount of energy in a medium. The results on the density, granular temperature, skew temperature, heat flux and the contracted fourth moment are compared among all models and it is found that the shock profiles are smoother for the NSF and 14-moment model compared to those predicted by the Euler equations and 10-moment equations; a shock-splitting phenomenon is observed in the skew temperature profiles for blast waves in both molecular and granular gases.

A detailed derivation of the "regularized" version of 14-moment equations (dubbed "R14" moment equations) for a dilute granular gas is presented in Chapter-7 following the Chapman-Enskog-like "order-of-magnitude" method of Struchtrup (2004)– these equations contain additional higher-order gradient terms that help to produce 'continuous/smooth' shock solutions at any Mach number. Subsequently, Navier-Stokes-Fourier (NSF) equations are obtained via the regularization of Euler equations (which admit 'discontinuous' shock solutions) by implementing the Maxwell-iteration procedure on (i) 13-field variables, and (ii) 14-field variables. It is shown that there is a difference between NSF equations obtained from these two approaches: while the heat flux vector is proportional only to the temperature gradient in the first approach (i.e. the well-known Fourier law), in the second approach the heat flux is found to be proportional to the temperature gradient as well as to the density gradient, leading to the generic "non-Fourier" law (Goldhirsch 2003) in a granular gas.

In the later part of Chapter-7 the regularized 10-moment (R10) equations are derived, and in order to clarify the advantage of regularized moment equations, the R10 equations have been employed to solve the Riemann problem for both molecular and granular gases. Based on a comparison of results between the 10-moment and R10-moment models, it is found that (i) while the 10-moment model fails to produce continuous shock structures beyond an upstream Mach number of $\mathrm{Ma}_1 = 1.34$, the R10-moment model predicts continuous and smooth shocks even beyond the upstream Mach number of $\mathrm{Ma}_1 = 1.34$, (iii) all profiles predicted by 10-moment model are steepened into a discontinuity (for $\mathrm{Ma}_1 > 1.34$) on the upstream part of the shock but this unwanted feature is not seen in the case of R10-moment model profiles, (iv) the profiles predicted by R10-moment model are less diffusive at the downstream end than the upstream end and, lastly for a granular gas, (v) both R10 and 10-moment models predict asymmetric density and temperature profiles, with the maxima of both density and temperature occurring within the shock-layer, and the profiles are found to be smooth for the regularized model for all $Ma$. Overall, from this chapter, it is concluded that the regularized moment equations produce continuous shock structures beyond the critical Mach number of respective moment equations and the shock profiles appear more realistic since they compare well with DSMC results. The regularized version of extended hydrodynamic equations is therefore recommended for shock calculations in both molecular and granular gases.

# Nomenclature

### Roman Letters

| | | |
|---|---|---|
| $\mathbf{A}$ | : | Jacobian matrix of flux vector |
| $\mathbf{B}$ | : | Matrix of order $6 \times 6$ |
| $\mathbb{R}^{\boldsymbol{n}}$ | : | n-dimensional real space |
| $\boldsymbol{U}$ | : | Vector of variables |
| $\boldsymbol{F}(\boldsymbol{U})$ | : | Flux Vector of $\boldsymbol{U}$ |
| $x$ | : | One-dimensional position vector |
| $t$ | : | Time |
| $n$ | : | Particle number density |
| $m$ | : | Mass of a particle |
| $d$ | : | Diameter of a particle |
| $\mathbf{v}, \mathbf{v}_1$ | : | Pre-collisional velocities of two hard sphere particles |
| $\mathbf{v}', \mathbf{v}_1'$ | : | Post-collisional velocities of two hard sphere particles |
| $\boldsymbol{g}, \boldsymbol{g}'$ | : | Pre and post collision relative velocities |
| $\boldsymbol{k}$ | : | Unit collison vector |
| $\mathbf{r}, \mathbf{r}_1$ | : | Position vectors |
| $\mathbf{v}, \mathbf{v}_1$ | : | Particle velocity vectors |
| $f(\mathbf{r}, \mathbf{v}, t)$ | : | Single-particle distribution function |
| $\mathbf{F}$ | : | External force |
| $E$ | : | Granular kinetic energy |
| $\mathcal{J}$ | : | Determinant of the Jacobian matrix for the transformation $(\mathbf{v}'', \mathbf{v}_1'') \rightarrow (\mathbf{v}, \mathbf{v}_1)$ |
| $\chi(\mathbf{r}_1, \mathbf{r})$ | : | Pair distribution function |
| $\boldsymbol{\Omega}(f, f)$ | : | Collision integral |
| $u_i$ | : | Hydrodynamic velocity vector |
| $\boldsymbol{C}$ | : | Peculiar velocity |
| $p_{ij}$ | : | Pressure tensor |
| $q_i$ | : | Heat flux vector |
| $q$ | : | Heat flux in x-direction |
| $\mathcal{D}$ | : | Rate of energy dissipation per unit volume |
| $Q_{\langle ijk \rangle}$ | : | Traceless part of the third-order moment of $f$ |
| $R_{\langle ij \rangle}, R$ | : | Single and double contracted fourth-order moments of $f$ |
| $S_i$ | : | Double-contracted fifth-order moment |
| $Q$ | : | Shock asymmetry |

| | | |
|---|---|---|
| $\mathcal{H}^{(i)}$ | : | $i$th-order Hermite polynomial |
| $a^{(i)}$ | : | Expansion coefficients |
| $\sigma_{ij}^s, q_i^s, R^s$ | : | Collisional source terms |
| Ma | : | Mach number |
| $c$ | : | Adiabatic sound speed |
| $l$ | : | Mean free path |
| $\mathcal{L}$ | : | Characteristic length scale of a system |
| Kn | : | Knudsen number |
| Re | : | Reynolds number |
| $\mathcal{C}$ | : | The Courant-Friedrichs-Lewy (CFL) number |
| $L$ | : | Length of space domain |
| $u_N$ | : | Normalized velocity |
| $v_{sh}$ | : | Shock speed |
| $v_s$ | : | Speed of the density-peak |
| $\tilde{v}_s$ | : | Normalized shock speed |
| $\tilde{v}_s^\infty$ | : | Asymptotic shock speed |
| $\mathcal{D}_{reg}$ | : | Regularized dissipation rate |
| $\mathcal{F}$ | : | Regularization factor |
| $v_{cut}, V_c$ | : | Cut-off velocities |
| $s$ | : | Characteristic direction |
| $\mathcal{R}_{ijkl}, \mathcal{N}_{ijk}, \mathcal{M}_{ij}^{(6)}$ | : | Higher-order moments of $f$ |

**Greek Letters**

| | | |
|---|---|---|
| $\alpha$ | : | The coefficient of restitution |
| $\rho$ | : | The mass density |
| $\theta$ | : | Scalar temperature |
| $\theta_s$ | : | Skew temperature |
| $\sigma$ | : | Longitudinal stress |
| $\mu$ | : | Shear viscosity |
| $\kappa$ | : | Coefficient of thermal conductivity |
| $\kappa_h$ | : | Higher order coefficient of thermal conductivity |
| $\boldsymbol{\phi}$ | : | Arbitrary function of the velocity |
| $\vartheta$ | : | Relaxation rate in Burger's equation |
| $\gamma$ | : | Adiabatic index |
| $\sigma_{ij}$ | : | stress tensor |
| $\Delta$ | : | Dimensionless non-equilibrium part of the full contracted fourth-order moment $R$ |

| | | |
|---|---|---|
| $\epsilon$ | : | Relaxation rate in numerical schemes |
| $\rho_N, \theta_N$ | : | Normalized density and temperature |
| $\delta_1, \delta_2$ | : | Shock thickness |
| $\boldsymbol{\nabla}$ | : | Differential operator |
| $\triangle\rho$ | : | Density-overshoot |
| $\rho_{max}$ | : | Density maximum |
| $\theta_{\max}$ | : | Maximum granular temperature |
| $\tau_H$ | : | Relaxation time in Haff's law |
| $\theta_{cut}$ | : | Cut-off impact energy |
| $\delta, \epsilon_1, \epsilon_2$ | : | Small positive quantities which are of the same order |
| $\rho_J$ | : | Density at the shock state |
| $\psi$ | : | Higher-order moment/Non-conserved moment |
| $\varepsilon$ | : | A small parameter |
| $\tau_r$ | : | Relaxation time in regularization |

**Subscripts**

1 : Upstream state quantity

2 : Downstream state quantity

$c/cr$ : Critical value of a quantity

**Superscripts**

$s$ : Collisional source of a quantity

# List of Figures

# List of Tables

# Contents

# Chapter 1

# Introduction

## 1.1 Granular Materials

Granular materials are usually defined to be a collection of large number of discrete, dissipative, solid particles, which are ubiquitous in nature. They are one of the most used materials in the real world after water, and are of substantial importance in many industrial and natural processes [Campbell (1990); Jaeger *et al.* (1992); Ottino & Khakhar (2000); Goldhirsch (2003); Rao & Nott (2008); Forterre & Pouliquen (2008); Umbanhowar (2003)] such as agriculture, energy production, storms, avalanche, etc. They are so prevalent in the world that we eat them (rice, food grains), drink them (pharmaceutical powders), some times breathe them (dust), use them as cosmetics, and play with them (sand, snow) in our daily life. Granular materials play a very important role in many industrial processes because almost every industry (food industry, agriculture industry, chemical industry, construction industry, and pharmaceutical industry, etc.) relies on the bulk transport of granular materials such as sand, cement, coal, crushed stones, food grains, pharmaceuticals, chemicals, etc [Jaeger *et al.* (1992)].

(a) Red soil (b) Gravel (c) Coal

(d) Fertilizers (e) Food grains (f) Pills

Figure 1.1: Few examples of granular matter that we see them in our daily life.

The size of granular particles may range from micro scale (chemical powders, pills, fertilizer, etc.) to macro scale (infrastructure materials), and they occur in various geometries. In fact, the particle size depends on the phenomena in which granular particles are taking place [for example

packing powders may range from 1 $\mu$m to mm, a box of cereal ranges from mm to cm, food grains in a silo, rocks and boulders ranges from cm to m]. Furthermore, most granular particles are large enough in size such that Brownian motion is irrelevant and hence they interact solely by friction and collision [Aranson & Tsimring (2006)]. Some examples of granular matter are shown in the Fig. 1.1.

(a) Dry sand pile (b) Wet sand pile

Figure 1.2: Difference between dry and wet granular materials [Mitarai & Nori (2006)].

Granular materials are mainly classified into two namely dry and wet granular materials, depending on the interstitial fluid between the granules. The interstitial fluid is a gas (usually air) in case of dry granular materials and hence the effects of interstitial fluids are negligible for the particle dynamics in dry granular materials [Mitarai & Nori (2006); Herminghaus (2005)]. Moreover, for dry granular media, the dominant interactions are inelastic collisions and friction, which are short-range and non-cohesive. On the other hand, the interstitial fluid in wet granular materials is a liquid, for example, water. The major effect that the liquid can induce in granular materials is cohesion between the granules [Mitarai & Nori (2006)]. Some times, even humidity in the air may introduce cohesion. Further, if the wet granular media become overwet, that means the system is completely immersed in a liquid, they are referred to as saturated granular materials or suspensions.

(a) Sand castle (b) Hour glass (c) Dust devil

Figure 1.3: Solid like, liquid like, and gas like behaviour of granular materials [Van der Weele (2008)].

In the physical world, we often see both dry and wet granular materials, such as dry sand and beach sand, respectively. Although both have many aspects in common, but one major difference between dry and wet granular materials is that wet granular materials are cohesive due to surface tension where as dry granular materials are non-cohesive in nature (see Fig. 1.2). Both dry and wet granular materials show unique and striking behaviours, which have attracted the attention of many physicists, mathematicians and engineers for centuries.

According to Jaeger *et al.* (1996), the granular material behaves differently from any of the other familiar forms of matter - solids, liquids, or gases and should therefore be considered an additional state of matter in its own right. This argument follows from the observations that the properties of granular materials are very different from the well-known three states of matter. It has been shown that they can stay at rest like a solid, flow like a liquid, or behave like a gas, and they can behave differently apart from these states too, depending on the rate of external energy input to activate the granules [Mitarai & Nori (2006)]. Figure 1.3 shows that the granular material can exist in all three states of matter. Apart from their practical and natural significance, they also exhibit many interesting, complex and diverse phenomena such as clustering, jamming, segregation, patterns formation, Leidenfrost effect, granular convection, Brazil and inverse-Brazil nut effects, and roll waves [Jenkins & Savage (1983); Campbell (1990); Ottino & Khakhar (2000); Samadani & Kudrolli (2000); Goldhirsch (2003); Aranson & Tsimring (2006); Forterre & Pouliquen (2008); Razis *et al.* (2014)]. They also exhibit multiple metastable steady states which are far from equilibrium and they may exhibit a transition from a granular solid to a liquid and various ordered patterns under a variety of large driving forces [Aranson & Tsimring (2006)]. Few phenomena exhibited by granular materials are shown in Fig. 1.4.

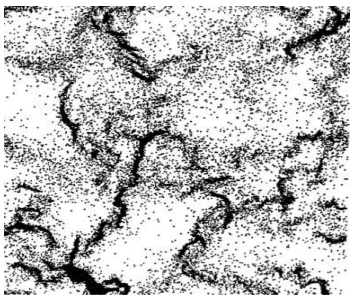

(a) Cluster formation [Goldhirsch & Zanetti (1993)]

(b) Granular convection [Shukla *et al.* (2014)]

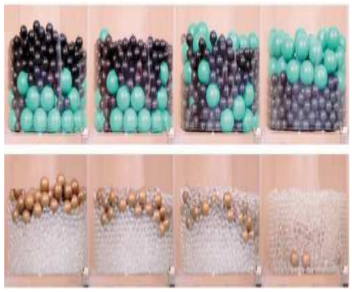

(c) Brazil nut and reverse Brazil nut effect [Breu *et al.* (2003)]

Figure 1.4: Phenomena exhibited by granular matter.

One extreme state of driven granular materials is a *granular gas* [Pöschel & Luding (2001); Goldhirsch & Zanetti (1993); Goldhirsch (2003)] which can be realized under strong external driving (such as shaking, shearing, stirring or other means), the particles move around randomly, resembling the motion of atoms in a molecular gas, but it differs from a molecular gas in that the macroscopic particles collide inelastically, resulting in a loss of kinetic energy $\sim (1-\alpha^2)$, where $0 \leq \alpha \leq 1$ is the coefficient of restitution, which characterize inelastic collisions, with $\alpha = 0$ and 1 referring to perfectly sticky and elastic collisions, respectively. Due to inelastic collisions there is a transformation of the translational kinetic energy into heat and the mechanical energy is lost which implies a decay of granular temperature with time unless it is replenished by some

external source. Granular gases fall under the category of *rapid flows* which are well-described by hydrodynamic-like equations. The coarse-graining of pertinent "inelastic" Boltzmann equation results in Euler and Navier-Stokes-type equations, modified to account for inelastic dissipation that appears as an extra term in the energy equation. Such hydrodynamic equations have been employed to understand the dynamics of granular fluids in different flow-configurations (vibrated bed, Couette flow, Chute flow, etc.) up-to a moderate density. One noteworthy feature of rapid granular flows is that they can be supersonic [Haff (1983)] and shock waves form even under normal conditions [e.g. flow around obstacles [Buchholtz & Pöschel (1998); Rericha *et al.* (2001); Amarouchene & Kellay (2006); Boudet *et al.* (2008)], strong shaking [Bougie *et al.* (2002); Carrillo *et al.* (2008)], and shallow free-surface flows [Hutter & Savage (1988); Savage & Hutter (1989); Gray *et al.* (2003); Gray & Thornton (2005)]]. Rapid flows of granular materials also occur in geophysical and other natural phenomena such as interstellar dust, rock and land slides, debris flows, snow avalanches, sand dunes, and planetary rings. Figure 1.5 shows some rapid granular flows which are seen in the different parts of the world.

(a) Snow avalanche (b) Sanddune

Figure 1.5: Real life examples of rapid granular flows.

## 1.2 Shock Waves in Molecular Gas

A plane shock wave is generated when a supersonic gas flows into a subsonic gas; mathematically, this is nothing but a discontinuity across which the hydrodynamic fields undergo discontinuous jumps [Courant & Friedrichs (1948)]. The simplest nonlinear equation that admits shock solutions is the inviscid Burger equation which represents a nonlinear "hyperbolic" conservation equation and is given by

$$\frac{\partial u}{\partial t} + u\frac{\partial u}{\partial x} = 0. \tag{1.1}$$

This equation serves as a beautiful example of an equation whose solutions represent nonlinear waves in which the propagation velocity of a point on the pulse is equal to the amplitude at that point and also appears as a best natural model for a significant class of physical phenomena governed by a single conservation law [(Whitham 1974; Prasad 2001)]. Now we will briefly show how this equation (1.1) admits a shock by using a particular initial condition which is taken to be

$$u(x,0) = e^{-x^2}, \quad x \in \mathbb{R}. \tag{1.2}$$

In this regard we consider a successive geometrical shapes of the initial pulse given by (1.2). The pulse of the nonlinear wave deforms as $t$ increases, which is clear from the left panel of Fig. 1.6.

From the Fig. 1.6 it may be noted that at a critical time ($t \approx 1.166$) the pulse has a tangent with slope $\infty$ for the first time at some point on it and later the pulse ceases to represent the graph of a function hence the physical interpretation fails. It has been observed that immediately after the critical time, a moving discontinuity built up in the quantity $u$, which is called a shock. Shock fits into the multi-valued part of the solution in such a way that it cuts off lobes of areas on both sides of it in a certain ratio at any time greater than critical time and makes the solution single valued, which is shown in the right panel of Fig.1.6 [(Prasad 2001)]. The formation of shock can also be explained from the geometry of the characteristic curves of the equation (1.1), for details we refer to Courant & Friedrichs (1948); Smoller (1983); Prasad (2001). Now we

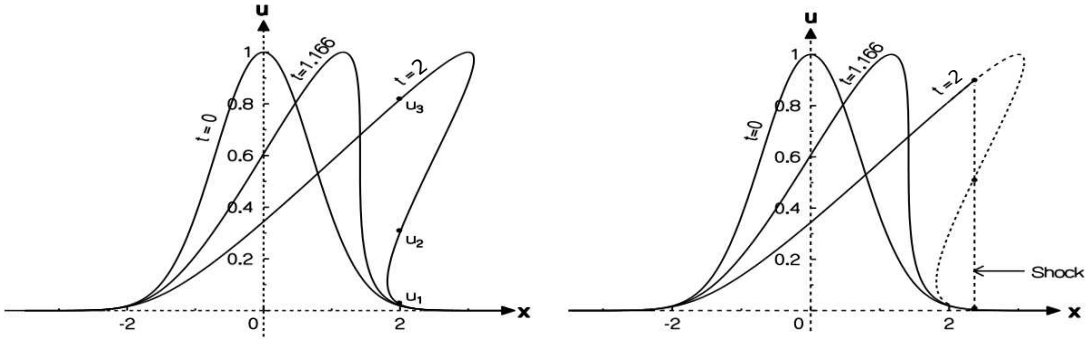


Figure 1.6: Deformation of the pulse with time (on left) and formation of shock in inviscid Burger equation. Both figures are adopted from Prasad (2001)

consider the equation originally studied by Burger [(Burgers 1948)] which includes a diffusive term as a source term to the equation (1.1) and is given as

$$\frac{\partial u}{\partial t} + u\,\frac{\partial u}{\partial x} = \vartheta\,\frac{\partial^2 u}{\partial x^2}, \tag{1.3}$$

which is also called viscous Burger equation and this is the simplest model equation which combines the nonlinear and viscous effects of fluid mechanics [(LeVeque 1992)]. Left panel of Fig. 1.7 shows that after some finite time, there are some points $x$ at which the characteristics have crossed and there are three characteristics which can be traced back to $t = 0$. Moreover, at this point the solution $u(x, t)$ represents a triple-valued function which does not make sense in physical processes. At the time where the characteristics first cross, the solution $u(x, t)$ has an infinite slope– the wave solution breaks and forms a shock. In contrast this phenomena is absent in the solution of viscous Burger equation, which is evident from the right panel of Fig. 1.7.

By adopting the vanishing viscosity method, one can determine the feasible solutions to the physical problems using inviscid Burger equation for large time. Since the equation (1.1) is a model of (1.3) for small $\vartheta$. If $\vartheta$ is very small and the initial data is smooth, before the wave begins to break the viscous term $\vartheta\,(\partial^2 u/\partial x^2)$ is negligible as compared to the other terms and hence the solutions to both equations look identical. Nevertheless, as the wave starts to break,

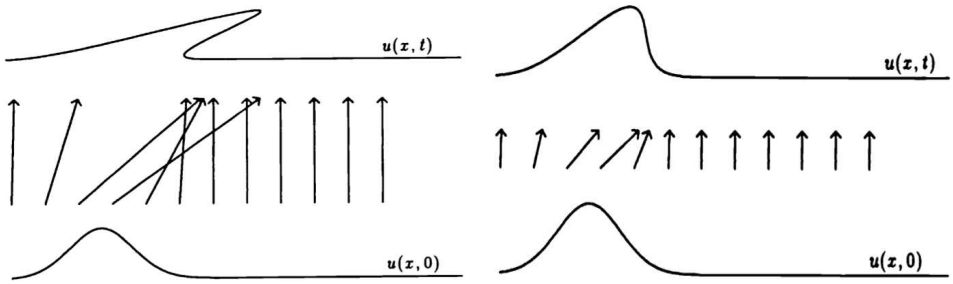


Figure 1.7: Triple valued solution which leads to formation of shock in inviscid Burger equation (1.1) (on left), solution and characteristics of viscous Burger equation (1.3) for small $t$ (on right). Both are adopted from LeVeque (1992)

the second derivative term $(\partial^2 u/\partial x^2)$ grows faster than $\partial u/\partial x$. Hence at some point the term $\vartheta\,(\partial^2 u/\partial x^2)$ begins to play a role as this term is comparable to the other terms and this keeps the solution smooth for all time, preventing the breakup of solutions that occurs for a inviscid Burger equation or for the hyperbolic problem [(LeVeque 1992)], which is clearly evident from the Fig. 1.8.


Figure 1.8: Solution to the viscous Burger's equation for different values of $\vartheta$ LeVeque (1992)

A system of conservation laws given by

$$\frac{\partial \boldsymbol{U}}{\partial t} + \frac{\partial \boldsymbol{F}(\boldsymbol{U})}{\partial x} = 0, \tag{1.4}$$

where $\boldsymbol{U} \in \mathbb{R}^n$, is hyperbolic if the Jacobian matrix of $\boldsymbol{F}(\boldsymbol{U}) = \mathbf{A}$ has $n$ distinct real eigen values, which means that matrix $\mathbf{A}$ is diagonalizable. A hyperbolic system in an infinite domain $(-\infty < x < -\infty)$ with discontinuous initial conditions constitutes the "Riemann problem" of shock waves [Courant & Friedrichs (1948); Prasad (2001)]. This means that the Riemann problem for a system of conservation laws is as follows:

$$\frac{\partial \boldsymbol{U}}{\partial t} + \mathbf{A}\frac{\partial \boldsymbol{U}}{\partial x} = 0, \tag{1.5}$$

where $\boldsymbol{U} \in \mathbb{R}^{\boldsymbol{n}}$ and $\mathbf{A}$ is a $n \times n$ matrix with $n$ distinct real eigen values with the following initial condition

$$\boldsymbol{U}_0(x) = \begin{cases} \boldsymbol{U}_1 & x \leq 0 \\ \boldsymbol{U}_2 & x > 0 \end{cases} \tag{1.6}$$

From experimental viewpoints, the Riemann problem can be mimicked by the one-dimensional version of the shock-tube problem which comprises of a gas-filled long-tube separated into two chambers by a membrane. The gases in two chambers are in equilibrium, but differ in pressure and density. After the membrane is burst, a shock wave and a contact discontinuity travel into

the low pressure region of the tube at supersonic speeds and a rarefaction wave travels into the opposite direction. Apart from its interesting physical properties, the shock-tube problem also serves as a standard benchmark to check (i) the accuracy of gas dynamics models as well as (ii) the robustness of the numerical scheme to reproduce the shock profiles. Some advantages of the Riemann problem which make it so attractive for numerical simulations are [(Grad 1952; LeVeque 2002; Greenshields & Reese 2007)]: (i) its one-dimensional nature, (ii) the upstream and downstream boundary conditions are clearly specified by the Rankine-Hugoniot conditions, (iii) the gradients of hydrodynamic fields vanish far upstream and downstream of the shock, and (iv) solid boundaries are absent.

Figure 1.9 shows the schematic of a shock wave caused by a piston. A plane piston moving with a constant velocity $U$ compresses an initially resting gas, with constant density $\rho_0$ and pressure $P_0$ and the resulting flow can be divided into three regions, namely, compression, undisturbed and transition regions, as shown in Fig. 1.9. The transition region connecting compression and undisturbed regions reduces to a discontinuity, which is considered to be shock wave front [(Pöschel & Brilliantov 2003)].

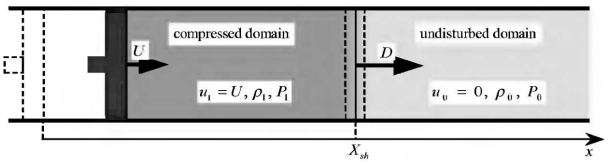


Figure 1.9: Schematic of piston driven shock wave within a molecular gas. Adopted from Pöschel & Brilliantov (2003)

## 1.3 Shock Waves in Granular Gas

The analogous Riemann problem of shock waves in "granular" gas is interesting in its own right and might be helpful for a better understanding of macroscopic properties of granular gases as well as to check the validity of adopted hydrodynamic equations [Haff (1983); Jenkins & Savage (1983); Goldshtein & Shapiro (1995); Esipov & Pöschel (1997); Sela & Goldhirsch (1998); Garzó *et al.* (2007); Saha & Alam (2014)]. In previous works on plane shock-waves in granular gases [Goldshtein *et al.* (1995); Kamenetsky *et al.* (2000); Serna & Marquina (2005)], the Euler-level hydrodynamic equations, with dense-gas corrections for pressure and inelastic dissipation, were employed to analyse the well-known "piston" problem: *a rigid piston moves through an undisturbed granular gas with a constant velocity, resulting in a steadily propagating shock front.* Specific assumptions were made on the state of the gas adjacent to the piston, yielding a "solid" region (with maximum density and zero granular temperature) next to the piston that coexisted with a non-uniform region having a propagating shock-front at the downstream end. The primary motivation of these works was to understand a possible relation between the transport of mass and energy in a vertically vibrated bed of granular materials and the shock-wave propagation through the bed.

Latter works [Bougie *et al.* (2002); Carrillo *et al.* (2008)] investigated the role of shock-wave propagation on 'pattern-formation' scenario in a vertically vibrated bed by solving Navier-Stokes-order equations but supplemented with boundary conditions. Deriving/postulating the correct forms of boundary conditions still remains an active field of research [Nott (2011)] in rapid granular flows.

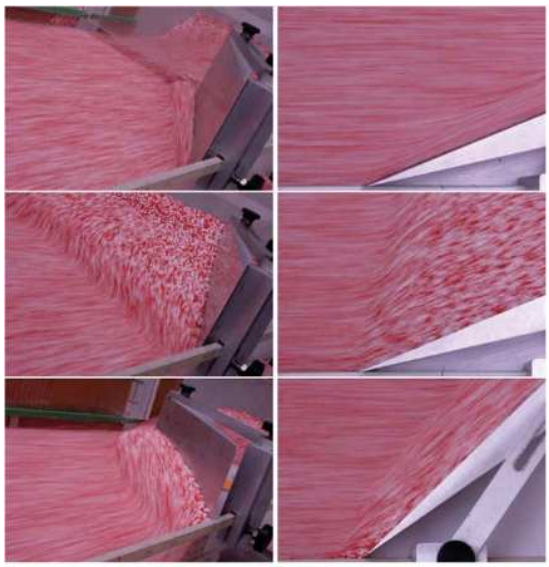

Figure 1.10: Perspective (on the left) and overhead (on the right) views of Weak (top), strong (middle) and detached oblique (bottom) shock formation in granular free surface flows. This is taken from Gray & Cui (2007)

Propagation of shock wave arising from one-dimensional motion of a solid piston while advancing in granular gas was first treated theoretically by Goldshtein *et al.* (1996*a*). When the solid piston moves into a cold motionless gas with a finite speed $U$ in the absence of gravity generates a shock. Granules gains kinetic energy when passing through the shock front and granular collisions lead to a continuous decrease of granular energy. This phenomena give rise to formation of a layer of densely packed granules (solid block) on the moving piston which is separated from the shock front by a fluidized region [(Goldshtein *et al.* 1996*a*; Kamenetsky *et al.* 2000)]. More recently, the molecular dynamics (MD) simulations have been used to analyse the instability of the granular shock front [(Sirmas & Radulescu 2014)] in a visco-elastic granular gas.

Experimentally, oblique shock waves and bow shock waves have been observed in granular free surface flows [(Gray *et al.* 2003; Gray & Thornton 2005; Gray & Cui 2007; Cui & Gray 2013)]. Figure 1.10 shows the formation of weak, strong and detached oblique shocks when dry granular avalanches composed of non-pareille sugar grains flows on a chute, inclined at $38^{\circ}$ to the horizontal [(Gray & Cui 2007)]. The teardrop shaped shock generated when the flow of sand from a funnel with a circular mouth impacting with the inclined plane [(Johnson & Gray 2011)], which is shown in the left panel of Fig. 1.11. The right panel of Fig. 1.11 shows the top view of a bow shock, stagnation point and particle-free granular vacuum, generated when a sand avalanche flows around a circular cylinder on a chute which is inclined at $36^{\circ}$ to the horizontal [Cui & Gray (2013)].

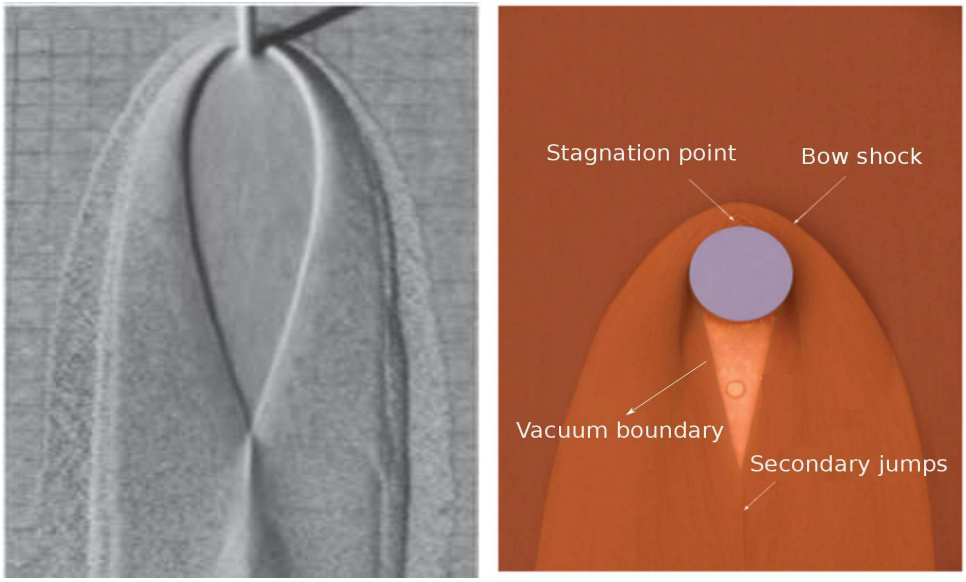


Figure 1.11: On left: Steady state teardrop shaped shock [(Johnson & Gray 2011)], on right: bow shock [Cui & Gray (2013)].

## 1.4 Objectives and Motivation of Present Work

A rapid granular flow resembles the classical picture of a molecular gas and therefore the fluidized state of granules is termed as granular gas [Goldhirsch & Zanetti (1993)]. The study of granular shock waves might be helpful for a better understanding of macroscopic properties of granular gases. In all previous works [Goldshtein & Shapiro (1995); Goldshtein *et al.* (1995, 1996*a*,*b*); Kamenetsky *et al.* (2000); Serna & Marquina (2005)] on shock-waves in granular gases, the Euler and Navier-Stokes equations were employed but such equations are valid when the Knudsen number (Kn) is close to zero and hence are not suitable when the flow is in the rarefied regime (Kn $>$ 0.1). It may be noted, however, that the standard Navier-Stokes-level hydrodynamic equations are not adequate to capture macroscopic behavior of granular gases when the restitution coefficient is much smaller than its elastic limit and/or when the Knudsen number (Kn) is close to zero.

Since the normal stress differences [Alam & Luding (2003, 2005)] are of order one in a granular gas which requires a Burnett-order description in terms of an extended set of hydrodynamic fields. Understanding the possible effects of such order-one normal stresses [Alam & Luding (2003, 2005)] in rarefied granular gases on shock-wave dynamics forms one motivation of the present work. As the dynamics is well described by the 'inelastic' Boltzmann equation, the solution of it via DSMC (direct simulation Monte Carlo) technique will be very useful but this method is prohibitive with regards to computational requirements [Torrilhon & Struchtrup (2004)]. Hence extended hydrodynamic models are appropriate for studying molecular/granular gases in the rarefied regime and are also used for the modeling of granular gas [Goldhirsch (2003); Garzó (2013)]. In an extended hydrodynamic approach the problem of solving the "inelastic" Boltzmann equation is replaced by solving a system of generalized transport equations, which is discussed in Chapter 2 in detail.

In the remainder of this thesis, we analyse the well-known Riemann problem of the plane shock waves propagating in an unbounded granular gas which, to our knowledge, has not been studied before. The supersonic and subsonic granular gases are taken as the left and right states, separated by a discontinuity whose time-evolution is analysed. We study the one-dimensional shock waves in a dilute granular gas: using five levels of granular hydrodynamic equations: (i) Euler equations, (ii) Navier-Stokes equations, (iii) 10-moment equations, (iv) 13-moment equations and (v) 14-moment equations. We solve all these hydrodynamic equations of a dilute granular gas using a relaxation-type numerical scheme. Our focus is to identify the structural features of granular shock profiles (of density, temperature and velocity) and contrast them with those of an ideal molecular gas. In addition, the validity of Haff's law Haff (1983) is critically assessed in the presence of a shock wave and certain scaling relations are uncovered. The large-time evolution of shock profiles is briefly discussed.

To summarize, the primary goals of this thesis are to (i) study the well-known Riemann problem of plane shock waves propagating in a granular gas using hydrodynamic-like equations (Chapters 3 and 4), (ii) develop numerical schemes to solve the related inhomogeneous PDEs (Chapter 3), (iii) analyse and identify the unique characteristics of granular shock-waves in comparison to their molecular counterparts (Chapter 4), (iv) a comparative analysis between the predictions of the Euler- and Navier-Stokes-order hydrodynamic equations and the "extended" (beyond Navier-Stokes-order) hydrodynamic models (Chapter 6), (v) analyse the characteristics and the well-posedness of extended granular hydrodynamic models (Chapter 5) and finally (vi) suggest ways to 'regularize' the extended moment models for a granular gas (Chapter 7) so as to obtain smooth solutions at any Mach number.

## 1.5 Organization of Present Thesis

This work begins with a brief review of kinetic theory of dilute granular gas along with the moment closure approaches. In Chapter 2, we derive the 'inelastic' Boltzmann equation and discuss moment closure approaches. We also briefly discuss about different moment models of a dilute granular gas, namely, the ten moment, thirteen moment and fourteen moment models based on Grad's procedure along with Euler and Navier-Stokes models. We adopt the 14-moment model for a granular gas derived by Kremer and Marques (2011) and use it to derive the lower-oder models and related constitutive relations.

Chapter 3 presents the theory of normal shock waves and numerical schemes used to solve the hydrodynamic and extended hydrodynamic equations along with the validation of numerical schemes.

The analysis of the Riemann problem of plane shock waves for a dilute granular gas is presented in Chapter 4 by solving Euler and Navier-Stokes level of hydrodynamic equations numerically.

Chapter 5 shows the reduction of extended hydrodynamic equations to one-dimension and their characteristics analysis along with their critical Mach number analysis. The derivation of Haff's law from the 14-moment model is also presented in this chapter.

Plane shock wave structure is analysed for a molecular gas and dilute granular gas by solving different sets of moment equations numerically in Chapter 6. Results obtained from these models are compared with Navier-Stokes hydrodynamic equations and with the available literature.

In Chapter 7, we derive the "regularized" moment equations for a dilute granular gas. An investigation of plane shock wave via "regularized" ten moment equations is presented and the results are compared with the Grad-type 10-moment equations.

Finally the summary and the future work are presented in Chapter 8.

Characteristics of plane blast waves in a granular gas is studied using the extended hydrodynamic models and Navier-Stokes model. Results on blast waves are presented in Appendix: A.

# Chapter 2

# Kinetic Theory of Dilute Granular Gas

## 2.1 Introduction

In classical mechanics the flow of a gas composed of monatomic molecules is completely described by Newton's equation of motion with given initial conditions (the position and the velocity of each and every molecule) at a particular instant. This approach to the theory of a gas has two drawbacks. Firstly, the lack of detailed initial conditions at a prescribed initial instant; secondly, the number of molecules that compose the gas are so enormously large (one mole of a gas contains $6.022 \times 10^{23}$ molecules) that even if we know the initial conditions exactly, in the task of following the subsequent motions of each and every molecule, the calculations are unimaginable. Hence this description is not manageable even for a dilute gas. The alternative description is to consider the statistical averages in terms of the velocity distribution function $f(\mathbf{r}, \mathbf{v}, t)$, whose evolution is governed by the well-known Boltzmann equation [(Boltzmann 1878; Burnett 1935; Grad 1949; Chapman & Cowling 1970; Sone & Aoki 1987)]. In this chapter, we briefly review the "inelastic" Boltzmann equation and discuss the closure problem of moment equations. Finally we present the transport equations and constitutive relations for the "extended" hydrodynamic equations [(Kremer & Marques Jr 2011; Brilliantov & Pöschel 2003; Struchtrup 2005*b*)] that are more appropriate for rarefied dilute gases.

## 2.2 The Inelastic Boltzmann Equation

The fundamental equation of kinetic theory of molecular gases is the Boltzmann equation derived by Ludwig Eduard Boltzmann in 1872. It is a non-linear integro-differential equation for the one particle distribution function that describes the evolution in space and time of a monatomic ideal gas due to collisions and free flight of particles. To understand the macroscopic nature of granular gases, the kinetic theory of granular gases has been developed by many authors [(Jenkins & Richman 1985*a*; Brey *et al.* 1997, 1998, 1999; Garzó & Dufty 1999; Alam *et al.* 2002; Goldhirsch 2003; Brilliantov & Pöschel 2004; Pöschel & Luding 2001; Rao & Nott 2008)]. The collisions in granular gases are inelastic, unlike in molecular gases, and hence one needs to modify the collisional source term to take into account the effect of inelasticity. Like molecular gases, when applying kinetic theory to granular gases, the following assumptions are taken into account while deriving the inelastic Boltzmann equation [(Goldhirsch 2003; Brilliantov & Pöschel 2004; Kremer 2010)]:

- Granular gas is composed of smooth and frictionless hard spherical molecules.

- Collisions are binary and instantaneous.
- The energy is dissipated due to inelastic collision.

In this section, we derive the inelastic Boltzmann equation for granular gases by using the above assumptions.

We consider a granular gas, where the particles are of mass $m$ and diameter $d$ and interact via binary collisions. The velocities of two particles before collision and after collision are given by $(\mathbf{v}, \mathbf{v}_1)$ and $(\mathbf{v}', \mathbf{v}_1')$ respectively. The geometry of the collision may range from a head-on collision to a glancing one. The schematic picture of a binary collision between two spherical granular particles is depicted in Fig. 2.1. We specify the geometry of the collision by the unit collision vector $\boldsymbol{k}$ pointing from the center of the particle denoted by index 1 to the center of the other particle without index. The collisions in a granular gas are inelastic and are characterized by the following relation:

$$(\boldsymbol{g}' \cdot \boldsymbol{k}) = -\alpha(\boldsymbol{g} \cdot \boldsymbol{k}), \tag{2.1}$$

where $\boldsymbol{g} = (\mathbf{v}_1 - \mathbf{v})$ and $\boldsymbol{g}' = (\mathbf{v}_1' - \mathbf{v}')$ denote the relative velocities before and after a collision, respectively, and $\alpha$ is the coefficient of restitution. Note that $\alpha \in [0, 1]$, with $\alpha = 1$ and 0 representing perfectly elastic and sticky collisions, respectively. The binary collision between two spherical granular particles leads to the following collision law:

$$\mathbf{v}' = \mathbf{v} + \frac{(1+\alpha)}{2}(\boldsymbol{g} \cdot \boldsymbol{k})\boldsymbol{k}, \qquad \mathbf{v}_1' = \mathbf{v}_1 - \frac{(1+\alpha)}{2}(\boldsymbol{g} \cdot \boldsymbol{k})\boldsymbol{k}. \tag{2.2}$$

It follows that the change in kinetic energy upon a collision is given by

$$\Delta E = \frac{m}{2}\mathbf{v}'^2 + \frac{m}{2}\mathbf{v}_1'^2 - \frac{m}{2}\mathbf{v}^2 - \frac{m}{2}\mathbf{v}'^2 = -\frac{m}{4}(1-\alpha^2)(\boldsymbol{g} \cdot \boldsymbol{k})^2, \tag{2.3}$$

which is zero for perfectly elastic collisions ($\alpha = 1$, i.e., in a molecular gas).

The state of the granular gas is described by single-particle distribution function $f(\mathbf{r}, \mathbf{v}, t)$ which characterizes the spatial and velocity distribution of individual particles. The single-particle distribution function is defined such that $f(\mathbf{r}, \mathbf{v}, t)\mathrm{d}\mathbf{r}\mathrm{d}\mathbf{v}$ gives the number of particles at time t in a differential volume d$\mathbf{r}$ around the position $\mathbf{r}$ and a differential velocity volume $d\mathbf{v}$ around the velocity $\mathbf{v}$.

In the absence of collisions within an infinitesimal time interval d$t$, all particles in the phase space volume d$\mathbf{r}$d$\mathbf{v}$ at time $t$ will be found in the phase space $\mathrm{d}(\mathbf{r}+\mathbf{v}\mathrm{d}t)\mathrm{d}(\mathbf{v}+\frac{\mathbf{F}}{m}\mathrm{d}t)$, where $\mathbf{F}$ is the external force. Since the volume of the phase space is conserved, we have $\mathrm{d}(\mathbf{r}+\mathbf{v}\mathrm{d}t)\mathrm{d}(\mathbf{v}+\frac{\mathbf{F}}{m}\mathrm{d}t) = \mathrm{d}\mathbf{r}\mathrm{d}\mathbf{v}$. This statement can be written in terms of distribution function as

$$f(\mathbf{r} + \mathbf{v}\mathrm{d}t, \mathbf{v} + \frac{\mathbf{F}}{m}\mathrm{d}t, t + \mathrm{d}t)\mathrm{d}\mathbf{r}\mathrm{d}\mathbf{v} - f(\mathbf{r}, \mathbf{v}, t)\mathrm{d}\mathbf{r}\mathrm{d}\mathbf{v} = 0. \tag{2.4}$$

If collisions are allowed, some particles collide during the time interval d$t$ and hence the R.H.S of Eq. (2.4) is not identically equal to zero. The net increase of the number of particles in the volume d$\mathbf{r}$d$\mathbf{v}$ during the time interval d$t$ is proportional to d$\mathbf{r}$d$\mathbf{v}$d$t$. So in the presence of

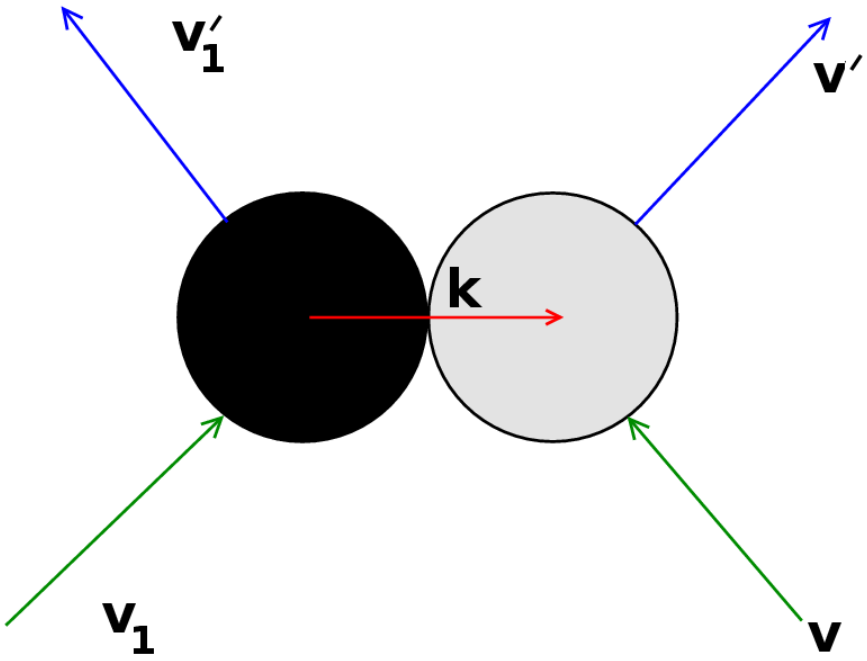


Figure 2.1: Schematic of a binary collision between two hard sphere particles.

collisions, Eq. (2.4) is modified as

$$f(\mathbf{r}+\mathbf{v}\mathrm{d}t, \mathbf{v}+\frac{\mathbf{F}}{m}\mathrm{d}t, t+\mathrm{d}t)\mathrm{d}\mathbf{r}\mathrm{d}\mathbf{v} - f(\mathbf{r},\mathbf{v},t)\mathrm{d}\mathbf{r}\mathrm{d}\mathbf{v} = \left(\frac{\partial f}{\partial t}\right)_{coll}\mathrm{d}\mathbf{r}\mathrm{d}\mathbf{v}\mathrm{d}t, \tag{2.5}$$

where

$$\left(\frac{\partial f}{\partial t}\right)_{coll} = \text{Gain due to inverse collisions} - \text{Loss due to direct collisions}, \tag{2.6}$$

represents the rate of change of distribution function due to collisions [(Chapman & Cowling 1970)]. Using Taylor's series expansion of $f(\mathbf{r}+\mathbf{v}\mathrm{d}t, \mathbf{v}+\frac{\mathbf{F}}{m}\mathrm{d}t, t+\mathrm{d}t)$ about $(\mathbf{r},\mathbf{v},t)$ up-to the terms containing $\mathrm{d}t$ we arrive at the Boltzmann equation

$$\frac{\partial f}{\partial t} + \mathbf{v}.\frac{\partial f}{\partial \mathbf{r}} + \frac{\mathbf{F}}{m}.\frac{\partial f}{\partial \mathbf{v}} = \left(\frac{\partial f}{\partial t}\right)_{coll}. \tag{2.7}$$

In the absence of external body force the Boltzmann equation becomes

$$\frac{\partial f}{\partial t} + \mathbf{v}.\frac{\partial f}{\partial \mathbf{r}} = \left(\frac{\partial f}{\partial t}\right)_{coll}. \tag{2.8}$$

To find an expression for $\left(\frac{\partial f}{\partial t}\right)_{coll}$, we consider only binary collisions between particles and introduce the two-particle distribution function such that

$$f^{(2)}(\mathbf{r},\mathbf{v},\mathbf{r}_1,\mathbf{v}_1,t)\,\mathrm{d}\mathbf{r}\,\mathrm{d}\mathbf{r}_1\,\mathrm{d}\mathbf{v}\,\mathrm{d}\mathbf{v}_1 \tag{2.9}$$

is the number of particles at time $t$ with one particle having position within $d\mathbf{r}$ around $\mathbf{r}$ and velocity within $d\mathbf{v}$ around $\mathbf{v}$ and the other particles within $d\mathbf{r}_1$ around $\mathbf{r}_1$ and velocity within

$d\mathbf{v}_1$ around $\mathbf{v}_1$.

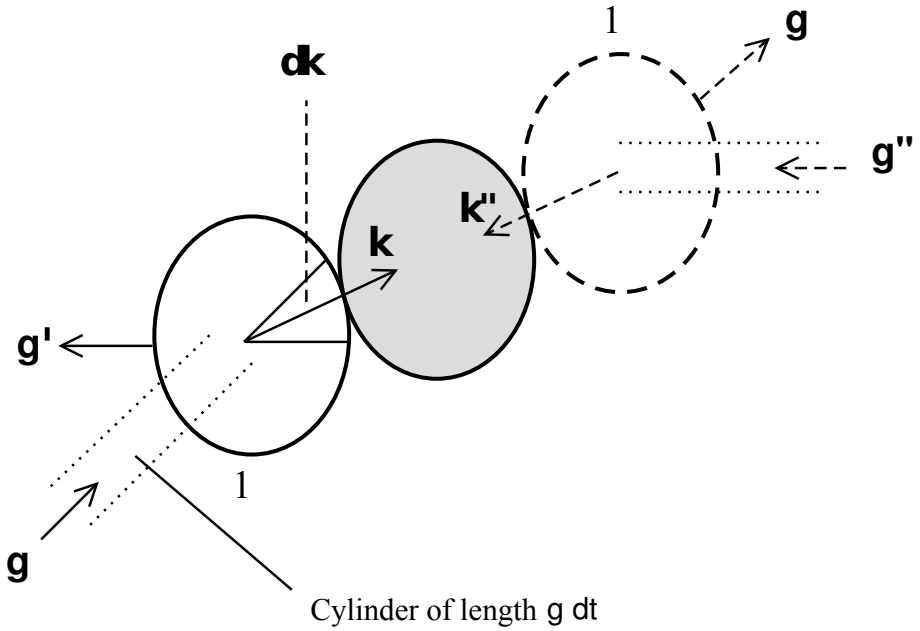


Figure 2.2: The velocity and trajectory of particle 1 before and after it collides with test particle. The position vector of test particle in the laboratory reference frame is $\mathbf{r}$, and $\boldsymbol{k}$ is the unit vector pointing toward the center of test particle from the center of particle 1. The dashed circle represents particle 1 in the restituting/inverse collision.

Let the particle without index (see Fig. 2.2) be our test particle which lives in the phase space $d\mathbf{r}d\mathbf{v}$. Now consider the collision of particle 1 with the test particle during the time interval $\mathrm{d}t$. First we determine the rate at which the particles will leave the volume $\mathrm{d}\mathbf{r}\mathrm{d}\mathbf{v}$ by direct collisions and later determine the rate at which particles will enter into this volume by inverse collisions. The collisional contact of particle 1 with the test particle is to occur on an infinitesimal element of its surface defined by the solid angle $\mathrm{d}\boldsymbol{k}$ around $\boldsymbol{k}$ and its center at the instant of contact must be in a region around $\mathbf{r} - \boldsymbol{k}\, d$. During the time interval $\mathrm{d}t$ the center of particle 1 will move a distance $|\boldsymbol{g}|\mathrm{d}t$. i.e, the center of particle 1 must reside in a cylinder of length $|\boldsymbol{g}|\mathrm{d}t$ and a cross-section area $d^2\mathrm{d}\boldsymbol{k}(\frac{\boldsymbol{g}\cdot\boldsymbol{k}}{|\boldsymbol{g}|})$. So the volume in which particle 1 resides during the time interval $\mathrm{d}t$ before collision and having the velocity in the range $\mathrm{d}\mathbf{v}_1$ is $\mathrm{d}\mathbf{r}_1 = d^2\mathrm{d}\boldsymbol{k}(\boldsymbol{g}\cdot\boldsymbol{k})\mathrm{d}t$. Hence the number of collisions which are responsible for decrease of particles in the phase space $\mathrm{d}\mathbf{r}\mathrm{d}\mathbf{v}$ during the time interval $\mathrm{d}t$ is

$$f^{(2)}(\mathbf{r} - d\,\boldsymbol{k}, \mathbf{v}_1, \mathbf{r}, \mathbf{v}, t)\, d^2\, (\boldsymbol{g}\cdot\boldsymbol{k})\, \mathrm{d}\boldsymbol{k}\, \mathrm{d}\mathbf{r}\, \mathrm{d}\mathbf{v}\, \mathrm{d}\mathbf{v}_1\, \mathrm{d}t \tag{2.10}$$

with $\boldsymbol{g}\cdot\boldsymbol{k} > 0$ so that only impending collisions are counted.

Now we determine the rate at which particles enter into the range $\mathrm{d}\mathbf{r}\mathrm{d}\mathbf{v}$ by inverse/restituting collisions [Chapman & Cowling (1970)]. Let us consider the pre-collisional velocities of particle 1 and test particle for inverse collision be $\mathbf{v}_1''$ and $\mathbf{v}''$, respectively, and after collision their velocities will be $\mathbf{v}_1$ and $\mathbf{v}$, respectively. The accumulation of particles in the phase space volume $\mathrm{d}\mathbf{r}\mathrm{d}\mathbf{v}$

during the time interval $\mathrm{d}t$ due to inverse collisions is

$$f^{(2)}(\mathbf{r} - d\,\boldsymbol{k}'', \mathbf{v}_1'', \mathbf{r}, \mathbf{v}'', t)\, d^2\,(\boldsymbol{g}'' \cdot \boldsymbol{k}'')\, \mathrm{d}\boldsymbol{k}''\, \mathrm{d}\mathbf{r}\, \mathrm{d}\mathbf{v}''\, \mathrm{d}\mathbf{v}_1''\, \mathrm{d}t \tag{2.11}$$

with the constraint $\boldsymbol{g} \cdot \boldsymbol{k}'' < 0$.

From Eq. (2.1), we have

$$\boldsymbol{g} \cdot \boldsymbol{k}'' = -\alpha\,(\boldsymbol{g}'' \cdot \boldsymbol{k}''). \tag{2.12}$$

It is convenient to choose $\boldsymbol{k}'' = -\boldsymbol{k}$. Consequently, the collision rule gives $\mathbf{v}_1''$ and $\mathbf{v}''$ in terms of $\mathbf{v}_1$ and $\mathbf{v}$ as

$$\mathbf{v}'' = \mathbf{v} + \frac{(1+\alpha)}{2\alpha}\,(\boldsymbol{g} \cdot \boldsymbol{k})\,\boldsymbol{k}, \qquad \mathbf{v}_1'' = \mathbf{v}_1 - \frac{(1+\alpha)}{2\alpha}\,(\boldsymbol{g} \cdot \boldsymbol{k})\,\boldsymbol{k}. \tag{2.13}$$

The volumes in velocity space before and after collisions are related by

$$\mathrm{d}\mathbf{v}''\, \mathrm{d}\mathbf{v}_1'' = |\mathcal{J}|\, \mathrm{d}\mathbf{v}\, \mathrm{d}\mathbf{v}_1, \tag{2.14}$$

where $\mathcal{J}$ the determinant of the Jacobian for the transformation $(\mathbf{v}'', \mathbf{v}_1'') \to (\mathbf{v}, \mathbf{v}_1)$ which is given in Eq. (2.13). Clearly we have $|\mathcal{J}| = 1/\alpha$, where $\alpha$ is the restitution coefficient.

By substituting Eq. (2.12) and Eq. (2.14) into Eq. (2.11) we get,

$$\frac{1}{\alpha^2}\, f^{(2)}(\mathbf{r} + d\,\boldsymbol{k}, \mathbf{v}_1'', \mathbf{r}, \mathbf{v}'', t)\, d^2\,(\boldsymbol{g}.\boldsymbol{k})\, \mathrm{d}\boldsymbol{k}\, \mathrm{d}\mathbf{r}\, \mathrm{d}\mathbf{v}\, \mathrm{d}\mathbf{v}_1\, \mathrm{d}t. \tag{2.15}$$

The net gain of particles within $\mathrm{d}\mathbf{r}\,\mathrm{d}\mathbf{v}$ due to collisions with particles whose velocity before and after collision is near $\mathbf{v}_1$ can be obtained by subtracting Eq. (2.10) from Eq. (2.15) as

$$\left[\frac{1}{\alpha^2}\, f^{(2)}(\mathbf{r} + d\,\boldsymbol{k}, \mathbf{v}_1'', \mathbf{r}, \mathbf{v}'', t) - f^{(2)}(\mathbf{r} - d\,\boldsymbol{k}, \mathbf{v}_1, \mathbf{r}, \mathbf{v}, t)\right]\, d^2\,(\boldsymbol{g} \cdot \boldsymbol{k})\, \mathrm{d}\boldsymbol{k}\, \mathrm{d}\mathbf{v}_1\, \mathrm{d}\mathbf{r}\, \mathrm{d}\mathbf{v}\, \mathrm{d}t. \tag{2.16}$$

Integrating the above equation over all $\boldsymbol{k}$ and over all velocities $\mathbf{v}_1$, i.e., over the entire surface of particle 1 yields the net gain of particles $\left(\frac{\partial f}{\partial t}\right)_{coll} \mathrm{d}\mathbf{r}\,\mathrm{d}\mathbf{v}\,\mathrm{d}t$ within $\mathrm{d}\mathbf{r}\,\mathrm{d}\mathbf{v}$ due to collisions during the time interval $\mathrm{d}t$. Hence the expression for $\left(\frac{\partial f}{\partial t}\right)_{coll}$ is given by

$$\left(\frac{\partial f}{\partial t}\right)_{coll} = d^2 \int_{(\boldsymbol{g}\cdot\boldsymbol{k})>0} \left[\frac{1}{\alpha^2}\, f^{(2)}(\mathbf{r} + d\,\boldsymbol{k}, \mathbf{v}_1'', \mathbf{r}, \mathbf{v}'', t) - f^{(2)}(\mathbf{r} - d\,\boldsymbol{k}, \mathbf{v}_1, \mathbf{r}, \mathbf{v}, t)\right]\, (\boldsymbol{g}\cdot\boldsymbol{k})\, \mathrm{d}\boldsymbol{k}\, \mathrm{d}\mathbf{v}_1 \equiv \boldsymbol{\Omega}(f, f), \tag{2.17}$$

which is also called collision integral. Hence the Boltzmann equation assumes the following form

$$\frac{\partial f}{\partial t} + \mathbf{v}.\frac{\partial f}{\partial \mathbf{r}} + \frac{\mathbf{F}}{m}.\frac{\partial f}{\partial \mathbf{v}} = d^2 \int_{(\boldsymbol{g}\cdot\boldsymbol{k})>0} \left[\frac{1}{\alpha^2}\, f^{(2)}(\mathbf{r} + d\,\boldsymbol{k}, \mathbf{v}_1'', \mathbf{r}, \mathbf{v}'', t) - f^{(2)}(\mathbf{r} - d\,\boldsymbol{k}, \mathbf{v}_1, \mathbf{r}, \mathbf{v}, t)\right]\, (\boldsymbol{g}\cdot\boldsymbol{k})\, \mathrm{d}\boldsymbol{k}\, \mathrm{d}\mathbf{v}_1. \tag{2.18}$$

For dilute granular gases, the two-particle distribution function can be written as

$$f^{(2)}(\mathbf{r}_1, \mathbf{v}_1, \mathbf{r}, \mathbf{v}, t) = f(\mathbf{r}_1, \mathbf{v}_1, t)\, f(\mathbf{r}, \mathbf{v}, t) \tag{2.19}$$

This follows from the assumption of molecular chaos [(Boltzmann 1878)] which means that the velocities of two particles just prior to a collision are uncorrelated. If the system is dilute, we can assume that the velocity distribution function does not change with slightly changing the

position. Hence for a dilute granular gas, the Boltzmann equation in the absence of external forces reads

$$\frac{\partial f}{\partial t} + \mathbf{v}.\frac{\partial f}{\partial \mathbf{r}} = d^2 \int_{(\boldsymbol{g}\cdot\boldsymbol{k})>0} \left[\frac{1}{\alpha^2} f(\mathbf{r},\mathbf{v}_1'',t)\, f(\mathbf{r},\mathbf{v}'',t) - f(\mathbf{r},\mathbf{v}_1,t)\, f(\mathbf{r},\mathbf{v},t)\right] (\boldsymbol{g}\cdot\boldsymbol{k})\, \mathrm{d}\boldsymbol{k}\, \mathrm{d}\mathbf{v}_1. \quad (2.20)$$

For dense gases, Enskog [Enskog (1923)] proposed a correction to the form of two-particle distribution function as

$$f^{(2)}(\mathbf{r}_1,\mathbf{v}_1,\mathbf{r},\mathbf{v},t) = \chi(\mathbf{r}_1,\mathbf{r})\, f(\mathbf{r}_1,\mathbf{v}_1,t)\, f(\mathbf{r},\mathbf{v},t) \quad (2.21)$$

where $\chi(\mathbf{r}_1,\mathbf{r})$ is the pair distribution function [Chapman & Cowling (1970)] which is unity for a dilute gas.

## 2.3 Moment Transfer Equation and the Closure Problem

Before deriving the moment chain for macroscopic/hydrodynamic fields, we discuss about important properties of collision integral. The explicit form of collision integral for dilute granular gases is given by

$$\boldsymbol{\Omega}(f,f) = d^2 \int_{(\boldsymbol{g}\cdot\boldsymbol{k})>0} \left[\frac{1}{\alpha^2} f(\mathbf{r},\mathbf{v}_1'',t)\, f(\mathbf{r},\mathbf{v}'',t) - f(\mathbf{r},\mathbf{v}_1,t)\, f(\mathbf{r},\mathbf{v},t)\right] (\boldsymbol{g}\cdot\boldsymbol{k})\, \mathrm{d}\boldsymbol{k}\, \mathrm{d}\mathbf{v}_1. \quad (2.22)$$

The collision integral $\boldsymbol{\Omega}(f,f)$ satisfies the following two properties.

$$\begin{aligned} \boldsymbol{\Omega}(f+h_1, f+h_2) &= \boldsymbol{\Omega}(f,f) + \boldsymbol{\Omega}(f,h_2) + \boldsymbol{\Omega}(h_1,f) + \boldsymbol{\Omega}(h_1,h_2), \\ \boldsymbol{\Omega}(a_1 f, a_2 f) &= a_1\, a_2\, \boldsymbol{\Omega}(f,f), \end{aligned} \quad (2.23)$$

where $h_1$ and $h_2$ are functions of the velocity and $a_1$ and $a_2$ are constants.

Let us consider any arbitrary function of the velocity $\boldsymbol{\phi} \equiv \boldsymbol{\phi}(\mathbf{r},\mathbf{v},t)$. Multiply $\boldsymbol{\Omega}(f,f)$ with $\boldsymbol{\phi}(\mathbf{r},\mathbf{v},t)$ and integrate over all velocities $\mathbf{v}$ we get

$$\begin{aligned} \int \mathrm{d}\mathbf{v}\, \boldsymbol{\phi}(\mathbf{v})\, \boldsymbol{\Omega}(f,f) = d^2 \int \mathrm{d}\mathbf{v} \int \mathrm{d}\mathbf{v}_1 \int_{(\boldsymbol{g}\cdot\boldsymbol{k})>0} \mathrm{d}\boldsymbol{k}\, (\boldsymbol{g}\cdot\boldsymbol{k})\, \frac{1}{\alpha^2} f(\mathbf{r},\mathbf{v}_1'',t)\, f(\mathbf{r},\mathbf{v}'',t)\, \boldsymbol{\phi}(\mathbf{v}) \\ - d^2 \int \mathrm{d}\mathbf{v} \int \mathrm{d}\mathbf{v}_1 \int_{(\boldsymbol{g}\cdot\boldsymbol{k})>0} \mathrm{d}\boldsymbol{k}\, (\boldsymbol{g}\cdot\boldsymbol{k})\, f(\mathbf{r},\mathbf{v}_1,t)\, f(\mathbf{r},\mathbf{v},t)\, \boldsymbol{\phi}(\mathbf{v}). \end{aligned} \quad (2.24)$$

From Eq. (2.12) and Eq. (2.14) we have the following relation,

$$\frac{1}{\alpha^2} (\boldsymbol{g}\cdot\boldsymbol{k})\, \mathrm{d}\mathbf{v}\, \mathrm{d}\mathbf{v}_1 = (\boldsymbol{g}''\cdot\boldsymbol{k})\, \mathrm{d}\mathbf{v}''\, \mathrm{d}\mathbf{v}_1''. \quad (2.25)$$

By using above relation the first term on the R.H.S of Eq. (2.24) becomes

$$d^2 \int \mathrm{d}\mathbf{v}'' \int \mathrm{d}\mathbf{v}_1'' \int_{(\boldsymbol{g}''\cdot\boldsymbol{k})>0} \mathrm{d}\boldsymbol{k}\, (\boldsymbol{g}''\cdot\boldsymbol{k})\, f(\mathbf{r},\mathbf{v}_1'',t)\, f(\mathbf{r},\mathbf{v}'',t)\, \boldsymbol{\phi}(\mathbf{v}). \quad (2.26)$$

Since the relation $(\mathbf{v}'',\mathbf{v}_1'') \to (\mathbf{v},\mathbf{v}_1)$ is equivalent to $(\mathbf{v},\mathbf{v}_1) \to (\mathbf{v}',\mathbf{v}_1')$, we can rewrite the above

equation as

$$d^2 \int \mathrm{d}\mathbf{v} \int \mathrm{d}\mathbf{v}_1 \int_{(\boldsymbol{g}\cdot\boldsymbol{k})>0} \mathrm{d}\boldsymbol{k}\,(\boldsymbol{g}\cdot\boldsymbol{k})\, f(\mathbf{r},\mathbf{v}_1,t)\, f(\mathbf{r},\mathbf{v},t)\, \boldsymbol{\phi}(\mathbf{v}'). \tag{2.27}$$

Eq. (2.27) is symmetric about $\mathbf{v}$ and $\mathbf{v}_1$, so this is equivalent to

$$d^2 \int \mathrm{d}\mathbf{v} \int \mathrm{d}\mathbf{v}_1 \int_{(\boldsymbol{g}\cdot\boldsymbol{k})>0} \mathrm{d}\boldsymbol{k}\,(\boldsymbol{g}\cdot\boldsymbol{k})\, f(\mathbf{r},\mathbf{v}_1,t)\, f(\mathbf{r},\mathbf{v},t)\, \boldsymbol{\phi}(\mathbf{v}'_1). \tag{2.28}$$

From Eq. (2.27) and Eq. (2.28), the first term on the R.H.S of (2.24) takes the following form

$$\frac{d^2}{2} \int \mathrm{d}\mathbf{v} \int \mathrm{d}\mathbf{v}_1 \int_{(\boldsymbol{g}\cdot\boldsymbol{k})>0} \mathrm{d}\boldsymbol{k}\,(\boldsymbol{g}\cdot\boldsymbol{k})\, f(\mathbf{r},\mathbf{v}_1,t)\, f(\mathbf{r},\mathbf{v},t)\, \left[\boldsymbol{\phi}(\mathbf{v}') + \boldsymbol{\phi}(\mathbf{v}'_1)\right]. \tag{2.29}$$

The second term on the R.H.S of (2.24) is also symmetric about $\mathbf{v}$ and $\mathbf{v}_1$ and hence it can be rewritten as

$$\frac{d^2}{2} \int \mathrm{d}\mathbf{v} \int \mathrm{d}\mathbf{v}_1 \int_{(\boldsymbol{g}\cdot\boldsymbol{k})>0} \mathrm{d}\boldsymbol{k}\,(\boldsymbol{g}\cdot\boldsymbol{k})\, f(\mathbf{r},\mathbf{v}_1,t)\, f(\mathbf{r},\mathbf{v},t)\, \left[\boldsymbol{\phi}(\mathbf{v}) + \boldsymbol{\phi}(\mathbf{v}_1)\right]. \tag{2.30}$$

Finally, Eq. (2.24) is given by

$$\int \mathrm{d}\mathbf{v}\, \boldsymbol{\phi}(\mathbf{v})\, \boldsymbol{\Omega}(f,f) = \frac{d^2}{2} \int \mathrm{d}\mathbf{v} \int \mathrm{d}\mathbf{v}_1 \int_{(\boldsymbol{g}\cdot\boldsymbol{k})>0} \mathrm{d}\boldsymbol{k}\,(\boldsymbol{g}\cdot\boldsymbol{k})\, f_1\, f\, \boldsymbol{\Xi}[\boldsymbol{\phi}(\mathbf{v})], \tag{2.31}$$

where

$$\boldsymbol{\Xi}[\boldsymbol{\phi}(\mathbf{v})] = \left[\boldsymbol{\phi}(\mathbf{v}') + \boldsymbol{\phi}(\mathbf{v}'_1) - \boldsymbol{\phi}(\mathbf{v}) - \boldsymbol{\phi}(\mathbf{v}_1)\right] \tag{2.32}$$

and further more two abbreviation $f \equiv f(\mathbf{r},\mathbf{v},t)$, $f_1 \equiv f(\mathbf{r},\mathbf{v}_1,t)$ were introduced.

The moment transfer equation is now obtained by the multiplication of the Boltzmann equation (2.20) by an arbitrary function $\boldsymbol{\phi}(\mathbf{r},\mathbf{v},t)$ and then carrying out integration of the resulting equation over all values of velocity $\mathbf{v}$. This leads to the following equation,

$$\frac{\partial}{\partial t}\int \boldsymbol{\phi}\, f\, \mathrm{d}\mathbf{v} + \frac{\partial}{\partial x_i}\int \boldsymbol{\phi}\, v_i\, f\, \mathrm{d}\mathbf{v} - \int \left[\frac{\partial \boldsymbol{\phi}}{\partial t} + v_i \frac{\partial \boldsymbol{\phi}}{\partial x_i}\right] f \mathrm{d}\mathbf{v} = \int \mathrm{d}\mathbf{v}\, \boldsymbol{\phi}(\mathbf{v})\, \boldsymbol{\Omega}(f,f). \tag{2.33}$$

Hence using Eq. (2.31), the moment-transfer (coarse-grained or hydrodynamic) equation reads

$$\frac{\partial}{\partial t}\int \boldsymbol{\phi}\, f\, \mathrm{d}\mathbf{v} + \frac{\partial}{\partial x_i}\int \boldsymbol{\phi}\, v_i\, f\, \mathrm{d}\mathbf{v} - \int \left[\frac{\partial \boldsymbol{\phi}}{\partial t} + v_i \frac{\partial \boldsymbol{\phi}}{\partial x_i}\right] f \mathrm{d}\mathbf{v} = \frac{d^2}{2} \int \mathrm{d}\mathbf{v} \int \mathrm{d}\mathbf{v}_1 \int_{(\boldsymbol{g}\cdot\boldsymbol{k})>0} \mathrm{d}\boldsymbol{k}\,(\boldsymbol{g}\cdot\boldsymbol{k})\, f_1\, f\, \boldsymbol{\Xi}[\boldsymbol{\phi}(\mathbf{v})]. \tag{2.34}$$

From the right-hand side of Eq. (2.34) we may infer that for any kind of distribution function it vanishes when $\boldsymbol{\Xi}[\boldsymbol{\phi}(\mathbf{v})] = 0$. A function $\boldsymbol{\phi}$ which fulfills such condition is called a "collision

invariant" or a "summational invariant". From Eq. (2.2) and (2.3) we find that

$$\begin{aligned} \boldsymbol{\Xi}[m] &= 0, \\ \boldsymbol{\Xi}[m\,\mathbf{v}] &= 0, \\ \boldsymbol{\Xi}[\frac{m}{2}\,\mathbf{v}^2] &= -\frac{m}{4}\,(1-\alpha^2)\,(\boldsymbol{g}\cdot\boldsymbol{k})^2. \end{aligned} \tag{2.35}$$

From Eq. (2.35), we can see that the set $\boldsymbol{\phi}(\mathbf{v}) = \{m, m\,\mathbf{v}, \frac{m}{2}\,\mathbf{v}^2\}$ forms the set of collision invariants for the case of a molecular gas, corresponding to the conservation of mass, momentum and energy, respectively. But for the granular gas the set $\boldsymbol{\phi}(\mathbf{v}) = \{m, m\,\mathbf{v}\}$ forms the set of collision invariants corresponding to the conservation of mass and momentum.

From Eq. (2.34) one finds that if an $n^{th}$ order system of moment transport equations is obtained, then there is an $(n+1)^{th}$ order velocity moment contained in the moment system and therefore, an equation is needed that governs the transport of $(n+1)^{th}$ higher-order moment. This is the problem of "closure". This problem is remedied if the form of the non-equilibrium distribution function $f$ is specified in terms of $n^{th}$ order moments so that the highest-order velocity moment contained in the moment system can be related to the lower-order moment quantities. It is worth mentioning that there may be more than one phase-space distribution that leads to the same closure [Groth & McDonald (2009)], i.e., a system of moment equations is not defined by a unique distribution function. In the next section we discuss about moment closure methods.

### 2.3.1 Moment Closure Methods

This section provides a brief description of moment closure approaches. In a moment closure approach the problem of solving the Boltzmann equation is replaced by solving a system of generalized transport equations which are obtained from the moment transfer equation (2.34). Moment closure methods play an important role in handling the behaviour of non-equilibrium gas by assuming the distribution function with more degrees of freedom. In general it is assumed that the addition of more moments in a closure give rise to a system of moment equations, which approximate non-equilibrium flows accurately [(Groth & McDonald 2009)]. A few advantages of moment closure methods: they model non-equilibrium gas flows with minify expense as compared to particle-based methods, they render a protracted range of physical credibility over the standard continuum models, namely the Euler and Navier-Stokes equations [(McDonald & Groth 2013)]. A few techniques of moment closure or "extended" hydrodynamic approaches are: (i) the Chapman-Enskog expansion, (ii) Grad's moment method and (iii) maximum entropy method.

The Chapman-Enskog method [(Chapman 1918; Enskog 1917; Chapman & Cowling 1970)] is based on a singular perturbation series expansion in terms of the Knudsen number, which gives the Euler equations at zeroth-order expansion, the equations of Navier-Stokes and Fourier at the first-order expansion, the Burnett equations at the second-order expansion, the Super-Burnett equations at the third-order expansion, and so on. This is the best known approach to derive transport equations from the Boltzmann equation [(Chapman & Cowling 1970; Cercignani 1975; Struchtrup 2005*b*)]. The main advantage of the Chapman-Enskog method [(Chapman & Cowling

1970)] is that no additional hydrodynamic variables are introduced and the drawback is that the higher-order systems of transport equations which are obtained based on Chapman-Enskog method are unstable for very small disturbances.

An alternative approach for obtaining a closed moment system is Grad's moment method [(Grad 1949)] in which the distribution function is expanded in terms of Hermite polynomials in the components of the fluctuating velocity with the Maxwellian distribution function (equilibrium distribution function) as an weight function. This method introduces new sets of unknowns such as stress tensor, heat fluxes and higher-order moments of the distribution function. The closure can be obtained by truncating the Hermite polynomial expansion [(Grad 1949; Goldreich & Tremaine 1978; Jenkins & Richman 1985*a*)]. By using the truncated distribution function one can obtain a closed moment system up to desired moments of interest. Moment equations obtained from Grad's method are hyperbolic for near-equilibrium flows and they loose hyperbolicity if relative deviations occur from local-equilibrium [(Torrilhon 2000; Struchtrup 2005*b*; Torrilhon 2010; McDonald & Torrilhon 2013)]. In addition to the restrictive region of hyperbolicity, Grad's system suffers from closure breakdown [(Torrilhon 2000; Struchtrup 2005*b*; McDonald & Groth 2013; McDonald & Torrilhon 2013)]. The Grad's method has been extended to inelastic granular gas by Goldreich & Tremaine (1978) and later by Jenkins & Richman (1985*a*, 1988) and Saha & Alam (2014, 2016). In particular, Goldreich & Tremaine (1978) used an anisotropic Gaussian to obtain constitutive relations in the context of modeling Saturn's ring as a dilute granular gas.

Later in 1996, Levermore developed an alternative hierarchy of moment closures [(Levermore 1996; Müller & Ruggeri 2013)] based on maximum-entropy approximation (also called "quasi-equilibrium" approximation), following the original idea of Holway Jr (1966). This closure approach assumes a phase space distribution function which maximizes entropy, which is consistent with a given set of moments [(Gorban & Karlin 1994; Levermore 1996; McDonald & Groth 2013; Jaynes 1957*a*,*b*)], instead of a series expansion (CE expansion) and a polynomial expansion (Grad expansion). The Levermore hierarchy has a number of desirable properties including strict hyperbolicity. The resulting PDEs remain hyperbolic with realizable moment solutions for all physically realistic situations. The first member of Levermore hierarchy of closure corresponds to the Euler system, while the second member results in 10-moment closure, which is also known as the Gaussian closure [(Levermore 1996; Levermore & Morokoff 1998; Lam 2011)]. The Gaussian closure furnishes a set of equations for an anisotropic pressure tensor in addition to the typical continuity and moment equations. The Gaussian closure is a simplified model as it does not predict the effects of heat-flux. So this closure is unsuitable for situations in which heat-flux plays a significant role. The higher-order closure of the Levermore moment closure hierarchy would provide moment equations for heat-transfer, unfortunately explicit analytic expressions of the transport equations for the moments of interest are complicated to determine.

## 2.4 14-Moment Theory for a Dilute Granular Gas

Once the distribution function is known, one can calculate its moments. Here we will derive and discuss the set of equations for the 14-moments. The extended set of 14 hydrodynamic fields is

required to deal with rarefied regime of a granular gas. The macroscopic variables, namely, the mass density $\rho$, the hydrodynamic velocity $u_i$ and the pressure $p$ are defined via:

$$\begin{aligned} \rho &= \int m\, f \mathrm{d}\mathbf{v} \equiv mn, \\ \rho u_i &= \int m\, v_i f \mathrm{d}\mathbf{v}, \\ p &= \int m\, \frac{C^2}{3} f \mathrm{d}\mathbf{v}, \end{aligned} \tag{2.36}$$

where $\boldsymbol{C} = \mathbf{v} - \boldsymbol{u}$ is the peculiar velocity and the kinetic temperature is

$$\theta \equiv \frac{p}{\rho} = \frac{1}{3n} \int C^2 f \mathrm{d}\mathbf{v}. \tag{2.37}$$

The other relevant moments are pressure tensor $p_{ij}$ and heat flux vector $q_i$:

$$p_{ij} = \int m\, C_i C_j f \mathrm{d}\mathbf{v}, \qquad q_i = \int \frac{m}{2}\, C^2 C_i f \mathrm{d}\mathbf{v}. \tag{2.38}$$

It is convenient to decompose the pressure tensor $p_{ij}$ into its trace $p$ and a deviatoric part

$$\sigma_{ij} = p_{ij} - \rho\theta\delta_{ij} \equiv p_{<ij>}, \tag{2.39}$$

where the angular bracket on the subscripts of a tensorial quantity denotes the traceless/deviatoric part of the tensor. From Eq. (2.34), it follows that the mass and the momentum conservation equations are same as in a fluid,

$$\begin{aligned} \frac{\partial \rho}{\partial t} + \frac{\partial (\rho\, u_i)}{\partial x_i} &= 0, \\ \frac{\partial (\rho\, u_i)}{\partial t} + \frac{\partial (\rho\, u_i\, u_j)}{\partial x_j} + \frac{\partial p}{\partial x_i} + \frac{\partial \sigma_{ij}}{\partial x_j} &= 0, \end{aligned} \tag{2.40}$$

but the energy balance equation is

$$\frac{3}{2}\frac{\partial p}{\partial t} + \frac{3}{2}\frac{\partial (p\, u_i)}{\partial x_i} + \frac{\partial q_i}{\partial x_i} + p\frac{\partial u_i}{\partial x_i} + \sigma_{ij}\frac{\partial u_i}{\partial x_j} = -\frac{3}{2}\mathcal{D}, \tag{2.41}$$

that contains a non-conservative term given by

$$\mathcal{D} = \frac{m\, d^2\, (1 - \alpha^2)}{12} \int_{\boldsymbol{g}\cdot\boldsymbol{k} > 0} (\boldsymbol{g}\cdot\boldsymbol{k})^3\, f_1\, f \mathrm{d}\boldsymbol{k} \mathrm{d}\mathbf{v}_1 \mathrm{d}\mathbf{v}. \tag{2.42}$$

The above term $\mathcal{D}$ is the rate of energy dissipation per unit volume and takes care of the fact that the energy is not conserved in a granular gas; of course, $\mathcal{D} \to 0$ as $\alpha \to 1$ and we recover the standard energy balance equation for a molecular gas by setting $\mathcal{D} = 0$ in Eq. (2.41).

The set of balance equations (2.40) and (2.41) are not closed due to the presence of higher-order moments $\sigma_{ij}$ and $q_i$. In the standard Euler/Navier-Stokes hydrodynamics, these higher-order moments are expressed in terms of the gradients of lower-order moments, known as constitutive relations (Newton's law of viscosity and Fourier's law of heat-flux), and thereby closing

the system of equations. In the realm of "extended" hydrodynamics (i.e., going beyond Navier-Stokes order [Müller & Ruggeri (1993*a*); Torrilhon & Struchtrup (2004); Kremer (2010)]), the time evolution equations for $\sigma_{ij}$ and $q_i$ are written down. For example, we can write down an evolution equation for the stress tensor, using Eq. (2.34), as

$$\frac{\partial \sigma_{ij}}{\partial t} + \frac{\partial(\sigma_{ij}\, u_k)}{\partial x_k} + \frac{4}{5}\frac{\partial q_{\langle i}}{\partial x_{j\rangle}} + \frac{\partial Q_{\langle ijk\rangle}}{\partial x_k} + 2\,p\,\frac{\partial u_{\langle i}}{\partial x_{j\rangle}} + 2\,\sigma_{k\langle i}\frac{\partial u_{j\rangle}}{\partial x_k} = \sigma^s_{ij}, \tag{2.43}$$

where the source term $\sigma^s_{ij}$ due to particle collisions is

$$\sigma^s_{ij} = \frac{1}{2}\int_{(\boldsymbol{g}\cdot\boldsymbol{k})>0} m\,(\,\acute{C}_{\langle i}\acute{C}_{j\rangle} + \acute{C}_{1\langle i}\acute{C}_{1j\rangle} - C_{\langle i}C_{j\rangle} - C_{1\langle i}C_{1j\rangle}\,) f_1\, f\, d^2\,(\boldsymbol{g}\cdot\boldsymbol{k})\,\mathrm{d}\boldsymbol{k}\mathrm{d}\mathbf{v}_1\mathrm{d}\mathbf{v} \tag{2.44}$$

and $Q_{\langle ijk\rangle}$ is the traceless part of the third-order moment given by

$$Q_{\langle ijk\rangle} = \int m\, C_{\langle i}C_jC_{k\rangle} f \mathrm{d}\mathbf{v}. \tag{2.45}$$

Note that for any third-order tensor $A_{ijk}$, symmetric in all indices, its traceless part $A_{\langle ijk\rangle}$ can be expressed as

$$A_{\langle ijk\rangle} = A_{ijk} - \frac{1}{5}\,(A_{imm}\delta_{jk} + A_{jmm}\delta_{ik} + A_{kmm}\delta_{ij})\,. \tag{2.46}$$

Similarly, the evolution equation for the heat flux is

$$\begin{aligned}&\frac{\partial q_i}{\partial t} + \frac{\partial(q_i\, u_j)}{\partial x_j} + \frac{1}{2}\frac{\partial R_{\langle ij\rangle}}{\partial x_j} + \frac{1}{6}\frac{\partial R}{\partial x_j} - \frac{5}{2}\frac{p}{\rho}\frac{\partial p_{ij}}{\partial x_j} - \frac{\sigma_{ij}}{\rho}\frac{\partial p_{jk}}{\partial x_k}\\ &+\frac{7}{5}\,q_j\frac{\partial u_i}{\partial x_j} + \frac{2}{5}\,q_i\frac{\partial u_j}{\partial x_j} + \frac{2}{5}\,q_k\frac{\partial u_k}{\partial x_i} + Q_{\langle ijk\rangle}\frac{\partial u_j}{\partial x_k} = q^s_i,\end{aligned} \tag{2.47}$$

where the source term due to collisions $q^s_i$ is

$$q^s_i = \frac{1}{2}\int_{(\boldsymbol{g}\cdot\boldsymbol{k})>0} \frac{m}{2}(\,\acute{C}^2\acute{C}_i + \acute{C}_1{}^2\acute{C}_{1_i} - C^2\,C_i - C_1^2\,C_{1_i}\,)\, f_1\, f\, d^2\,(\boldsymbol{g}\cdot\boldsymbol{k})\,\mathrm{d}\boldsymbol{k}\mathrm{d}\mathbf{v}_1\mathrm{d}\mathbf{v}, \tag{2.48}$$

and the higher-order moments of the distribution function on the left-hand side of Eq. (2.47),

$$R_{\langle ij\rangle} = \int m\, C^2 C_{\langle i}C_{j\rangle} f \mathrm{d}\mathbf{v} \quad \text{and} \quad R = \int m\, C^4 f d\boldsymbol{v}, \tag{2.49}$$

are the single- and double-contracted fourth-order moments, respectively. Lastly, we obtain an evolution equation for the full contracted fourth-order moment $R$ by putting $\boldsymbol{\phi} = m\,C^4$ into Eq. (2.34):

$$\frac{\partial R}{\partial t} + \frac{\partial(R\, u_i)}{\partial x_i} + \frac{\partial S_i}{\partial x_i} - \frac{8}{\rho}\,q_i\,\frac{\partial(p\delta_{ij}+\sigma_{ij})}{\partial x_j} + 4R_{\langle ij\rangle}\frac{\partial u_i}{\partial x_j} + \frac{4}{3}R\frac{\partial u_i}{\partial x_i} = R^s, \tag{2.50}$$

where the collisional source term is

$$R^s = \frac{1}{2}\int m\,[\,\acute{C}^4 + \acute{C}_1{}^4 - C^4 - C_1^4\,]\, f_1\, f\, d^2\,(\boldsymbol{g}\cdot\boldsymbol{k})\,\mathrm{d}\boldsymbol{k}\mathrm{d}\mathbf{v}_1\mathrm{d}\mathbf{v}, \tag{2.51}$$

and $S_i$ is the double-contracted fifth-order moment

$$S_i = \int m\, C^2 C^2 C_i f \mathrm{d}\mathbf{v}. \tag{2.52}$$

The standard hydrodynamic equations (2.40) and (2.41), augmented by the balance equations for higher-order fields (2.43), (2.47) and (2.50), constitutes an "extended" hydrodynamic model for a granular gas in terms of 14-field variables $[\rho, u_i, p, \sigma_{ij}, q_i, R]$. As in the case of standard hydrodynamics, the above moment chain [(2.43),(2.47) and (2.50)] for extended hydrodynamics also contains higher-order terms ($Q_{\langle ijk\rangle}$, $R_{\langle ij\rangle}$ and $S_i$) that require a suitable ansatz for closure. The relevance of Eq. (2.50) in the context of a granular gas is most important since this is responsible for the non-Fourier contribution to the heat flux [see Eq. (2.61)]. When Eq. (2.50) is removed, we obtain the standard 13-moment theory of a molecular gas [(Grad 1949)].

### 2.4.1 Closure from Grad's Method

The higher-order terms in Eqs. (2.43),(2.47) and (2.50) can be closed by providing closures for the distribution function. One common way to provide closure approximation for kinetic equations is to use Grad's moment method [Grad (1949)] in which one represents the non-equilibrium distribution function as

$$f(\mathbf{r}, \mathbf{v}, t) = \frac{n}{(2\pi\theta)^{\frac{3}{2}}} e^{-\frac{C^2}{2\theta}} \left( \sum_{i=0}^{M} a^{(i)}\, \mathcal{H}^{(i)} \right), \tag{2.53}$$

where $n = \rho/m$ is the particle number density and $\mathcal{H}^{(i)}$ denotes $i$th-order Hermite polynomials and $a^{(i)}$ are the expansion coefficients which are related to the moments of the distribution function. The number of terms $M$ retained in the expansion (2.53) is dictated by the physical considerations. It is often argued [Grad (1949); Goldreich & Tremaine (1978); Jenkins & Richman (1988); Struchtrup (2005*b*); Kremer & Marques Jr (2011)] that the macroscopic state of a gas can be characterized by the ten, thirteen, and fourteen basic field variables for 10-moment, 13-moment and 14-moment closures, respectively.

Following Grad's method, Kremer & Marques Jr (2011) proposed the following form for the non-equilibrium distribution function

$$f = \frac{n}{(2\pi\theta)^{\frac{3}{2}}} e^{-\frac{C^2}{2\theta}} \left( 1 + \frac{\sigma_{ij}}{2\rho\theta^2} C_i C_j + \frac{q_i}{5\rho\theta^3} \Big( C^2 - 5\theta \Big) C_i + \Big( \frac{C^4 - 10C^2\theta + 15\theta^2}{8\theta^2} \Big) \Delta \right), \tag{2.54}$$

where

$$\Delta = \frac{1}{15\,\rho\,\theta^2} (R - R^{eq}) \tag{2.55}$$

is the dimensionless non-equilibrium part of the full contracted fourth-order moment $R$. Using the closure (2.54) for distribution function, the constitutive relations for the higher-order moments of the distribution function are

$$Q_{\langle ijk\rangle} = 0, \qquad R_{\langle ij\rangle} = 7\,\theta\,\sigma_{ij}, \qquad R = 15\,\rho\,\theta^2\,(1 + \Delta), \qquad S_i = 28\,\theta\,q_i. \tag{2.56}$$

Following linearization of moments, the collisional source terms were also evaluated by Kremer & Marques (2011) as:

$$\begin{aligned}
\mathcal{D} &= \frac{4}{3}\frac{d^2}{m}\sqrt{\pi}\,(1-\alpha^2)\left[1+\frac{3\,\Delta}{16}\right]\rho^2\,\theta^{\frac{3}{2}},\\
\sigma^s_{ij} &= -\frac{4}{5}\frac{d^2}{m}\sqrt{\pi\,\theta}\,(1+\alpha)\,(3-\alpha)\left[1-\frac{\Delta}{32}\right]\rho\,\sigma_{ij},\\
q^s_i &= -\frac{1}{15}\frac{d^2}{m}\sqrt{\pi\,\theta}\,(1+\alpha)\left[49-33\,\alpha+(19-3\,\alpha)\,\frac{\Delta}{32}\right]\rho\,q_i,\\
R^s &= -4\,\frac{d^2}{m}\sqrt{\pi\,\theta}\,(1+\alpha)\left[(2\,\alpha^2+9)\,(1-\alpha)+(30\,\alpha^2\,(1-\alpha)+271-207\,\alpha)\,\frac{\Delta}{16}\right]\rho^2\,\theta^2.
\end{aligned} \tag{2.57}$$

To determine the source terms $\mathcal{D}$ and $R^s$, only linear terms in $\Delta$ are retained but to determine $\sigma^s_{ij}$ and $q^s_i$ the products of $\Delta$ with $\sigma_{ij}$ and $q_i$, in addition to the linear terms, are retained. Equations (2.40),(2.41), (2.43),(2.47) and (2.50), together with constitutive relations (2.56) and (2.57), constitute the complete set of 14-moment system for a dilute granular gas.

## 2.5 Constitutive Relations for 13-moment and 10-moment Systems

For the 13-moment closure, the non-equilibrium distribution function $f$ is the same as Eq. (2.54) with $\Delta = 0$ since the full contracted fourth moment is not treated as a field variable in the 13-moment model. With this closure the corresponding constitutive relations for the higher-order moments and the linear source terms are obtained from Eqs. (2.56) and (2.57) by setting $\Delta$ to zero. Therefore, the extended hydrodynamic equations at 13-moment level consist of equations (2.40),(2.41), (2.43) and (2.47) with constitutive relations (2.56) and (2.57) and $\Delta = 0$.

Similarly, for 10-moment closure, the non-equilibrium distribution function $f$ is obtained from Eq. (2.54) by setting $q_i$ and $\Delta$ to zero, and the related constitutive relations are obtained from Eqs. (2.56) and (2.57) in the same limit. The extended hydrodynamic equations at 10-moment level correspond to equations (2.40),(2.41) and (2.43).

## 2.6 Constitutive Relations for Standard Hydrodynamic Models

### 2.6.1 Euler system

The structure of Euler equations for a granular gas, consisting of Eqs. (2.40) and (2.41), is the same as that for gases of elastic particles except for the energy sink term $\mathcal{D}$ which accounts for inelastic collisions [Jenkins & Richman (1985*a*); Goldshtein & Shapiro (1995); Goldshtein *et al.* (1995)]. For a Maxwellian distribution function, it is straightforward to verify that

$$\sigma_{ij} = 0, \qquad q_i = 0, \qquad R = 15\rho\theta^2. \tag{2.58}$$

The energy loss term $\mathcal{D}^E$ for Euler system can be obtained from Eq. (2.57) by setting $\Delta$ to be zero. Hence the Eqs. (2.40) and (2.41) with the above constitutive relations (2.58) will form

the hydrodynamic equations at Euler-level for a dilute granular gas. It is noteworthy here that the hydrodynamic equations at Euler level for a molecular gas remain the same as (2.40) and (2.41), but the restitution coefficient is set to $\alpha = 1$ such that the collisional dissipation term in the energy balance equation vanishes identically (i.e., $\mathcal{D}^E = 0$).

### 2.6.2 Navier-Stokes hydrodynamics

The laws of Navier-Stokes and Fourier are obtained from 14-moment equations using the Maxwell iteration procedure [Kremer & Marques Jr (2011); Ikenberry & Truesdell (1956)]. The hydrodynamic equations at NS-level consist of Eqs. (2.40) and (2.41) with the following constitutive relations:

$$\mathcal{D}^{NS} = \frac{4}{3} n d^2 \sqrt{\pi}\,(1-\alpha^2)\left[1 + \frac{3}{16} a_2\right] \rho\, \theta^{\frac{3}{2}}, \tag{2.59}$$

$$\sigma_{ij} = -2\mu \frac{\partial u_{\langle i}}{\partial x_{j\rangle}}, \tag{2.60}$$

$$q_i = -\kappa \frac{\partial \theta}{\partial x_i} - \kappa_h \frac{\partial \rho}{\partial x_i}, \tag{2.61}$$

$$\text{with} \quad a_2 = \frac{16(1-\alpha)(1-2\alpha^2)}{30\alpha^2(1-\alpha) + 81 - 17\alpha} = \Delta_\infty, \tag{2.62}$$

where $a_2 = \Delta_\infty = \Delta(t \to \infty)$ is the stationary value of the non-equilibrium part of the full-contracted fourth-moment. The simplified expressions for the shear viscosity $\mu$, thermal conductivity $\kappa$ and the higher-order thermal conductivity $\kappa_h$ are given by [Garzó *et al.* (2007); Kremer & Marques Jr (2011)]:

$$\mu = \frac{5}{4}\frac{m}{d^2}\sqrt{\frac{\theta}{\pi}}\frac{1}{(1+\alpha)(3-\alpha)[1-\frac{a_2}{32}]}, \tag{2.63}$$

$$\kappa = \frac{75}{2}\frac{m}{d^2}\sqrt{\frac{\theta}{\pi}}\frac{1+2a_2}{(1+\alpha)[49-33\alpha+(19-3\alpha)\frac{a_2}{32}]}, \tag{2.64}$$

$$\kappa_h = \frac{75}{2\rho}\frac{m}{d^2}\theta\sqrt{\frac{\theta}{\pi}}\frac{a_2}{(1+\alpha)[49-33\alpha+(19-3\alpha)\frac{a_2}{32}]}. \tag{2.65}$$

It may be noted that the hydrodynamic equations at Navier-Stokes level for a molecular gas are obtained by setting the restitution coefficient $\alpha = 1$, i.e., for a molecular gas the hydrodynamic equations at Navier-Stokes level remain same as (2.40) and (2.41), with vanishing values for the collisional dissipation term in the energy balance equation and the stationary value of the non-equilibrium part of the full-contracted fourth-moment (i.e., $\mathcal{D}^{NS} = 0 = a_2$). Moreover, the transport coefficients for a molecular gas of elastic particles are same as in (2.64) - (2.65), with the restitution coefficient is set to one. Hence the transport coefficients for a molecular gas of

elastic particles are given by the following expressions.

$$\mu = \frac{5}{16}\frac{m}{d^2}\sqrt{\frac{\theta}{\pi}}, \tag{2.66}$$

$$\kappa = \frac{75}{64}\frac{m}{d^2}\sqrt{\frac{\theta}{\pi}}, \tag{2.67}$$

$$\kappa_h = 0. \tag{2.68}$$

## 2.7 Flow chart of hydrodynamic models

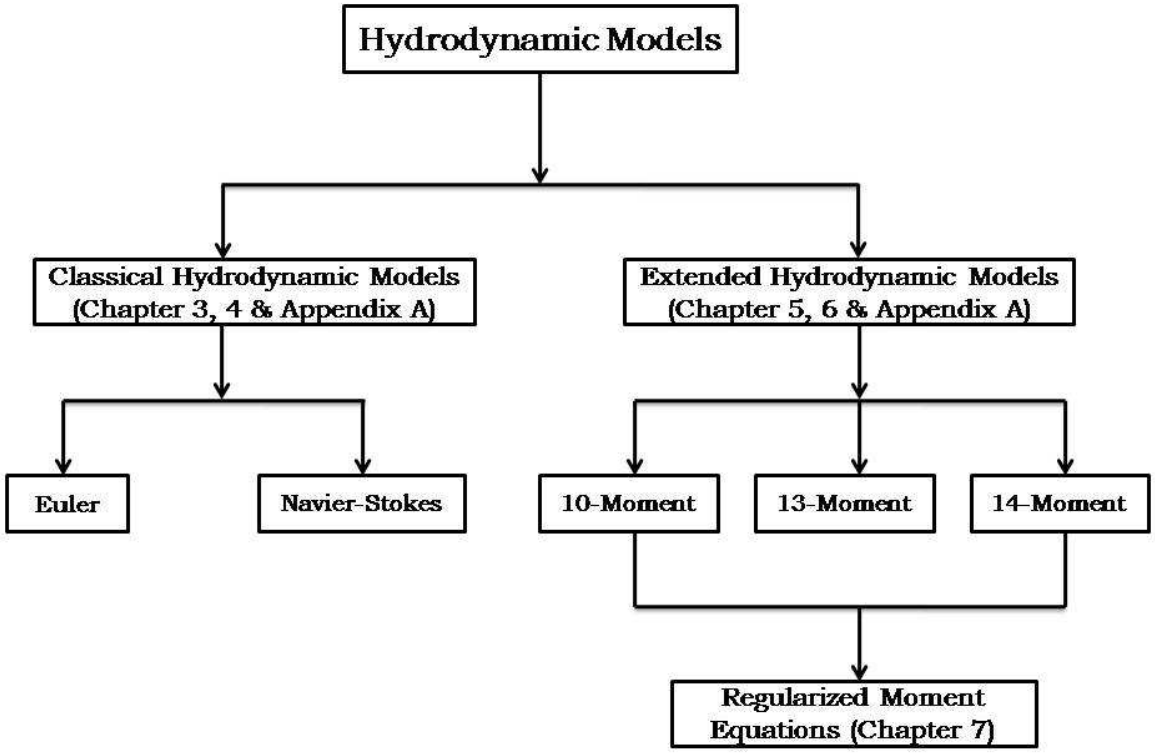


Figure 2.3: An overview of all hydrodynamic models used in this thesis.

## Appendix 2A. Derivation of the non-equilibrium distribution function with fourteen field variables

In Grad's moment method [Grad (1949)] the non-equilibrium distribution function is expanded in terms of Hermite polynomials around the base state as Maxwellian distribution (see, Eq. (2.53)). The relevant physical moments we considered here are the mass density $\rho$, the hydrodynamic velocity $u$, the pressure $p$, the shear stress $\sigma_{ij}$, the heat flux $q_i$ and the dimensionless non-equilibrium part of the fully contracted fourth-order moment $\Delta$. Hence at this moments the expansion contains up to 4th-order Hermite polynomial. At the fourteen moment order the relavent Hermite polynomials are $\{1\,,\, C_i\,,\, C_i\,C_j\,,\, C^2\,C_i\,,\, C^4\}$. In terms of these Hermite polynomials the non-equilibrium distribution function can be written as

$$f = f^M \left(a^{(0)} + a_i^{(1)}\,C_i + a_{ij}^{(2)}\,C_i\,C_j + a_i^{(3)}\,C^2\,C_i + a^{(4)}\,C^4\right), \tag{2.69}$$

where $f^M$ is the equilibrium Maxwellian distribution function and is given by

$$f^M = \frac{n}{(2\pi\theta)^{\frac{3}{2}}} e^{-\frac{C^2}{2\theta}}. \tag{2.70}$$

In order to find the fourteen expansion coefficients $a^{(0)}, a_i^{(1)}, a_{ij}^{(2)}, a_i^{(3)}$ and $a^{(4)}$ one has to multiply the Eq. (2.69) with corresponding Hermite polynomial and then integrate the resultant equation over all values of velocity. Following the above procedure one can obtain the expressions for the fourteen expansion coefficients as

$$a^{(0)} = 1 + \frac{15}{8}\Delta; \quad a_i^{(1)} = 0; \quad a_{ij}^{(2)} = \frac{\sigma_{ij}}{2\rho\theta^2} - \frac{5}{4\theta}\Delta\,\delta_{ij}; \tag{2.71}$$

$$a_i^{(3)} = -\frac{q_i}{5\,\rho\,\theta^3}; \quad a^{(4)} = \frac{\Delta}{8\,\theta^2}. \tag{2.72}$$

Finally with inclusion of expressions of expansion coefficients $a^{(0)}, a_i^{(1)}, a_{ij}^{(2)}, a_i^{(3)}$ and $a^{(4)}$, the complete non-equilibrium distribution function at fourteen moments reads

$$f = \frac{n}{(2\pi\theta)^{\frac{3}{2}}} e^{-\frac{C^2}{2\theta}} \left(1 + \frac{\sigma_{ij}}{2\rho\theta^2} C_i C_j + \frac{q_i}{5\rho\theta^3}\Big(C^2 - 5\theta\Big) C_i + \Big(\frac{C^4 - 10C^2\theta + 15\theta^2}{8\theta^2}\Big)\Delta\right). \tag{2.73}$$

Different closures can be obtained via the above expansion by truncating the terms with in the bracket. For example, by truncating at the first term, the second term, the third term and the fourth term one can obtain 5-moment, 10-moment, 13-moment and 14-moment closures, respectively.

# Chapter 3

# Normal Shock Waves and Numerical Method

## 3.1 Introduction

The best example for simple and highly non-equilibrium flow phenomena is a normal shock wave. The structure of shock wave has been studied extensively via numerically, theoretically and experimentally since middle of the 19th century using different techniques [(Courant & Friedrichs 1948)]. A normal shock wave is a disturbance propagating between a supersonic fluid and a subsonic fluid, distinguished by a sharp change in its fluid properties. In other words, a normal shock involves a transition between a uniform upstream flow and a uniform downstream flow, i.e., we can treat the shock wave as an interface of finite thickness between two different equilibrium states of a gas [(Courant & Friedrichs 1948; Grad 1952; Bird 1994; Narasimha & Das 1990; Matsuo & Aoki 1992; Reese *et al.* 1995; Greenshields & Reese 2007; Sone *et al.* 2001; Xu & Josyula 2006)]. Shock waves arise at explosions, detonations, supersonic movements of bodies, and so on. This chapter presents (i) an overview of the theory of plane shock waves and (ii) the validation of two numerical schemes used to solve the shock wave problem via Navier-Stokes hydrodynamic model.

## 3.2 Formulation of the Problem

For one-dimensional (1D) planar shock waves, all variables are functions of a single spatial coordinate $x$ and time $t$ [Courant & Friedrichs (1948)] and the system is assumed to be uniform (having no gradients) and infinite along the y- and z- directions, see Fig. 3.1. The flow velocity in the $x$-direction is $u(x,t)$ and the velocities in the two remaining orthogonal directions are set to zero. The heat flux in the $x$-direction is taken to be $q(x,t)$ and zero in remaining orthogonal directions. In this system there are two relevant temperatures: (i) the temperature in the direction of flow is $\theta_{xx}$ and (ii) the temperature in two orthogonal directions are uniform ($\theta_{yy} = \theta_{zz}$). In the following we focus on Navier-Stokes model.

It is convenient to work with following two variables:

$$\theta = \frac{1}{3}(\theta_{xx} + 2\,\theta_{yy}) \quad \text{and} \quad \theta_s = \frac{1}{3}(\theta_{xx} - \theta_{yy}), \tag{3.1}$$

called the mean scalar temperature $\theta$ and the skew temperature $\theta_s$, respectively. Note that the skew temperature $\theta_s$ vanishes when the directional temperatures are equal, i.e., for $\theta_{xx} = \theta_{yy}$, and hence the scalar temperature is $\theta = \theta_{xx} = \theta_{yy}$ in this limit. The latter condition is strictly valid at equilibrium of a molecular gas. It is straightforward to verify that the deviatoric stress

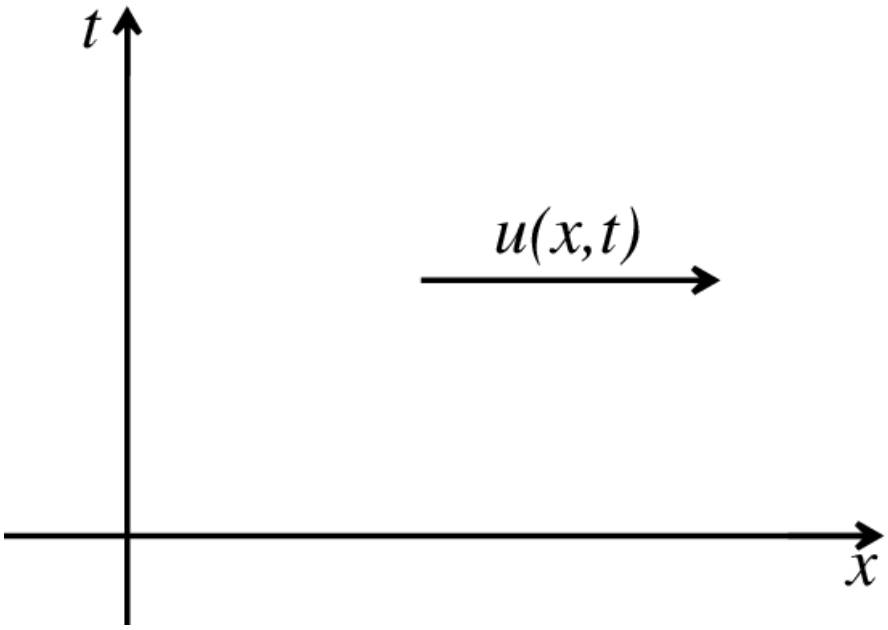


Figure 3.1: Sketch of one-dimensional flow.

tensor has one non-zero component namely the longitudinal stress, which can be expressed as $\sigma_{xx} = 2\,\rho\,\theta_s$, in terms of the skew temperature. Furthermore from the constitutive relation of the stress tensor (2.59) we have the following relation

$$\sigma_{xx} = -\frac{4}{3}\,\mu\,\frac{\partial u}{\partial x} = 2\,\rho\,\theta_s \equiv \sigma. \tag{3.2}$$

### 3.2.1 One-dimensional reduced hydrodynamic models

Here we present the one-dimensional form of hydrodynamic models using (3.1) and (3.2). For one-dimensional version of Navier-Stokes system, the continuity, momentum and energy balance equations are:

$$\frac{\partial \rho}{\partial t} + \frac{\partial}{\partial x}\Big(\rho\,u\Big) = 0, \tag{3.3}$$

$$\frac{\partial}{\partial t}\Big(\rho\,u\Big) + \frac{\partial}{\partial x}\Big(\rho\,u^2 + \rho\,\theta + \sigma\Big) = 0, \tag{3.4}$$

$$\frac{\partial}{\partial t}\Big(\rho\,u^2 + 3\,\rho\,\theta\Big) + \frac{\partial}{\partial x}\Big(\rho\,u^3 + 5\,\rho\,\theta u + 2\,u\,\sigma + 2\,q\Big) = -3\,\mathcal{D}^{NS}. \tag{3.5}$$

The constitutive relations for longitudinal stress $\sigma$ and the dissipation rate $\mathcal{D}^{NS}$ are given by (3.2) and (2.59), respectively. The constitutive relation for heat flux is

$$q = -\kappa\,\frac{\partial \theta}{\partial x} - \kappa_h\,\frac{\partial \rho}{\partial x}. \tag{3.6}$$

The one-dimensional Euler system is obtained by setting $\sigma = 0$ and $q = 0$ into (2.3 -2.5) and $D^{NS}$ is replaced by $D^E$.

## 3.3 Normal Shock Waves

A normal shock occurs when a supersonic gas enters into a subsonic gas [(Courant & Friedrichs 1948; Prasad 2001; Mackenzie 2006)]. Due to the interaction with the subsonic gas particles, the supersonic gas particles are slowed down and causes a sharp increase in the density and temperature at this point, see Fig. 3.2. For instance, the normal shock wave can be easily visualized in a balloon bursting [(Mackenzie 2006)]. When a balloon bursts, the interior gas is expelled outward radially and it collides with the stationary exterior gas and causes a build up of particles at the boundary between the two gases, which moves radially outward.

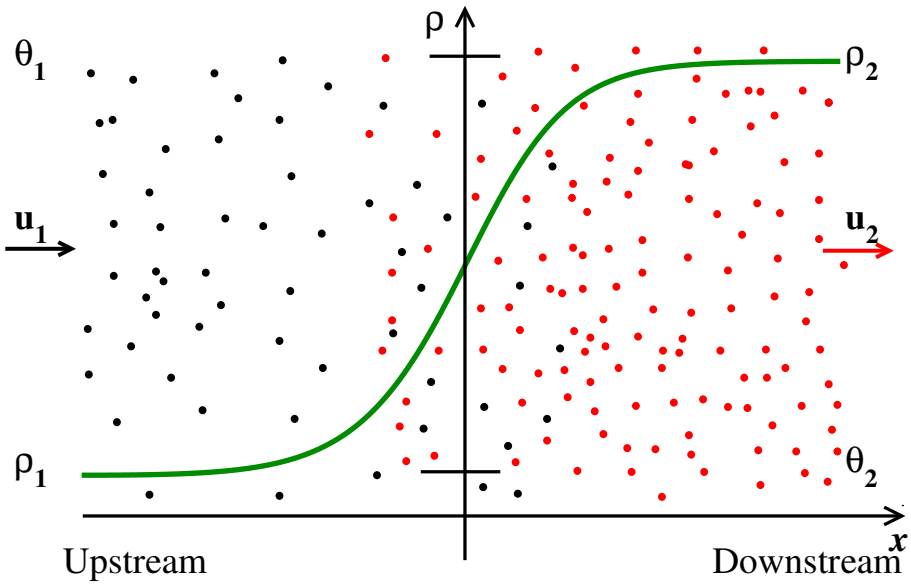


Figure 3.2: Schematic of normal shock wave density profile.

Let us denote the upstream ($x \to -\infty$) and downstream ($x \to \infty$) states of a shock, located at $x = 0$, by $(\rho_1, u_1, \theta_1)$ and $(\rho_2, u_2, \theta_2)$, respectively. The finite jump in each state variable across a shock is given by the so-called Rankine-Hugoniot (RH) relations [Courant & Friedrichs (1948); Liepmann & Roshko (1957)] which connect the upstream and downstream states of a shock. These relations can be obtained from the balance laws (3.3 - 3.5), by using the fact that the terms which are independent of the gradients of hydrodynamic fields do not contribute [Courant & Friedrichs (1948); Goldshtein & Shapiro (1995); Goldshtein *et al.* (1995, 1996*a*)]:

$$\begin{aligned} \rho_1\, v_1 &= \rho_2\, v_2 \\ \rho_1\, v_1^2 + \rho_1\, \theta_1 + \sigma_1 &= \rho_2\, v_2^2 + \rho_2\, \theta_2 + \sigma_2 \\ \rho_1\, v_1^3 + 5\,\rho_1\, \theta_1\, v_1 + 2\,\sigma_1\, v_1 + 2\,q_1 &= \rho_2\, v_2^3 + 5\,\rho_2\, \theta_2\, v_2 + 2\,\sigma_2\, v_2 + 2\,q_2. \end{aligned} \tag{3.7}$$

where $v_i = u_i - v_{sh}$, with $v_{sh}$ being the shock speed. In the stationary coordinate frame of the shock (i.e., the coordinate reference frame is moving with the shock speed), the above relations

becomes

$$\begin{aligned} \rho_1\, u_1 &= \rho_2\, u_2 \\ \rho_1\, u_1^2 \,+\, \rho_1\, \theta_1 \,+\, \sigma_1 &= \rho_2\, u_2^2 \,+\, \rho_2\, \theta_2 \,+\, \sigma_2 \\ \rho_1\, u_1^3 \,+\, 5\,\rho_1\, \theta_1\, u_1 \,+\, 2\,\sigma_1\, u_1 \,+\, 2\,q_1 &= \rho_2\, u_2^3 \,+\, 5\,\rho_2\, \theta_2\, u_2 \,+\, 2\,\sigma_2\, u_2 \,+\, 2\,q_2. \end{aligned} \tag{3.8}$$

These relations provide necessary conditions for any solution of the system (3.3 - 3.5). The conditions given in (3.8) can be further simplified by assuming that the end states are in "local" equilibrium such that the higher-order moment variables $\sigma$, $q$ and $\Delta$ are zero at upstream and downstream ends. Substituting these boundary conditions in (3.8) we arrive at the standard Rankine-Hugoniot relations,

$$\begin{aligned} \rho_1 u_1 &= \rho_2 u_2 \\ \rho_1 u_1^2 + \rho_1 \theta_1 &= \rho_2 u_2^2 + \rho_2 \theta_2 \\ \rho_1 u_1^3 + 5\rho_1 \theta_1 u_1 &= \rho_2 u_2^3 + 5\rho_2 \theta_2 u_2, \end{aligned} \tag{3.9}$$

for a molecular gas described by Euler/Navier-Stokes-order of hydrodynamics.

The local Mach number Ma is defined as the ratio of velocity of the gas to the speed of sound through the molecular gas / granular gas [Goldshtein & Shapiro (1995)]

$$\mathrm{Ma} = \frac{|u|}{c} \equiv \frac{|u|}{\sqrt{\gamma\,\theta}}, \tag{3.10}$$

where $\gamma$ is the adiabatic index (the ratio between two specific heats) whose numerical value for a monatomic molecular / granular gas is 5/3, and $c = \sqrt{\gamma\theta}$ is the adiabatic sound speed which is also the characteristic slope [Courant & Friedrichs (1948)] obtained from Euler equations. Assuming that the flow is adiabatic and solving the RH relations (3.9), the downstream quantities can be expressed as in terms of their upstream counterparts,

$$\begin{aligned} \frac{\rho_2}{\rho_1} &= \frac{(\gamma+1)\mathrm{Ma}_1^2}{2+(\gamma-1)\mathrm{Ma}_1^2} \\ \frac{u_2}{u_1} &= \frac{2+(\gamma-1)\mathrm{Ma}_1^2}{(\gamma+1)\mathrm{Ma}_1^2} \\ \frac{\theta_2}{\theta_1} &= \frac{(2\gamma\mathrm{Ma}_1^2-(\gamma-1))((\gamma-1)\mathrm{Ma}_1^2+2)}{(\gamma+1)^2\mathrm{Ma}_1^2}, \end{aligned} \tag{3.11}$$

where $\mathrm{Ma}_1 = |u_1|/\sqrt{\gamma\,\theta}$ is the upstream Mach number. For the Riemann problem, the local Mach number is maximum at the upstream state and decreases through the shock by reaching its minimum value at the downstream state.

## 3.4 Reference Scales and Dimensionless Equations

The changes through the shock profile occur due to collisions, so the mean free path ($l$) is a natural choice for the length scale. The expression for the mean free path of a gas is

$$l = \frac{16\,\mu}{5\,\sqrt{2\pi}\rho\sqrt{\theta}}, \tag{3.12}$$

where the shear viscosity coefficient $\mu$ for hard-spheres molecules is given by:

$$\mu = \frac{5m}{4d^2}\sqrt{\frac{\theta}{\pi}}\frac{1}{(1+\alpha)(3-\alpha)}. \tag{3.13}$$

For shock wave calculations below, all quantities are non-dimensionalized by the "upstream" reference state quantities. The dimensionless variables are given by

$$\begin{aligned} &\hat{\rho} = \frac{\rho}{\rho_1}, \qquad \hat{u} = \frac{u}{\sqrt{\theta_1}}, \qquad \hat{\theta} = \frac{\theta}{\theta_1}, \qquad \hat{\theta}_s = \frac{\theta_s}{\theta_1}, \\ &\hat{\sigma} = \frac{\sigma}{\rho_1\theta_1}, \qquad \hat{q} = \frac{q}{\rho_1\theta_1\sqrt{\theta_1}}, \qquad \hat{x} = \frac{x}{l_1}, \qquad \hat{t} = \frac{t\sqrt{\theta_1}}{l_1}. \end{aligned} \tag{3.14}$$

For simplicity we remove hat for non-dimensional quantities.

### 3.4.1 Navier-Stokes system in dimensionless form

The one-dimensional balance equations for Navier-Stokes system in dimensionless form take the following form:

$$\frac{\partial\rho}{\partial t} + \frac{\partial}{\partial x}\Big(\rho\,u\Big) = 0, \tag{3.15}$$

$$\frac{\partial}{\partial t}\Big(\rho\,u\Big) + \frac{\partial}{\partial x}\Big(\rho\,u^2 + \rho\,\theta\Big) = \frac{5\sqrt{2\,\pi}}{12}\Big(\frac{1}{2\,\sqrt{\theta}}\,\frac{\partial\theta}{\partial x}\,\frac{\partial u}{\partial x} + \sqrt{\theta}\frac{\partial^2 u}{\partial x^2}\Big), \tag{3.16}$$

$$\begin{aligned} \frac{\partial}{\partial t}\Big(\rho\,u^2 + 3\,\rho\,\theta\Big) + \frac{\partial}{\partial x}\Big(\rho\,u^3 + 5\,\rho\,\theta u\Big) &= \frac{5\sqrt{2\,\pi}}{6}\,u\,\Big(\frac{1}{2\,\sqrt{\theta}}\,\frac{\partial\theta}{\partial x}\,\frac{\partial u}{\partial x} + \sqrt{\theta}\,\frac{\partial^2 u}{\partial x^2}\Big) \\ &+ \frac{5\sqrt{2\,\pi}}{6}\,\sqrt{\theta}\,\Big(\frac{\partial u}{\partial x}\Big)^2 + \frac{5\sqrt{2\,\pi}}{8}\,\Big(\frac{b_2}{b_1}\Big)\,\Big[\frac{1}{2\,\sqrt{\theta}}\,\Big(\frac{\partial\theta}{\partial x}\Big)^2 + \sqrt{\theta}\,\frac{\partial^2\theta}{\partial x^2}\Big] \\ &+ \frac{5\sqrt{2\,\pi}}{8}\,\Big(\frac{b_3}{b_1}\Big)\,\Big[\frac{3}{2}\,\frac{\sqrt{\theta}}{\rho}\,\frac{\partial\theta}{\partial x}\,\frac{\partial\rho}{\partial x} + \theta^{\frac{3}{2}}\,\Big(\frac{1}{\rho}\,\frac{\partial^2\rho}{\partial x^2} - \frac{1}{\rho^2}\,\Big(\frac{\partial\rho}{\partial x}\Big)^2\Big)\Big] \\ &- \frac{64\,b_1}{5\,\sqrt{2}}\,(1-\alpha^2)\,\rho^2\,\theta^{\frac{3}{2}}\,\Big(1 + \frac{3}{16}\,a_2\Big), \end{aligned} \tag{3.17}$$

where

$$
\begin{aligned}
b_1 &= \frac{5}{4\sqrt{\pi}}\,\frac{1}{(1+\alpha)\,(3-\alpha)\,[1\,-\,\frac{a_2}{32}]},\\
b_2 &= \frac{75}{2\sqrt{\pi}}\,\frac{1\,+\,2\,a_2}{(1+\alpha)[49\,-\,33\,\alpha\,+\,(19\,-\,3\,\alpha)\,\frac{a_2}{32}]},\\
b_3 &= \frac{75}{2\sqrt{\pi}}\,\frac{a_2}{(1+\alpha)[49\,-\,33\,\alpha\,+\,(19\,-\,3\,\alpha)\,\frac{a_2}{32}]}.
\end{aligned}
\tag{3.18}
$$

The constitutive relations for longitudinal stress and heat flux are given by

$$
\begin{aligned}
\sigma &= -\frac{5\sqrt{2\,\pi}}{12}\,\sqrt{\theta}\,\frac{\partial u}{\partial x},\\
q &= -\frac{5\sqrt{2\,\pi}}{16}\,\Big[\frac{b_2}{b_1}\,\sqrt{\theta}\,\frac{\partial \theta}{\partial x}\,+\,\frac{b_3}{b_1}\,\frac{\theta^{\frac{3}{2}}}{\rho}\,\frac{\partial \rho}{\partial x}\Big].
\end{aligned}
\tag{3.19}
$$

From Eqs. (3.18) and (3.19), we note that for a molecular gas (i.e., $\alpha = 1$), $b_2$ and $b_3$ reduce to $\frac{75}{64\sqrt{\pi}}$ and 0. Therefore, for a molecular gas, the constitutive relation of heat flux contains only temperature gradient.

### 3.4.2 Euler system in dimensionless form

The dimensionless Euler system can be obtained from the dimensionless Navier-Stokes system (3.15 - 3.17) for which there are no gradient terms on the right hand side. Moreover, in the dissipation rate we have to set $a_2$ to zero, since $a_2$ is related to the fourth-order moment. Hence, by setting all gradients terms on the right hand side of equations (3.15 - 3.17) to zero and further setting $a_2 = 0$, we obtain the dimensionless Euler system as:

$$
\frac{\partial \rho}{\partial t} + \frac{\partial}{\partial x}\Big(\rho\, u\Big) \;=\; 0, \tag{3.20}
$$

$$
\frac{\partial}{\partial t}\Big(\rho\, u\Big) + \frac{\partial}{\partial x}\Big(\rho\, u^2 + \rho\,\theta\Big) \;=\; 0, \tag{3.21}
$$

$$
\frac{\partial}{\partial t}\Big(\rho\, u^2\,+\,3\,\rho\,\theta\Big) + \frac{\partial}{\partial x}\Big(\rho\, u^3\,+\,5\,\rho\,\theta u\Big) \;=\; -\,\frac{64\,b_1}{5\,\sqrt{2}}\,(1\,-\,\alpha^2)\,\rho^2\,\theta^{\frac{3}{2}}. \tag{3.22}
$$

## 3.5 Numerical Scheme for Shock Waves

Our main task is to solve the one dimensional reduced models of Sec. 3.4 which can be expressed in operator form

$$
\frac{\partial}{\partial t}\boldsymbol{U} + \frac{\partial}{\partial x}\boldsymbol{F}(\boldsymbol{U}) = \boldsymbol{G}(\boldsymbol{U}), \tag{3.23}
$$

where $\boldsymbol{U}$ is the vector of variables, $\boldsymbol{F}(\boldsymbol{U})$ is the vector of flux and $\boldsymbol{G}(\boldsymbol{U})$ is the vector of source terms. The explicit forms of $\boldsymbol{U}$, $\boldsymbol{F}(\boldsymbol{U})$ and $\boldsymbol{G}(\boldsymbol{U})$ for Navier-Stokes model are clearly

seen from the equations (3.15 - 3.17) and are given by:

$$\boldsymbol{U} = \begin{pmatrix} \rho \\ \rho\, u \\ \rho u^2 + 3\rho\theta \end{pmatrix}, \tag{3.24}$$

$$\boldsymbol{F}(\boldsymbol{U}) = \begin{pmatrix} \rho\, u \\ \rho u^2 + \rho\theta \\ \rho u^3 + 5\rho\theta u \end{pmatrix}, \tag{3.25}$$

$$\boldsymbol{G}(\boldsymbol{U}) = \begin{pmatrix} 0 \\ \frac{5\sqrt{2\,\pi}}{12}\left(\frac{1}{2\,\sqrt{\theta}}\,\frac{\partial\theta}{\partial x}\,\frac{\partial u}{\partial x} + \sqrt{\theta}\frac{\partial^2 u}{\partial x^2}\right) \\ \frac{5\sqrt{2\,\pi}}{6}\,u\left(\frac{1}{2\,\sqrt{\theta}}\,\frac{\partial\theta}{\partial x}\,\frac{\partial u}{\partial x} + \sqrt{\theta}\,\frac{\partial^2 u}{\partial x^2}\right) + \frac{5\sqrt{2\,\pi}}{6}\,\sqrt{\theta}\left(\frac{\partial u}{\partial x}\right)^2 \\ + \frac{5\sqrt{2\,\pi}}{8}\left(\frac{b_2}{b_1}\right)\left[\frac{1}{2\,\sqrt{\theta}}\left(\frac{\partial\theta}{\partial x}\right)^2 + \sqrt{\theta}\,\frac{\partial^2\theta}{\partial x^2}\right] + \frac{5\sqrt{2\,\pi}}{8}\left(\frac{b_3}{b_1}\right)\left[\frac{3}{2}\,\frac{\sqrt{\theta}}{\rho}\,\frac{\partial\theta}{\partial x}\,\frac{\partial\rho}{\partial x}\right. \\ \left. + \theta^{\frac{3}{2}}\left(\frac{1}{\rho}\,\frac{\partial^2\rho}{\partial x^2} - \frac{1}{\rho^2}\left(\frac{\partial\rho}{\partial x}\right)^2\right)\right] - \frac{64\,b_1}{5\,\sqrt{2}}\,(1-\alpha^2)\,\rho^2\,\theta^{\frac{3}{2}}\left(1 + \frac{3}{16}\,a_2\right) \end{pmatrix}. \tag{3.26}$$

The system (3.23) is called hyperbolic in $\boldsymbol{U}$ and $t$ if the eigenvalues of the Jacobian matrix, $\partial\boldsymbol{F}(\boldsymbol{U})/\partial\boldsymbol{U}$, are real and distinct [Courant & Friedrichs (1948)], and hence the characteristic speeds are finite.

An appropriate shock-capturing scheme [Shu & Osher (1988); Yee *et al.* (1990); Jin & Xin (1995); Liu & Osher (1996); LeVeque (2002); Xu (2002); Delis & Katsaounis (2003); Serna & Marquina (2005); Xu & Huang (2010)] needs to be employed to solve (3.23) along with Rankine-Hugoniot conditions (3.11). We solve the system of inhomogeneous partial differential equations (3.23) using relaxation schemes via two different approaches: (1) the relaxation scheme of Jin & Xin (1995) and (2) the relaxation scheme of Delis & Katsaounis (2003). In the first approach the source terms are incorporated via the well known PDE splitting technique and in later approach the source terms are incorporated in the relaxation scheme itself. It must be noted that the original relaxation scheme of Jin & Xin (1995) was developed to solve a hyperbolic system of the form (3.23) which does not contain any source term (i.e., $\boldsymbol{G}(\boldsymbol{U}) = 0$).

### 3.5.1 PDE splitting technique[†]

The solution of (3.23) using PDE splitting technique approach involves a 'two-stage' procedure: in the first stage, the homogeneous equation

$$\frac{\partial \boldsymbol{U}^h}{\partial t} + \frac{\partial \boldsymbol{F}(\boldsymbol{U}^h)}{\partial x} = 0, \quad \text{with} \quad \boldsymbol{U}^h(x, t=0) = \boldsymbol{U}(x, t=0), \tag{3.27}$$

[†]This numerical technique has been developed in collaboration with Dr. Santosh Ansumali

is solved, and in the second stage the solution of the homogeneous part (3.27) is used to solve

$$\frac{\partial \boldsymbol{U}}{\partial t} = \boldsymbol{G}(\boldsymbol{U}), \quad \text{with} \quad \boldsymbol{U}(x, t=0) = \boldsymbol{U}^h(x, t=0), \tag{3.28}$$

and thereby construct the full solution.

The homogeneous system (3.27) is solved by employing the same relaxation scheme of Jin & Xin (1995) that finds the solution of an equivalent relaxation system

$$\frac{\partial \boldsymbol{U}^h}{\partial t} + \frac{\partial \boldsymbol{V}}{\partial x} = 0, \tag{3.29}$$

$$\frac{\partial \boldsymbol{V}}{\partial t} + \mathbf{A}\frac{\partial \boldsymbol{U}^h}{\partial x} = -\frac{1}{\epsilon}(\boldsymbol{V} - \boldsymbol{F}(\boldsymbol{U}^h)), \tag{3.30}$$

where $\boldsymbol{U}^h \in \mathbb{R}^n$, $\boldsymbol{V} \in \mathbb{R}^n$, $x \in \mathbb{R}^1$, $t > 0$ and $\epsilon$ is a small positive parameter called the relaxation rate. Putting $\epsilon \to 0$ into the hyperbolic part of the relaxation system (3.30), we obtain the local equilibrium solution $\boldsymbol{V} = \boldsymbol{F}(\boldsymbol{U}^h)$ which, along with (3.29), retrieves the original homogeneous system (3.27). The hyperbolic part of the relaxation system (3.30) has two characteristic variables $\boldsymbol{V} \pm \mathbf{A}^{\frac{1}{2}}\boldsymbol{U}$ that travel with the characteristic speeds $\pm\mathbf{A}^{\frac{1}{2}}$, respectively. For the convergence and the dissipative nature of the relaxation system (3.29) - (3.30), it is necessary that

$$\boldsymbol{F}'(\boldsymbol{U}^h) - \mathbf{A} \le 0 \quad \textit{for all } \boldsymbol{U}^h, \tag{3.31}$$

which is known as the subcharacteristic condition, where $\boldsymbol{F}'(\boldsymbol{U}^h)$ is the Jacobian matrix of flux $\boldsymbol{F}(\boldsymbol{U}^h)$. By choosing sufficiently large $\mathbf{A}$, Eq. (3.31) can always be satisfied. But it is desirable to obtain the smallest $\mathbf{A}$ meeting the above criterion, because of the CFL constraints on numerical stability. For simplicity we assume that $\mathbf{A}$ has a special form,

$$\mathbf{A} = \text{diag}\{a_1, a_2, \cdots, a_n\}, \quad a_m > 0 \quad (1 \le m \le n). \tag{3.32}$$

The Jacobian matrix of flux $\boldsymbol{F}(\boldsymbol{U}^h)$ constitutes a "complete" eigen-system $\{\lambda_1, \lambda_2, \cdots, \lambda_n\}$, and hence we can either take $a_1 = \sup|\lambda_1|$, $a_2 = \sup|\lambda_2|$, $\cdots$, $a_n = \sup|\lambda_n|$ or simply $a_1 = a_2 = \cdots = a_n = \max(\sup|\lambda_1|, \sup|\lambda_2|, \cdots, \sup|\lambda_n|)$ for all $t$ and $x$, both satisfying the subcharacteristic condition $-\sqrt{a_m} \le \lambda_m \le \sqrt{a_m}$ for all $\boldsymbol{U}^h$ and $1 \le m \le n$. For the present purpose we choose

$$a_1 = a_2 = \cdots = a_n = \max(\sup|\lambda_1|, \sup|\lambda_2|, \cdots, \sup|\lambda_n|) \tag{3.33}$$

for all $t$ and $x$ to construct the diagonal matrix (3.32). Hence by doing this we ensure that the characteristic speeds of the hyperbolic part of the relaxation system (3.30) are always as large as the characteristic speeds of the original problem (3.27), so that the subcharacteristic condition holds always.

In the following we briefly discuss about this relaxation scheme of Jin & Xin (1995). Let us consider the spatially-uniform spatial grid points $x_{i+\frac{1}{2}}$ with a step size $\Delta x = x_{i+\frac{1}{2}} - x_{i-\frac{1}{2}}$ for $i = 1, ..., N$; the time discretization $t_n$ is also taken as uniform with a time step $\Delta t = t_{j+1} - t_j$ for $j = 0, 1, 2, \cdots$. We denote the approximate cell average of a quantity $\boldsymbol{W}$ at time $t_j$ in the

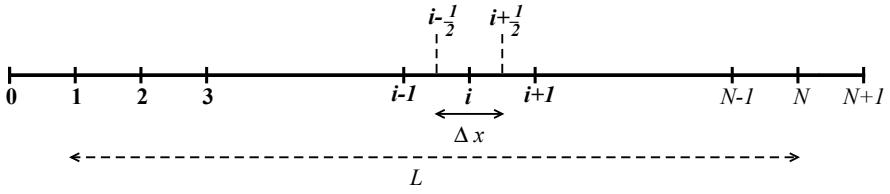


Figure 3.3: Schematic of the one-dimensional grid.

cell $[x_{i-\frac{1}{2}}, x_{i+\frac{1}{2}}]$ by $\boldsymbol{W}_i^j$ and the approximate point value of $\boldsymbol{W}$ at $x = x_{i+\frac{1}{2}}$ by $\boldsymbol{W}^j_{i+\frac{1}{2}}$. Let

$$D_+ \boldsymbol{W}_i = \frac{1}{\Delta x}\left(\boldsymbol{W}_{i+\frac{1}{2}} - \boldsymbol{W}_{i-\frac{1}{2}}\right). \tag{3.34}$$

A classical first-order accurate upwind scheme for spatial discretization and a second order accurate TVD (total variation diminishing) Runge-Kutta time-splitting scheme applied to the system (3.29) - (3.30) compute $(\boldsymbol{U}_i^{j+1}, \boldsymbol{V}_i^{j+1})$ for given $(\boldsymbol{U}_i^j, \boldsymbol{V}_i^j)$ as:

$$\begin{aligned}
\boldsymbol{U}_i^* &= \boldsymbol{U}_i^j, \\
\boldsymbol{V}_i^* &= \boldsymbol{V}_i^j + \frac{\Delta t}{\epsilon}(\boldsymbol{V}_i^* - \boldsymbol{F}(\boldsymbol{U}_i^*)), \\
\boldsymbol{U}_i^{(1)} &= \boldsymbol{U}_i^* - \Delta t\, D_+ \boldsymbol{V}_i^*, \\
\boldsymbol{V}_i^{(1)} &= \boldsymbol{V}_i^* - \Delta t\, \mathbf{A}\, D_+ \boldsymbol{U}_i^*, \\
\boldsymbol{U}_i^{**} &= \boldsymbol{U}_i^{(1)}, \\
\boldsymbol{V}_i^{**} &= \boldsymbol{V}_i^{(1)} - \frac{\Delta t}{\epsilon}(\boldsymbol{V}_i^{**} - \boldsymbol{F}(\boldsymbol{U}_i^{**})) - 2\frac{\Delta t}{\epsilon}(\boldsymbol{V}_i^* - \boldsymbol{F}(\boldsymbol{U}_i^*)), \\
\boldsymbol{U}_i^{(2)} &= \boldsymbol{U}_i^{**} - \Delta t\, D_+ \boldsymbol{V}_i^{**}, \\
\boldsymbol{V}_i^{(2)} &= \boldsymbol{V}_i^{**} - \Delta t\, \mathbf{A}\, D_+ \boldsymbol{U}_i^{**}, \\
\boldsymbol{U}_i^{j+1} &= \frac{1}{2}(\boldsymbol{U}_i^j + \boldsymbol{U}_i^{(2)}), \\
\boldsymbol{V}_i^{j+1} &= \frac{1}{2}(\boldsymbol{V}_i^j + \boldsymbol{V}_i^{(2)}),
\end{aligned} \tag{3.35}$$

with

$$\begin{aligned}
\boldsymbol{U}_{i+\frac{1}{2}} &= \frac{1}{2}(\boldsymbol{U}_i + \boldsymbol{U}_{i+1}) - \frac{1}{2}\mathbf{A}^{-\frac{1}{2}}(\boldsymbol{V}_{i+1} - \boldsymbol{V}_i), \\
\boldsymbol{V}_{i+\frac{1}{2}} &= \frac{1}{2}(\boldsymbol{V}_i + \boldsymbol{V}_{i+1}) - \frac{1}{2}\mathbf{A}^{\frac{1}{2}}(\boldsymbol{U}_{i+1} - \boldsymbol{U}_i).
\end{aligned} \tag{3.36}$$

This splitting scheme takes two implicit stiff source steps and two explicit convection steps alternatively. Here we omitted the superscript $h$ on $\boldsymbol{U}$. Once the solution of the homogeneous part $\boldsymbol{U}_i^{(h)}$ is known, we can find the solution $\boldsymbol{U}_i$ of (3.28)

$$\boldsymbol{U}_i = \boldsymbol{U}_i^{(h)} + \Delta t\, \boldsymbol{G}(\boldsymbol{U}_i^{(h)}). \tag{3.37}$$

The spatial $(\Delta x)$ and temporal $(\Delta t)$ steps must be chosen such that the Courant-Friedrichs-Lewy

(CFL) condition,

$$\mathcal{C} = max(a_i\,\Delta t/\Delta x) < 1, \tag{3.38}$$

is satisfied. In the present numerical scheme, the source terms are incorporated via the well-known splitting technique for inhomogeneous partial-differential equations: (3.23) is solved by solving (3.27) and (3.37) sequentially in two stages as described above. More details of the algorithm can be found in Jin & Xin (1995). Few advantages of relaxation schemes over a typical Riemann solver are:

- The main advantage of the relaxation-type numerical scheme is that they neither use spatial Riemann solvers nor use the solution of nonlinear algebraic equations temporally.
- One can apply standard upwind schemes without solving the Riemann problem, because of the constant linear characteristic fields.
- One can design highly efficient and vectorized algorithms.
- One can easily extend this methodology to the systems of higher dimensions.

### 3.5.2 Numerical scheme of Delis & Katsaounis

Instead of solving the system (3.23) by PDE splitting technique, we also implemented the numerical scheme of Delis & Katsaounis (2003) that incorporates the source terms in the relaxation scheme itself. Let us consider an inhomogeneous system (3.23), the corresponding equivalent relaxation system is given by Delis & Katsaounis (2003):

$$\frac{\partial \boldsymbol{U}}{\partial t} + \frac{\partial \boldsymbol{V}}{\partial x} = \boldsymbol{G}(\boldsymbol{U}), \tag{3.39}$$

$$\frac{\partial \boldsymbol{V}}{\partial t} + \mathbf{A}\frac{\partial \boldsymbol{U}}{\partial x} = -\frac{1}{\epsilon}(\boldsymbol{V} - \boldsymbol{F}(\boldsymbol{U})), \tag{3.40}$$

Here the original inhomogeneous system (3.23) has been replaced by a linear hyperbolic system (3.39) - (3.40) with a relaxation source term, which in the relaxation limit $\epsilon \to 0$ recovers the original system (i.e., the relaxation limit $\epsilon \to 0$ rapidly drives $\boldsymbol{V} \to \boldsymbol{F}(\boldsymbol{U})$). Moreover, if the following condition, the so called subcharacteristic condition holds [Evje & Fjelde (2002); Lattanzio & Serre (2001); Li *et al.* (2002)]

$$\boldsymbol{F}'(\boldsymbol{U}) - \mathbf{A} \leq 0 \quad \textit{for all}\ \boldsymbol{U}, \tag{3.41}$$

the solution of the system (3.39) - (3.40) approaches the solution of the original inhomogeneous system (3.23) as $\epsilon \to 0$, where $\boldsymbol{F}'(\boldsymbol{U})$ is the Jacobian matrix of flux function $\boldsymbol{F}(\boldsymbol{U})$ and $\mathbf{A} = \text{diag}\{a_1, a_2, \cdots, a_n\}$ with $a_m$'s $(1 \leq m \leq n)$ are positive constants. It is evident that for varying $\boldsymbol{U}$ in a bounded domain, the subcharacteristic condition can always be satisfied by choosing sufficiently large $a_m$ $(1 \leq m \leq n)$. However it is desirable to choose smallest $a_m$ $(1 \leq m \leq n)$ which can meet the above subcharacteristic condition.

Here the spatial discretization, the time discretization and cell averages are same as in Sec. 3.5.1. For the source term application, we adapt the upwind scheme for spatial discretization

and TVD Runge-Kutta time-splitting scheme for time discretization like in Sec. 3.5.1. Hence for given $(\boldsymbol{U}_i^j, \boldsymbol{V}_i^j)$, $(\boldsymbol{U}_i^{j+1}, \boldsymbol{V}_i^{j+1})$ are computed as follows:

$$
\begin{aligned}
\boldsymbol{U}_i^* &= \boldsymbol{U}_i^j, \\
\boldsymbol{V}_i^* &= \boldsymbol{V}_i^j + \frac{\Delta t}{\epsilon}(\boldsymbol{V}_i^* - \boldsymbol{F}(\boldsymbol{U}_i^*)), \\
\boldsymbol{U}_i^{(1)} &= \boldsymbol{U}_i^* - \Delta t\, D_+\, \boldsymbol{V}_i^* + \Delta t\, \boldsymbol{G}(\boldsymbol{U}_i^*), \\
\boldsymbol{V}_i^{(1)} &= \boldsymbol{V}_i^* - \Delta t\, \mathbf{A}\, D_+ \boldsymbol{U}_i^*, \\
\boldsymbol{U}_i^{**} &= \boldsymbol{U}_i^{(1)}, \\
\boldsymbol{V}_i^{**} &= \boldsymbol{V}_i^{(1)} - \frac{\Delta t}{\epsilon}(\boldsymbol{V}_i^{**} - \boldsymbol{F}(\boldsymbol{U}_i^{**})) - 2\frac{\Delta t}{\epsilon}(\boldsymbol{V}_i^* - \boldsymbol{F}(\boldsymbol{U}_i^*)), \\
\boldsymbol{U}_i^{(2)} &= \boldsymbol{U}_i^{**} - \Delta t\, D_+\, \boldsymbol{V}_i^{**} + \Delta t\, \boldsymbol{G}(\boldsymbol{U}_i^{**}), \\
\boldsymbol{V}_i^{(2)} &= \boldsymbol{V}_i^{**} - \Delta t\, \mathbf{A}\, D_+ \boldsymbol{U}_i^{**}, \\
\boldsymbol{U}_i^{j+1} &= \frac{1}{2}(\boldsymbol{U}_i^j + \boldsymbol{U}_i^{(2)}), \\
\boldsymbol{V}_i^{j+1} &= \frac{1}{2}(\boldsymbol{V}_i^j + \boldsymbol{V}_i^{(2)}).
\end{aligned}
\tag{3.42}
$$

Finally, the spatial ($\Delta x$) and temporal ($\Delta t$) steps must satisfy the Courant-Friedrichs-Lewy (CFL) condition, $\mathcal{C} = max(a_i\, \Delta t/\Delta x) < 1$. The relaxation rate $\epsilon$ plays the role of numerical viscosity, so more numerical diffusion will be added if we take the larger values for $\epsilon$. Hence the relaxation rate $\epsilon$ must be very small compared to the time step size and the spatial step size (i.e., $\epsilon \ll \Delta t$ and $\epsilon \ll \Delta x$). Further details of this scheme are found in Delis & Katsaounis (2003, 2005).

### 3.5.3 Boundary conditions for Relaxation scheme

As we know that the relaxation schemes [Jin & Xin (1995); Delis & Katsaounis (2003)] introduce a new artificial variable $\boldsymbol{V}$ to the problem, so a natural question arises is that what are the boundary conditions for $\boldsymbol{V}$. We implement the boundary conditions for $\boldsymbol{V}$ that are consistent to the local equilibrium $\boldsymbol{V} = \boldsymbol{F}(\boldsymbol{U})$. Let the integration domain be $\Phi$ and $\partial\Phi$ be its boundary. Suppose that $\boldsymbol{U}|_{\partial\Phi}$ is specified, then we set $\boldsymbol{V}|_{\partial\Phi} = \boldsymbol{F}(\boldsymbol{U}|_{\partial\Phi})$. It means that if $\boldsymbol{U}$ satisfies Dirichlet boundary condition and so does $\boldsymbol{V}$. Suppose that $\boldsymbol{U}$ satisfies the Neumann boundary condition that is $\frac{\partial}{\partial x}\boldsymbol{U} = 0$, then we get $\frac{\partial}{\partial x}\boldsymbol{V} = 0$ because we have $\frac{\partial}{\partial x}\boldsymbol{V} = \boldsymbol{F}'(\boldsymbol{U})\frac{\partial}{\partial x}\boldsymbol{U}$. Similarly other boundary conditions which are satisfied by $\boldsymbol{U}$ can be imposed for $\boldsymbol{V}$ also. We use the boundary conditions for $\boldsymbol{V}$ as discussed above in our numerical experiments.

## 3.6 Validation of Numerical Schemes

To validate two numerical schemes, which are discussed in Sec. 3.5.1 and 3.5.2, we consider normal shock waves propagating in a molecular gas (the coefficient of restitution is $\alpha = 1$). The

upstream boundary conditions for normal shock wave problem are taken as

$$\rho_1 = 1, \quad u_1 = \mathrm{Ma}_1 \sqrt{\gamma}, \quad \theta_1 = 1, \tag{3.43}$$

and the downstream boundary conditions are provided by the Rankine-Hugoniot conditions (3.11). The initial discontinuity is placed at $x = 0$. The numerical experiments are carried out over a domain of length $L = 50$ covering $(-L/2, L/2)$ with a 2000 grid points, with a time step of $\Delta t = (\mathcal{C}\,\Delta x/\max a_i)$. For all calculations we set the CFL number to $\mathcal{C} = 0.01$ and the relaxation rate in (3.30) and (3.40) is set to be $\epsilon = 10^{-8}$ as this provides converged results. To obtain a time-invariant state as expected for shocks propagating in an ideal gas, the computations are carried out over a long time ($t \geq 100$).

### 3.6.1 Molecular shock: comparison with previous results

To validate the PDE-splitting technique, we present the results of molecular shock waves obtained by Navier-Stokes model. The density and velocity profiles, predicted by Navier-Stokes model, are presented in Fig. 3.4. Note that the profiles shown in Fig. 3.4 have been normalized via the following relations:

$$\rho_N = \frac{\rho - \rho_1}{\rho_2 - \rho_1}, \tag{3.44}$$

$$u_N = \frac{u - u_2}{u_1 - u_2}. \tag{3.45}$$

From Fig. 3.4, it is noteworthy that there are strong gradients across the shock layer for

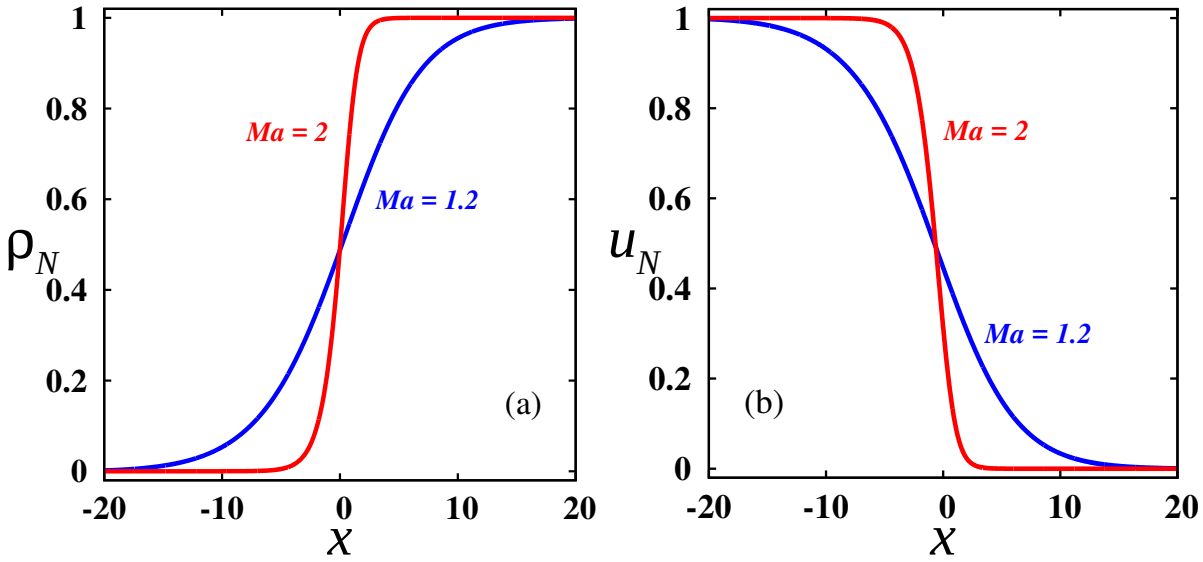


Figure 3.4: Shock wave profiles for a molecular gas: (a) density and (b) velocity.

each hydrodynamic variable, and moreover the thickness of this layer decreases with increasing upstream Mach number $\mathrm{Ma}_1$, as expected.

As in previous works [Gilbarg & Paolucci (1953); Pham-Van-Diep *et al.* (1991); Torrilhon & Struchtrup (2004)], here we introduce a characteristic width of the density profile to define the thickness of the shock. The shock thickness, which is often used to characterize the shock wave

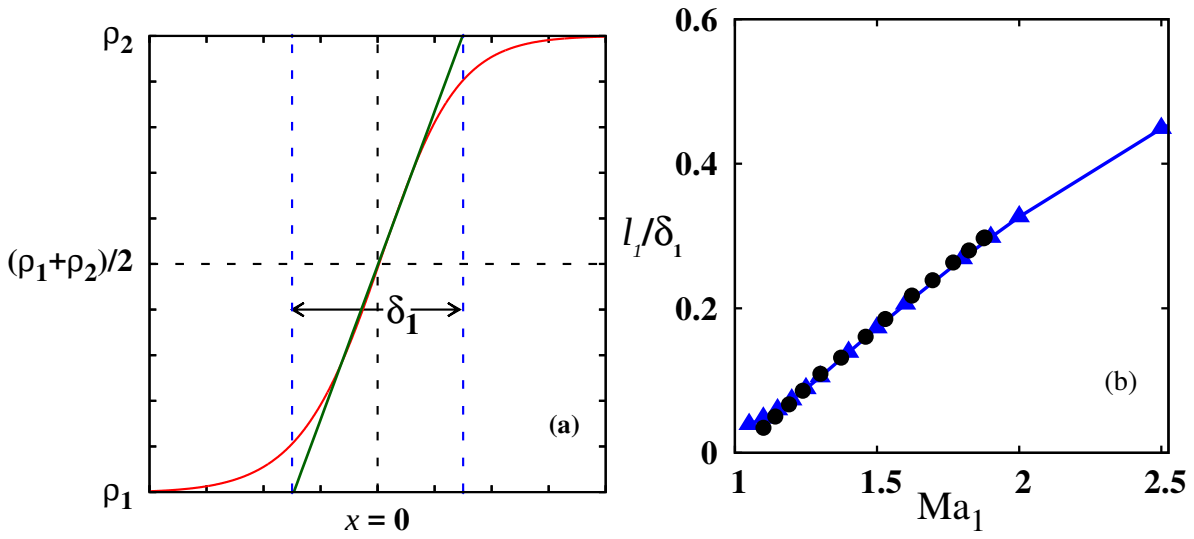


Figure 3.5: (a) Schematic picture of the definition of shock width $\delta_1$: The red line indicates the density and the green line indicates the tangent to the density profile with the maximum slope; the distance between points of intersections of this tangent line with $\rho_1$ and $\rho_2$ is the shock width or shock thickness $\delta_1$, (b) Variation of inverse shock width ($l_1 \,/\, \delta_1$), with $\mathrm{Ma}_1$. The triangles represent the present solution of Navier-Stokes model and the circles denote Navier-Stokes solution of Torrilhon & Struchtrup (2004).

properties instead of comparing full shock wave profiles, is defined as:

$$\delta_1 = \frac{\rho_2 - \rho_1}{\max(\partial\rho/\partial x)}. \tag{3.46}$$

From the definition of $\delta_1$, we infer that it has a linear dependence on the density values at

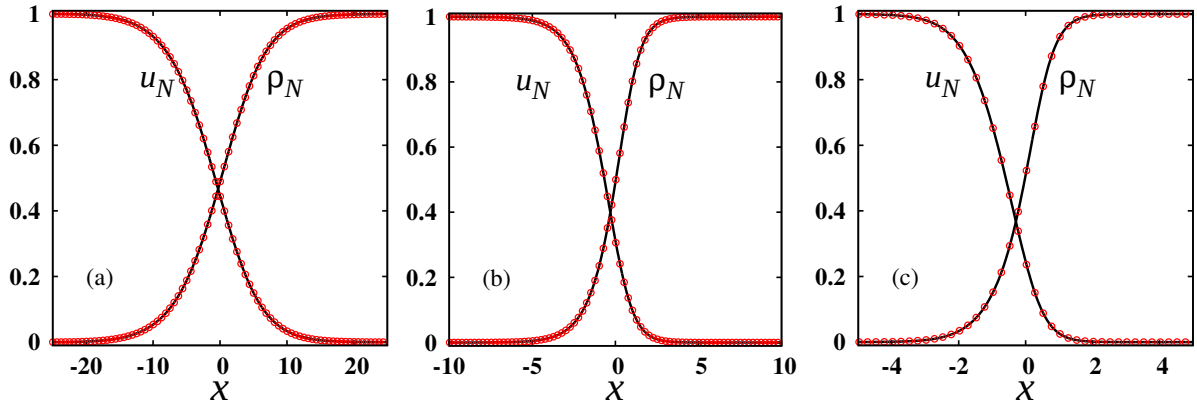


Figure 3.6: Comparison between PDE splitting technique using Jin & Xin (1995) scheme(black line) and Delis & Katsaounis (2003) scheme(red circles). Left: $\mathrm{Ma}_1 = 1.2$, middle: $\mathrm{Ma}_1 = 2$, right: $\mathrm{Ma}_1 = 3$.

upstream and downstream and a slope corresponding to the maximum density gradient and is schematically depicted in Fig. 3.5 (a). The variation of the inverse of the shock thickness ($l_1 \,/\, \delta_1$) with upstream Mach number ($\mathrm{Ma}_1$) is shown in Fig. 3.5 (b). The solutions obtained from the PDE-splitting technique are denoted by blue triangles which almost overlap with the black circles

which represent the data of Torrilhon & Struchtrup (2004) using a different numerical method. On the whole, Fig. 3.5 (b) confirms the accuracy of the PDE-splitting technique.

### 3.6.2 Comparison between two numerical schemes

Here we validate the two numerical approaches discussed in Sec. 3.5. The density and velocity profiles, obtained by Navier-Stokes model for inflow Mach number of $\mathrm{Ma}_1 = 1.2$, $\mathrm{Ma}_1 = 2$ and $\mathrm{Ma}_1 = 3$, are displayed in Fig. 3.6 (a,b,c), respectively. From Fig. 3.6, we conclude that both numerical schemes predict the same behavior accurately. On the other hand, Tables 3.1 and 3.2 indicate that the PDE-splitting technique is a little faster than the numerical scheme of Delis & Katsaounis (2003). The numerical simulations in Table 3.1 are carried out for a molecular gas over a time ($t = 100$) by taking a spatial domain of length $L = 50$ covering $(-L/2, L, 2)$ and the numerical simulations in Table 3.2 are carried out for a granular gas with the coefficient of restitution ($\alpha = 0.9$) over a time ($t = 100$) by taking a spatial domain of length $L = 300$ covering $(-L/6, 5L/6)$. We set the CFL number $\mathcal{C} = 0.01$ and the relaxation rate $\epsilon = 10^{-8}$ for all computations listed in Tables 3.1 and 3.2. Moreover the discontinuity is placed at $x = 0$.

Table 3.1: Time taken for converged solution (Molecular gas)

| $\Delta x$ | $\Delta t$ | Numerical scheme-1 | Numerical scheme-2 |
|---|---|---|---|
| 0.05 | $1.76045 \times 10^{-4}$ | 5.133 min. | 6.632 min. |
| 0.025 | $8.80223 \times 10^{-5}$ | 20.575 min. | 26.570 min. |

Table 3.2: Time taken for converged solution (Granular gas)

| $\Delta x$ | $\Delta t$ | Numerical scheme-1 | Numerical scheme-2 |
|---|---|---|---|
| 0.025 | $8.80223 \times 10^{-5}$ | 120.387 min. | 155.798 min. |
| 0.01 | $3.52089 \times 10^{-5}$ | 779.952 min. | 1018.852 min. |

## 3.7 Relationship between Mach number, Reynolds number and Knudsen number

In §3.6.1, we discussed about the effect of Mach number on shock wave profiles. We are also interested to see the effect of Knudsen number (Kn) on shock wave profiles. In this regard, we show that the Mach number and Knudsen number are linearly related. The Mach number is defined as the ratio of velocity of the gas to the speed of sound through the gas and the expression for Mach number is given in (3.10).

Now we introduce two more dimensionless numbers namely Knudsen number (Kn) and Reynolds number (Re). The Knudsen number is defined as the ratio between the mean free path ($l$) to the characteristic length scale ($\mathcal{L}$) of the system and for a hard-sphere gas the expression for Knudsen number is given by

$$\mathrm{Kn} = \frac{l}{L} \equiv \frac{16\,\mu}{5\sqrt{2\,\pi\,\theta}\rho\,\mathcal{L}}. \tag{3.47}$$

The Reynold's number is defined as the ratio of the inertial forces to the viscous forces and the expression for this is given by

$$\mathrm{Re} = \frac{\rho\, u\, \mathcal{L}}{\mu}. \tag{3.48}$$

From equations (3.10), (3.47) and (3.48), we arrive at the following relation which relates the Knudsen number to Mach number via Reynold's number as

$$\mathrm{Kn} = \frac{16}{5}\sqrt{\frac{\gamma}{2\,\pi}}\,\frac{\mathrm{Ma}}{\mathrm{Re}}. \tag{3.49}$$

Using Eq. (3.49), one can relate the effect of Mach number on shock profiles to the effect of Knudsen number on shock profiles.

## 3.8 Summary

The theory of normal shocks in molecular/granular gases and the formulation of Euler and Navier-Stokes-order hydrodynamic equations for plane shock waves have been described. The Rankine-Hugoniot conditions for a dilute granular gas are found to be identical as those for a molecular gas. The resulting one-dimensional PDEs have been solved by two relaxation-type numerical schemes: (i) PDE-splitting technique following Jin & Xin (1995) and (ii) the numerical scheme of Delis & Katsaounis (2003). Both numerical schemes produce shock-profiles accurately, and the shock thickness results extracted from both schemes have been compared with the data of Torrilhon & Struchtrup (2004) [who used a different numerical method], which further confirms the accuracy of both numerical schemes. The relative performance of two numerical schemes has been evaluated, and it is shown that the PDE-splitting technique is faster than the method of Delis & Katsaounis. All numerical computations carried out in chapters 4, 6, 7 and A of this thesis are performed using two numerical schemes: the PDE-splitting technique with Jin & Xin relaxation scheme and the method of Delis & Katsaounis.

# Chapter 4

# Plane Shock Waves, Haff's Law and Regularized Energy Equation[†]

## 4.1 Introduction

In this chapter, the Riemann problem of planar shock waves is analysed for a dilute granular gas by solving Euler- and Navier-Stokes-order equations numerically. The density and temperature profiles are found to be asymmetric, with the maxima of both density and temperature occurring within the shock-layer. The density-peak increases with increasing Mach number and inelasticity, and is found to propagate at a steady speed at late times. The granular temperature at the upstream and downstream end of the shock decay according to Haff's law [$\theta(t) \sim t^{-2}$]. The Haff's law seems to hold inside the shock up-to a certain time for weak shocks, but deviations occur for strong shocks. The time at which the maximum temperature deviates from Haff's law follows a power-law scaling with upstream Mach number and the restitution coefficient. The origin of the continual build-up of density with time is discussed, and it is shown that the granular energy equation must be 'regularized' to arrest the maximum density.

## 4.2 Hydrodynamic Equations for a Granular Gas and Plane Shock Waves

At Navier-Stokes (NS) order, the relevant physical variables are the mass density $\rho$, the hydrodynamic velocity $\mathbf{u}$ and the granular/kinetic temperature $\theta$, the pressure tensor $p_{ij}$ and the heat flux vector $q_i$. The pressure tensor is decomposed such that $p = \rho\theta$ is pressure and $\sigma_{ij}$ is its deviatoric part. The hydrodynamic balance equations for the mass, momentum and energy are discussed in §2.4 and are given by:

$$\frac{\partial \rho}{\partial t} + \frac{\partial (\rho\, u_i)}{\partial x_i} = 0, \tag{4.1}$$

$$\frac{\partial (\rho\, u_i)}{\partial t} + \frac{\partial (\rho\, u_i\, u_j)}{\partial x_j} + \frac{\partial p}{\partial x_i} + \frac{\partial \sigma_{ij}}{\partial x_j} = 0, \tag{4.2}$$

$$\frac{3}{2}\frac{\partial p}{\partial t} + \frac{3}{2}\frac{\partial (p\, u_i)}{\partial x_i} + \frac{\partial q_i}{\partial x_i} + p\frac{\partial u_i}{\partial x_i} + \sigma_{ij}\frac{\partial u_i}{\partial x_j} = -\frac{3}{2}\mathcal{D}. \tag{4.3}$$

[†]This chapter has been published in Journal of Fluid Mechanics (M. H. L. Reddy and M. Alam, vol. 779, R2, 2015)

The term on the right-hand side of (4.3) represents the rate of energy dissipation per unit volume,

$$\mathcal{D} = \frac{4}{3} n d^2 \sqrt{\pi} \left(1 - \alpha^2\right) \left(1 + \frac{3}{16} a_2\right) \rho \, \theta^{\frac{3}{2}}, \tag{4.4}$$

with

$$a_2 = \frac{16(1-\alpha)(1-2\alpha^2)}{30\alpha^2(1-\alpha) + 81 - 17\alpha} \tag{4.5}$$

representing the contracted fourth moment of the distribution function. The set of balance equations (4.1-4.3) is made closed by providing constitutive relations for $\sigma_{ij}$ and $q_i$:

$$\sigma_{ij} = -2\mu \left( \frac{1}{2} \left( \frac{\partial u_i}{\partial x_j} + \frac{\partial u_i}{\partial x_i} \right) - \frac{1}{3} \frac{\partial u_i}{\partial x_i} \right) \tag{4.6}$$

$$q_i = -\kappa \frac{\partial \theta}{\partial x_i} - \kappa_h \frac{\partial \rho}{\partial x_i}. \tag{4.7}$$

The expressions for the shear viscosity $\mu$, the thermal conductivity $\kappa$ and the higher-order thermal conductivity $\kappa_h$ are given in Chapter 2 (§2.6.2). For the Euler model too, the balance equations are (4.1-4.3), but with constitutive relations $\sigma_{ij} = 0 = q_i$ and the contracted fourth moment of the distribution function $a_2$ is set to zero.

### 4.2.1 Equations for plane shock waves: Navier-Stokes (NS) and Euler models

For plane shock waves, the NS-model can be written in "quasi-conservation" form,

$$\frac{\partial \rho}{\partial t} + \frac{\partial}{\partial x}\Big(\rho u\Big) = 0, \tag{4.8}$$

$$\frac{\partial}{\partial t}\Big(\rho u\Big) + \frac{\partial}{\partial x}\Big(\rho u^2 + \rho\theta + \sigma\Big) = 0, \tag{4.9}$$

$$\frac{\partial}{\partial t}\Big(\rho u^2 + 3\rho\theta\Big) + \frac{\partial}{\partial x}\Big(\rho u^3 + 5\rho\theta u + 2\,u\sigma + 2\,q\Big) = -3\mathcal{D}, \tag{4.10}$$

with a non-conservative term $\mathcal{D}$ in the energy equation (4.10). The constitutive relations for the "longitudinal" stress and the heat flux are given by

$$\sigma_{xx} = -\frac{4}{3}\mu \frac{\partial u}{\partial x} \equiv \sigma, \tag{4.11}$$

$$q = -\kappa \frac{\partial \theta}{\partial x} - \kappa_h \frac{\partial \rho}{\partial x}, \tag{4.12}$$

and the dissipation rate $\mathcal{D}$ is given by (4.4). The one-dimensional Euler system is obtained by setting $\sigma = 0$ and $q = 0$ into (4.8-4.10).

### 4.2.2 Rankine-Hugoniot conditions of a granular gas and the end states

We already discussed the Rankine-Hugoniot conditions for a molecular gas in §3.3. As we know that if the volume fraction is very small the granular gas resembles an ideal gas. Hence the dilute granular gas resembles an ideal gas (Goldhirsch 2003). So the R-H condition for dilute granular case are same as that of molecular gas. These relations are given in Eq. (3.7) of §3.3 and are reproduced below:

$$\rho_1 v_1 = \rho_2 v_2, \tag{4.13}$$

$$\rho_1 v_1^2 + \rho_1\theta_1 + \sigma_1 = \rho_2 v_2^2 + \rho_2\theta_2 + \sigma_2, \tag{4.14}$$

$$\rho_1 v_1^3 + 5\rho_1\theta_1 v_1 + 2\sigma_1 v_1 + 2q_1 = \rho_2 v_2^3 + 5\rho_2\theta_2 v_2 + 2\sigma_2 v_2 + 2q_2, \tag{4.15}$$

where $v_i = u_i - v_{sh}$, with $v_{sh}$ being the shock speed.

One thing we need to point out here is that there is no equilibrium state in granular gas which in contrast to the molecular gas. So an additional ansatz is now made: the upstream and downstream states are *spatially uniform* (which, along with a temporally decaying temperature field, represents the "local" equilibrium of a granular gas (Haff 1983), known as the *homogeneous cooling state*, see Eq. (4.21) in §4.3.3). The spatial homogeneity [i.e. $\boldsymbol{\nabla}(\rho, \boldsymbol{u}, \theta) = 0$] of end-states implies that the flux terms $\sigma$, (4.11), and $q$, (4.12), vanish at $x \to \pm\infty$. Therefore, putting $\sigma = 0 = q$ into (4.13-4.15) we arrive at the RH-conditions for a granular gas. Moreover the numerical value of the adiabatic index $\gamma$, which is the ratio between two specific heats for a monatomic granular gas is same as in molecular gas. The initial ($t = 0$) shock profiles are given by $(\rho_1, u_1, \theta_1)$ for $x \leq 0$ and $(\rho_2, u_2, \theta_2)$ for $x > 0$, and the shock speed is zero at $t = 0$. Assuming that the flow is adiabatic and solving the RH-relations (4.13 - 4.15) for a stationary shock, the downstream quantities can be expressed in terms of their upstream counterparts, as given in Eq. (3.11) of §3.3. It may be noted that the resulting RH-conditions are identical for both molecular and 'smooth' granular gases (Goldshtein *et al.* 1995) at Euler/NS-order of hydrodynamics.

### 4.2.3 Reference scales for granular shock wave problem

One should be careful in choosing the reference scales for non-dimensionalization, since, unlike in an equilibrium molecular gas, the hydrodynamic fields in a granular gas can vary with time. We use all "upstream" state quantities evaluated at $t = 0$ as reference scales for non-dimensionalization. The dimensionless variables are therefore given by

$$\hat{\rho} = \frac{\rho}{\rho_1(0)}, \quad \hat{u} = \frac{u}{\sqrt{\theta_1(0)}}, \quad \hat{\theta} = \frac{\theta}{\theta_1(0)}, \quad \hat{\sigma} = \frac{\sigma}{\rho_1(0)\theta_1(0)}, \quad \hat{x} = \frac{x}{l_1}, \quad \hat{t} = \frac{t\sqrt{\theta_1(0)}}{l_1}, \tag{4.16}$$

where the length scale used is the mean free path, $l = 16\,\mu/5\sqrt{2\pi}\rho\sqrt{\theta}$, with the shear viscosity $\mu$ being given by (3.13).

The one-dimensional balance equations in dimensionless form have the same form as in

(4.8-4.10) which can be written in operator form (removing hat from dimensionless quantities)

$$\frac{\partial}{\partial t}\boldsymbol{U} + \frac{\partial}{\partial x}\boldsymbol{F}(\boldsymbol{U}) = \boldsymbol{G}(\boldsymbol{U}), \tag{4.17}$$

where $\boldsymbol{U}$ is the vector of variables, $\boldsymbol{F}(\boldsymbol{U})$ is the vector of flux and $\boldsymbol{G}(\boldsymbol{U})$ is the vector of source terms. For Navier-Stokes model the forms of $\boldsymbol{U}$, $\boldsymbol{F}(\boldsymbol{U})$ and $\boldsymbol{G}(\boldsymbol{U})$ are given by

$$\boldsymbol{U} = \begin{pmatrix} \rho \\ \rho\, u \\ \rho u^2 + 3\rho\theta \end{pmatrix}, \qquad \boldsymbol{F}(\boldsymbol{U}) = \begin{pmatrix} \rho\, u \\ \rho u^2 + \rho\theta \\ \rho u^3 + 5\rho\theta u \end{pmatrix}, \tag{4.18}$$

$$\boldsymbol{G}(\boldsymbol{U}) = \begin{pmatrix} 0 \\ \frac{\partial \sigma}{\partial x} \\ -2\frac{\partial (u\,\sigma)}{\partial x} - 2\frac{\partial q}{\partial x} - 3\,\mathcal{D} \end{pmatrix}. \tag{4.19}$$

## 4.3 Results and Discussion: Granular Shock Waves and Regularization

Here we consider normal shock-waves propagating in a dilute granular gas (i.e. the restitution coefficient is $\alpha \neq 1$). The upstream boundary conditions are taken as

$$\rho_1 = 1, \quad u_1 = \mathrm{Ma}_1\sqrt{\gamma}, \quad \theta_1 = 1, \tag{4.20}$$

where $\mathrm{Ma}_1 = |u_1|/\sqrt{\gamma\,\theta_1(0)}$ is the upstream Mach number at $t = 0$, while the downstream boundary conditions are provided by RH conditions (3.11). The initial discontinuity is placed at $x = 0$. For early time evolution of shocks in a granular gas, all computations were carried out in a domain of length $L = 100$ covering $(-L/2, L/2)$ and for long time evolution of shocks in a granular gas, numerical experiments were carried out in a domain of length $L = 4000$ covering $(-2000, 2000)$ with varying number of grid points and a time-step of $\triangle t = (\mathcal{C}\triangle x/\max a_i)$. A spatial step size of $\triangle x = 0.05$ was found to be sufficient for the results at early times, but for the results at late times were obtained with $\triangle x = 0.01$. Finally for all calculations we set the spatial step size to $\triangle x = 0.01$; the CFL number to $\mathcal{C} = 0.01$; the relaxation rate in (3.30 and 3.40) is set to $\epsilon = 10^{-8}$ as this provided converged results. Fig. 4.1 shows the convergence of Navier-Stokes solutions for different $\triangle x$ using the numerical scheme discussed in §3.5.1 and Fig. 4.2 shows the convergence of Navier-Stokes solutions for different $\triangle x$ using the numerical scheme discussed in §3.5.2.

### 4.3.1 Shock structures in a granular gas

Firstly we present the results of early time dynamics (up-to $t = 10$) of the density $\rho(x,t)$, the granular temperature $\theta(x,t)$, and the gas velocity $u(x,t)$ are shown in figure 4.3 for $\mathrm{Ma}_1 = 1.2$ and $\alpha = 0.9$. To show the effect of inelasticity and the effect of Mach number on the shock profiles, we also displayed the results for $\mathrm{Ma}_1 = 1.2$ and $\alpha = 0.75$ in figure 4.4 and for $\mathrm{Ma}_1 = 2$

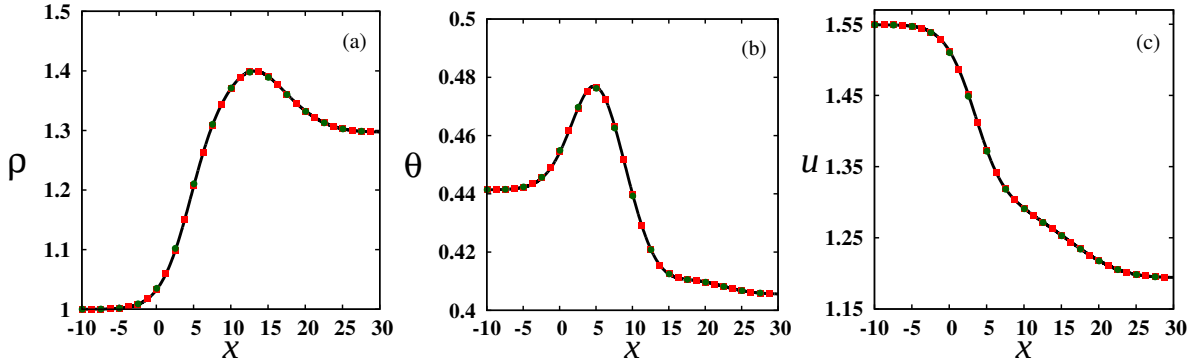


Figure 4.1: Comparison of Navier-Stokes shock profiles of (a) density, (b) granular temperature and (c) velocity at time $t = 10$ for $\mathrm{Ma}_1 = 1.2$ and $\alpha = 0.9$ and for a different values of step size $\triangle x$. In all panels, the filled green circles, filled red squares and solid black line indicates the results for $\triangle x = 0.05, 0.025$ and $0.01$, respectively.

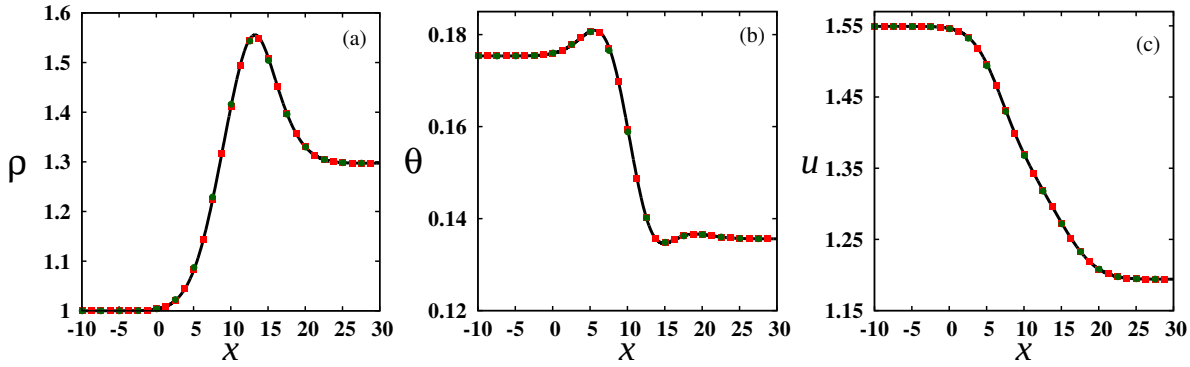


Figure 4.2: Comparison of Navier-Stokes shock profiles of (a) density, (b) granular temperature and (c) velocity at time $t = 10$ for $\mathrm{Ma}_1 = 1.2$ and $\alpha = 0.7$ and for a different values of step size $\triangle x$. In all panels, the filled green circles, filled red squares and solid black line indicates the results for $\triangle x = 0.05, 0.025$ and $0.01$, respectively.

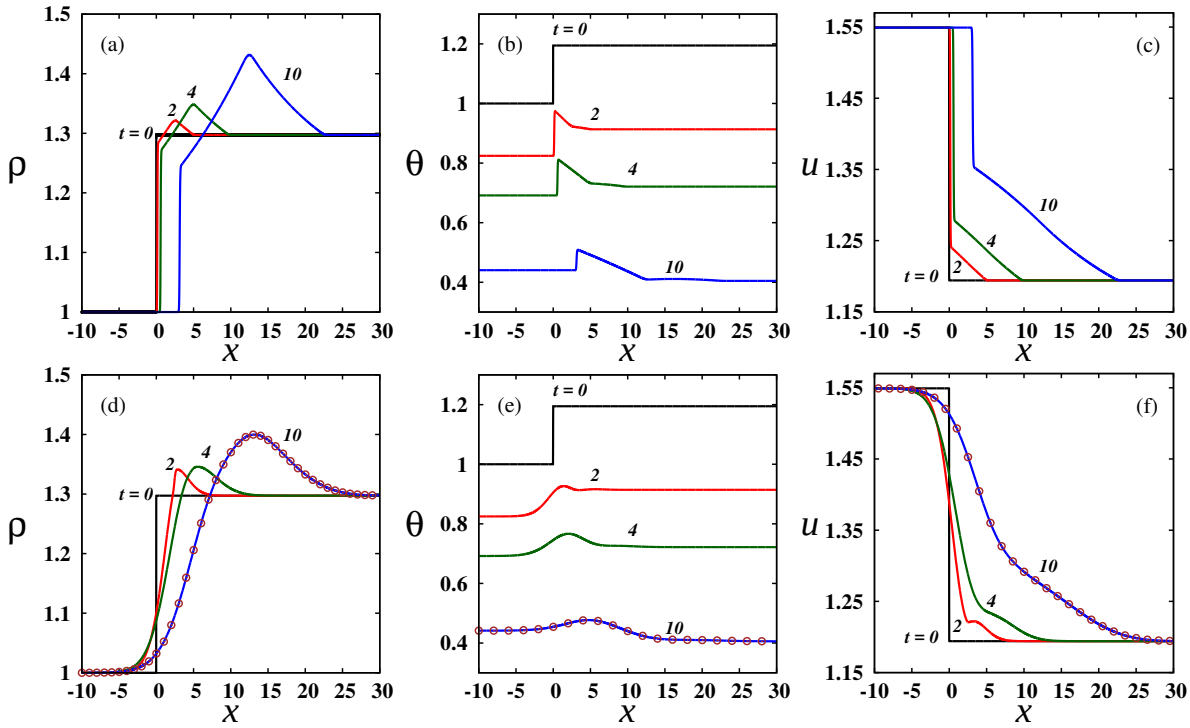


Figure 4.3: Predictions of Euler model (top row) and Navier-Stokes model (bottom row) for shock profiles of (a, d) density, (b, e) granular temperature and (c, f) velocity at different times ($t = 0, 2, 4, 10$) for $\mathrm{Ma}_1 = 1.2$ and $\alpha = 0.9$. Circles in panel $d$ represent the density profile at $t = 10$, obtained from the numerical scheme of Delis & Katsaounis (which is discussed in §3.5.2.)

and $\alpha = 0.9$ in figure 4.5, respectively. In all figures the profiles obtained from Euler and Navier-Stokes models are contrasted in the top and bottom rows, respectively. It is seen that while the initial discontinuity of hydrodynamic fields seem to persist at all times for the Euler model, all profiles become smoother with time due to the diffusive action of viscosity for NS model.

We also observe that the density profile (panels $a$ and $d$) develops an "over-shoot" within the shock in the sense that the maximum density ($\rho_{\max}$) is larger than its downstream value and this overshoot ($= \rho_{\max} - \rho_2$) increases as time progresses; this will be discussed in detail in §4.3.2. Moreover from the panels $(a, d)$ of figures (4.3 - 4.5), one can comment that the density overshoot increases as inelasticity and Mach number increases. Panels $b$ and $e$ indicate that both upstream and downstream temperatures decay with time, and the maximum temperature ($\theta_{\max}$) occurs within the shock layer; this will be discussed in detail in §4.3.3. It is noteworthy that the value of the maximum temperature decreases as we increase the inelasticity, which is evident from the panels $(b, e)$ of figures 4.3 and 4.5. The velocity profiles in panels $(c, f)$ indicate that the local Mach number is maximum at the upstream state and decreases through the shock by reaching its minimum value at the downstream state. The qualitative nature of hydrodynamic profiles at higher $\mathrm{Ma}_1$ and the lower values of $\alpha$ remain similar to those of in figures (4.3 - 4.5).

### 4.3.2 Density overshoot and its propagation speed

The time evolution of the density overshoot, $\triangle\rho \equiv (\rho_{\max} - \rho_2)$, for an upstream Mach number of $\mathrm{Ma}_1 = 1.2$ and a restitution coefficient of $\alpha = 0.9$ is shown in figure 4.6(a) – the red-

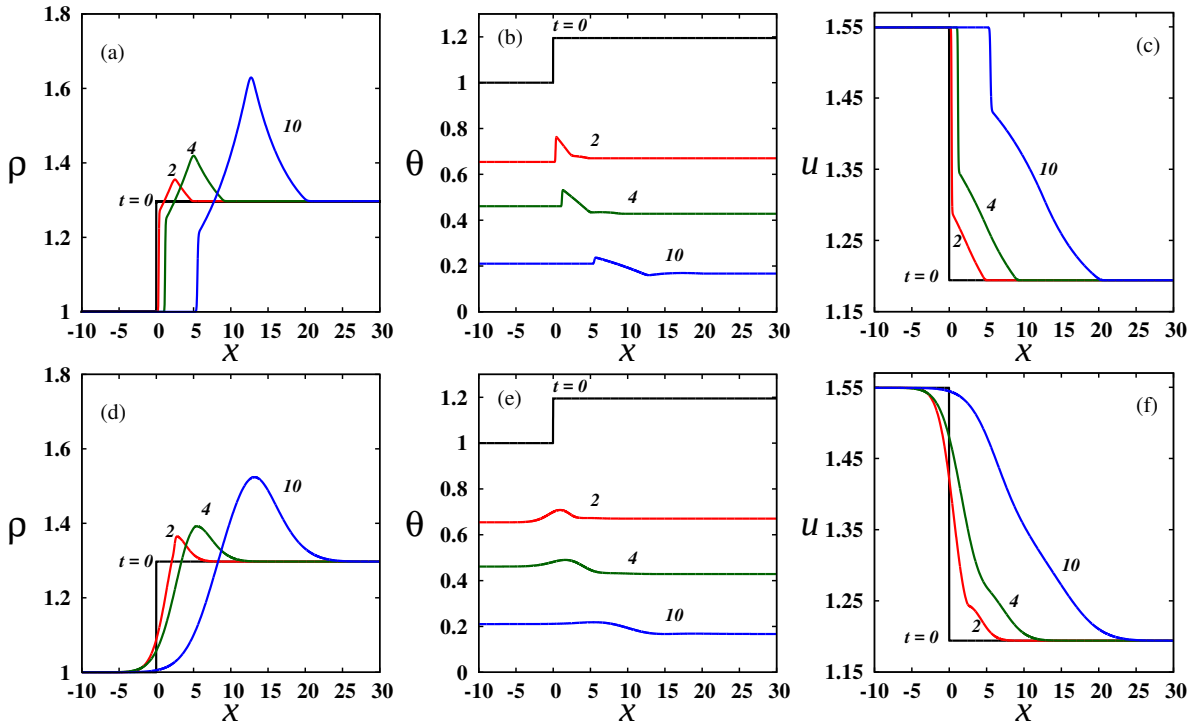


Figure 4.4: Predictions of Euler model (top row) and Navier-Stokes model (bottom row) for shock profiles of (a, d) density, (b, e) granular temperature and (c, f) velocity at different times ($t = 0, 2, 4, 10$) for $\mathrm{Ma}_1 = 1.2$ and $\alpha = 0.75$.

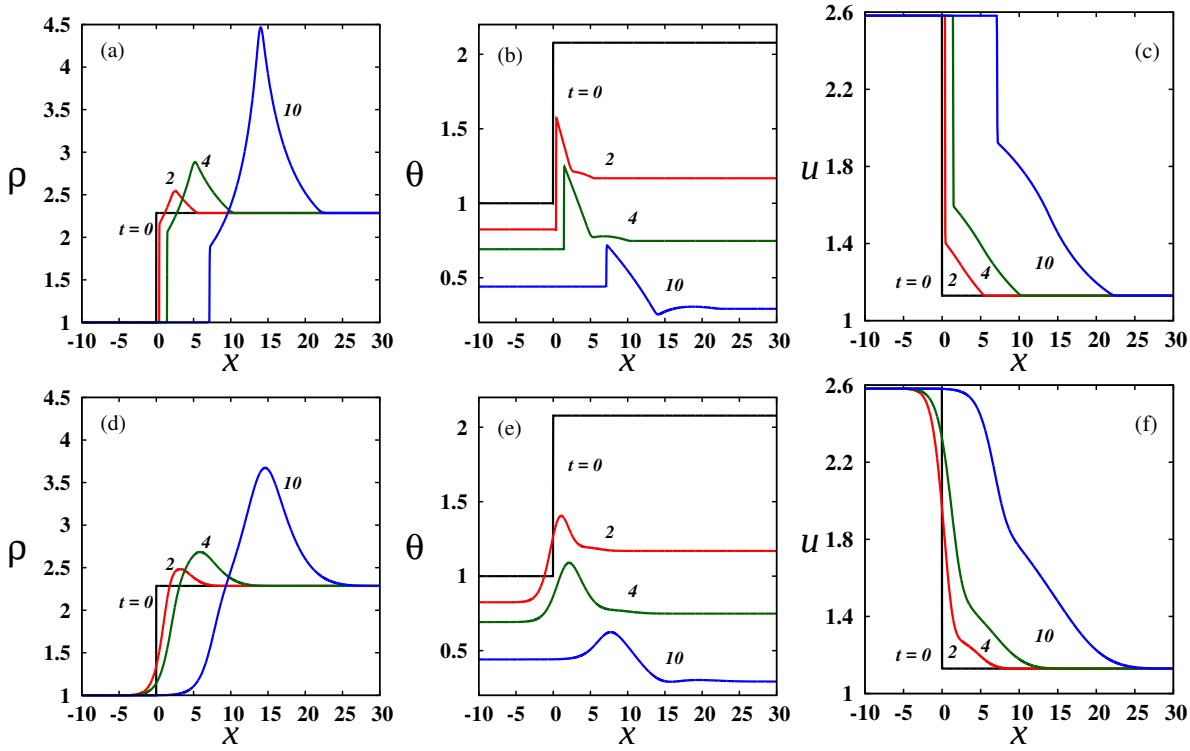


Figure 4.5: Predictions of Euler model (top row) and Navier-Stokes model (bottom row) for shock profiles of (a, d) density, (b, e) granular temperature and (c, f) velocity at different times ($t = 0, 2, 4, 10$) for $\mathrm{Ma}_1 = 2$ and $\alpha = 0.9$.

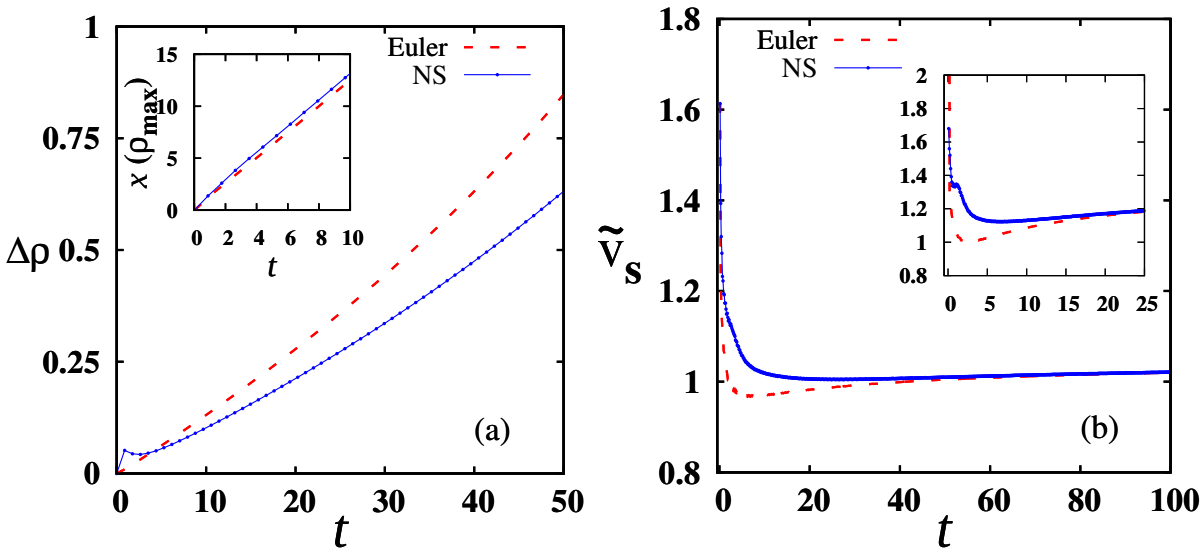


Figure 4.6: (a) Temporal evolution of the density-overshoot, $\triangle\rho \equiv (\rho_{\max} - \rho_2)$, for $\mathrm{Ma}_1 = 1.2$ and $\alpha = 0.9$. Inset shows the variation of the spatial location of $\rho_{\max}$ with time. (b) Evolution of normalized shock speed, $\tilde{v}_s = v_s/c$, where $v_s = x(\rho = \rho_{\max})/t$ is the speed of the density-peak and $c = \sqrt{\gamma\theta_1}$ is the adiabatic sound speed, for $\mathrm{Ma}_1 = 1.2$ (main panel) and $\mathrm{Ma}_1 = 2$ (inset) with $\alpha = 0.9$.

dashed and blue-solid lines denote predictions of Euler and NS models, respectively. While $\triangle\rho = 0$ for a molecular gas (figure 3.4*b* and (Gilbarg & Paolucci 1953; Torrilhon & Struchtrup 2004)), we find that $\triangle\rho > 0$ in a granular gas and its magnitude increases with time; note that $(\triangle\rho)_{NS} < (\triangle\rho)_{Euler}$, except for very short early times. We also found that $\triangle\rho$ increases as the Mach number and/or the dissipation are increased, which is evident from the figures (4.3 - 4.5). The occurrence of density-overshoot is a novel feature of "granular" shock waves and its large-time behaviour is discussed in §4.3.4.

The inset of figure 4.6(a) indicates that the spatial position of $\rho_{\max}$ shifts to the right with time, from which a shock speed can be estimated. The speed of propagation of the density maximum is defined as $v_s = x(\rho = \rho_{\max})/t$, and its temporal variations for $\mathrm{Ma}_1 = 1.2$ and 2 are displayed in the main panel and the inset of figure 4.6(b), respectively, with $\alpha = 0.9$. It is seen that the normalized shock speed, $\tilde{v}_s = v_s/c$ (where $c$ is the adiabatic sound speed, (3.10)), reaches a steady asymptotic value at large times for both Euler (red curve) and NS (blue curve) models. Comparing the inset with the main panel, we find that $\tilde{v}_s^{\infty} \equiv \tilde{v}_s(t \to \infty)$ is higher at higher $\mathrm{Ma}_1$. This is further evident from figure 4.7 which shows the variation of $\tilde{v}_s^{\infty}$ with $(1-\alpha)$ for a range of $\mathrm{Ma}_1$. While $\tilde{v}_s^{\infty}$ does not depend on the restitution coefficient, it increases almost linearly with increasing $\mathrm{Ma}_1$ (see the inset of figure 4.7). Overall, we may conclude from figures 4.6(b) and 4.7 that the density-peak travels with a steady constant speed at sufficiently late times; this conclusion is similar to that found for the piston-driven shock wave too (Kamenetsky *et al.* 2000).

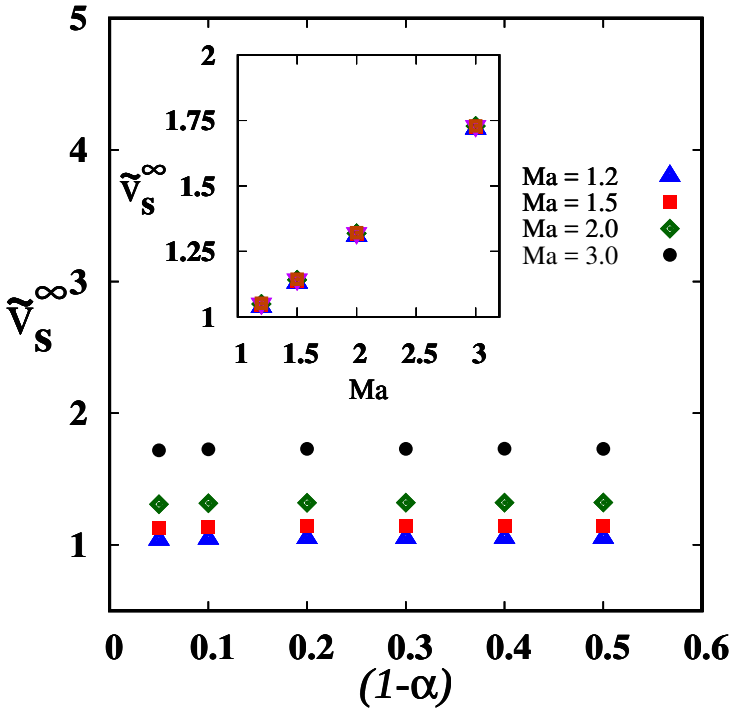


Figure 4.7: Variation of asymptotic shock speed $\tilde{v}_s^\infty$ (extracted from the numerical solution of granular Navier-Stokes equations, dubbed 'NS-solution') with $\mathrm{Ma}_1$ (inset) and inelasticity (main panel).

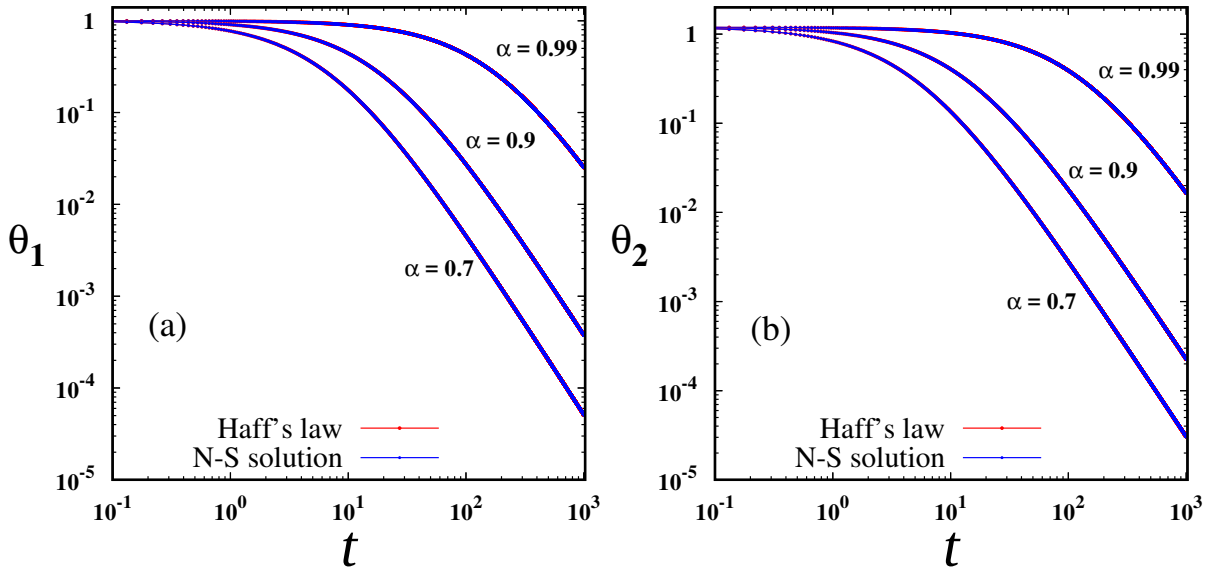


Figure 4.8: (a, b) Comparison of Haff's law (red curve) with the numerical solution of NS equations for $\mathrm{Ma}_1 = 1.2$: (a) upstream temperature $\theta_1$ and (b) downstream temperature $\theta_2$

### 4.3.3 Temperature profiles: Haff's law and scaling relations

For an undriven granular gas with initial temperature $\theta(0)$, the hydrodynamic equations admit a spatially homogeneous solution [$\boldsymbol{\nabla}(\rho, \boldsymbol{u}, \theta) = 0$] with a time-dependent temperature [$\theta(x,t) \equiv \theta(t)$] such that the gas cools according to Haff's law (Haff 1983):

$$\theta(t) = \frac{\theta(0)}{(1 + t/\tau_H)^2}, \quad \text{where} \quad \tau_H = \frac{3}{2nd^2\sqrt{\pi\theta(0)}(1-\alpha^2)(1+3a_2/16)} \tag{4.21}$$

is the relaxation time. The full derivation of Haff's law is shown in Appendix 4A. Equation (4.21) represents the well-known 'homogeneous cooling state' (HCS) of a granular gas. The departure from (4.21) occurs when the system becomes inhomogeneous with cluster formation, called 'inhomogeneous cooling state' (ICS, Luding & Herrmann (1999)). Note that, for homogeneous solutions density and velocities are constant in time and hence for all Haff's law comparison we fix the density to be constant by taking the upstream reference density.

Recall from the panels $(b, e)$ of figures (4.3 - 4.5) that the temperatures at the upstream ($\theta_1 \equiv \theta(x = -L/2)$) and downstream ($\theta_2 \equiv \theta(x = L/2)$) ends decay as time progresses. The temporal evolutions of $\theta_1$ and $\theta_2$ are compared with (4.21) in figures 4.8(a) and 4.8(b), respectively. It is clear that both the upstream and downstream temperatures closely follow Haff's law for all $\alpha$.

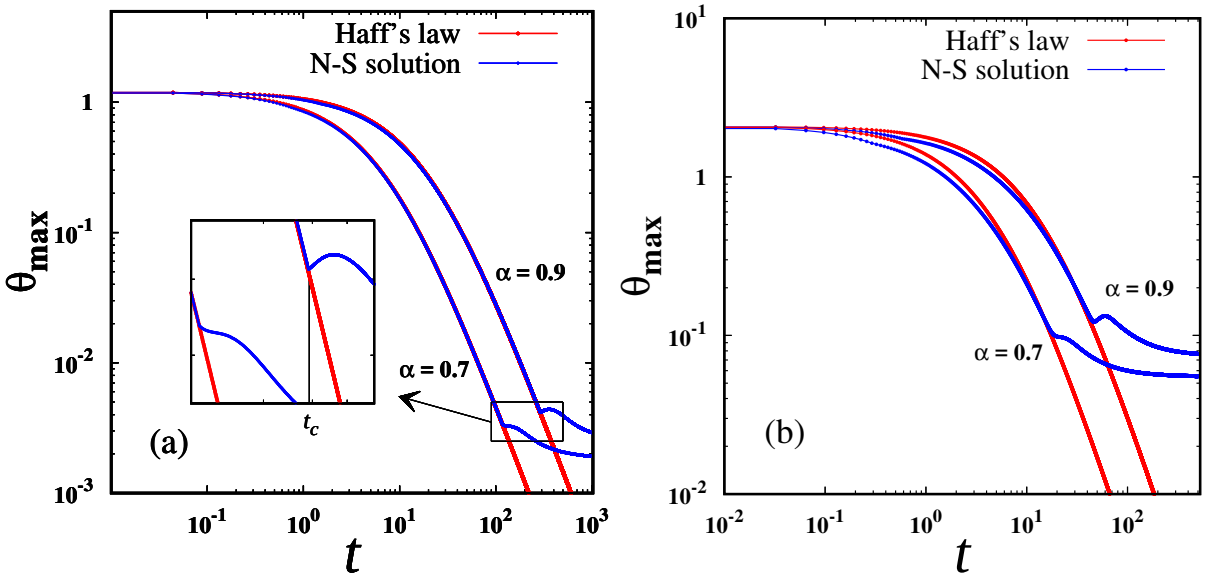


Figure 4.9: (a) Temporal evolution of maximum granular temperature $\theta_{\max}$ for $\mathrm{Ma}_1 = 1.2$; Haff's law is denoted by the red curve and the blue curves represent numerical solutions for $\alpha = 0.9$ and 0.7; inset shows a zoomed part of the same figure. (b) Same as panel $a$ but for $\mathrm{Ma}_1 = 2$.

The time evolution of the maximum granular temperature ($\theta_{\max}$) is shown in figures 4.9($a$) and 4.9($b$) for $\mathrm{Ma}_1 = 1.2$ and 2, respectively, with $\alpha = 0.9$ (upper curve) and 0.7 (lower curve) – the Haff's solution (corresponding to $\theta(0) = \theta_2$ and $\rho(0) = \rho_1$), denoted by the red line, is also superimposed for each $\alpha$. For the case of a weak shock* ($\mathrm{Ma}_1 = 1.2$), $\theta_{\max}$ seems to follow Haff's

*The weak and strong shocks correspond to Mach numbers of $\mathrm{Ma} \sim 1$ and $\mathrm{Ma} >> 1$, respectively. In the present work, we followed Grad's moment theory (Grad 1949) that gives a critical Mach number of $\mathrm{Ma}_{cr} \approx 1.65$ above

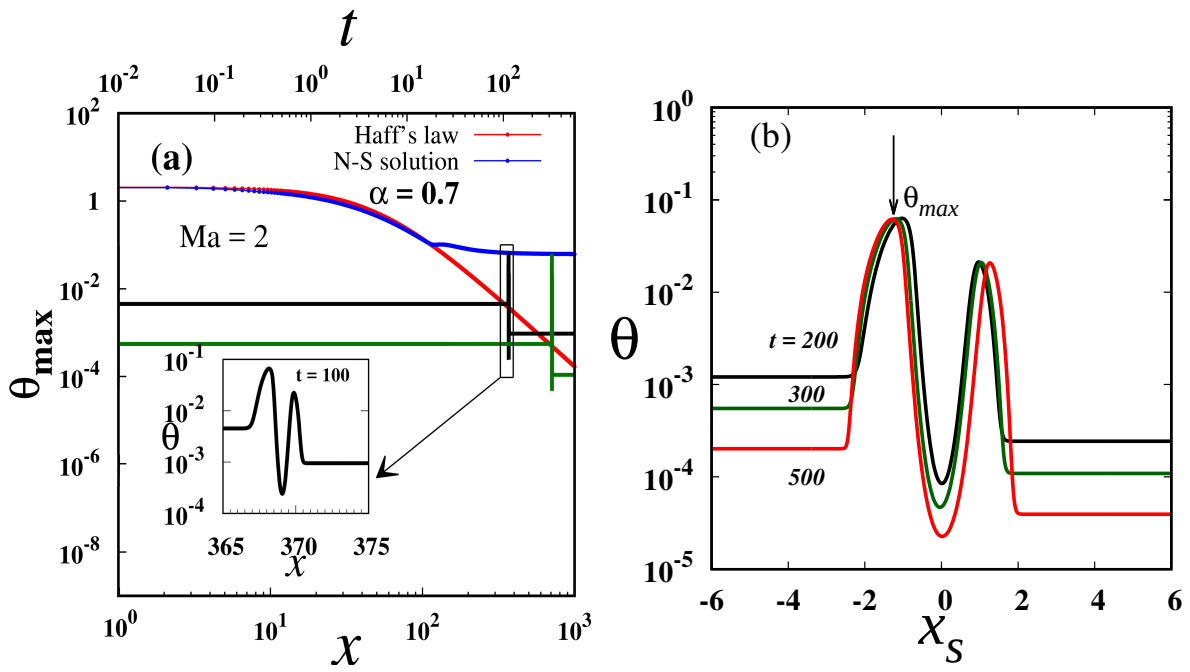


Figure 4.10: (a) Temporal evolution of maximum granular temperature $\theta_{\max}$ and spatial evolution of granular temperature $\theta$ for $\mathrm{Ma}_1 = 2$ and $\alpha = 0.7$; (b) shows the spatial evolution of granular temperature for long times $t \gg t_c$.

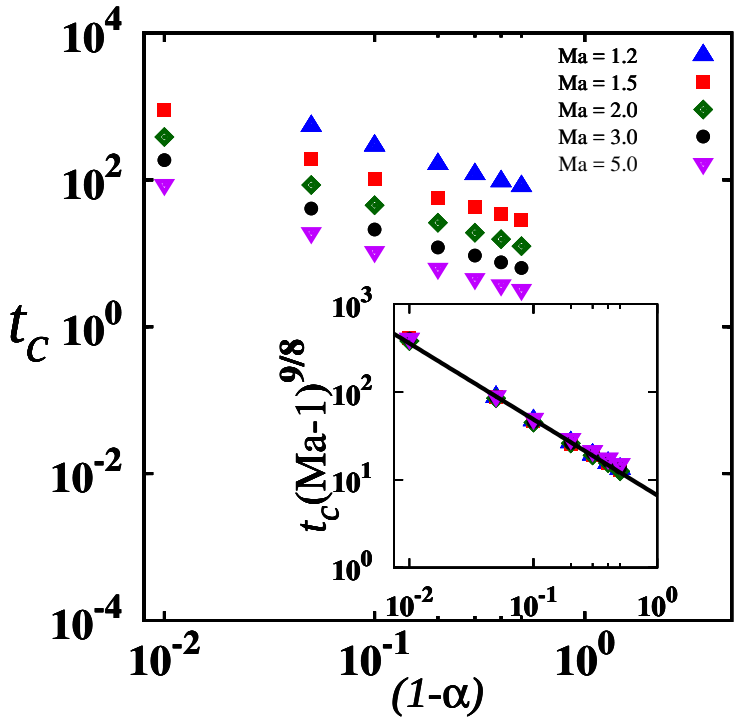


Figure 4.11: Variation of critical time $t_c$ (at which numerical solution $\theta_{\max}$ crosses/overtakes Haff's solution) with $(1-\alpha)$ for different $\mathrm{Ma}_1$; the inset shows scaling (4.22) for data collapse.

law up-to a critical time (marked by the vertical black line in the inset of figure 4.9*a* for $\alpha = 0.9$), but decays much slower thereafter. For a strong shock ($\mathrm{Ma}_1 = 2$), however, $\theta_{\max}$ decays at a faster rate than the Haff's law for $t < t_c$ and at a slower rate for $t > t_c$. The gradients of hydrodynamic fields in the shock-layer (viz. figure 4.4) might be responsible for the faster decay of $\theta_{\max}$ at early times. On the other hand, the departure of $\theta_{\max}$ from Haff's law beyond $t > t_c$, leading to a near-saturation of $\theta_{\max}$ at large times (see the blue curves for $t > 200$ in figures 4.9*b*) is reminiscent of the temperature evolution in the inhomogeneous cooling state (Luding & Herrmann 1999). A similar kind of behaviour (keeping physical relevance aside) "deviation from Haff's law" which is found in Fig. 4.9 has been observed in freely cooling systems (Gonzalez *et al.* 2014; Luding & Goldshtein 2003) at long times. Panels (a) and (b) of Fig. 4.10 show the temporal and spatial evolution of maximum granular temperature for $\mathrm{Ma}_1 = 2$ and $\alpha = 0.7$. The maximum of granular temperature attains a quasi-steady state at long time (for which $t \gg t_c$) which is evident from Figs. 4.10 (a) and (b). Further one can observe from Fig. 4.10 (b) that the minimum granular temperature is not attaining a quasi-steady state even at long times which is responsible for increase of the density maximum with time [See §4.3.4].

The critical time ($t_c$) at which the shock solution $\theta_{\max}$ crosses/overtakes Haff's solution (viz. figures 4.9 *a*,*b*) decreases with increasing inelasticity $(1 - \alpha)$ and upstream Mach number $\mathrm{Ma}_1$ as it is evident from the main panel of figure 4.11. Interestingly, the data for all $\mathrm{Ma}_1$ can be collapsed via the following scaling relation,

$$t_c \sim (\mathrm{Ma}_1 - 1)^{-9/8}(1 - \alpha)^{-17/20}, \tag{4.22}$$

denoted by the black line in the inset of figure 4.11. The exponents in (4.22) have been determined via a least-square fitting of all data, with a standard deviation of less than 2%.

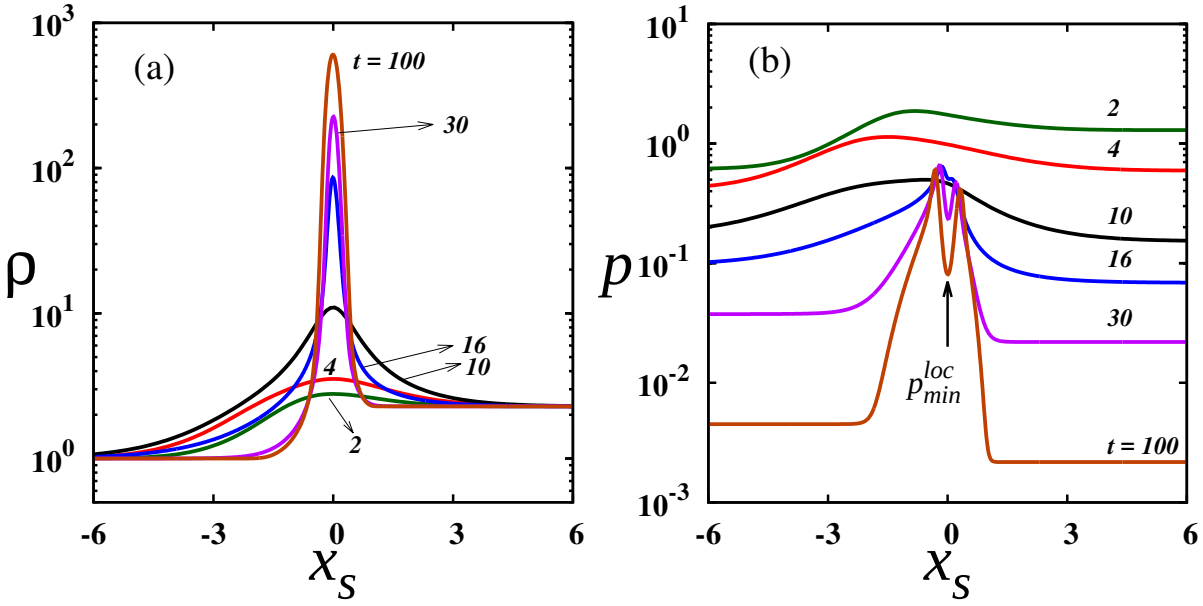


Figure 4.12: Temporal evolutions of (*a*) density (*b*) pressure for $\mathrm{Ma}_1 = 2$ and $\alpha = 0.7$.

which the 13-moment equations do not admit continuous solutions: a shock is considered weak if $\mathrm{Ma} < \mathrm{Ma}_{cr}$ and strong otherwise.

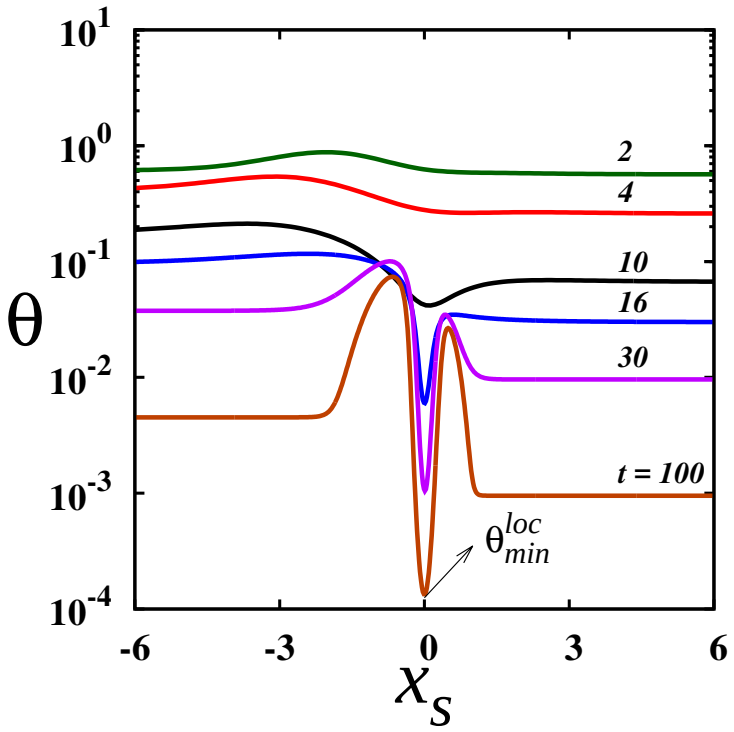


Figure 4.13: Temporal evolutions of granular temperature for $\mathrm{Ma}_1 = 2$ and $\alpha = 0.7$.

### 4.3.4 Large time behaviour: density overshoot and pressure instability

In this subsection, we address the issue of large time behaviour of granular shock profiles. Figures 4.12($a$) and 4.12($b$) display the density and pressure profiles at different times for parameter values of $\mathrm{Ma}_1 = 2$ and $\alpha = 0.7$. In both panels, the abscissa, $x_s = x - x(\rho_{\max})$, has been scaled with respect to the location of the maximum density $\rho_{\max}$. For this parameter set, the location of the density-maximum (panel $a$) is found to coincide with that of a local pressure minimum $p^{loc}_{\min}$ (panel $b$) for $t \geq 16$ (which also coincides with a local minimum of granular temperature $\theta_{\min} \equiv \theta(\rho = \rho_{\max})$, see figure 4.13). These overall findings also hold for other parameter values of $\mathrm{Ma}_1$ and $\alpha$. The higher pressures on both sides of $\rho_{\max}$ create pressure differences that drive the particles to rush-in from both sides, thereby enhancing $\rho_{\max}$ with time (see, the green line in Fig. 4.14). This mechanism is akin to the well-known *pressure instability* which drives cluster formation due to collisional cooling in both (i) undriven [(Goldhirsch & Zanetti 1993)] and (ii) driven [(Alam & Nott 1997, 1998; Gayen & Alam 2006; Alam *et al.* 2008)] granular gases.

Figure 4.14 confirms that $\rho_{\max}$ keeps increasing with time and hence the density profile $\rho(x,t)$ would keep changing as $t \to \infty$. This points toward an apparent deficiency of the inelastic hard-sphere model and some important physics is missing in it: *within the denser/clustered region, the impact velocities are likely lower compared to those in the dilute homogeneous region and hence the collisional dissipation would be lower in the denser regions.* The latter point can be justified by recalling the fact that the restitution coefficient (of real particles) approaches its elastic limit ($\alpha \to 1$) as the impact velocity decreases (Goldhirsch 2003).

### 4.3.5 A simple regularization procedure: energy equation

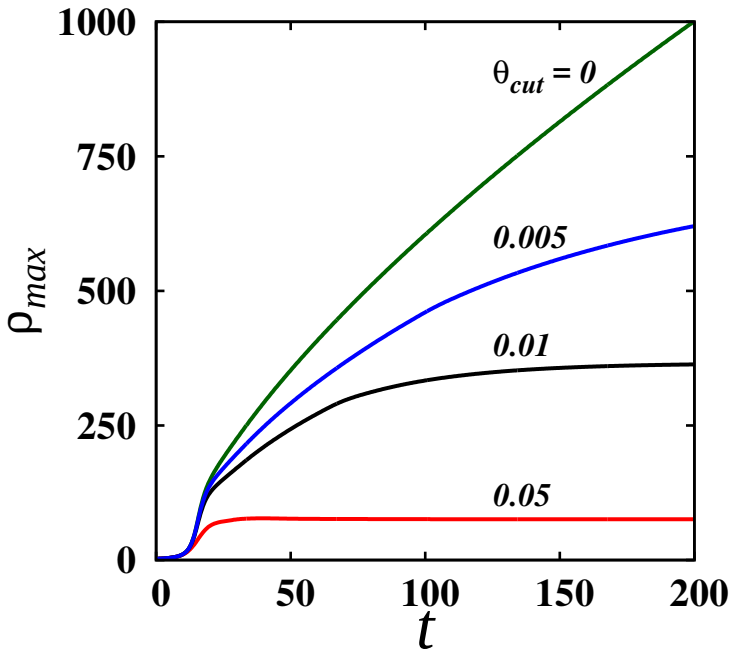


Figure 4.14: Arrest of maximum density $\rho_{\max}$ via a regularization procedure.

Here we propose a simple regularization procedure to arrest the maximum density. As stated in the previous subsection, the collisional dissipation is much lower in the denser/clustered region as the impact velocities in a granular gas are much slower in the denser/clustered region. It means that when the granular system approaches clustered region, the restitution coefficient can be taken to approach to its elastic limit. This can be incorporated in the present model by rewriting the collisional dissipation rate in the granular energy equation as

$$\mathcal{D}_{reg} = \mathcal{F}(\xi)\mathcal{D} \equiv (1+\xi^2)\exp(-\xi^2)\mathcal{D} \tag{4.23}$$

where the "regularization" factor $\mathcal{F}(\xi)$ has been exactly evaluated by Luding & Goldshtein (2003) to which the readers are referred for related details on the collision model with a "cut-off" restitution coefficient. In (4.23),

$$\xi^2(x,t) = \frac{v_{cut}^2}{v^2} \equiv \frac{\theta_{cut}}{\theta(x,t)} \tag{4.24}$$

is identified with the ratio between a critical/cut-off impact energy $\theta_{cut}$ and the local fluctuation energy (granular temperature). It is clear that $\mathcal{D}_{reg} = \mathcal{D}$ for $\xi^2 = 0 = \theta_{cut}$, recovering the original constitutive model of §4.2, and $\mathcal{D}_{reg} < \mathcal{D}$ for $\xi^2 > 0$. Lastly, we set $\mathcal{D}_{reg} = 0$ whenever $\mathcal{F}(\xi(x,t)) < \mathcal{F}_{cr} << 1$; as an illustration we have used $\mathcal{F}_{cr} = 0.05$ which translates into a critical value of $\xi_{cr}^2 \approx 4.75$ (and hence $\theta_{\min} \approx 0.21\theta_{cut}$) below which the particle collisions are treated as elastic.

With the dissipation rate being given by (4.23) and assuming that other transport coefficients ($\mu$, $p$, $\kappa$ and $\kappa_h$) remain unaffected, we have solved (4.8-4.10) for the same shock-wave problem

by specifying different values of $\theta_{cut}$. As a proof-of-concept, the results are shown in figure 4.14 which confirms that the continual increase of $\rho_{\max}$ can indeed be arrested, see the black and red lines for $\theta_{cut} = 0.01$ and 0.05, respectively. The smaller the value of $\theta_{cut}$, the larger the time to reach the arrested state of $\rho_{\max}$. For a "dense" granular gas, the arrested maximum density can be tied with the random-packing limit, suggesting a "gas-solid" transition as in the work of Kamenetsky *et al.* (2000) for piston-driven granular shock-waves. The same transition can also be addressed within the present regularized model (4.23) by employing the transport coefficients for a dense granular gas. A detailed investigation of these issues is relegated to a future work.

## 4.4 Conclusions

The Riemann problem of granular shock waves was analysed by numerically solving the granular hydrodynamic equations, namely, Euler and Navier-Stokes equations. The density and temperature profiles were found to be asymmetric, with the maxima of both density and temperature occurring within the shock layer which constitute two distinguishing features of the "granular" Riemann problem (compared to that for ideal gases). The fundamental difference of the granular shock problem from its ideal-gas counterpart can be tied to 'inelastic dissipation' since this makes the upstream and downstream states of a granular shock to live in non-equilibrium 'decaying' states (similar to HCS), which, in turn, is responsible for the non-trivial shock structures uncovered here. Inside the shock too, the Haff's law was found to hold for the maximum temperature, but for weak shocks ($\mathrm{Ma}_1 \sim 1$) only, and deviations occurred for strong shocks. A scaling relation (4.22) was uncovered that expresses the critical time (at which the maximum temperature deviates from Haff's law) as a function of Mach number and inelasticity. The origin of asymmetric density profiles, leading to the continual build-up of density inside the shock, seems to be tied to a pressure instability in granular gases. A simple regularization procedure to arrest the maximum density has been proposed.

## Appendix 4A. Dimensionless Form of Haff's Law

Here we derive the well known Haff's law from Navier-Stokes model discussed in the chapter: 4. We are looking for the spatially homogeneous solution of Navier-Stokes model which means that all the field variables are depend only on time ($t$). Hence in one dimension the spatially homogeneous solutions of Navier-Stokes model given in Eqs. (4.8) - (4.10) reduces to the following system for the basic field variables, namely density ($\rho$), velocity ($u$), and scalar temperature ($\theta$):

$$\begin{aligned}
\frac{\mathrm{d}\rho}{\mathrm{d}t} &= 0, \\
\frac{\mathrm{d}u}{\mathrm{d}t} &= 0, \\
\frac{\mathrm{d}\theta}{\mathrm{d}t} &= -\frac{8\sqrt{2}}{3\sqrt{\pi}}\frac{(1-\alpha)}{(3-\alpha)}\left(1+\frac{3}{16}a_2\right)\rho\,\theta^{\frac{3}{2}}.
\end{aligned} \tag{4.25}$$

All the above equations are non-dimensionalized using the reference scales discussed in 4.2.3. The mass density and the velocity remain constant in time which is evident from the first two equations of (4.25). On integrating the last equation of (4.25) and using initial condition, we arrive at the well known Haff's law:

$$\theta(t) = \frac{\theta(t=0)}{\left(1+\frac{4\sqrt{2}}{3\sqrt{\pi}}\frac{(1-\alpha)}{(3-\alpha)}\left(1+\frac{3}{16}a_2\right)\sqrt{\theta(t=0)}\,\rho(t=0)\,t\right)^2}. \tag{4.26}$$

The Haff's law (4.26) derived from Navier-Stokes model is slightly different from the classical Haff's law which can be derived from the Euler level hydrodynamics as

$$\theta(t) = \frac{\theta(t=0)}{\left(1+\frac{4\sqrt{2}}{3\sqrt{\pi}}\frac{(1-\alpha)}{(3-\alpha)}\sqrt{\theta(t=0)}\,\rho(t=0)\,t\right)^2}. \tag{4.27}$$

## Appendix 4B. Initial Ratio of Downstream and Upstream Field Variables

Unlike in molecular gas we have to specify the Rankine-Hugoniot conditions (boundary conditions) for granular gas at time $t = 0$. The ratio of downstream to upstream density, velocity and granular temperature are given as:

$$\begin{aligned}
\frac{\rho_2(t=0)}{\rho_1(t=0)} &= \frac{(\gamma+1)\mathrm{Ma}_1^2}{2+(\gamma-1)\mathrm{Ma}_1^2}, \\
\frac{u_2(t=0)}{u_1(t=0)} &= \frac{2+(\gamma-1)\mathrm{Ma}_1^2}{(\gamma+1)\mathrm{Ma}_1^2}, \\
\frac{\theta_2(t=0)}{\theta_1(t=0)} &= \frac{(2\gamma\mathrm{Ma}_1^2-(\gamma-1))((\gamma-1)\mathrm{Ma}_1^2+2)}{(\gamma+1)^2\mathrm{Ma}_1^2},
\end{aligned} \tag{4.28}$$

where $\mathrm{Ma}_1 = u_1(0)/\sqrt{\gamma\,\theta_1(0)}$ is the upstream Mach number at $t = 0$ and $\gamma$ is the ratio of specific heats which is $5/3$ for the dilute granular case.

# Chapter 5

# Analysis of Extended Hydrodynamic Equations: Characteristics, Critical Mach Number and Discontinuous Shock Solution[†]

## 5.1 Introduction

In this chapter, all moment models, namely, the ten moment, thirteen moment and fourteen moment models which were discussed in §2.4 and §2.5 are reduced to one-dimension and all of them are written in conservation form. We discuss about the characteristics of all these moment models and analyze the conditions for their hyperbolicity. An analysis of the characteristics of the 14-moment model indicates that the extended hydrodynamic models remain hyperbolic even in the presence of stress and heat flux. Unlike the Navier-Stokes equations, the extended hydrodynamic models admit continuous shock solutions up-to a critical Mach number whose value increases with increasing the number of moments (i.e. hydrodynamic fields) retained. The related analysis for the critical Mach number of moment models and the derivation of Haff's law from the 14-moment model are presented.

## 5.2 Equations for Plane Shock Waves

For plane shock waves, the flow velocity in the $x$-direction is $u(x,t)$ and zero in the other two orthogonal directions and the heat flux in the $x$-direction is taken to be $q(x,t)$ and zero in remaining orthogonal directions. As discussed in §3.2, we work with the mean scalar temperature $\theta$ and the skew temperature $\theta_s$.

$$\theta = \frac{1}{3}(\theta_{xx} + 2\,\theta_{yy}) \quad \text{and} \quad \theta_s = \frac{1}{3}(\theta_{xx} - \theta_{yy}). \tag{5.1}$$

The the longitudinal stress is given by

$$\sigma = -\frac{4}{3}\,\mu\,\frac{\partial u}{\partial x} = 2\,\rho\,\theta_s. \tag{5.2}$$

[†]Part of this chapter (§5.2 - §5.4) has been done in collaboration with Dr. Santosh Ansumali.

### 5.2.1 10-moment model

For one-dimensional planar shock wave problem, the 10-moment model is reduced to a system of four coupled PDEs for four physical variables namely, the density ($\rho(x,t)$), the velocity ($u(x,t)$), the scalar temperature ($\theta(x,t)$) and the longitudinal stress ($\sigma(x,t)$), as given by:

$$\frac{\partial \rho}{\partial t} + \frac{\partial}{\partial x}(\rho u) = 0, \tag{5.3}$$

$$\frac{\partial}{\partial t}(\rho u) + \frac{\partial}{\partial x}\left(\rho u^2 + \rho\theta + \sigma\right) = 0, \tag{5.4}$$

$$\frac{\partial}{\partial t}\left(\rho u^2 + 3\rho\theta\right) + \frac{\partial}{\partial x}\left(\rho u^3 + 5\rho\theta u + 2\sigma u\right) = -3\,\mathcal{D}, \tag{5.5}$$

$$\frac{\partial}{\partial t}\left(\frac{2}{3}\rho u^2 + \sigma\right) + \frac{\partial}{\partial x}\left(\frac{2}{3}\rho u^3 + \frac{4}{3}\rho\theta u + \frac{7}{3}\sigma u\right) = \sigma^s. \tag{5.6}$$

The expressions for the energy dissipation rate $\mathcal{D}$ and the source term $\sigma^s$ are

$$\begin{aligned} \mathcal{D} &= \frac{4}{3}\frac{d^2}{m}\sqrt{\pi}\,(1-\alpha^2)\,\rho^2\,\theta^{\frac{3}{2}}, \\ \sigma^s &= -\frac{4}{5}\frac{d^2}{m}\sqrt{\pi\,\theta}\,(1+\alpha)\,(3-\alpha)\,\rho\,\sigma. \end{aligned} \tag{5.7}$$

### 5.2.2 13-moment model

The reduced 13-moment system for the plane shock wave problem, contains an additional field variable namely, the heat flux $q(x,t)$, in addition to the variables of the 10-moment system. Hence the 13-moment extended hydrodynamic equations are given by:

$$\frac{\partial \rho}{\partial t} + \frac{\partial}{\partial x}(\rho u) = 0, \tag{5.8}$$

$$\frac{\partial}{\partial t}(\rho u) + \frac{\partial}{\partial x}\left(\rho u^2 + \rho\theta + \sigma\right) = 0, \tag{5.9}$$

$$\frac{\partial}{\partial t}\left(\rho u^2 + 3\rho\theta\right) + \frac{\partial}{\partial x}\left(\rho u^3 + 5\rho\theta u + 2\sigma u + 2q\right) = -3\,\mathcal{D}, \tag{5.10}$$

$$\frac{\partial}{\partial t}\left(\frac{2}{3}\rho u^2 + \sigma\right) + \frac{\partial}{\partial x}\left(\frac{2}{3}\rho u^3 + \frac{4}{3}\rho\theta u + \frac{7}{3}\sigma u + \frac{8}{15}q\right) = \sigma^s, \tag{5.11}$$

$$\begin{aligned} &\frac{\partial}{\partial t}\left(\frac{1}{2}\rho u^3 + \frac{5}{2}\rho\theta u + \sigma u + q\right) + \frac{\partial}{\partial x}\left(\frac{1}{2}\rho u^4 + 4\rho\theta u^2 + \frac{5}{2}\sigma u^2\right. \\ &\left. + \frac{16}{5}qu + \frac{7}{2}\sigma\theta + \frac{5}{2}\rho\theta^2\right) = q^s + \sigma^s u - \frac{5}{2}\mathcal{D}u. \end{aligned} \tag{5.12}$$

The source term $q^s$ is given by

$$q^s = -\frac{1}{15}\frac{d^2}{m}\sqrt{\pi\,\theta}\,(1+\alpha)\,(49\,-33\,\alpha)\,\rho\,q, \tag{5.13}$$

and the expressions for the energy dissipation rate $\mathcal{D}$ and the source term $\sigma^s$ are given by (5.7).

### 5.2.3 14-moment model

The 14-moment model is reduced to a system of six equations for the plane shock wave problem. The one-dimensional field equations for 14-moment system, which involves six field variables namely, the density $(\rho(x,t))$, the velocity $(u(x,t))$, the scalar temperature $(\theta(x,t))$, the longitudinal stress $(\sigma(x,t))$, the heat flux $q(x,t)$, and the dimensionless non-equilibrium part of the full contracted fourth-order moment $\Delta$ defined as

$$\Delta = \frac{1}{15\,\rho\,\theta^2}(R - R^{eq}). \tag{5.14}$$

The one-dimensional equations for the 14-moment extended hydrodynamic model are

$$\frac{\partial \rho}{\partial t} + \frac{\partial}{\partial x}(\rho u) = 0, \tag{5.15}$$

$$\frac{\partial}{\partial t}(\rho u) + \frac{\partial}{\partial x}\left(\rho u^2 + \rho\theta + \sigma\right) = 0, \tag{5.16}$$

$$\frac{\partial}{\partial t}\left(\rho u^2 + 3\rho\theta\right) + \frac{\partial}{\partial x}\left(\rho u^3 + 5\rho\theta u + 2\sigma u + 2q\right) = -3\,\mathcal{D}, \tag{5.17}$$

$$\frac{\partial}{\partial t}\left(\frac{2}{3}\rho u^2 + \sigma\right) + \frac{\partial}{\partial x}\left(\frac{2}{3}\rho u^3 + \frac{4}{3}\rho\theta u + \frac{7}{3}\sigma u + \frac{8}{15}q\right) = \sigma^s, \tag{5.18}$$

$$\frac{\partial}{\partial t}\Big(\frac{1}{2}\rho u^3 + \frac{5}{2}\rho\theta u + \sigma u + q\Big) + \frac{\partial}{\partial x}\left(\frac{1}{2}\rho u^4 + 4\rho\theta u^2 + \frac{5}{2}\sigma u^2 + \frac{16}{5}qu + \frac{7}{2}\sigma\theta + \frac{5}{2}\rho\theta^2(1+\Delta)\right) = q^s + \sigma^s u - \frac{5}{2}\mathcal{D}u, \tag{5.19}$$

$$\frac{\partial}{\partial t}\Big(\rho u^4 + 10\rho\theta u^2 + 4\sigma u^2 + 8qu + 15\rho\theta^2(1+\Delta)\Big) + \frac{\partial}{\partial x}\left(\rho u^5 + 14\rho\theta u^3 + 8\sigma u^3 + \frac{84}{5}qu^2 + 35\rho\theta^2(1+\Delta)u + 28\sigma\theta u + 28\theta q\right) = R^s + 8q^s u + 4\sigma^s u^2 - 10\mathcal{D}u^2. \tag{5.20}$$

The expressions for the energy dissipation $\mathcal{D}$ and the source terms $\sigma^s$, $q^s$, $R^S$ given as:

$$\mathcal{D} = \frac{4}{3}\frac{d^2}{m}\sqrt{\pi}\,(1-\alpha^2)\left[1 + \frac{3\,\Delta}{16}\right]\rho^2\,\theta^{\frac{3}{2}}, \tag{5.21}$$

$$\sigma^s = -\frac{4}{5}\frac{d^2}{m}\sqrt{\pi\,\theta}\,(1+\alpha)\,(3-\alpha)\left[1 - \frac{\Delta}{32}\right]\rho\,\sigma, \tag{5.22}$$

$$q^s = -\frac{1}{15}\frac{d^2}{m}\sqrt{\pi\,\theta}\,(1+\alpha)\left[49 - 33\,\alpha + (19 - 3\,\alpha)\,\frac{\Delta}{32}\right]\rho\,q, \tag{5.23}$$

$$R^s = -4\,\frac{d^2}{m}\,\sqrt{\pi\,\theta}\,(1+\alpha)\left[(2\,\alpha^2 + 9)\,(1 - \alpha) + (30\,\alpha^2\,(1 - \alpha) + 271 - 207\,\alpha)\,\frac{\Delta}{16}\right]\rho^2\,\theta^2. \tag{5.24}$$

## 5.3 Characteristics of Extended Hydrodynamic Equations

Let us first determine the characteristics of the 14-moment model for a stationary shock; our analysis follows the original work of Grad (1949). The one-dimensional 14-moment system [Eqs. (5.15) - (5.20)] can be simplified by choosing a coordinate system in which $u = 0$ at the observation point and is written in terms of primitive variables $(\rho, u, p, \sigma, q, R)$ as

$$\frac{\partial \rho}{\partial t} + \rho \frac{\partial u}{\partial x} = 0, \tag{5.25}$$

$$\frac{\partial u}{\partial t} + \frac{1}{\rho}\frac{\partial p}{\partial x} + \frac{1}{\rho}\frac{\partial \sigma}{\partial x} = 0, \tag{5.26}$$

$$\frac{\partial p}{\partial t} + \left(\frac{5}{3}p + \frac{2}{3}\sigma\right)\frac{\partial u}{\partial x} + \frac{2}{3}\frac{\partial q}{\partial x} = -\mathcal{D}, \tag{5.27}$$

$$\frac{\partial \sigma}{\partial t} + \left(\frac{4}{3}p + \frac{7}{3}\sigma\right)\frac{\partial u}{\partial x} + \frac{8}{15}\frac{\partial q}{\partial x} = \sigma^s, \tag{5.28}$$

$$\frac{\partial q}{\partial t} + \frac{16}{5}q\frac{\partial u}{\partial x} + \frac{1}{6}\frac{\partial R}{\partial x} - \frac{5}{2}\left(\frac{p}{\rho} - \frac{\sigma}{\rho}\right)\frac{\partial p}{\partial x} + \left(\frac{p}{\rho} - \frac{\sigma}{\rho}\right)\frac{\partial \sigma}{\partial x} - \frac{7}{2}\frac{\sigma p}{\rho^2}\frac{\partial \rho}{\partial x} = q^s \tag{5.29}$$

$$\frac{\partial R}{\partial t} + \frac{7}{3}R\frac{\partial u}{\partial x} + 28\frac{p}{\rho}\frac{\partial q}{\partial x} + 20\frac{q}{\rho}\frac{\partial p}{\partial x} - 8\frac{q}{\rho}\frac{\partial \sigma}{\partial x} + 28\frac{p\sigma}{\rho}\frac{\partial u}{\partial x} - 28\frac{q\,p}{\rho^2}\frac{\partial \rho}{\partial x} = R^s, \tag{5.30}$$

where the source terms are given by Eqs. (5.21) - (5.24). The evolution equation of a characteristic curve $\varphi(x,t) = 0$ is obtained by solving the equation $|\mathbf{B}| = 0$, where $\mathbf{B}$ is a $6 \times 6$ matrix given by:

$$\mathbf{B} = \begin{pmatrix} \varphi_t & \rho\varphi_x & 0 & 0 & 0 & 0 \\ 0 & \varphi_t & \frac{1}{\rho}\varphi_x & \frac{1}{\rho}\varphi_x & 0 & 0 \\ 0 & (\frac{5}{3}p + \frac{2}{3}\sigma)\varphi_x & \varphi_t & 0 & \frac{2}{3}\varphi_x & 0 \\ 0 & (\frac{4}{3}p + \frac{7}{3}\sigma)\varphi_x & 0 & \varphi_t & \frac{8}{15}\varphi_x & 0 \\ -\frac{7}{2}\frac{p\sigma}{\rho^2}\varphi_x & \frac{16}{5}q\varphi_x & -\frac{5}{2}(\frac{p}{\rho} - \frac{\sigma}{\rho})\,\varphi_x & (\frac{p}{\rho} - \frac{\sigma}{\rho})\varphi_x & \varphi_t & \frac{1}{6}\varphi_x \\ -28\frac{p\,q}{\rho^2}\varphi_x & (\frac{7}{3}R + 28\frac{p\sigma}{\rho})\varphi_x & 20\frac{q}{\rho}\varphi_x & -8\frac{q}{\rho}\varphi_x & 28\frac{p}{\rho}\varphi_x & \varphi_t \end{pmatrix}. \tag{5.31}$$

The characteristic equation in present case is

$$\varphi_t\Big\{225\,\rho^2\,\varphi_t^5 - 1260\,q\,(p+\sigma)\,\varphi_x^5 + \Big(3150\,p^2 - 105\,\rho\,R + 1890\,p\,\sigma + 945\,\sigma^2\Big)\varphi_x^4\varphi_t + 1204\,\rho\,q\,\varphi_x^3\varphi_t^2 - 1470\,\rho\,p\,\varphi_x^2\varphi_t^3 - 930\,\rho\,\sigma\,\varphi_x^2\varphi_t^3\Big\} = 0. \tag{5.32}$$

Introducing the slope of the characteristic direction as

$$s = \frac{\mathrm{d}x}{\mathrm{d}t} = -\frac{\varphi_t}{\varphi_x}, \tag{5.33}$$

the characteristic equation (5.32) can be rewritten in terms of $s$ which can be further decomposed as $s = 0$ and a fifth-order polynomial in $s$:

$$225\,\rho^2\,s^5 - 1470\,\rho\,p\,s^3 - 930\,\rho\,\sigma\,s^3 - 1204\,\rho\,q\,s^2 + 1260\,q\,(p+\sigma) + \Big(3150\,p^2 - 105\,\rho\,R + 1890\,p\,\sigma + 945\,\sigma^2\Big)s = 0. \tag{5.34}$$

If we assume that the heat flux and stresses are negligible and using the equilibrium value for $R = 15\frac{p^2}{\rho}$, Eq. (5.34) reduces to

$$s\left(s^4 - \frac{1470}{225}\frac{p}{\rho} + \frac{1575}{225}\frac{p^2}{\rho^2}\right) = 0, \tag{5.35}$$

which has five roots

$$s = 0,\ s^2 = c_1\,\theta \text{ and } s^2 = c_2\,\theta \tag{5.36}$$

where $c_1 = \frac{49+\sqrt{826}}{15} \sim 5.18$ and $c_2 = \frac{49-\sqrt{826}}{15} \sim 1.35$. Hence the characteristic speeds for the 14-moment model are

$$s = 0, \quad 0, \quad \pm\sqrt{5.18\,\theta}, \quad \pm\sqrt{1.35\,\theta}, \tag{5.37}$$

which are real and hence the 14-moment model is hyperbolic.

In a similar manner we obtain the characteristic speeds of 13-moment and 10-moment models:

$$s = 0, \quad \pm\sqrt{4.54\,\theta}, \quad \pm\sqrt{0.661\,\theta}, \tag{5.38}$$

$$s = 0, \quad 0, \quad \pm\sqrt{3\,\theta}, \tag{5.39}$$

respectively. Therefore, all three extended hydrodynamics models (10-, 13- and 14-moment models) yield hyperbolic systems. Note that the slope $s$ must be replaced by $u + s$ for an arbitrary coordinate system in which $u$ is non zero. The solution $s = 0$ represents characteristics along the particle path and the solutions $s \neq 0$ represent characteristic directions given by $u \pm s$ with sound speeds $s$. The non-zero characteristic speed in (5.37 - 5.39) should be compared with the adiabatic sound speed

$$c = \sqrt{\gamma\,\theta} = \sqrt{5\,\theta/3} \quad \text{for a monatomic gas,} \tag{5.40}$$

which is the characteristic slope derived from Euler equations [(Courant & Friedrichs 1948)]. For all three extended hydrodynamic models that we are using, note that there are two sound speeds, one is larger and the other is smaller than the adiabatic sound speed (5.40). The above analysis also clarifies that the largest characteristic speed in extended hydrodynamics increases with increasing the number of moments [(Weiss 1995; Müller & Ruggeri 1993*b*)]: $s_{\max} = \sqrt{3\theta}$, $\sqrt{4.54\theta}$ and $\sqrt{5.18\theta}$ for 10, 13 and 14-moment models, respectively.

The inclusion of the heat flux and stresses to the characteristic equation is to slightly modify the numerical results on characteristic speeds as we show below.

### 5.3.1 Characteristics with inclusion of heat flux and stresses:

In the presence of small but finite values of the heat flux and stresses,we can solve Eq. (5.34) via a perturbation expansion. By inserting the equilibrium value of $R$ into Eq. (5.34) we get

$$225\rho^2 s^5 - (1470\,\rho\,p\ -\ 930\,\rho\,\sigma)s^3\ -\ 1204\,\rho\,q\,s^2\ +\ \Big(1575\,p^2\ +\ 1890\,p\,\sigma\ +\ 945\,\sigma^2\Big)s \\ +\ 1260\,q\,(p+\sigma)\ = 0. \tag{5.41}$$

We look for a solution of the form

$$s = s_0 + \delta s_1 + O(\delta^2), \tag{5.42}$$

with $\sigma = \epsilon_1$ and $q = \epsilon_2$, where $\delta$, $\epsilon_1$, and $\epsilon_2$ are small positive quantities which are assumed to be of the same order. Inserting the series-expansion for $s$ into Eq. (5.41) and equating the coefficients of $\delta^0$ and $\delta$ to zero, we obtain the leading- and first-order perturbation equations,

$$1575\,p^2\,s_0 - 1470\rho\,p\,s_0^3 + 225\,\rho^2\,s_0^5 = 0, \tag{5.43}$$

$$1890\,p\,s_0\,\epsilon_1 + 1260\,p\,\epsilon_2 + 1575\,p^2\,s_1 + 930\,\rho\,s_0^3\,\epsilon_1 - 1204\,\rho\,s_0^2\,\epsilon_2 - 4410\,\rho\,p\,s_0^2\,s_1 + 1125\,\rho^2\,s_0^4\,s_1 = 0, \tag{5.44}$$

respectively. The solutions of the leading-order perturbation equation are the same as (5.37):

$$s_0 = 0, \pm\sqrt{c_1\,\frac{p}{\rho}}, \pm\sqrt{c_2\,\frac{p}{\rho}}. \tag{5.45}$$

The first order perturbation equation (5.44) is solved in terms of $s_0$ to yield:

$$s_1 = -\frac{2\left(315\,p\,(3\,s_0\,\epsilon_1 + 2\,\epsilon_2) + \rho\,s_0^2\,(465\,s_0\,\epsilon_1 - 602\,\epsilon_2)\right)}{45\left(35\,p^2 - 98\,\rho\,p\,s_0^2 + 25\,\rho^2\,s_0^4\right)}. \tag{5.46}$$

Inserting (5.45) into (5.46), we obtain corrections to five roots of (5.41):

$$s_1 = -\frac{4\,\epsilon_2}{5\,p},\ \frac{14\,c_3\,\epsilon_2 \mp 15\,c_5\,\epsilon_1\sqrt{c_1\,p/\rho}}{210\,c_7\,p},\ \frac{14\,c_4\,\epsilon_2 \pm 15\,c_6\,\epsilon_1\sqrt{c_2\,p/\rho}}{210\,c_8\,p} \tag{5.47}$$

where

$$\begin{aligned} &c_3 = 43\sqrt{826} + 1432, \quad c_4 = 43\sqrt{826} - 1432, \quad c_5 = 2464 + 31\sqrt{826}, \\ &c_6 = 2464 - 31\sqrt{826}, \quad c_7 = 7\sqrt{826} + 118 \quad \text{and} \quad c_8 = 7\sqrt{826} - 118. \end{aligned} \tag{5.48}$$

The composite solutions of Eq. (5.41) are: $s = s_0 + \delta\,s_1$. It is easy to verify that the roots are real, implying that the system remains hyperbolic in the presence of finite stresses and heat flux. Hence the extended hydrodynamic equations form a hyperbolic system.

## 5.4 Critical Mach Number Analysis and the Weak Solution

It is well-known [(Grad 1949; Weiss 1995)] for a molecular gas that the extended hydrodynamic equations (10- and higher-order moment models) yield smooth/continuous solutions for the steady shock wave problem if the (upstream) Mach number is smaller than some critical value. Here we carry out the same analysis for a granular gas described by the 10-moment, 13-moment, and 14-moment models, and show that the system of ODEs for stationary plane shock waves breaks down at some critical Mach number, leading to discontinuous shock solutions, the so-called "weak" solution of hyperbolic equations.

To illustrate the above, we focus on the 10-moment system for a planar shock moving at a constant speed. The shock is stationary in a reference frame which is moving with the shock speed and hence the time derivatives vanish. For a planar stationary shock, the 10-moment

equations for a dilute granular gas boils down to:

$$\begin{aligned}
&\frac{\mathrm{d}}{\mathrm{d}x}\Big(\rho u\Big) = 0,\\
&\frac{\mathrm{d}}{\mathrm{d}x}\Big(\rho u^2 + \rho\theta + \sigma\Big) = 0,\\
&\frac{\mathrm{d}}{\mathrm{d}x}\Big(\rho u^3 + 5\rho\theta u + 2\sigma u\Big) = -3\,\mathcal{D},\\
&\frac{\mathrm{d}}{\mathrm{d}x}\Big(\frac{2}{3}\rho u^3 + \frac{4}{3}\rho\theta u + \frac{7}{3}\sigma u\Big) = \sigma^s,
\end{aligned} \tag{5.49}$$

where the expressions for the energy dissipation rate $\mathcal{D}$ and the source term $\sigma^s$ are given in (5.7). The boundary conditions for the above system of ODEs are supplied by the RH relations and $\theta_{s1} = 0 = \theta_{s2}$. Solving the first two equations of (5.49) and using the boundary conditions, we get:

$$\begin{aligned}
C_1 &= \rho u \;= \rho_1 u_1,\\
C_2 &= \rho u^2 + \rho\theta + \sigma \;=\; (\gamma \mathrm{Ma}_1^2 + 1)\rho_1\theta_1.
\end{aligned} \tag{5.50}$$

Recall that $\sigma = 0$ at both upstream and downstream ends. With the help of following two algebraic equations

$$u = \frac{C_1}{\rho}, \qquad \sigma = C_2 - \frac{C_1^2}{\rho} - \rho\,\theta, \tag{5.51}$$

which are arising from (5.50), the system of ODEs (5.49) can be combined to give a coupled ODEs for $\rho(x)$ and $\theta(x)$ as,

$$\frac{\mathrm{d}\rho}{\mathrm{d}x} = \frac{\rho^3}{3(\gamma \mathrm{Ma}_1^2 + 1)C_1\,\rho_1\,\theta_1}\left[\frac{\mathcal{D} - \sigma^s}{\rho - \rho_c}\right], \tag{5.52}$$

$$\frac{\mathrm{d}\theta}{\mathrm{d}x} = \frac{(-2\,\mathcal{D} - \sigma^s)}{3\,C_1} + \left(\frac{2\,C_1^2 - \rho\,C_2}{3\,\rho^3}\right)\frac{\mathrm{d}\rho}{\mathrm{d}x}, \tag{5.53}$$

where

$$\rho_c = \frac{4\gamma \mathrm{Ma}_1^2}{3(\gamma \mathrm{Ma}_1^2 + 1)}\rho_1 \tag{5.54}$$

is the critical density at which the density gradient (5.52) blows up. Equation (5.52) has a smooth solution which connects two end states $\rho_1$ and $\rho_2$ if the upstream density is smaller than the critical density (i.e. $\rho_1 < \rho_c$). The condition for this critical state can be obtained from $\rho_c = \rho_1$:

$$\mathrm{Ma}_1 = \sqrt{\frac{3}{\gamma}} = \frac{3}{\sqrt{5}}. \tag{5.55}$$

Hence the 10-moment system admits a continuous/smooth solution up-to a Mach number of $\mathrm{Ma}_1 = 3/\sqrt{5} \approx 1.34$. In other words, if the shock speed is smaller than the acoustic wave speed in the system, a smooth solution exists for the system [(Levermore & Morokoff 1998)].

This overall conclusion holds for 13- and 14-moment models too, but the critical Mach numbers of different moment models are different as given in Table 5.1. It is noteworthy that the value of the critical Mach number as well as the critical density (5.54) do not depend on the restitution coefficient ($\alpha$); this is due to the fact that the source terms (which are functions of

$\alpha$) do not influence the critical density, see Eq. 5.52. Table 5.1 confirms that the critical Mach number increases with increasing the number of moments retained in extended hydrodynamics [(Weiss 1995)]. This implies that the range of Mach number over which the continuous shock solution exists becomes larger with increasing the number of moments.

Table 5.1: Critical Mach number

| Moment model | 10-moment | 13-moment | 14-moment |
|---|---|---|---|
| $\mathrm{Ma}_{cr}$ | $\frac{3}{\sqrt{5}} \sim 1.34$ | $\sim 1.65$ | $\sim 1.763$ |

The above analysis clarifies that the extended hydrodynamic equations will yield continuous solutions only for a finite range of Mach number, although the continuous solution exists at any Mach number for the Navier-Stokes model. If we retain an infinite number of moments, then it is possible to push the critical Mach number to infinity, thereby obtaining continuous solutions for the whole range of Mach number, which is equivalent to solving the original Boltzmann equation. It is pertinent to ask: what happens to the stationary shock solutions of extended hydrodynamic equations with a finite number of moments for $\mathrm{Ma} > \mathrm{Ma}_{cr}$? A "weak" solution of extended hydrodynamic equations can be constructed for $\mathrm{Ma} > \mathrm{Ma}_{cr}$, following the well-known procedure of "equal-area" rule [(Courant & Friedrichs 1948)]. We consider this in §5.5 to compare ODE and PDE solutions of 10-moment model.

## 5.5 10-moment model: Comparison of ODE solution with PDE solution

For planar stationary shocks in molecular gas, the 10-moment system takes the following form.

$$\frac{\mathrm{d}}{\mathrm{d}x}\Big(\rho\, u\Big) = 0, \tag{5.56}$$

$$\frac{\mathrm{d}}{\mathrm{d}x}\Big(\rho\, u^2 \,+\, \rho\,\theta \,+\, \sigma\Big) = 0, \tag{5.57}$$

$$\frac{\mathrm{d}}{\mathrm{d}x}\Big(\rho\, u^3 \,+\, 5\,\rho\,\theta\, u \,+\, 2\,\sigma\, u\Big) = 0, \tag{5.58}$$

$$\frac{\mathrm{d}}{\mathrm{d}x}\Big(2\,\rho\, u\,\theta \,-\, \sigma\, u\Big) = \frac{16}{5}\frac{d^2}{m}\sqrt{\pi\,\theta}\,\rho\,\sigma. \tag{5.59}$$

Recall that the longitudinal stress $\sigma = 2\,\rho\,\theta_s$, where $\theta_s = (\theta_{xx} - \theta_{yy})/3$ is the skew temperature. The boundary conditions for the above ODE system are specified in terms of jump conditions, also called Rankine-Hugoniot relations. Using the Rankine-Hugoniot relations, first three equations (5.56 -5.58) are solved easily and one can deduce $u$, $\theta$, and $\theta_s$ as a function of $\rho$ and the

upstream reference values as

$$
\begin{aligned}
u &= \frac{\rho_1\, u_1}{\rho} \\
\theta &= \frac{1}{3\,\rho^2}\left[\rho^2\,\theta\left(\gamma\,\mathrm{Ma}_1^2\,+\,5\right) - 2\,\rho\,\rho_1\,\theta_1\left(\gamma\,\mathrm{Ma}_1^2\,+\,1\right) + \gamma\,\mathrm{Ma}_1^2\,\rho_1^2\,\theta_1\right], \\
\theta_s &= \frac{1}{6\rho^2}\left[-\rho^2\,\theta_1\left(\gamma\,\mathrm{Ma}_1^2\,+\,5\right) + 5\,\rho\,\rho_1\,\theta_1\left(\gamma\,\mathrm{Ma}_1^2\,+\,1\right) - 4\,\gamma\,\mathrm{Ma}_1^2\,\rho_1^2\,\theta_1\right].
\end{aligned}
\tag{5.60}
$$

In the above we make use of the fact that the skew-temperature vanishes at both upstream and downstream equilibria. Finally, the ten-moment system for a steady shock in a molecular gas is reduced to the following single ODE for density $\rho$:

$$
\frac{\mathrm{d}\rho}{\mathrm{d}x} = \frac{32\sqrt{\pi}}{5\,\rho_1^2\,u_1\,\theta_1}\frac{d^2}{m}\left[\frac{\rho^5\,\sqrt{\theta}\,\theta_s}{3(\gamma\mathrm{Ma}_1^2+1)\rho - 4\gamma\mathrm{Ma}_1^2\rho_1}\right], \tag{5.61}
$$

upon substituting values of $u$, $\theta$, and $\theta_s$ into the Eq. (5.59).

After non-dimensionalization, using (6.1) and (6.2), this ODE takes the following form:

$$
\frac{\mathrm{d}\rho}{\mathrm{d}x} = \frac{32}{5\sqrt{2\pi}\mathrm{Kn}\,\mathrm{Ma}_1\sqrt{\gamma}}\left[\frac{\rho^5\,\sqrt{\theta}\,\theta_s}{3(\gamma\mathrm{Ma}_1^2+1)\rho - 4\gamma\mathrm{Ma}_1^2}\right], \tag{5.62}
$$

where

$$
\theta = \frac{1}{3\,\rho^2}\left[\rho^2\,\left(\gamma\,\mathrm{Ma}_1^2\,+\,5\right) - 2\,\rho\,\left(\gamma\,\mathrm{Ma}_1^2\,+\,1\right) + \gamma\,\mathrm{Ma}_1^2\right], \tag{5.63}
$$

and

$$
\theta_s = \frac{1}{6\rho^2}\left[-\rho^2\,\left(\gamma\,\mathrm{Ma}_1^2\,+\,5\right) + 5\,\rho\,\left(\gamma\,\mathrm{Ma}_1^2\,+\,1\right) - 4\,\gamma\,\mathrm{Ma}_1^2\right]. \tag{5.64}
$$

This constitutes an initial-value problem which can be solved numerically by using the fourth order Runge-Kutta method. Care must be taken while solving this ODE since above the critical Mach number ($\mathrm{Ma}_1 > \mathrm{Ma}_{cr}$) a discontinuity appears embedded in the solution. If the upstream Mach number is above the critical Mach number, then the initial value for $\rho$ becomes its frozen jump value $\rho_J$, i.e. when $\mathrm{Ma}_1 > \frac{3}{\sqrt{5}}$, the upstream state may be connected by a jump to the shock state $\rho_J$, which is then connected to the downstream state. The first three jump relations which are arising from the mass conservation, momentum conservation and energy conservation (associated with (5.56 -5.58)) are inevitably satisfied by any solution of (5.62). The value of the density at the shock state $\rho_J$ can be obtained from an additional constraint associated with the Eq. (5.59). It is necessary that the condition [(Levermore & Morokoff 1998)]

$$
[\rho\,u\,(\theta\,-\,\theta_s)]_{Up} = [\rho\,u\,(\theta\,-\,\theta_s)]_{Down} \tag{5.65}
$$

holds in order for Eq. (5.59) to be satisfied weakly across a shock/jump - this is similar to Maxwell's equal-area rule in thermodynamics [(Callen 2006)] that guarantees admissible/stable thermodynamic states. The subscripts Up and Down in Eq. (5.65) indicates the evaluation of the term with in the square brackets on either side of the jump. Hence by considering the left state being the upstream reference state and the right state being the state just after the jump

(shock state), the relation (5.65) dictates that

$$\theta_1 = \theta_J - \theta_{s_J}. \tag{5.66}$$

We arrive at the following equation by substituting the values of $\theta_J$ and $\theta_{s_J}$ with the help of Eq. (5.63) and Eq. (5.64).

$$\gamma \,\mathrm{Ma}_1^2 \frac{1}{\rho_J^2} - \frac{3}{2\,\rho_J}(\gamma \,\mathrm{Ma}_1^2 + 1) + \frac{1}{2}(\gamma \,\mathrm{Ma}_1^2 + 3) = 0. \tag{5.67}$$

Equation (5.67) is a quadratic equation in $\frac{1}{\rho_j}$ whose roots are as follows:

$$\frac{1}{\rho_J} = \frac{\gamma \,\mathrm{Ma}_1^2 + 3}{2\gamma \,\mathrm{Ma}_1^2}, \quad \text{and} \quad \frac{1}{\rho_J} = 1 = \rho_1. \tag{5.68}$$

Hence the value of the density at the shock state $\rho_J$ is given by [(Levermore & Morokoff 1998)]:

$$\rho_J = \frac{2\gamma \,\mathrm{Ma}_1^2}{\gamma \,\mathrm{Ma}_1^2 + 3}. \tag{5.69}$$

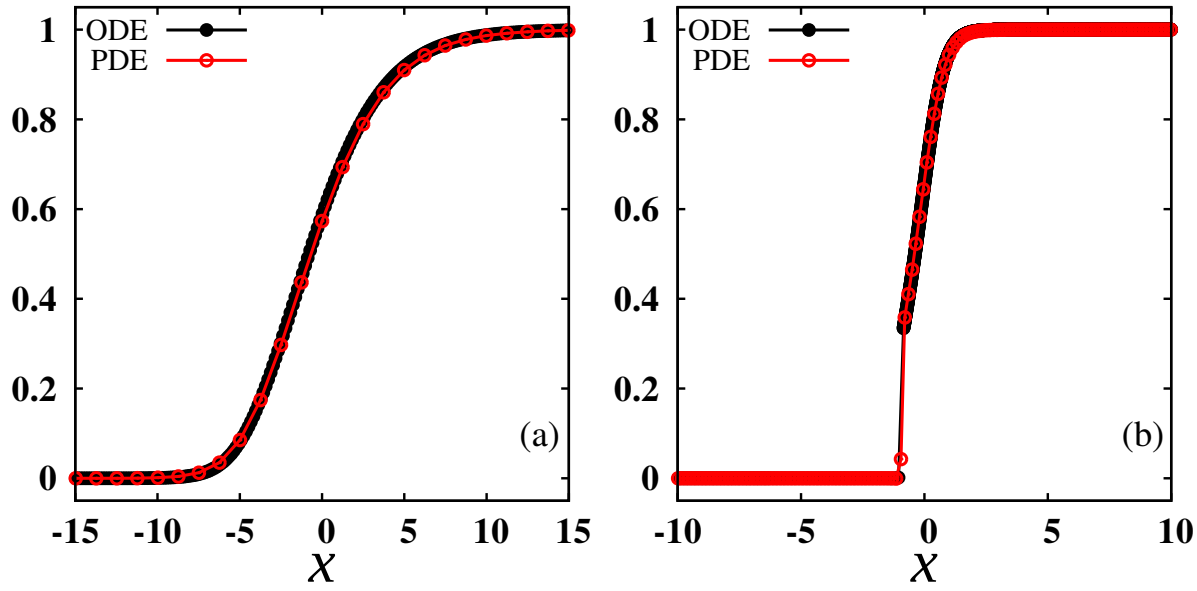


Figure 5.1: Comparison of density profiles using ODE and PDE solutions. Left: $\mathrm{Ma}_1 = 1.2$, right: $\mathrm{Ma}_1 = 3$.

Finally we compare the density profiles obtained from the solution of the ODE (5.62) with that obtained from the solution of the system of PDEs via the numerical schemes as discussed in §3.5. Note that the density is normalized as in (3.44). Figure 5.1(a,b) displays a comparison of ODE and PDE solutions for $\mathrm{Ma}_1 = 1.2$ and $\mathrm{Ma}_1 = 3$. For the Mach number $\mathrm{Ma}_1 = 1.2$, which is below the critical Mach number ($\mathrm{Ma}_{cr}$), there is no embedded shock and the PDE solution lies on the top of the ODE solution, see Fig. 5.1(a). For an upstream Mach number $\mathrm{Ma}_1 = 3$, which is above the critical Mach number ($\mathrm{Ma}_{cr} \approx 1.34$), the initial value of $\rho$ is taken as its frozen

jump value as given in (5.69) to solve (5.62). In this case too we observe excellent agreement between PDE and ODE solutions as seen in Fig. 5.1(b) which confirms that the PDE-solution obtained from the relaxation scheme captures the frozen-jump value of the density.

Collectively the comparisons in Figs. 5.1(a,b) further validate the relaxation-type numerical schemes (Chapter:3) that we have used to solve the PDE-system for the one-dimensional shock-wave problem. This also shows that the relaxation-type schemes are able to capture both smooth and discontinuous shock solutions of extended hydrodynamic models.

### 5.5.1 Regularization

It is clear from §5.4 that the moment models which are formulated from Grad's procedure, when applied to stationary shock problem, will suffer from a subshock in front of the shock for Mach numbers greater than critical Mach number of the moment model (see Fig.5.1(b)). Regularization or parabolization is one method to get a smooth shock profile beyond the critical Mach number of the respective moment model [(Struchtrup & Torrilhon 2003; Torrilhon & Struchtrup 2004)]. Regularization process changes the character of the hyperbolic system by adding some parabolic terms, for example the higher order gradient expressions obtained from Boltzmann's equation to Grad's system. In the original Grad's 10-moment system the contribution from the third order moments of the distribution function is zero. But if we follow the regularization procedure adopted by Struchtrup and Torrilhon [(Struchtrup & Torrilhon 2003; Torrilhon & Struchtrup 2004; Struchtrup 2005*b*)] for 10-moment model we will get the expressions for the higher-order moments like heat flux vector and the third order traceless moment. These expressions contain the gradient terms of the lower-order moments of the distribution function and change the hyperbolic nature of the 10-moment system to parabolic. By doing this we can get smooth shock profiles beyond the critical Mach number. These issues are dealt separately in Chapter 7 of this thesis.

## 5.6 Haff's Law from 14-Moment Model

Here we derive the Haff's law from the 14-moment model. For a spatially homogeneous system, all the basic field variables depend only on time. Hence, for the spatially homogeneous solution, the 14-moment model reduces to the following system of six equations in one-dimension for the density ($\rho$), velocity (u), scalar temperature ($\theta$), skew-temperature ($\theta_s$), heat-flux ($q$), and the

fourth order moment ($\Delta$) :

$$\begin{aligned}
\frac{\mathrm{d}\rho}{\mathrm{d}t} &= 0,\\
\frac{\mathrm{d}u}{\mathrm{d}t} &= 0,\\
\frac{\mathrm{d}\theta}{\mathrm{d}t} &= -\frac{8\sqrt{2}}{3\sqrt{\pi}}\frac{(1-\alpha)}{(3-\alpha)}\rho\,\theta^{\frac{3}{2}}\Big[1+\frac{3\Delta}{16}\Big],\\
\frac{\mathrm{d}\theta_s}{\mathrm{d}t} &= -\frac{8\sqrt{2}}{5\sqrt{\pi}}\sqrt{\theta}\Big[1-\frac{\Delta}{32}\Big]\rho\,\theta_s,\\
\frac{\mathrm{d}q}{\mathrm{d}t} &= -\frac{2\sqrt{2}}{15\sqrt{\pi}}\frac{\sqrt{\theta}}{(3-\alpha)}\Big[49-33\alpha+(19-3\alpha)\frac{\Delta}{32}\Big]\rho\,q,\\
\frac{\mathrm{d}\Delta}{\mathrm{d}t} &= -\frac{\sqrt{2}}{30\sqrt{\pi}}\frac{\rho\sqrt{\theta}}{(3-\alpha)}\Big[16(2\alpha^2-1)(1-\alpha)+\Delta\Big(30\alpha^2(1-\alpha)+81-17\alpha\Big)\Big].
\end{aligned} \tag{5.70}$$

All above equations have been scaled using the following scaling parameters and the hats are removed for simplicity.

$$\begin{aligned}
&\hat{\rho}=\frac{\rho}{\rho_1}, \qquad \hat{u}=\frac{u}{\sqrt{\theta_1}}, \qquad \hat{\theta}=\frac{\theta}{\theta_1}, \qquad \hat{\theta_s}=\frac{\theta_s}{\theta_1}, \qquad \hat{q}=\frac{q}{\rho_1\theta_1\sqrt{\theta_1}},\\
&\hat{t}=\frac{t}{\tau}, \qquad \text{where} \quad \tau=\frac{4}{\sqrt{2}n_1\pi d^2\sqrt{\theta_1}(1+\alpha)(3-\alpha)}.
\end{aligned} \tag{5.71}$$

When deriving the last equation in (5.70) we considered linear terms in $\Delta$. From the first two equations of (5.70), we can infer that the mass density and the velocity remain constant in time and furthermore the mass density ($\rho$)) is taken to be one. It is noteworthy to say that, from the fourth and fifth equations of (5.70), the skew temperature and the heat flux do not evolve in time when the initial conditions for these two variables vanish. From the last equation of (5.70), we may conclude that a vanishing initial condition for the fourth moment implies that it may evolve in time.

Let us consider a special case in which the fourth moment is constant in time,

$$\Delta_\infty \equiv \Delta(t\to\infty) = \frac{16(1-2\alpha^2)(1-\alpha)}{30\alpha^2(1-\alpha)+81-17\alpha}, \tag{5.72}$$

which follows from the last equation of (5.70). Substituting the above value of $\Delta$ into the third equation of (5.70) and integrating the resulting equation leads to the well-known Haff's law [(Haff 1983)]:

$$\theta(t) = \frac{\theta(t=0)}{\left(1+\frac{4\sqrt{2}}{3\sqrt{\pi}}\frac{(1-\alpha)}{(3-\alpha)}\Big[1+\frac{3(1-\alpha)(1-2\alpha^2)}{30\alpha^2(1-\alpha)+81-17\alpha}\Big]\sqrt{\theta(t=0)}\,\rho(t=0)\,t\right)^2}. \tag{5.73}$$

The above equation can be written in a simple form as

$$\theta(t) = \frac{1}{(k_0+k_1\,t)^2}, \tag{5.74}$$

with $k_0 = \frac{1}{\sqrt{\theta(t=0)}}$ and $k_1 = \frac{4\sqrt{2}}{3\sqrt{\pi}} \frac{(1-\alpha)}{(3-\alpha)} \left(1 + \frac{3}{16}\Delta_\infty\right) \rho$.

Now we solve the coupled non-linear system (5.70) semi-analytically by treating $\Delta_\infty$ as the stationary solution for $\Delta$. In terms of a new variable $\delta(t) = \Delta(t) - \Delta_\infty$, the last equation in the (5.70) can be rewritten as:

$$\frac{d\delta(t)}{dt} = -\frac{\sqrt{2}}{30\sqrt{\pi}} \frac{1}{(3-\alpha)} \Big[30\alpha^2(1-\alpha) + 81 - 17\alpha\Big] \rho \sqrt{\theta(t)}\, \delta(t). \tag{5.75}$$

Solving the above equation with the help of (5.73) we get the solution as:

$$\delta(t) = k_0^{(k_2/k_1)}\, \delta(0)\, (k_0 + k_1\, t)^{-\frac{k_2}{k_1}}, \tag{5.76}$$

where

$$k_2 = \frac{\sqrt{2}}{30\sqrt{\pi}} \frac{1}{(3-\alpha)} \Big[30\alpha^2(1-\alpha) + 81 - 17\alpha\Big] \rho. \tag{5.77}$$

Substituting $\delta(t)$ in the third equation of (5.70) we get

$$\frac{d\theta(t)}{dt} = -\Big[k_3 + k_4 (k_0 + k_1\, t)^{-(k_2/k_1)}\Big] \theta(t) \sqrt{\theta(t)}, \tag{5.78}$$

where

$$\begin{aligned} k_3 &= \frac{8\sqrt{2}}{3\sqrt{\pi}} \frac{(1-\alpha)}{(3-\alpha)} \Big[1 + \frac{3}{16}\Delta_\infty\Big] \rho, \\ k_4 &= \frac{1}{\sqrt{2\pi}} \frac{(1-\alpha)}{(3-\alpha)} k_0^{\frac{k_2}{k_1}} \rho\, \delta(0). \end{aligned} \tag{5.79}$$

The solution for (5.78) is:

$$\theta(t) = \frac{4(k_1-k_2)^2\, (k_0 + k_1\, t)^{2(k_2/k_1)}}{\left[k_4(k_0 + k_1\, t) + (k_1 - k_2)\, (k_0 + k_1\, t)^{(k_2/k_1)} \left(k_3\, t - \frac{k_4}{k_1 - k_2}\, k_0^{1-(k_2/k_1)} + \frac{2}{\sqrt{\theta(0)}}\right)\right]^2} \tag{5.80}$$

Using the expressions of $\theta(t)$ and $\delta(t)$ in the remaining equations of (5.70) we can obtain the expressions for $\theta_s(t)$ and $q(t)$. Due to integration complexity we solve the differential equations for $\theta_s(t)$ and $q(t)$ numerically by considering the initial conditions $\theta_s(0) = 1$, $q(0) = 1$, $\theta(0) = 1$ and $\delta(0) = 1 - \Delta_\infty$.

In Fig. 5.2 (a), the time decay of the temperature (black solid line) which is the solution of (5.80) is compared with the Haff's law (red dashed line) which is the solution of (5.73). Panel (b) of Fig. 5.2 shows the same as in panel (a), but plotted in log-scale. One observes from Fig. 5.2 that the temperature decay ($\theta$) exactly follows Haff's law. Moreover this decay rate is faster when the restitution coefficient is decreasing from 1, i.e. if the dissipation is increasing, the time decay of the temperature is faster (which is evident from Fig. 5.2).

Figure 5.3 shows the time evolutions of the fourth order moment $\delta$, the skew temperature $\theta_s$, and the heat flux $q$ for restitution coefficients of $\alpha = 0.95$, $\alpha = 0.9$ and $\alpha = 0.7$ respectively.

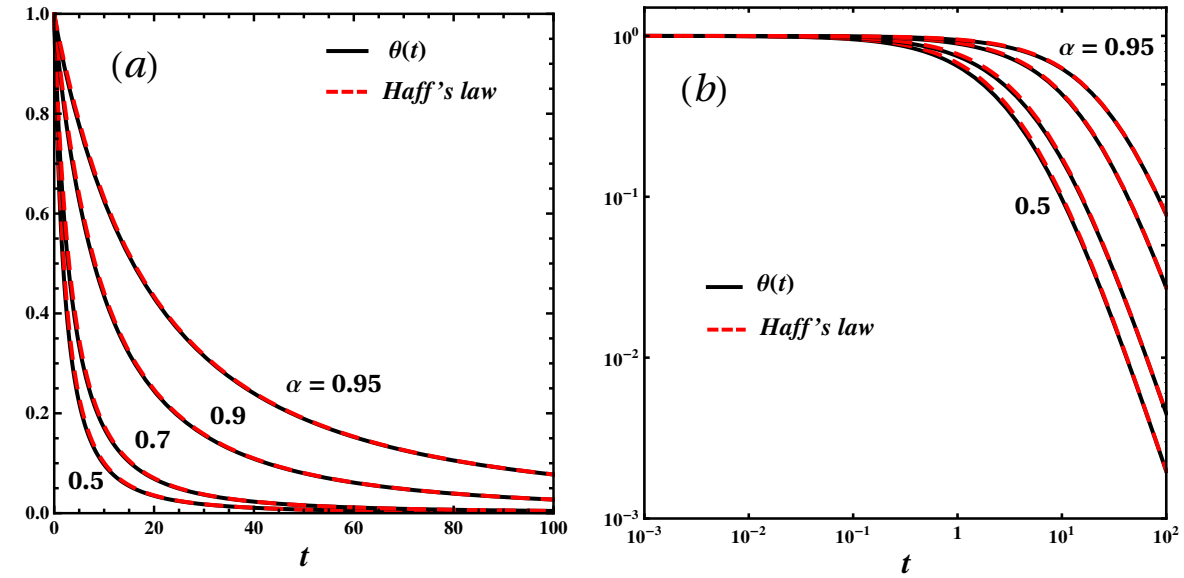


Figure 5.2: (a) Decay of the temperature with time: The black solid line represents the solution of (5.80) and the red dashed line indicating the Haff's law, which is given by (5.73), (b) same as in panel (a), but in log-scale.

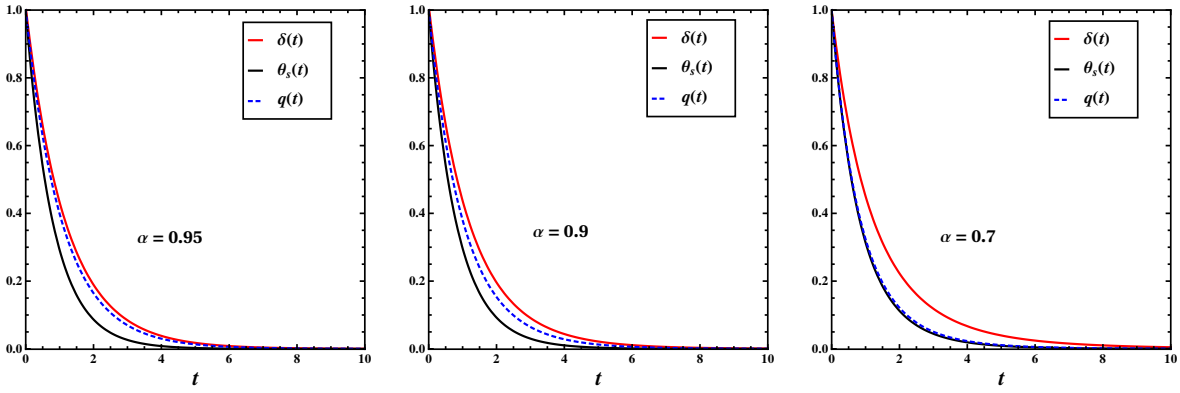


Figure 5.3: Decay of the fourth order moment, the skew-temperature,and the heat flux with respect to time for a coefficient of restitution $\alpha = 0.95$ (left panel), $\alpha = 0.9$ (center panel), and $\alpha = 0.7$ (right panel).

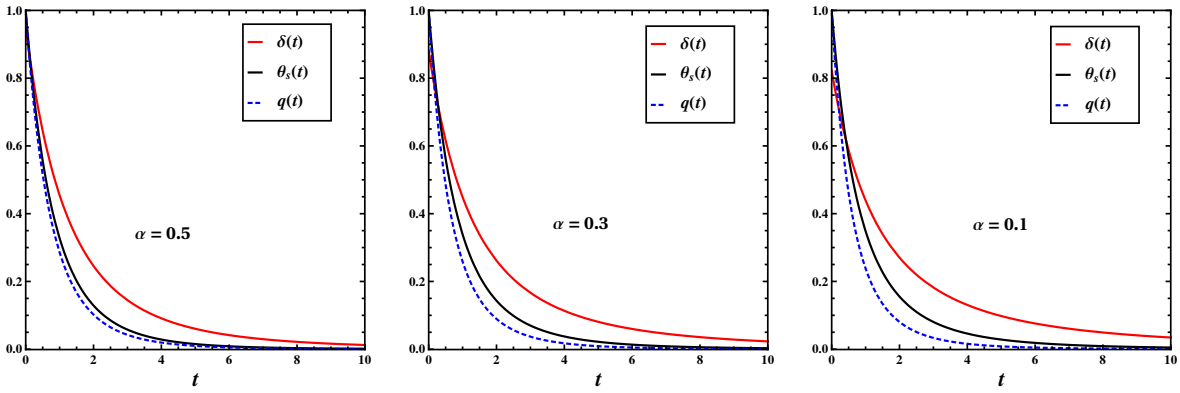


Figure 5.4: Decay of the fourth order moment, the skew-temperature,and the heat flux with respect to time for a coefficient of restitution $\alpha = 0.5$ (left panel), $\alpha = 0.3$ (center panel), and $\alpha = 0.1$ (right panel).

Figure 5.4 shows the same as in Fig. 5.3, but for restitution coefficients of $\alpha = 0.5$, $\alpha = 0.3$ and $\alpha = 0.1$, respectively. Observing the left, center and right panels of Figs. 5.3 and 5.4, we find that the decay of the fourth order moment and the skew-temperature is slower with increasing dissipation whereas the decay of the heat flux is faster with increasing dissipation. The reason for this might be that the heat flux is directly connected with the energy transportation, which is mostly affected by the dissipation (inelasticity). Moreover one can observe that the initial value of $\delta$ decreases from 1 in the limit of $\alpha \to 0$, since the initial value of $\delta$ depends on $\Delta_\infty$ whose value increases with increasing dissipation.

## 5.7 Summary

The extended hydrodynamic equations have been analysed with reference to the plane shock wave problem. An analysis on the characteristics of extended hydrodynamic models is presented and this analysis confirms that the largest characteristic speed in extended hydrodynamic equations depends on the number of moments retained in hydrodynamic equations. Moreover, the largest characteristic speed increases if the number of moments is increased: $s_{\max} = \sqrt{3\theta}$, $\sqrt{4.54\theta}$ and $\sqrt{5.18\theta}$ (where $\theta$ is the dimensionless granular temperature) for 10, 13 and 14-moment models, respectively. It is shown that inelastic dissipation does not affect the characteristic speeds of Navier-Stokes as well as moment models.

An analysis of the 10-moment model for a granular gas for plane shock waves reveals that the density gradient can blow up if the upstream Mach number exceeds a critical value; it is shown that this critical Mach number is not influenced by the restitution coefficient ($\alpha$) and the critical Mach number is increased when the number of moments increases in extended hydrodynamic models. Lastly, a derivation of Haff's law is presented by assuming a spatially homogeneous solution for the 14-moment model.

## Appendix 5A. Haff's Law from 10-Moment Model

Here we derive the well known Haff's law from 10-moment model discussed in chapter 5 and 2. We are looking for the spatially homogeneous solution of 10-moment model which means that all the field variables are depend only on time ($t$). The spatially homogeneous solutions of 10-moment model in one dimension [Eqs. (5.3) - (5.6)] reduces to the following system for the four basic field variables, namely density ($\rho$), velocity ($u$), scalar temperature ($\theta$), and ($\theta_s$):

$$\begin{aligned}
\frac{\mathrm{d}\rho}{\mathrm{d}t} &= 0, \\
\frac{\mathrm{d}u}{\mathrm{d}t} &= 0, \\
\frac{\mathrm{d}\theta}{\mathrm{d}t} &= -\frac{8\sqrt{2}}{3\sqrt{\pi}}\frac{(1-\alpha)}{(3-\alpha)}\rho\,\theta^{\frac{3}{2}}, \\
\frac{\mathrm{d}\theta_s}{\mathrm{d}t} &= -\frac{8\sqrt{2}}{5\sqrt{\pi}}\sqrt{\theta}\,\rho\,\theta_s.
\end{aligned} \tag{5.81}$$

All equations in (5.81) are made dimensionless by using the reference scales discussed in (5.71). The mass density and the velocity remain constant in time which is evident from the first two equations of (5.81). On integrating the third equation of (5.81) and using initial condition, we arrive at the Haff's law:

$$\theta(t) = \frac{\theta(t=0)}{\left(1+\frac{4\sqrt{2}}{3\sqrt{\pi}}\frac{(1-\alpha)}{(3-\alpha)}\sqrt{\theta(t=0)}\,\rho(t=0)\,t\right)^2}. \tag{5.82}$$

It is noteworthy to say here is that the Haff's law (5.82) derived from 10-moment model and 13-moment model (derivation not shown) is coincides with the classical Haff's law (4.27). Hence the main difference between the classical Haff's law and the Haff's law derived from the 14-moment model / Navier-Stokes model is that the factor $\left(1+\frac{3}{16}\,a_2\right)$ in the denominator, where $a_2$ is the stationary value of the non-equilibrium part of the full contracted fourth-moment ($\Delta_\infty$). One can say that the presence of the fourth-order contracted moment makes the Haff's law derived from 14-moment model different from the classical Haff's law.

Table 5.2: Haff's law

| Euler, 10-moment & 13-moment | Navier-Stokes & 14-moment |
|---|---|
| $\theta(t) = \frac{\theta(t=0)}{\left(1+\frac{4\sqrt{2}}{3\sqrt{\pi}}\frac{(1-\alpha)}{(3-\alpha)}\sqrt{\theta(t=0)}\,\rho(t=0)\,t\right)^2}$ | $\theta(t) = \frac{\theta(t=0)}{\left(1+\frac{4\sqrt{2}}{3\sqrt{\pi}}\frac{(1-\alpha)}{(3-\alpha)}\left(1+\frac{3}{16}\,a_2\right)\sqrt{\theta(t=0)}\,\rho(t=0)\,t\right)^2}$ |

# Chapter 6

# Numerical Analysis of Shock Waves via Extended Hydrodynamic Models[†]

## 6.1 Introduction

The results from Navier-Stokes-Fourier model, R13-moment model [(Struchtrup & Torrilhon 2003)] are compared with DSMC (direct simulation Mante Carlo, (Bird 1994)) calculations for the shock width (see Eq. 6.14) in Fig. 6.1. This comparison for the shock thickness shows the accuracy of the higher-order models like R13 (regularized 13-moment model) over Navier-Stokes-Fourier model. It is clear from Fig. 6.1 that the extended hydrodynamic model namely R13 is more accurate than the classical Navier-Stokes-Fourier hydrodynamic model as the results from R13 model show a better agreement with DSMC results. The results obtained from DSMC method are realistic since the Boltzmann equation is solved by DSMC method. This motivates us to use the extended hydrodynamic models to calculate the shock structure problem for a granular gas.

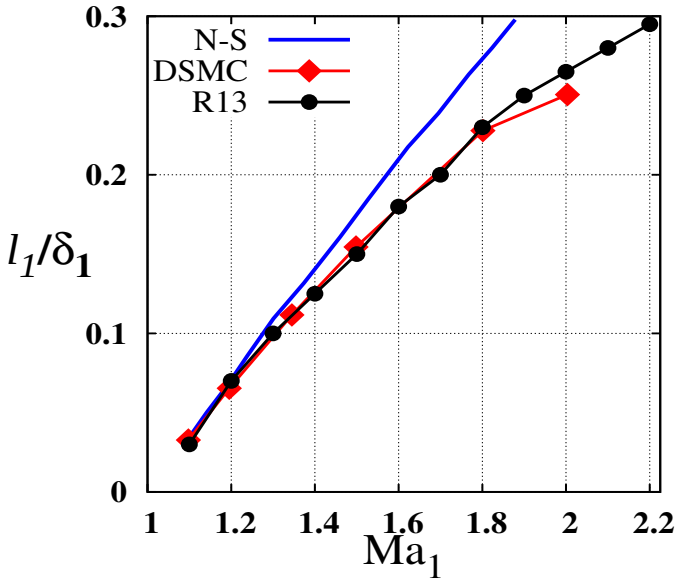


Figure 6.1: Shock width vs upstream Mach number for a hard spheres gas, data extracted from Torrilhon & Struchtrup (2004). R13 refers to "regularized" 13-moment equations [see Chapter 7].

[†]Part of this chapter (§6.3) has been done in collaboration with Dr. Santosh Ansumali; however he did not offer any comments on the contents of the original version of this Chapter.

In this chapter, we present numerical results for the Riemann problem of one-dimensional shock waves in a molecular gas as well as in a dilute granular gas using three levels of granular hydrodynamic equations: (i) 10-moment equations, (ii) 13-moment equations and (iii) 14-moment equations. We use the numerical schemes which are discussed in §3.5.1 and §3.5.2 to solve the above models numerically. First we present results obtained from the above models of a molecular gas. Next we show the early time behavior of unsteady plane shock waves in a dilute granular gas, and the results obtained from extended hydrodynamic (10-moment, 13-moment and 14-moment) models are compared with Navier-Stokes hydrodynamic model.

### 6.1.1 Non-dimensionalization

Since we are going to compare the results of plane shock wave problem between all extended hydrodynamic model with the classical hydrodynamic models, namely, Euler and Navier-Stokes, we use the same reference scales which are discussed in §3.4, for non-dimensionalization of extended hydrodynamic equations.

$$\begin{aligned} \hat{\rho} &= \frac{\rho}{\rho_1}, \qquad \hat{u} = \frac{u}{\sqrt{\theta_1}}, \qquad \hat{\theta} = \frac{\theta}{\theta_1}, \qquad \hat{\theta}_s = \frac{\theta_s}{\theta_1}, \\ \hat{\sigma} &= \frac{\sigma}{\rho_1\theta_1}, \qquad \hat{q} = \frac{q}{\rho_1\theta_1\sqrt{\theta_1}}, \qquad \hat{x} = \frac{x}{l_1}, \qquad \hat{t} = \frac{t\sqrt{\theta_1}}{l_1}, \end{aligned} \tag{6.1}$$

with the upstream mean free path ($l_1$) and the shear viscosity coefficient ($\mu_1$) given by

$$l_1 = \frac{16\,\mu_1}{5\,\sqrt{2\pi}\rho_1\sqrt{\theta_1}}, \qquad \mu_1 = \frac{5m}{4d^2}\sqrt{\frac{\theta_1}{\pi}}\frac{1}{(1+\alpha)(3-\alpha)}. \tag{6.2}$$

When we do non-dimensionalization, only the source terms in the extended hydrodynamic equations will change and the left hand side of the extended hydrodynamic equations have the same form as in §5.2.1, §5.2.2 and §5.2.3 for the 10-moment, 13-moment and 14-moment models, respectively. The dimensionless form of the 14-moment system is same as (5.15 - 5.20) with the following source terms:

$$\mathcal{D} = \frac{64\,b_1}{15\,\sqrt{2}}\,(1-\alpha^2)\left[1 + \frac{3\,\Delta}{16}\right]\rho^2\,\theta^{\frac{3}{2}}, \tag{6.3}$$

$$\sigma^s = -\frac{64\,b_1}{25\,\sqrt{2}}\,\sqrt{\theta}\,(1+\alpha)\,(3-\alpha)\left[1 - \frac{\Delta}{32}\right]\rho\,\sigma, \tag{6.4}$$

$$q^s = -\frac{16\,b_1}{75\,\sqrt{2}}\,\sqrt{\theta}\,(1+\alpha)\left[49 - 33\,\alpha + (19 - 3\,\alpha)\,\frac{\Delta}{32}\right]\rho\,q, \tag{6.5}$$

$$R^s = -\frac{64\,b_1}{5\,\sqrt{2}}\,\sqrt{\theta}\,(1+\alpha)\left[(2\,\alpha^2 + 9)\,(1 - \alpha)\right. \tag{6.6}$$

$$\left. + (30\,\alpha^2\,(1 - \alpha) + 271 - 207\,\alpha)\,\frac{\Delta}{16}\right]\rho^2\,\theta^2, \tag{6.7}$$

and the expression for $b_1$ given by

$$b_1 = \frac{5}{4\,\sqrt{\pi}}\,\frac{1}{(1+\alpha)\,(3-\alpha)}. \tag{6.8}$$

## 6.2 Steady Shock Waves in a Molecular Gas

Here we analyze the Riemann problem of planar shock waves for a molecular gas by solving the 10-moment, 13-moment and 14-moment equations, and the results are compared with those obtained from Navier-Stokes-order equations. The upstream boundary conditions are taken as

$$\rho_1 = 1, \quad u_1 = \mathrm{Ma}_1 \sqrt{\gamma}, \quad \theta_1 = 1, \quad \theta_{s1} = 0 = q_1 = \Delta_1, \tag{6.9}$$

while the downstream boundary conditions are provided by RH jump conditions (3.11). For the 14-moment model the downstream boundary conditions are given by

$$\begin{aligned}
\rho_2 &= \frac{(\gamma+1)\mathrm{Ma}_1^2}{2+(\gamma-1)\mathrm{Ma}_1^2}\,\rho_1, \\
u_2 &= \frac{2+(\gamma-1)\mathrm{Ma}_1^2}{(\gamma+1)\mathrm{Ma}_1^2}\,u_1, \\
\theta_2 &= \frac{(2\gamma\mathrm{Ma}_1^2-(\gamma-1))((\gamma-1)\mathrm{Ma}_1^2+2)}{(\gamma+1)^2\mathrm{Ma}_1^2}\,\theta_1, \\
\theta_{s2} &= 0, \qquad q_2 = 0, \qquad \text{and} \qquad \Delta_2 = 0.
\end{aligned} \tag{6.10}$$

The density and velocity profiles presented here are normalized as

$$\rho_N = \frac{\rho - \rho_1}{\rho_2 - \rho_1}, \qquad u_N = \frac{u - u_2}{u_1 - u_2}, \tag{6.11}$$

and the temperature profiles are normalized via:

$$\theta_N = \frac{\theta - \theta_1}{\theta_2 - \theta_1}, \tag{6.12}$$

for the case of a molecular gas.

We perform numerical simulations of shock waves in a molecular gas using the relaxation scheme described in Chapter 3. In all numerical experiments we take the relaxation rate $\epsilon$ in (3.30) to be $10^{-8}$ as this gives converged results for both molecular and granular gases. We perform numerical experiments by considering an one-dimensional domain of length 50 covering $(-25, 25)$ with 2000 grid points, until a time of 100 with $\Delta t = \mathcal{C} \cdot \Delta x / max(a_i)$ and placing the initial discontinuity at $x = 0$. Any CFL (Courant-Friedrichs-Lewy) number which is less than one gives a stable solution for 10, 13 and 14 moment models for the whole range of Knudsen number (Kn), i.e. for any value of Mach number (see Eq. (3.49) in §3.7 which relates the Mach number(Ma) and Knudsen number(Kn)). However, for Navier-Stokes model, the CFL-number($\mathcal{C}$) must be decreased with increasing Kn to obtain a stable solution; for example, we have found that the CFL numbers of 0.5, 0.1 and 0.01 give stable solutions for Kn = 0.0001, 0.1 and 1, respectively. For present computations of shocks in a molecular gas, we take the CFL($\mathcal{C}$) number for the moment models as 0.1 while for Navier-Stokes model it is taken as 0.01.

### 6.2.1 Effect of Mach number (Ma) on molecular shock wave structures

**Upstream Mach number = 1.2**

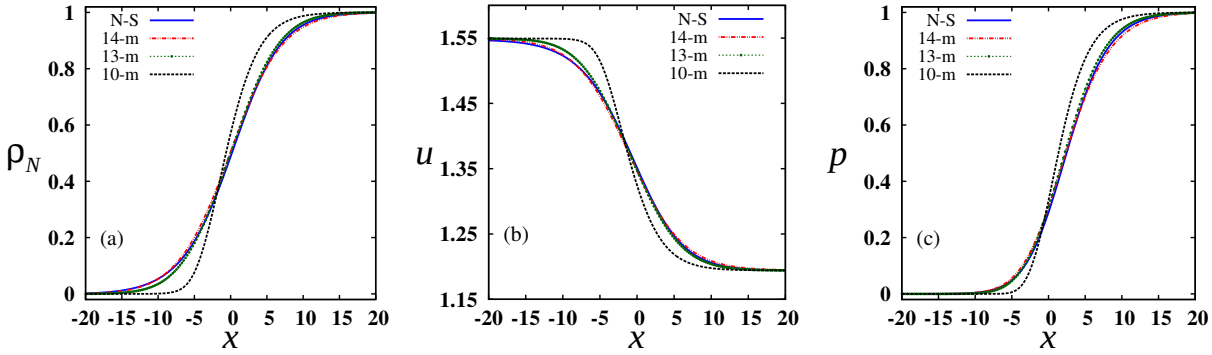


Figure 6.2: Density, velocity and pressure profiles from the moment models and Navier-Stokes model for an upstream Mach number of 1.2.

The first shock structure to be analyzed here is that of a "weak shock"* with the upstream number of $\mathrm{Ma}_1 = 1.2$. All moment models produce continuous shock structure for this Mach number since the critical Mach number for discontinuous solution is larger than 1.2. The density profiles as predicted by the moment models and Navier-Stokes model for this weak shock wave are presented in figure 6.2 (a). One can see from this figure that Navier-Stokes solution closely matches with the 14-moment and 13-moment solutions. Comparing Navier-Stokes and 14-moment density profiles, it appears that there is a minor disagreement on the downstream part of the shock wave. We can say that Navier-Stokes profiles are more diffusive than those of 14-moment model on the upstream part of the shock, and are less diffusive than 14-moment model on the downstream part of the shock.

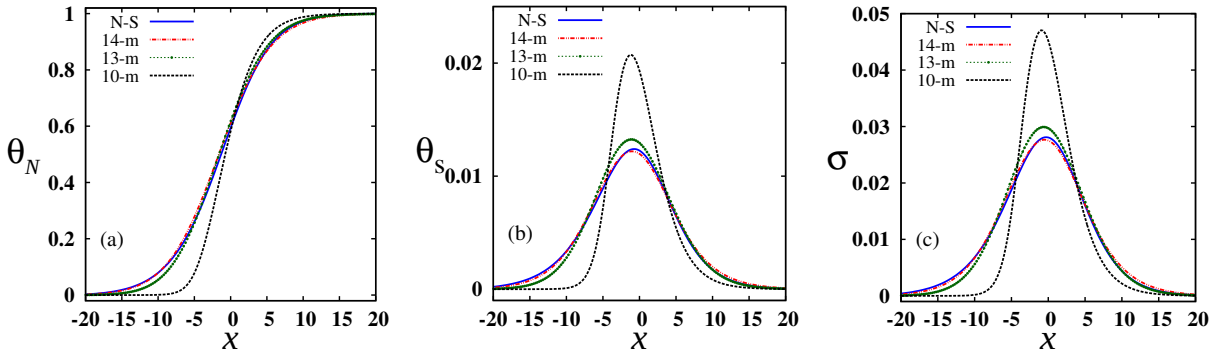


Figure 6.3: Scalar temperature , skew temperature and the longitudinal stress profiles from moment models and Navier-Stokes model for an upstream Mach number of 1.2.

Moreover we notice that the 10-moment model solution is not in agreement with other models discussed here, and this may be due to the fact that the 10-moment model is incapable of modelling heat-transfer effects. The density profile predicted by the 10-moment model is less

*The "weak" shock refers to Ma $\sim 1$, with Ma $<$ Ma$_{cr} \approx 1.65$ (as given by 13-moment model).

diffusive than any model which incorporate the heat transfer effects. One can notice that the 10-moment density profile looks steeper on the upstream side of the shock than the downstream side of the shock.

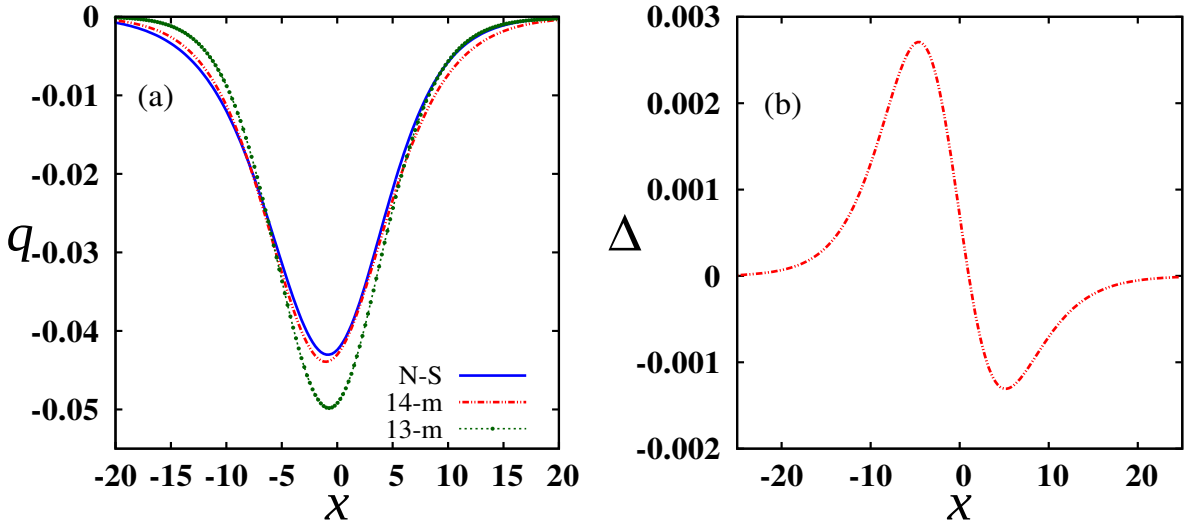


Figure 6.4: Heat flux and the fourth order contracted moment profiles from moment models and Navier-Stokes model for an upstream Mach number of 1.2.

The pressure profiles for the moment models and the N-S model shown in figure 6.2 (c) are calculated from the trace of the pressure tensor; i.e., $p = P_{ii}/3 \equiv \rho\theta$ by using the ideal gas equation of state. The velocity and the pressure profiles presented in figure 6.2 (b,c) predicted by the moment models and the N-S model look qualitatively similar. The scalar temperature, the skew temperature and the longitudinal stress profiles, predicted by the moment models and the N-S model, are displayed in Figs. 6.3 (a,b,c). From this figure one can see a qualitatively good agreement between the heat-transfer capable models. Although the 10-moment model can model deviatoric stresses, this model significantly over-predicts the skew temperature and the longitudinal stress, see 6.3 (b,c).

Figure 6.4 (a) shows the heat flux ($q$) profile from 13-moment model, 14-moment model and N-S model (10-moment model can not model the heat transfer effects). For the N-S model, the heat flux is calculated from the non-Fourier law:

$$q = -\kappa \frac{\partial \theta}{\partial x} - \kappa_h \frac{\partial \rho}{\partial x}. \tag{6.13}$$

Note that the N-S prediction for heat flux closely agrees with that for 14-moment model, however the heat flux for 13-moment model differs noticeably from N-S predictions.

The only model capable of predicting the fourth order fully contracted velocity moment is the 14-moment model, see 6.4 (b). It is found that $\Delta$ undergoes sign-change across the shock.

**Upstream Mach number = 1.5**

The second shock structure to be analyzed here is that of a weak shock with an upstream number of $\mathrm{Ma}_1 = 1.5$. For this inflow Mach number, except the 10-moment model, all other moment models produce continuous shock structure. The density profiles predicted by the moment

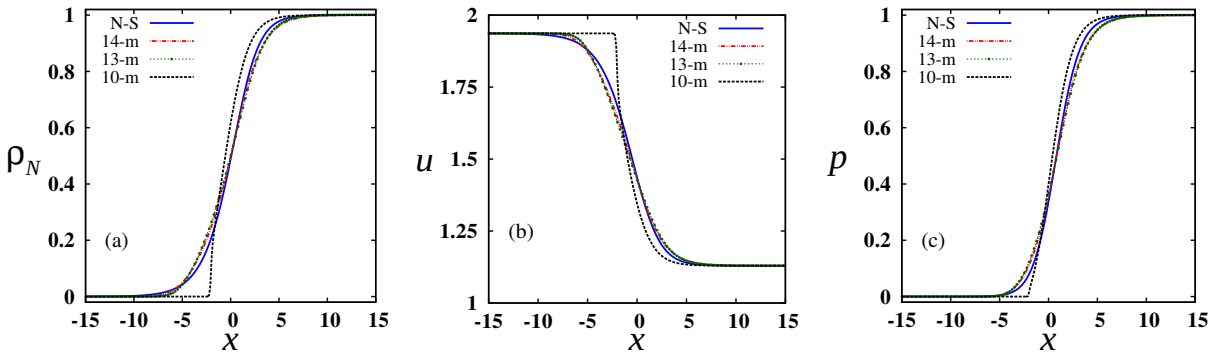


Figure 6.5: Density, velocity and pressure profiles from moment models and Navier-Stokes model for the upstream Mach number of 1.5.

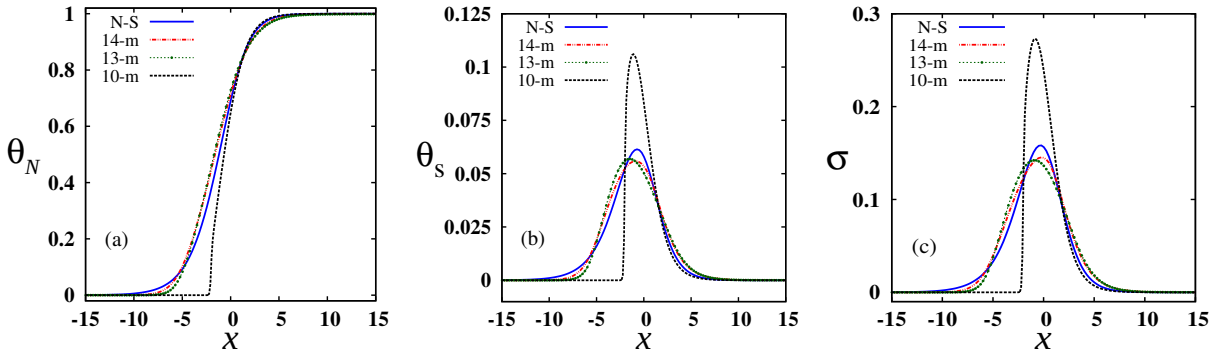


Figure 6.6: Scalar temperature , skew temperature and the longitudinal stress profiles from moment models and Navier-Stokes model for the upstream Mach number of 1.5.

models and Navier-Stokes model are depicted in figure 6.5 (a). An important noticeable feature of these results is that the density profile has steepened into a small discontinuity on the upstream side of the shock for the 10-moment model. As discussed in chapter 5, this type of discontinuous shock wave will form whenever the inflow velocity is higher relative to the largest frozen wave speed. The largest wave speed for the 10-moment model occurs when $\mathrm{Ma}_1 = 3/\sqrt{5} \approx 1.34$ (see Eq. (5.55) in chapter 5). Two additional numerical experiments (not shown) were performed for the 10-moment model with Mach numbers of 1.34 and 1.35. In fact, a discontinuity is observed for the case of Mach number 1.35, while a smooth transition is found for the case of Mach number 1.34. The velocity and the pressure profiles presented in Figs. 6.5 (b,c) as predicted by the moment models and the N-S model are qualitatively similar.

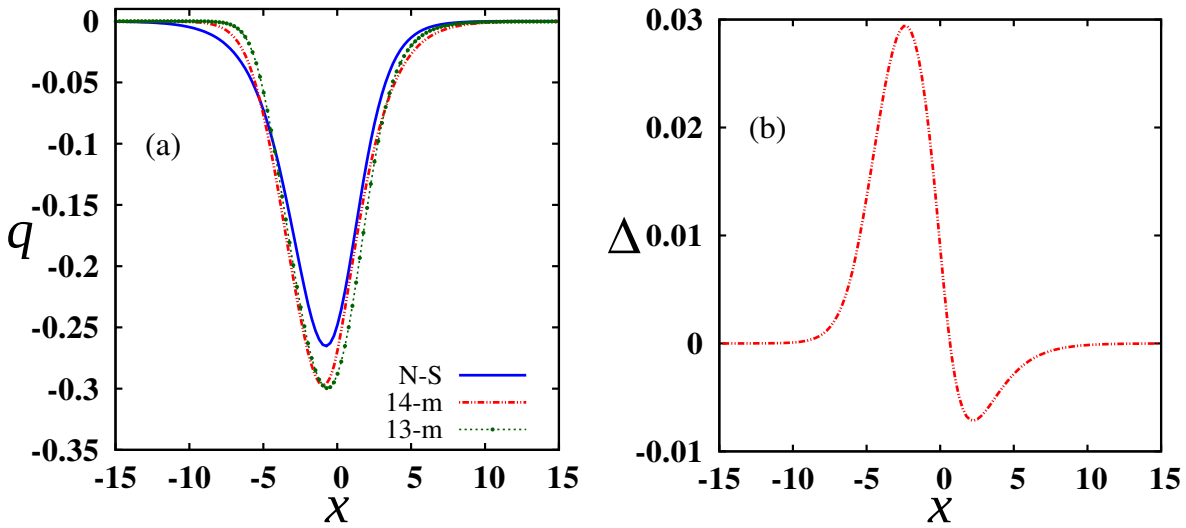


Figure 6.7: Heat flux and the fourth order contracted moment profiles from moment models and Navier-Stokes model for the upstream Mach number of 1.5.

The scalar temperature , the skew temperature and the longitudinal stress profiles, predicted by the moment models and the N-S model, are displayed in Figs. 6.6 (a,b,c). From this figure one can see a relatively good agreement between the heat-transfer capable models. Fig. 6.7 (a) shows the heat flux ($q$) profiles for 13-moment model, 14-moment model and N-S model; Fig. 6.7 (b) displays the fourth order contracted moment profile for 14-moment model. Comparing Fig. 6.4 (a) and Fig. 6.7 (a), it is found that the maximum of heat flux ($|q|^{max}$) for 13-moment and 14-moment models is larger than that of Navier-Stokes model and the difference increases with increasing Mach number. Further, comparing Fig. 6.4 (b) and Fig. 6.7 (b), it is evident that the maximum of fourth order contracted moment ($|\Delta|^{max}$) increases with increasing Mach number.

**Upstream Mach number = 2**

The third shock structure to be analyzed here is that of a shock with an upstream number of $\mathrm{Ma}_1 = 2$. For this inflow Mach number, the 10-,13- and 14-moment models fail to produce continuous shock structure. The density profiles as predicted by the moment models and Navier-Stokes model are depicted in Fig. 6.8 (a). An important feature of these results is that the density profile has steepened into a small discontinuity on the upstream side of the shock for

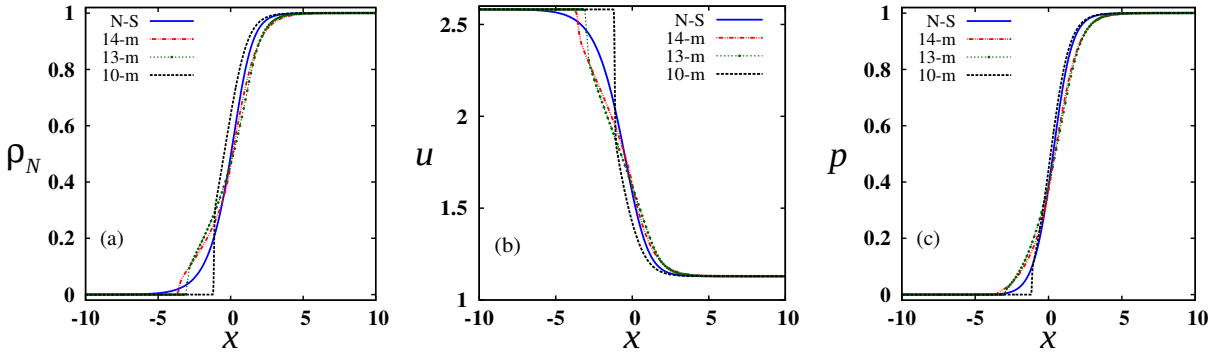


Figure 6.8: Density, velocity and pressure profiles from moment models and Navier-Stokes model for the upstream Mach number of 2.

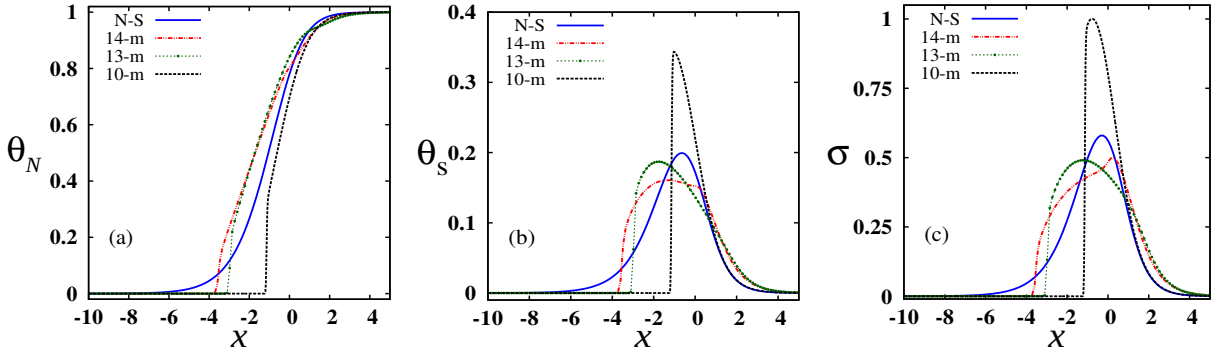


Figure 6.9: Scalar temperature, skew temperature and the longitudinal stress profiles from moment models and Navier-Stokes model for the upstream Mach number of 2.

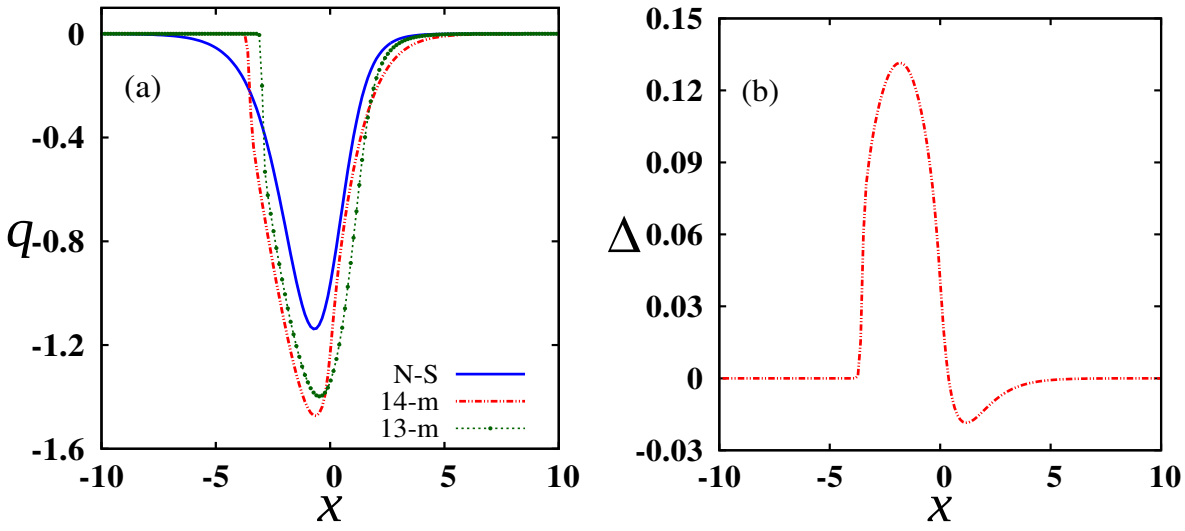


Figure 6.10: Heat flux and the fourth order contracted moment profiles from moment models and Navier-Stokes model for the upstream Mach number of 2.

all moment models. The velocity and the pressure profiles presented in Fig. 6.8 predicted by the moment models and the N-S model are qualitatively similar to those in Fig. 6.5 (b,c) for $\mathrm{Ma}_1 = 1.5$.

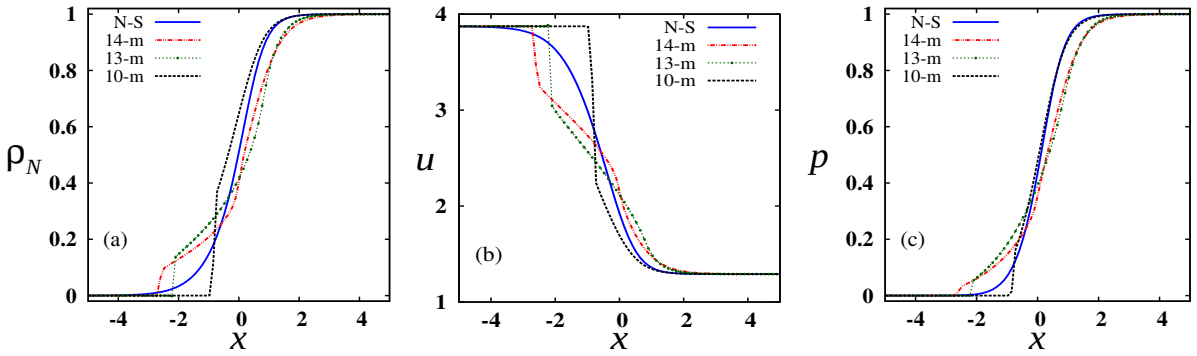


Figure 6.11: Density, velocity and pressure profiles from moment models and Navier-Stokes model for the upstream Mach number of 3.

The corresponding scalar temperature, the skew temperature and the longitudinal stress profiles are shown in Fig. 6.9. Figure 6.10 (a) shows the heat flux ($q$) profile for 13-moment model, 14-moment model and N-S model and Fig. 6.10 (b) shows the fourth-order contracted moment ($\Delta$) profile for 14-moment model. One can see that the heat flux profiles for 13-moment and 14-moment models closely follow each other at this Mach number.

**Upstream Mach number = 3**

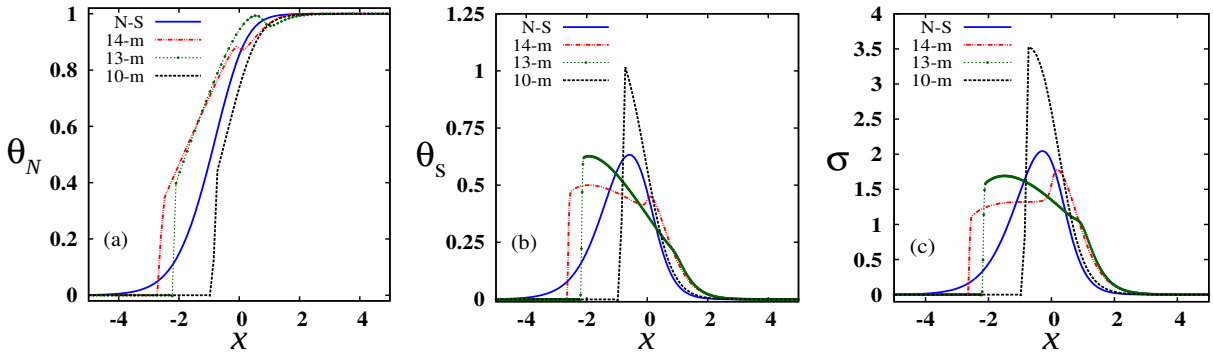


Figure 6.12: Scalar temperature, skew temperature and the longitudinal stress profiles from moment models and Navier-Stokes model for the upstream Mach number of 3.

The fourth shock structure to be analyzed here is that of a shock with the upstream number of $\mathrm{Ma}_1 = 3$. The density, velocity and pressure profiles predicted by the moment models along with Navier-Stokes model for this Mach number are depicted in figures 6.11 (a,b,c). The corresponding scalar temperature, the skew temperature and the longitudinal stress profiles are displayed in figures 6.12 (a,b,c). Figure 6.13 shows the heat flux ($q$) profile for 13-moment model, 14-moment model and N-S model and the fourth order contracted moment profile for 14-moment model. It is seen that the difference between the heat flux profiles obtained from the 13-moment and 14-moment models increases with increasing Mach number - this is evident from a comparison between Fig. 6.10 and Fig. 6.13.

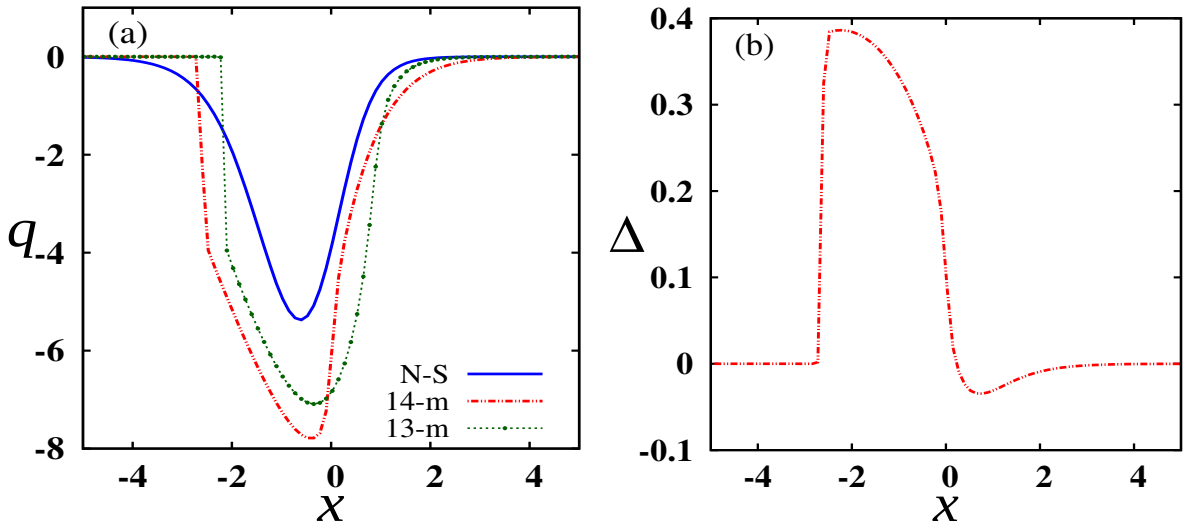


Figure 6.13: Heat flux and the fourth order contracted moment profiles from moment models and Navier-Stokes model for the upstream Mach number of 3.

### 6.2.2 Effect of Mach number (Ma) on peak values of higher-order field variables

First we discuss about the variation of maximum value of skew temperature $\theta_s^{max}$ as we increase the Mach number from 1.2 to 3: refer to Fig. 6.3 (b), Fig. 6.6 (b), Fig. 6.9 (b) and Fig. 6.12 (b). Figure 6.14 shows the variation of $\theta_s^{max}$ with upstream Mach number $\mathrm{Ma}_1$ as predicted by the 10-moment, 13-moment and 14-moment models and the N-S model. From this figure, we find that the maximum value of skew temperature increases with increasing Mach number ($\mathrm{Ma}_1$). We also infer that, for $\mathrm{Ma}_1 < 1.2$, all moment models and N-S model seem to predict the same maximum value for the skew temperature and as we further increase the Mach number, the 10-moment model predicts a large value for $\theta_s^{max}$; there is a good qualitative agreement for $\theta_s^{max}$ obtained from the heat transfer predicting models 13-moment, 14-moment and Navier-Stokes models.

Secondly we discuss the effect of increasing Mach number on the maximum values of the modulus of heat flux $|q|^{max}$. We know that, the 10-moment model can not predict the heat flux effects and hence the predictions for $|q|^{max}$ from 13-moment and 14-moment models along with the N-S model are presented in Fig. 6.15. Like the maximum value of scalar temperature, $|q|^{max}$ also increases with increasing Mach number. From this figure one can find a close agreement between all models up to a Mach number of around 1.5, but from Mach number 1.5 to 3 there is a small disagreement between the moment models and the N-S solutions. In particular, $|q|_{13}^{max} > |q|_{14}^{max} > |q|_{NS}^{max}$ for $\mathrm{Ma}_1 \leq 1.5$ and $|q|_{14}^{max} > |q|_{13}^{max} > |q|_{NS}^{max}$ for $\mathrm{Ma}_1 > 1.5$ (see Fig. 6.4 (a), Fig. 6.7 (a), Fig. 6.10 (a) and Fig. 6.13 (a)).

Finally we discuss about the variation of the maximum value of the fully-contracted fourth-order moment ($\Delta = \frac{1}{15\,\rho\,\theta^2}(R - R^{eq})$) when we increase the Mach number from 1 to 3. The 10-moment, 13-moment and N-S systems do not include the fully-contracted fourth-order moment; only the 14-moment system incorporates $\Delta$ as a separate field variable. Figure 6.16 shows how this quantity changes when Mach number is varied. It is evident that the maximum value of $|\Delta|$

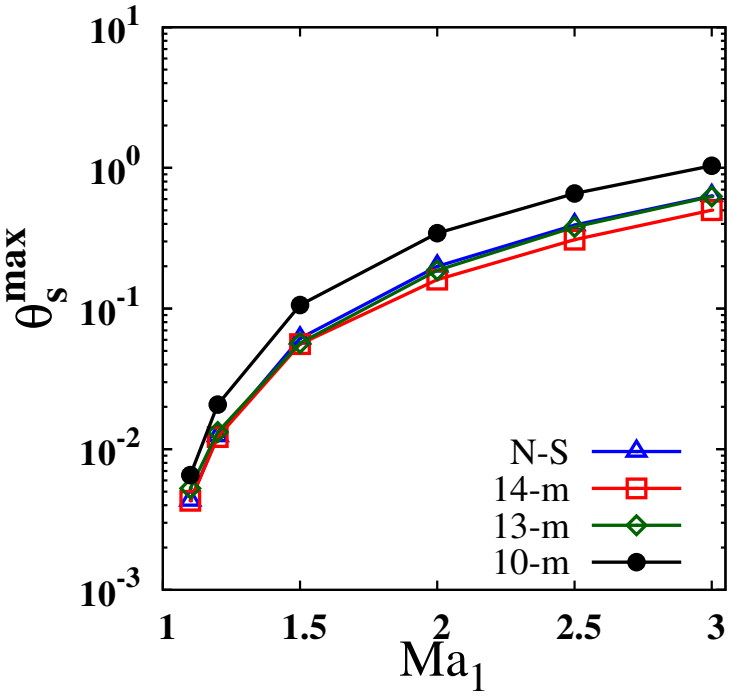


Figure 6.14: Maximum values of skew temperature profiles with varying Mach numbers.

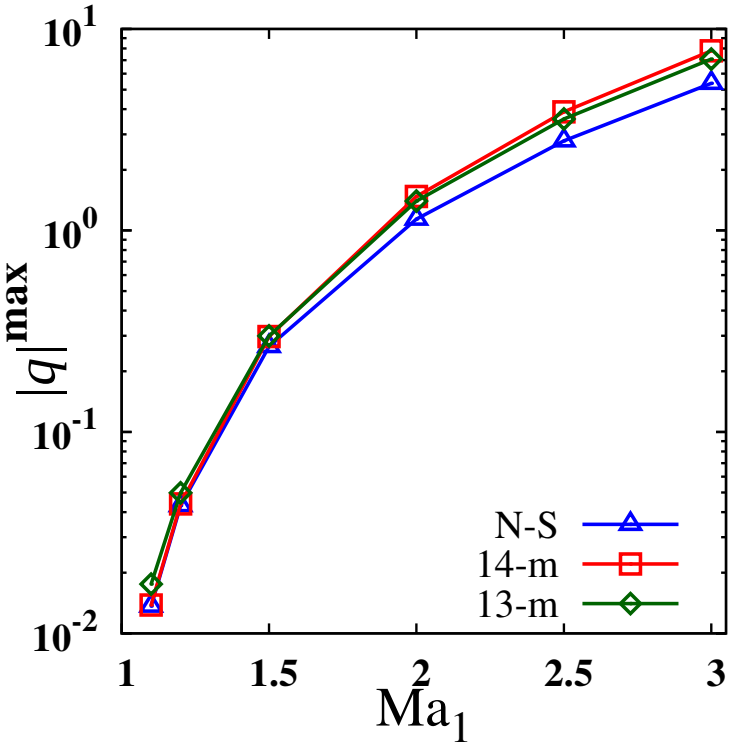


Figure 6.15: Maximum values of modulus of heat flux profiles for varying Mach numbers.

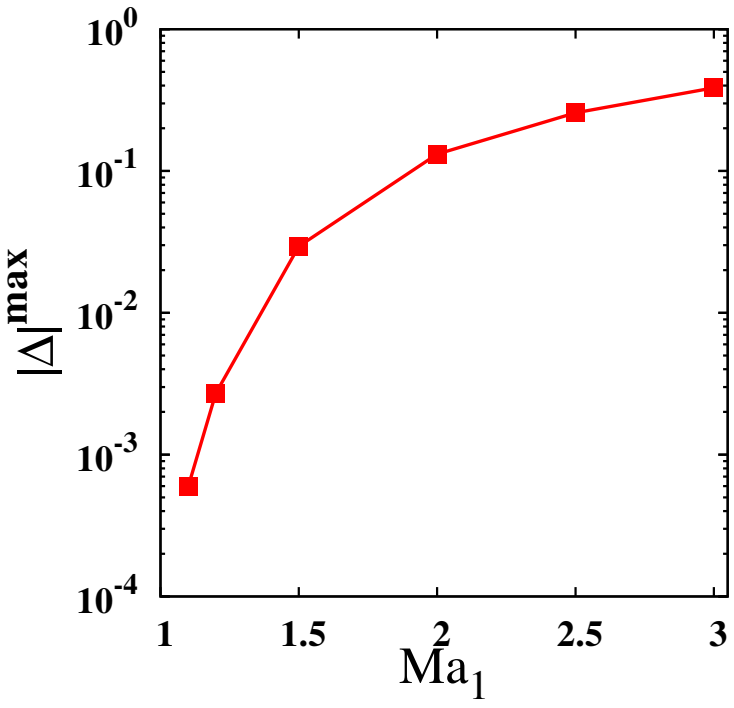


Figure 6.16: Maximum of the contracted fourth order moment profiles for varying Mach numbers.

increases with increasing Mach number. Collectively, figures 6.14, 6.15 and 6.16 suggest that the difference between the predictions of 14-moment model and 13-moment model is primarily due to the presence of an additional hydrodynamic field, $\Delta$, in the former.

### 6.2.3 Structure of shock waves: shock width and its asymmetry

Here we discuss about two important parameters namely, the shock thickness (width) and the shock asymmetry, which are often used to characterize the shock wave properties instead of comparing shock wave profiles. The usual shock width or shock thickness [Gilbarg & Paolucci (1953); Pham-Van-Diep *et al.* (1991); Torrilhon & Struchtrup (2004)] is defined as

$$\delta_1 = \frac{\rho_2 - \rho_1}{\max(\partial\rho/\partial x)}, \tag{6.14}$$

which is same as in Eq.(3.46). Note that $\delta_1$ has a linear dependence on the density difference between the upstream and downstream ends and a slope corresponding to the maximum density gradient and the schematic picture of the definition of the shock width is shown in Fig. 3.5(a). This definition of shock width is not appropriate for extended hydrodynamic models when $\mathrm{Ma}_1 > \mathrm{Ma}_{cr}$ for which the shock profiles are discontinuous. So we consider another definition of shock width as follows:

$$\delta_2 = x(88\%\rho) - x(12\%\rho) \tag{6.15}$$

and is used when $\mathrm{Ma}_1 > \mathrm{Ma}_{cr}$. When $\mathrm{Ma}_1 < \mathrm{Ma}_{cr}$, two definitions of shock width Eqs. (6.14) and (6.15) yield approximately the same value, i.e.,$\delta_1 \approxeq \delta_2$. A comparison between these two definitions of shock width is shown in Fig. 6.17 based on the 13-moment model. One can see a

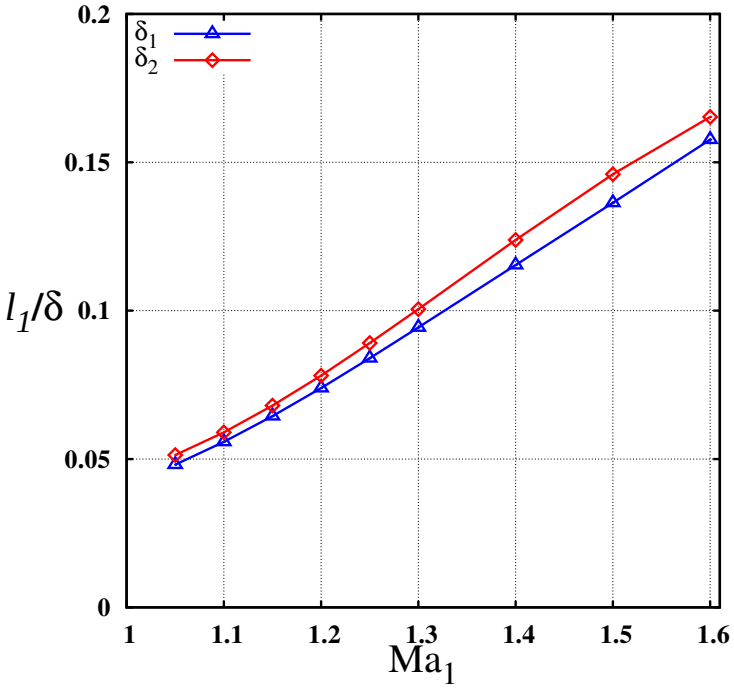


Figure 6.17: Comparison of shock width definitions [$\delta_1$ and $\delta_2$] Eqs.6.14 and 6.15 for the 13-moment model.

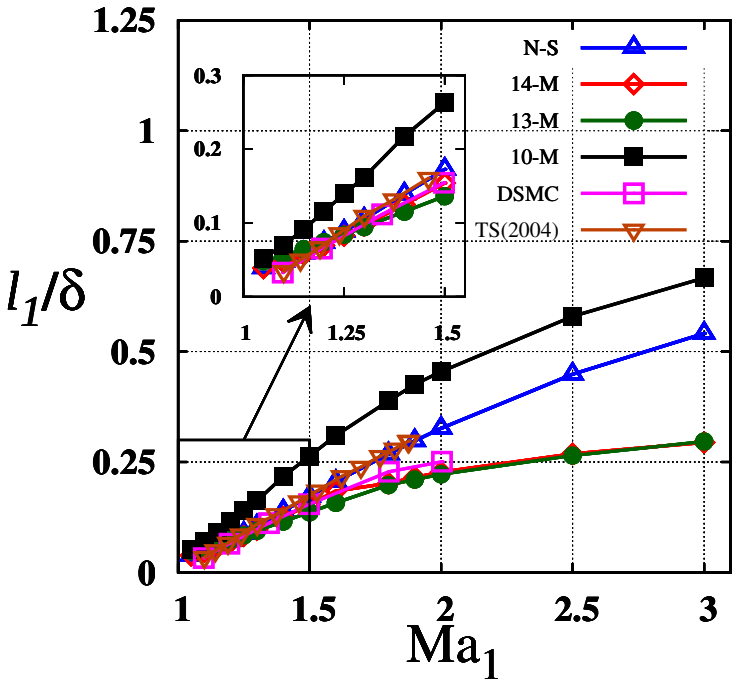


Figure 6.18: Inverse shock width vs upstream Mach number.

close agreement between the two definitions of shock width over a range of Mach number.

Usually the shock width is related to the upstream mean free path ($l_1$) and hence the inverse of shock width ($l_1/\delta$) is plotted in figure 6.18. Shock structure calculations are done for upstream Mach numbers of 1.05, 1.1, 1.15, 1.2, 1.25, 1.3, 1.4, 1.5, 1.6, 1.8, 1.9, 2, 2.25, 2.5, 3.0, 3.25, 3.45, 3.5, 4.0, 4.5 and 5.0 in order to show the change of shock thickness over Mach numbers, see table 6.1. The results of shock thickness are compared between the moment models, Navier-Stokes model and with the DSMC calculations: the DSMC results are taken from Torrilhon et al. (2004). Figure 6.18 shows variation of the inverse shock width for moment models and Navier-Stokes model along with DSMC results. It is seen that up to a Mach number $\approxeq$ 1.5, the results from 13-moment and 14-moment models and N-S model agree well with the DSMC results. But the predictions of 10-moment model disagree with the other models. The 14-moment results agree well with the DSMC results. The above comparison indicates the clear advantage of higher order models, like 13-moment and 14-moment models, over the 10-moment and Navier-Stokes models.

Table 6.1: Shock width vs Mach number

| $Ma_1$ | Inverse shock width ($l_1/\delta$) | | | |
|---|---|---|---|---|
| | 10-moment | 13-moment | 14-moment | N-S |
| 1.05 | 0.0523634 | 0.0481061 | 0.038683 | 0.0390735 |
| 1.1 | 0.0698972 | 0.0557781 | 0.0469007 | 0.0478085 |
| 1.15 | 0.0915001 | 0.0644482 | 0.0573205 | 0.0592405 |
| 1.2 | 0.115295 | 0.0739303 | 0.0695038 | 0.0730199 |
| 1.25 | 0.139207 | 0.0839853 | 0.0828064 | 0.0885076 |
| 1.3 | 0.162009 | 0.0943637 | 0.096658 | 0.105 |
| 1.4 | 0.217391 | 0.115369 | 0.12498 | 0.13896 |
| 1.5 | 0.263158 | 0.136349 | 0.154095 | 0.17268 |
| 1.6 | 0.310078 | 0.157666 | 0.184257 | 0.205598 |
| 1.8 | 0.38835 | 0.19802 | 0.20202 | 0.268374 |
| 1.9 | 0.425532 | 0.210526 | 0.215054 | 0.298009 |
| 2.0 | 0.454545 | 0.222222 | 0.227273 | 0.326368 |
| 2.25 | 0.52632 | 0.245399 | 0.251572 | 0.391575 |
| 2.5 | 0.57971 | 0.264901 | 0.268456 | 0.448679 |
| 3.0 | 0.666667 | 0.296296 | 0.294118 | 0.541148 |
| 3.25 | 0.689655 | 0.305344 | 0.30303 | 0.578135 |
| 3.45 | 0.701754 | 0.314961 | — | 0.604205 |
| 3.5 | 0.701754 | — | — | 0.610253 |
| 4.0 | 0.754717 | — | — | 0.661952 |
| 4.5 | 0.769231 | — | — | 0.701641 |
| 5.0 | 0.8 | — | — | 0.732221 |

Recall from §5.4 that the hyperbolic moment equations do not yield continuous shock structures if the Mach number exceeds its highest characteristic velocity [Weiss (1995); Ruggeri (1993); Struchtrup (2005*b*); Grad (1952)]. For example, the 13-moment model fails to predict continuous shock structure beyond the Mach number $Ma_1 = 1.65$, since at this Mach number they suffer from a subshock in front of the shock [Grad (1949, 1952, 1958)]. It may be noted from Table 6.1 that 13-moment model fails to describe the shock structure if the upstream Mach

number $\mathrm{Ma}_1$ exceeds $\approx 3.5$ this happens because of the first subshock that appears at a Mach number $\mathrm{Ma}_1 = 1.65$ which grows with increasing Mach number and the second subshock appears in the middle of the shock for a Mach number $\mathrm{Ma}_1 \approx 3.5$ [Torrilhon (2000); Struchtrup (2005*b*)]. In the same way we found that the 14-moment model also fails to describe the shock structure if the Mach number is approximately greater than 3.4, see Table 6.1.

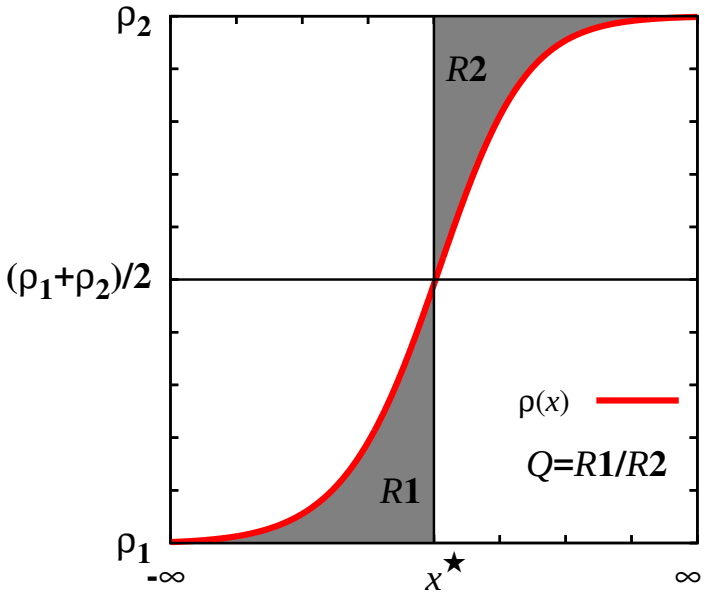


Figure 6.19: Schematic picture of the definition of shock asymmetry $Q$: the red curve indicates the density profile and $x^\star$ is the position at which the density is equal to the average of upstream and downstream density. The ratio of the areas of regions R1 and R2 defines the asymmetry of the shock wave profile for density.

The second important quantity, the shock asymmetry, gives more information about the shape of the shock wave profile. The schematic picture of the definition of the shock asymmetry is depicted in Fig. 6.19. The shock asymmetry of the density profile is defined as

$$Q = \frac{\int_{-\infty}^{x^\star}(\rho(x)-\rho_1)dx}{\int_{x^\star}^{\infty}(\rho_2-\rho(x))dx} = \frac{area(R1)}{area(R2)}, \tag{6.16}$$

where $x^\star$ satisfies the relation $\rho(x^\star) = (\rho_1+\rho_2)/2$. The shock asymmetry results for hard spheres obtained by DSMC simulations from Pham-Van-Diep et al. (1991) and Torrilhon et al. (2004) are presented in Fig. 6.20. This figure also shows the results of the N-S model and all moment models discussed in this chapter. From this figure it is evident that none of them exhibit a good agreement with the DSMC results. For realistic shock waves the value of asymmetry is approximately equal to unity, which means that the measured profiles are almost symmetric. The DSMC results for hard spheres tend to predict a smaller asymmetry value($Q < 1$) which is a clear contradiction. The results of N-S model predict an asymmetry value of more than unity for $\mathrm{Ma}_1 > 1$. The results of 13-moment and 14-moment models predict an asymmetry value of approximately around unity for $\mathrm{Ma}_1 < 1.4$, which is realistic and for $\mathrm{Ma}_1 > 1.4$ these models also indicate a qualitative failure like Navier-Stokes model. In contrast, the 10-moment model predicts $Q < 1$ for all $\mathrm{Ma}_1$ and shows a decreasing $Q$ with increasing $\mathrm{Ma}_1$. Therefore, the results

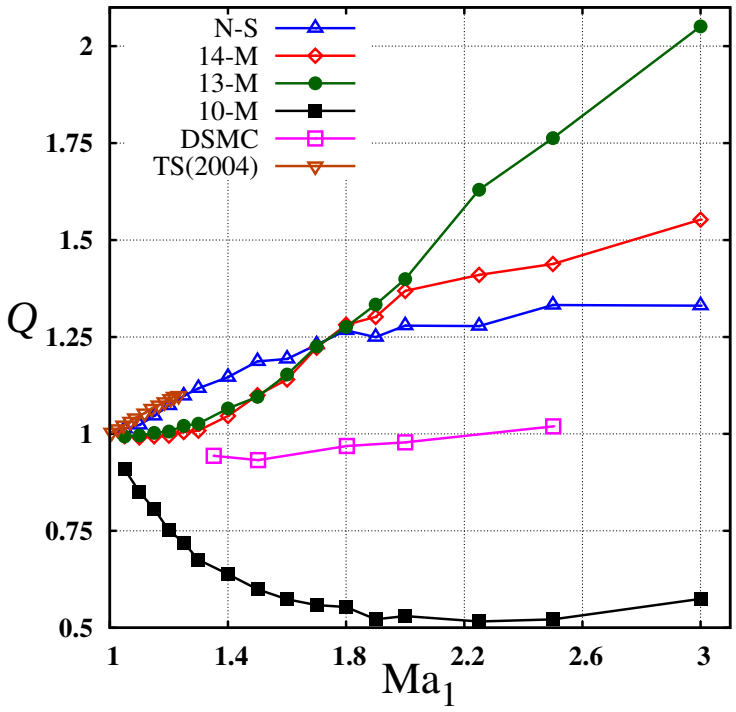


Figure 6.20: Shock asymmetry vs upstream Mach number.

of 10-moment model for $Q$ disagrees with DSMC results as well as with other models discussed here.

## 6.3 Shock Wave Structure in a Granular Gas

To study the early time dynamics of shock wave structures in a dilute granular gas, we consider one-dimensional domain of length $L = 100$ covering $(-50, 50)$, filled with a dilute granular gas of two different homogeneous cooling states at left and right, namely, upstream and downstream, respectively, with the shock being positioned at $x = 0$. The upstream boundary conditions for a dilute granular gas are taken as

$$\rho_1 = 1, \quad u_1 = \mathrm{Ma}_1 \sqrt{\gamma}, \quad \theta_1 = 1, \quad \theta_{s1} = 0 = q_1, \quad \Delta_1 = \frac{16(1-2\alpha^2)(1-\alpha)}{30\alpha^2(1-\alpha)+81-17\alpha} = \Delta_2, \tag{6.17}$$

while the downstream boundary conditions are provided by RH relations (3.11). The shock wave is located at $x = 0$ and propagates to the right(downstream) as time progresses. The numerical computations are performed using the numerical schemes which were discussed in §3.5 and by taking 4000 grid points, with a CFL number($\mathcal{C}$) of 0.1 for all moment models, while for Navier-Stokes model the CFL number($\mathcal{C}$) was taken as 0.01.

To ascertain the difference between granular and molecular shock structures, first we present the results of the Riemann-problem for a restitution coefficient of $\alpha = 0.99$, which corresponds to a nearly elastic system. The early time dynamics (up to $t = 10$) of density ($\rho$) obtained from Navier-Stokes model, 13-moment and 14-moment models for this value of the restitution coefficient are presented in Fig. 6.21 (a), (b) and (c), respectively. Fig. 6.22 shows the same

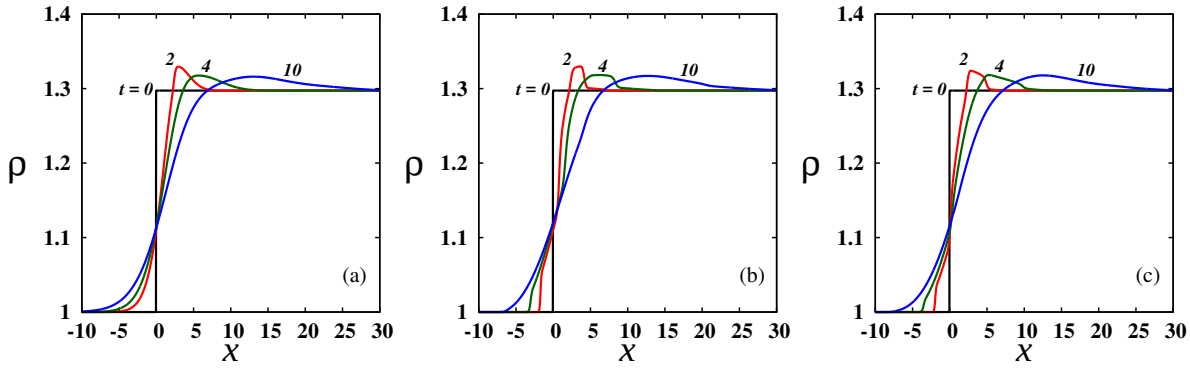


Figure 6.21: The early time evolution of granular density for $\mathrm{Ma}_1 = 1.2$ and the restitution coefficient is $\alpha = 0.99$. (a) Navier-Stokes model, (b) 13-moment model and (c) 14-moment model.

but for a larger time $t = 100$. From these two figures, we find that all models predict the qualitatively same behavior for the density ($\rho$). Comparing all panels of Fig. 6.22, we observe that the density maximum occurs within the "shock layer", which leads to a density overshoot

$$\triangle\rho \equiv (\rho_{\max} - \rho_2). \tag{6.18}$$

The density overshoot is non-zero for a granular gas ($\alpha \neq 1$) and is not present in the case of a molecular gas ($\alpha = 1$). This novel feature is predicted by all models discussed here, and was identified first by Reddy & Alam (2015) as detailed in Chapter 4. Moreover the density peak travels from left to right. Overall Figs. 6.21 and 6.22 confirm that the density overshoot is present even in the nearly elastic limit ($\alpha \approx 1$) and its magnitude increases with time.

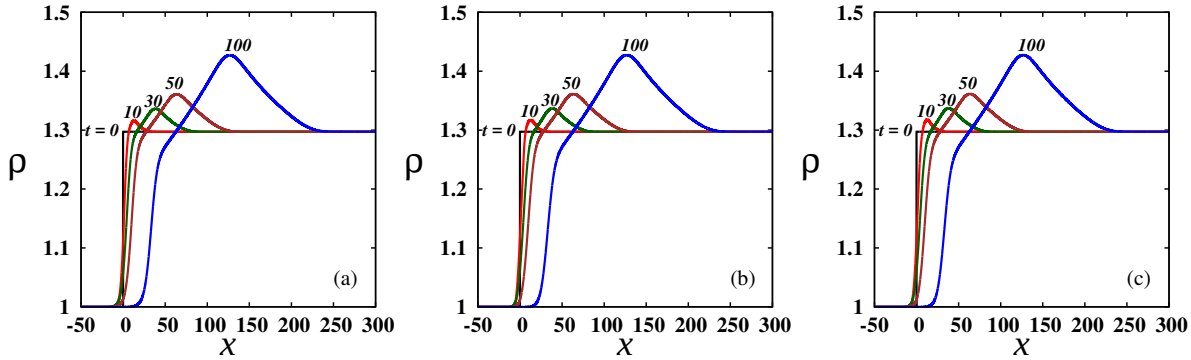


Figure 6.22: The time evolution of granular density for $\mathrm{Ma}_1 = 1.2$ and restitution coefficient is $\alpha = 0.99$, up to a time of $t = 100$. (a) Navier-Stokes model, (b) 13-moment model and (c) 14-moment model.

### 6.3.1 Effects of Mach number and the restitution coefficient on granular shocks

To show the effect of Mach number (Ma) on shock profiles, we present results for two values of the upstream Mach number $\mathrm{Ma}_1 = 1.2$ and $\mathrm{Ma}_1 = 2$ for a restitution coefficient of $\alpha = 0.9$.

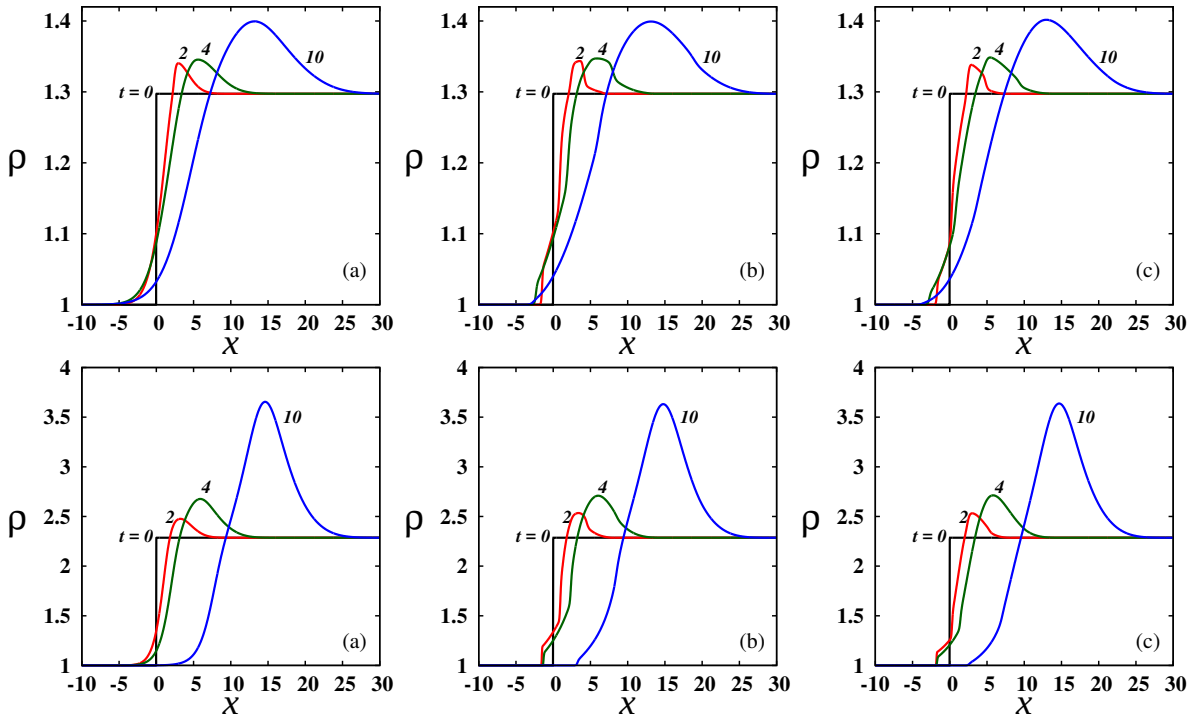


Figure 6.23: The early time evolution of granular density for a restitution coefficient of $\alpha = 0.9$. Top row: $\mathrm{Ma}_1 = 1.2$ and bottom row: $\mathrm{Ma}_1 = 2$, (a) Navier-Stokes model, (b) 13-moment model and (c) 14-moment model.

The results for density are presented in Fig. 6.23 with the top row indicating the results for $\mathrm{Ma}_1 = 1.2$ and the bottom row for $\mathrm{Ma}_1 = 2$, Moreover, the panel (a) displays the solutions of N-S model, panel (b) shows the solutions of 13-moment model and panel (c) shows the solutions of 14-moment model, respectively. All panels of Fig. 6.23 confirm that the density maximum ($\rho_{\max}$) occurs whithin the shock layer and it is moving to right with increasing time. There are some differences between Navier-Stokes model and moment models at $t \sim 0$, but at $t = 10$, the profiles look qualitatively same for all models. We also observe that, the profiles from moment models are not smooth at $t \leq 4$, but at time $t = 10$ all profiles look smooth.

To show the effect of the restitution coefficient on the structure of shock waves in a granular gas, we present the density profiles for $\alpha = 0.7$ in Figs. 6.24 (a), (b) and (c). Panels (a), (b) and (c) indicate the solutions of N-S model, 13-moment model and 14-moment model, respectively. Comparing the top row of Fig. 6.23 and Fig. 6.24, we find that the density maximum increases with the increasing dissipation. Overall, we may conclude from Figs. 6.23 and 6.24 that the density maximum occurs within the shock layer and its magnitude increases with increasing Mach number (Ma) and dissipation.

The early time dynamics of the granular temperature $\theta$ are shown in Fig. 6.25, with the top row representing the results for $\mathrm{Ma}_1 = 1.2$ and the bottom row for $\mathrm{Ma}_1 = 2$. All panels of Fig. 6.25 indicate that both the upstream and downstream temperatures decay with time. It is also evident from Fig. 6.25 that the temperature maximum occurs within the shock layer and the maximum temperature also decays with time.

The time evolution of the velocity profiles are depicted in Fig. 6.26 for the restitution coeffi-

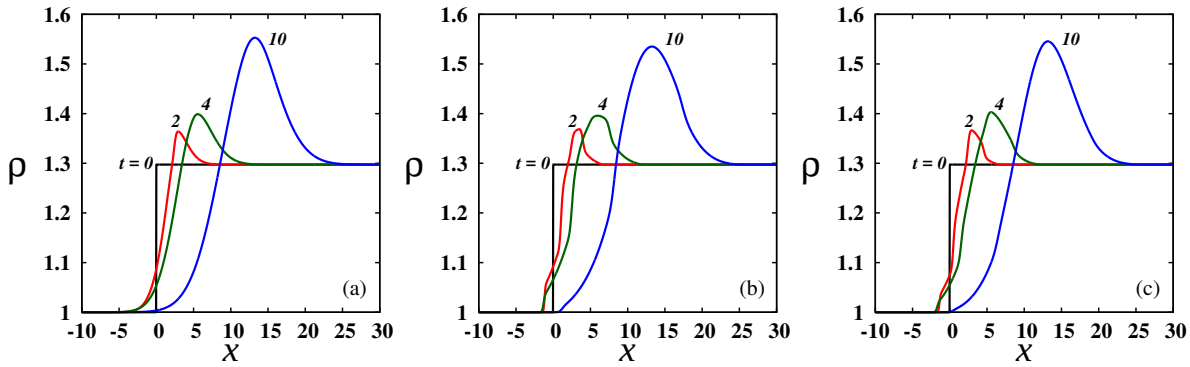


Figure 6.24: The early time evolution of granular density for a restitution coefficient of $\alpha = 0.7$ and $\mathrm{Ma}_1 = 1.2$, (a) Navier-Stokes model, (b) 13-moment model and (c) 14-moment model.

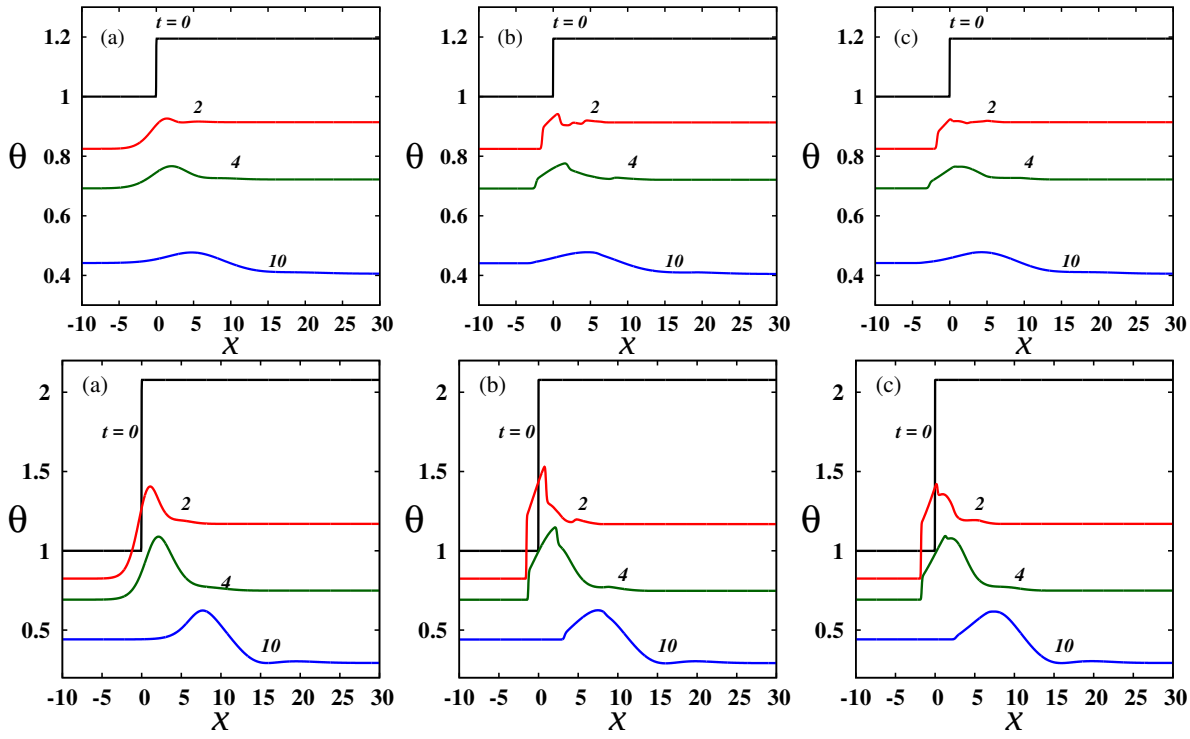


Figure 6.25: The early time evolution of granular temperature for a restitution coefficient of $\alpha = 0.9$. Top row: $\mathrm{Ma}_1 = 1.2$ and bottom row: $\mathrm{Ma}_1 = 2$, (a) Navier-Stokes model, (b) 13-moment model and (c) 14-moment model.

cient of $\alpha = 0.9$ and for Mach numbers of $\mathrm{Ma}_1 = 1.2$ and 2.0, using Navier-Stokes model (panel (a)), 13-moment model (panel (b)) and 14-moment model (panel (c)). All models qualitatively predict the same behavior for the velocity. It is evident from all velocity profiles that the local Mach number is maximum in the upstream reference state and decreases through the shock layer, reaching its minimum value in the down stream state. The velocity profiles at higher Mach numbers ($\mathrm{Ma}_1 = 2.0$) evolve in a similar fashion, see the bottom row of Fig. 6.26.

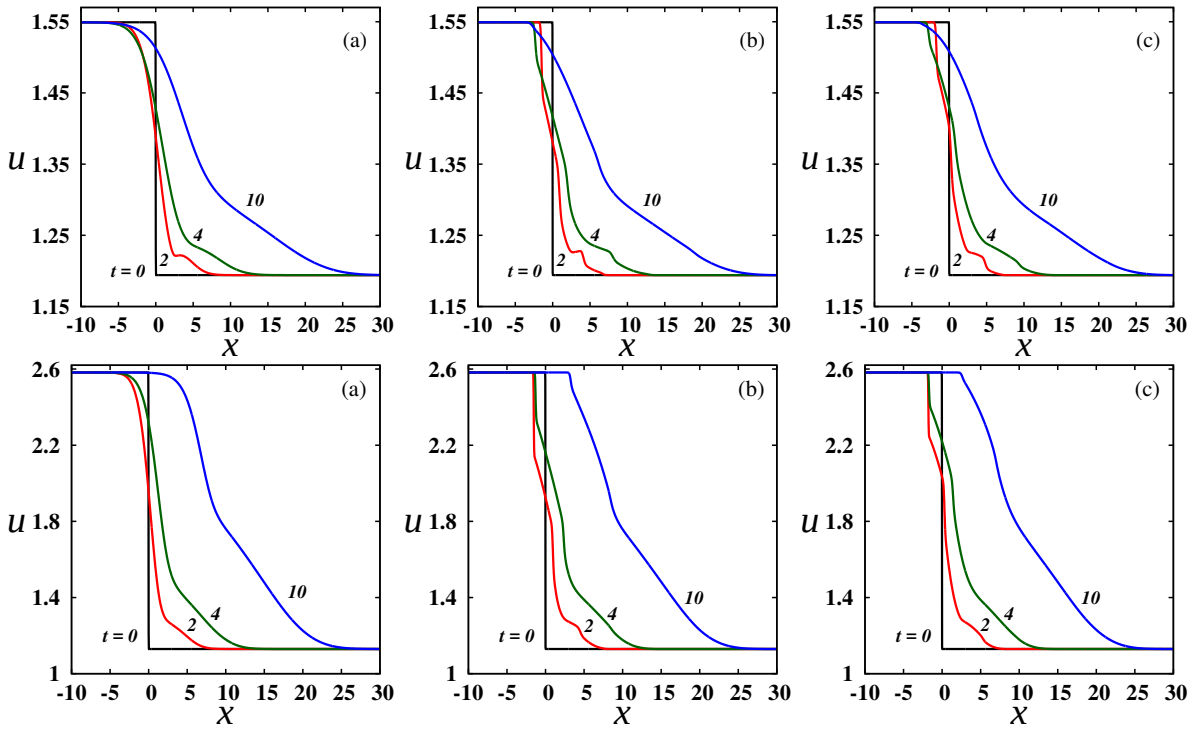


Figure 6.26: The early time evolution of velocity for a restitution coefficient of $\alpha = 0.9$. Top row: $\mathrm{Ma}_1 = 1.2$ and bottom row: $\mathrm{Ma}_1 = 2$, (a) Navier-Stokes model, (b) 13-moment model and (c) 14-moment model.

The early time evolution of the skew temperature ($\theta_s$) profiles are presented in Fig. 6.27 for the restitution coefficient of $\alpha = 0.9$ and for a Mach number of $\mathrm{Ma}_1 = 1.2$, using Navier-Stokes model (panel (a)), 13-moment model (panel (b)) and 14-moment model (panel (c)). The black, red and blue lines in each panel represent the solutions at $t = 2, 4$ and $t = 10$, respectively. From Fig. 6.27, we may conclude that the skew temperature, which is initially zero, attains a maximum value in very short time and there after it decrease with time. Moreover, a two-peak structure is observed in the skew temperature profiles (from moment models) at $t = 2$ and these two peaks are going to merge and form a single peak at time $t = 10$, this is evident from Fig. 6.27. The qualitative nature of the skew temperature profiles at higher Mach numbers ($\mathrm{Ma}_1 = 2.0$) and for the different values of the restitution coefficient remains similar, see the bottom row of Fig. 6.27.

The early time dynamics of the granular heat flux profiles are depicted in Fig. 6.28 for a restitution coefficient of $\alpha = 0.9$ and for a two different Mach number of $\mathrm{Ma}_1 = 1.2$ (top row panels) and $\mathrm{Ma}_1 = 2$ (bottom row panels), using Navier-Stokes model (panel (a)), 13-moment model (panel (b)) and 14-moment model (panel (c)) with the black, red and blue lines indicating

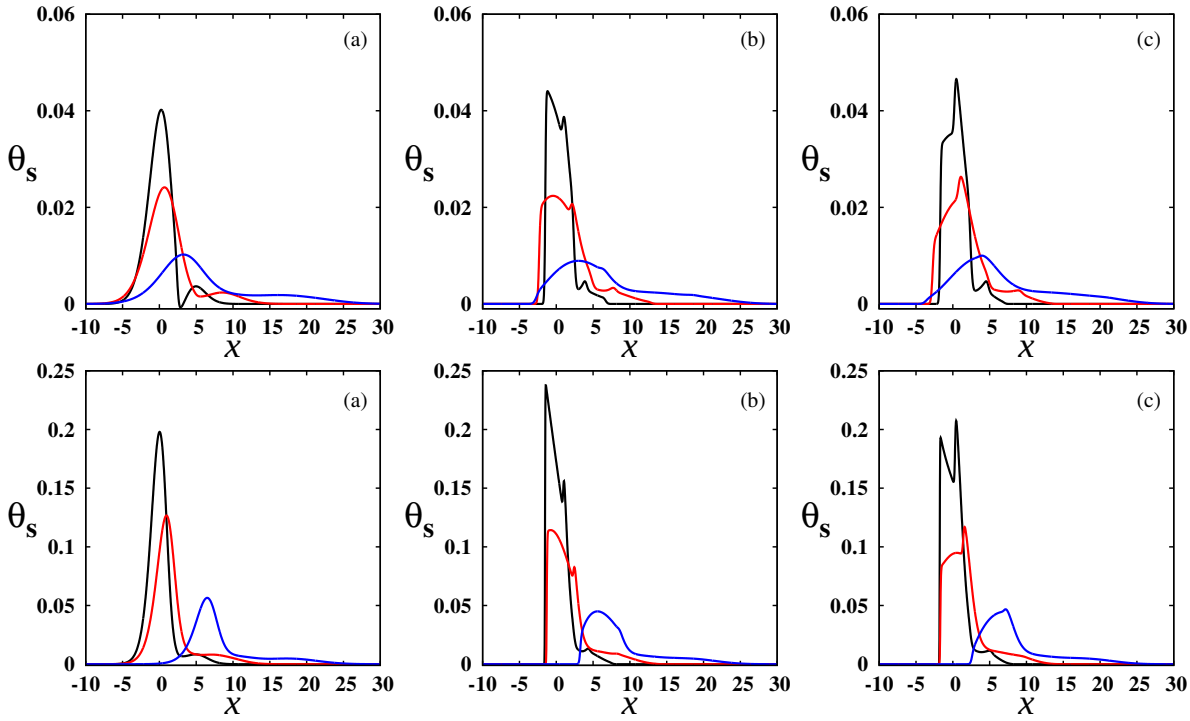


Figure 6.27: The early time evolution of the skew temperature ($\theta_s$) for a restitution coefficient of $\alpha = 0.9$. Top row: $\mathrm{Ma}_1 = 1.2$ and bottom row: $\mathrm{Ma}_1 = 2$, (a) Navier-Stokes model, (b) 13-moment model and (c) 14-moment model. In each panel black, red and blue lines indicates the solutions at $t = 2, 4$ and $t = 10$, respectively.

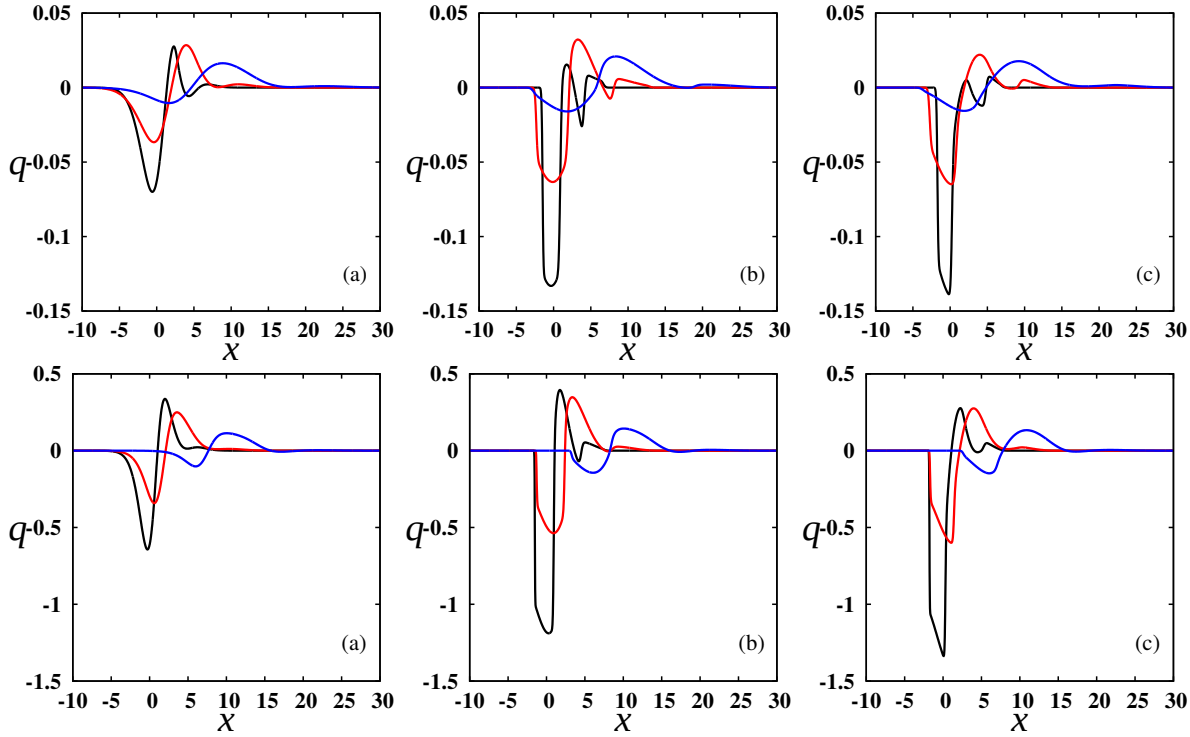


Figure 6.28: The early time dynamics of the granular heat flux ($q$) for a restitution coefficient of $\alpha = 0.9$. Top row: $\mathrm{Ma}_1 = 1.2$ and bottom row: $\mathrm{Ma}_1 = 2$, (a) Navier-Stokes model, (b) 13-moment model and (c) 14-moment model. In each panel black, red and blue lines indicate the solutions at $t = 2, 4$ and $t = 10$, respectively.

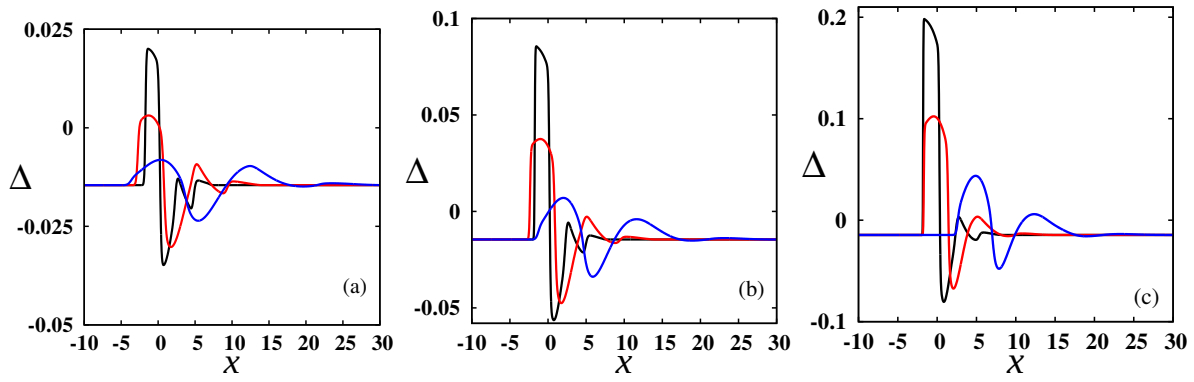


Figure 6.29: The time evolution of the fourth order fully contracted moment ($\Delta$) for the restitution coefficient of $\alpha = 0.9$ with panel (a) indicates the solutions for $\mathrm{Ma}_1 = 1.2$, panel (b) for $\mathrm{Ma}_1 = 1.5$ and panel (c) for $\mathrm{Ma}_1 = 2$. Coloured lines namely black, red and blue in each panel indicate the solutions at $t = 2, 4$ and $t = 10$, respectively.

the solutions at $t = 2, 4$ and $t = 10$, respectively. It seems that the granular heat flux which is initially zero at both upstream and downstream ends, approaches a negative value within the shock layer at very early times and the magnitude of this minimum decreases with time, which is evident from Fig. 6.28. We observe that the heat flux profiles predicted by Navier-Stokes model and extended hydrodynamic models are qualitatively similar at time $t = 10$, but some differences can be found between moment models and Navier-Stokes model at initial times. We also note that the absolute of minimum value of granular heat flux increases with increasing Mach number ($\mathrm{Ma}_1$) which is clear from the bottom panels of Fig. 6.28.

The time evolution of the fourth order moment ($\Delta$) is presented in Fig. 6.29 (a,b,c) for a restitution coefficient of $\alpha = 0.9$ for three Mach numbers $\mathrm{Ma}_1 = 1.2$ (panel(a)), $\mathrm{Ma}_1 = 1.5$ (panel(b)), and $\mathrm{Ma}_1 = 2$ (panel(c)), respectively. We observe that the the fourth order moment ($\Delta$), which has an initial value $\Delta_1 = \Delta_2 \approx -0.01456$, reaches its maximum value at an early time and its maximum decreases with time. We also observe that the magnitude of the fourth order moment increases with increasing Mach number ($\mathrm{Ma}_1$).

### 6.3.2 Density overshoot and its characterization

The density overshoot, ($\triangle\rho \equiv (\rho_{\max} - \rho_2)$), which is defined in Eq. (6.18) and its behavior was presented in chapter 4 from Euler and Navier-Stokes models. Here we present its temporal evolution using moment models and compare it with the predictions of Navier-Stokes model. The time evolution of $\triangle\rho$ is depicted in Fig. 6.30 (a,b,c). The evolution of $\triangle\rho$ with time, for an upstream Mach number of $\mathrm{Ma}_1 = 1.2$ and the restitution coefficients of $\alpha = 0.9, 0.7$ are shown in Fig. 6.30 (a),(b) respectively, whereas Fig. 6.30 (c) shows the same for an upstream Mach number of $\mathrm{Ma}_1 = 2$ and a restitution coefficient of $\alpha = 0.9$. From Fig. 6.30, we find that $\triangle\rho > 0$ in a granular gas and its magnitude increases with time (but $\triangle\rho = 0$ for a molecular gas), which is predicted by all models discussed here. It is noteworthy that

$$(\triangle\rho)_{14m} \approx (\triangle\rho)_{13m} < (\triangle\rho)_{NS} \leq (\triangle\rho)_{10m}, \tag{6.19}$$

except for very short early times. It is evident from Fig. 6.30 (a,b,c) that the magnitude of $\triangle\rho$ increases with increasing Mach number and the dissipation (i.e. with decreasing $\alpha$).

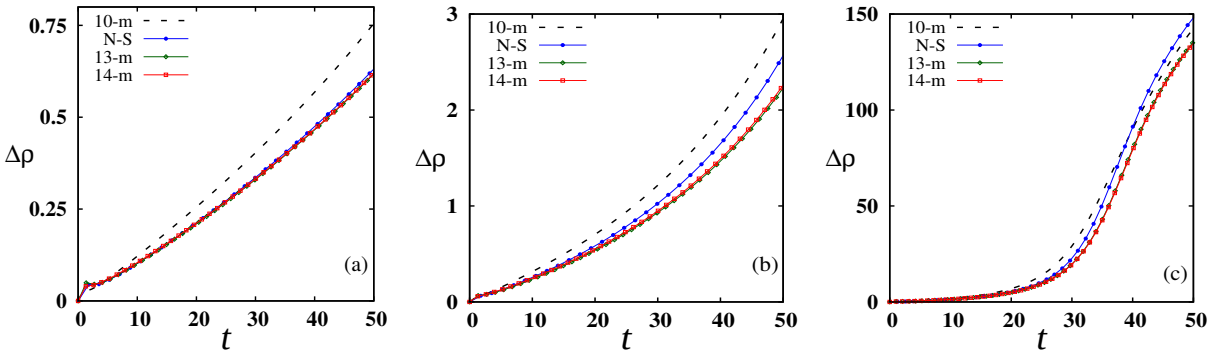


Figure 6.30: The temporal evolution of the density overshoot, ($\triangle\rho \equiv (\rho_{\max} - \rho_2)$). Panel (a) represents the evolution of $\triangle\rho$, for $\mathrm{Ma}_1 = 1.2$ and $\alpha = 0.9$. Panel (b) and panel (c) represents the same as panel (a), but for $\mathrm{Ma}_1 = 1.2$, $\alpha = 0.7$ and for $\mathrm{Ma}_1 = 2$ and $\alpha = 0.9$, respectively.

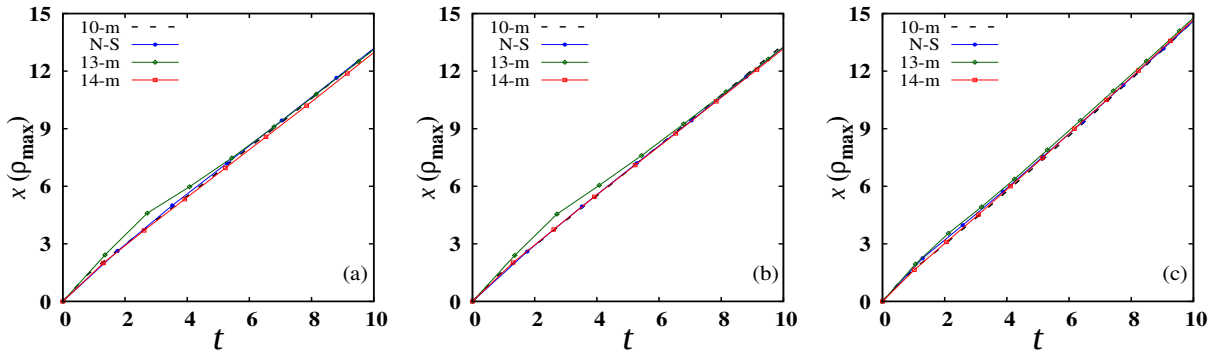


Figure 6.31: The temporal evolution of the spatial location of $\rho_{\max}$. Panel (a) represents the evolution of $\rho_{\max}$, for $\mathrm{Ma}_1 = 1.2$ and $\alpha = 0.9$. Panel (b) and panel (c) represents the same as panel (a), but for $\mathrm{Ma}_1 = 1.2$, $\alpha = 0.7$ and for $\mathrm{Ma}_1 = 2$ and $\alpha = 0.9$, respectively.

Figures 6.31 (a,b,c) confirm that the spatial location of $\rho_{max}$ is shifting to the right with time, from which one can estimate the shock speed. The normalized speed of density maximum is defined as

$$\tilde{v}_s = \frac{v_s}{c}, \tag{6.20}$$

where $c$ is the adiabatic sound speed (see Eq. 3.10). Its temporal evolution is presented in Fig. 6.32 (a,b,c). It is observed that the normalized shock speed, $\tilde{v}_s$, approaches a steady asymptotic value at long times, which is well predicted by all models. Comparing the main panels with the insets of Fig. 6.32 (a,b), we may conclude that the normalized shock speed $\tilde{v}_s$ has a weak dependence on the restitution coefficient. Moreover comparing the main panels of Fig. 6.32 (a,b) with the main and inset panels of Fig. 6.32 (c), we find that the normalized shock speed $\tilde{v}_s$ increases with the upstream Mach number ($\mathrm{Ma}_1$). Overall, we may conclude that all moment models predict the same normalized shock speed,

$$(\tilde{v}_s)_{14m} \approx (\tilde{v}_s)_{13m} \approx (\tilde{v}_s)_{10m} \approx (\tilde{v}_s)_{NS} \approx (\tilde{v}_s)_{Euler}, \tag{6.21}$$

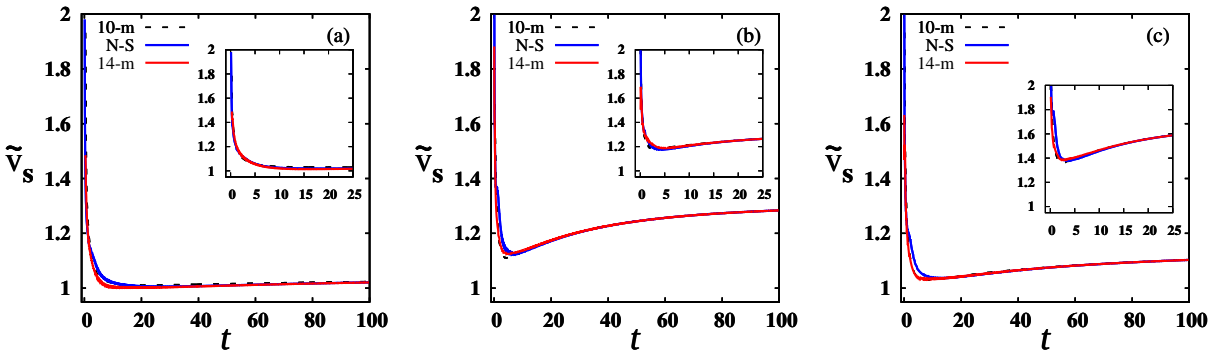


Figure 6.32: Evolution of normalized shock speed, $\tilde{v}_s = v_s/c$, where $v_s$ is the speed of the density-peak and $c = \sqrt{\gamma\theta_1(0)}$ is the adiabatic sound speed. Panel (a) indicates the evolution of $\tilde{v}_s$, for $\alpha = 0.9$ (main panel) and $\alpha = 0.7$ (inset) with $\mathrm{Ma}_1 = 1.2$. Panel (b) indicates the same as in panel (a) but for $\mathrm{Ma}_1 = 2$ and panel (c) indicates the evolution of $\tilde{v}_s$, for $\mathrm{Ma}_1 = 1.5$ (main panel) and $\mathrm{Ma}_1 = 3$ (inset) with $\alpha = 0.9$.

which means that the density peak travels with a steady constant speed at sufficiently late times.

### 6.3.3 Comparison of temperature decay with Haff's law

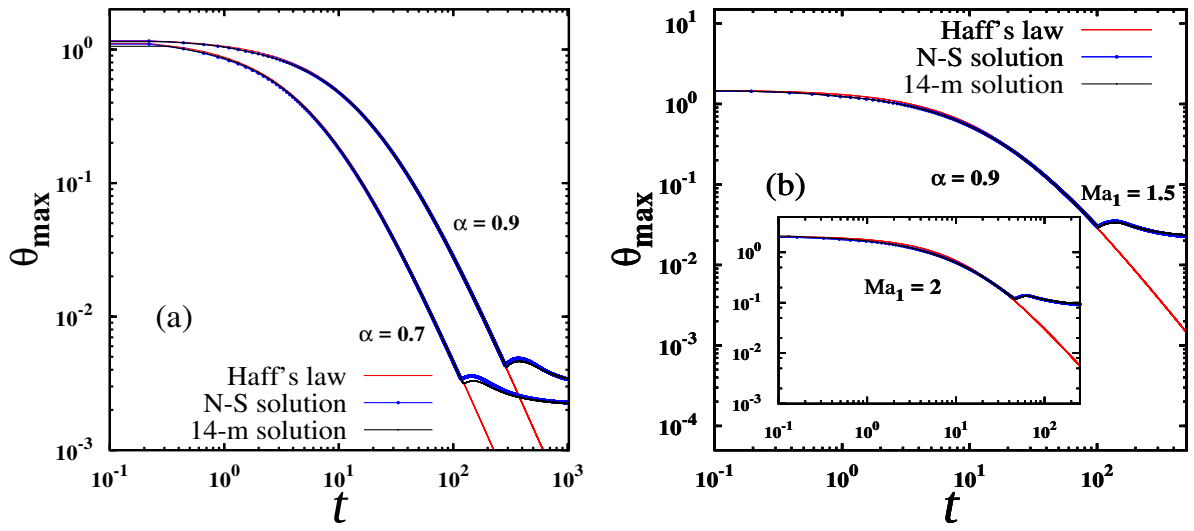


Figure 6.33: Temporal evolution of the maximum granular temperature $\theta_{max}$: (a) for $\mathrm{Ma}_1 = 1.2$,; the main panel of (b) for $\mathrm{Ma}_1 = 1.5$ and the inset for $\mathrm{Ma}_1 = 2$. The red curve in each panel represents Haff's law, blue and black curves represents numerical solutions from N-S model and 14-moment model, respectively.

We recall from Fig. 6.25 that the temperature maximum ($\theta_{max}$) occurs within the shock layer and it decays as time progresses. The predictions of 14-moment model and N-S model for the temporal evolution of $\theta_{max}$ are shown in Fig. 6.33 (a) for a Mach number of $\mathrm{Ma}_1 = 1.2$ with $\alpha = 0.9$ (upper curves) and 0.7 (lower curves). Figure 6.33 (b) shows the same but for the Mach number of $\mathrm{Ma}_1 = 1.5$ with $\alpha = 0.9$ (main panel) and for the Mach number of $\mathrm{Ma}_1 = 2$ with $\alpha = 0.9$ (inset). The red line denotes the Haff's law, Eq. (5.80), which is superimposed with the numerical solutions of 14-moment and N-S model. Surprisingly the maximum temperature

($\theta_{max}$) seems to follow Haff's law up to a critical time [$t_c$, defined in Eq. 4.22] for weak shock ($\mathrm{Ma}_1 = 1.2$), but thereafter it decays much slower compared to Haff's law. For strong shocks, $\theta_{max}$ decays faster than Haff's law for $t < t_c$ and much slower than Haff's law for $t > t_c$. From Fig. 6.33 (a,b), we conclude that 14-moment model and other moment models approximately predicts the same critical time ($t_c$) for all Mach numbers and the restitution coefficients, and the critical time decreases with increasing inelasticity $(1-\alpha)$ and upstream Mach number $\mathrm{Ma}_1$.

## 6.4 Summary: Predictions of Extended Hydrodynamic Models

We presented shock structure solutions in a molecular gas as well as in a dilute granular gas by solving the extended hydrodynamic equations, in particular, 10-moment, 13-moment, 14-moment equations along with Navier-Stokes equations for hard spheres. For both molecular and granular shock waves, the results on the density, the temperature, the skew temperature, the heat flux and the fourth moment are compared among these models. The extended hydrodynamic equations yield steady smooth shock solutions up to a critical Mach number ($\mathrm{Ma}_{cr}$) as elaborated in §5.3. For shock wave results in a molecular gas, the agreement for the shock solutions of the moment equations, namely, 13-moment and 14-moment equations, is better than those predicted by Navier-Stokes equations. The results show reliable qualitative and quantitative agreement with DSMC simulations for Mach numbers up to $\mathrm{Ma} \approx 2.0$ [see Fig. 6.18]. It is noted that for Mach numbers $\mathrm{Ma} \approx 1.3$, the shock width described by Navier-Stokes, the 13-moment and 14-moment equations are within the DSMC computational scatter, whereas the shock width described by the 10-moment equations is in poor agreement with DSMC data. For Mach numbers $\mathrm{Ma} > 1.3$, the 13-moment and 14-moment model predictions are more accurate than those of Navier-Stokes model.

For shock waves in a granular gas, we observed a density overshoot which is not present in the case of a molecular gas, and every model predicts this feature. Among all models presented here, the 14-moment model predicts a lesser density overshoot [Eq. (6.19)]. We also found that at sufficiently late times the density peaks travels with a steady constant speed. Interestingly, all models predict the same asymptotic value for the normalized shock speed. It is shown that the maximum temperature within the shock-layer follows the Haff's law up to a critical time and decays much slower for $t > t_c$. Different moment models do not seem to have any noticeable effect on the magnitude of the critical time for given control parameters.

# Chapter 7

# Regularized Moment Equations for a Granular Gas

## 7.1 Introduction

In Chapter 6, we presented shock wave solutions for both molecular and granular gases using 10-,13-, and 14-moment models. It was shown that the shock profiles predicted by all moment models are discontinuous when the Mach number is larger than the respective $\mathrm{Ma}_{cr}$ as discussed in §5.4. The smooth shock solutions can be obtained if the moment equations are made parabolic via some regularization technique [(Struchtrup 2004)].

In this chapter we present a detailed derivation of "regularized" moment equations for a dilute granular gas. To regularize the 14-moment equations and the 10-moment equations for inelastic hard-spheres we adopt the order-of-magnitude method of Struchtrup (2004). We also show that Navier-Stokes hydrodynamic model can be obtained by regularizing the Euler model. Finally, to show the difference between moment model and "regularized" moment model, we apply the R10-moment model to plane shock wave problem and the results are compared with the 10-moment model.

## 7.2 An Overview of the Order-of-Magnitude Method

The order-of magnitude method introduced by Struchtrup (2004) gives a new solution for the closure problem in kinetic theory of gases for the infinite set of moment system obtained from the Boltzmann equation. This means that the problem of solving the Boltzmann equation is moved to moment space from the phase space [(Struchtrup 2004)]. The order-of magnitude method of Struchtrup is motivated from the "consistent-order extended thermodynamics" (COET) of Müller *et al.* (2003). This method consists of three basic steps which are given [(Struchtrup 2004, 2005*a*,*b*)] as follows:

1. Finding the order of magnitude $\lambda$ of the moments.
   The main aim of this step is to see the order of magnitude of moments in powers of a small parameter ($\varepsilon$, usually this should be the Knudsen number). Towards this aim, a higher-order / non-conserved moment $\psi$ is expanded in powers of $\varepsilon$ as

$$\psi = \psi_0 + \varepsilon\,\psi_1 + \varepsilon^2\,\psi_2 + \cdots . \tag{7.1}$$

   The above expansion is similar to the Chapmann-Enskog expansion which is applied on the distribution function. In this method the primary focus is to determine the leading order of $\psi$, unlike usual Chapmann-Enskog expansion where we compute $\psi_i$'s for $i = 0, 1, 2, \cdots$.

The leading order of a moment $\psi$ is obtained by inserting the above ansatz (7.1) into the system of moment equations. If $\psi_i = 0$ for all $i < \lambda$, then a moment $\psi$ is said to be of leading order $\lambda$. The order of magnitude of a moment $\psi$ is nothing but the leading order of that moment. This step of the order-of-magnitude method [(Struchtrup 2004, 2005*b*)] follows from the idea of "Consistent order extended thermodynamics(COET)" [(Müller *et al.* 2003)], in which those authors performed a Maxwellian iteration procedure [(Truesdell & Muncaster 1980)] instead of a Chapmann-Enskog expansion.

2. Construction of moment set with minimum number of moments at order $\lambda$.
   In this step, a few of the moments chosen initially are combined linearly to introduce new variables in the system. The new variables are built in such a way that the number of moments at a given order $\lambda$ is minimum. This step provides an unambiguous set of moments at order $\lambda$ and ensures that the final result will not be dependent on the initial choice of moments (Struchtrup 2004).

3. Removal of all terms in all equations that would lead to contributions of orders $\lambda > \lambda_0$ in the balance laws.
   This follows from the definition of the order of accuracy $\lambda_0$: "A set of equations is said to have a accurate of order $\lambda_0$, if the stress tensor $\sigma_{ij}$ and the heat flux vector $q_i$ are known within the order $O(\varepsilon^{\lambda_0})$". This definition of the order of accuracy relies on the fact that all moment equations are strongly coupled. This means that each term in every moment equation has some influence on all other equations, especially on the conservation laws.

   The influence of every term can be weighted by powers of $\varepsilon$ (usually the Knudsen number Kn), and is related, but not same as the order of magnitude of the moments present in that term. A theory of order $\lambda_0$ will only consider those terms in all the equations whose leading order of influence in the conservation laws is $\lambda \leq \lambda_0$. This implies that all terms in the moment equations that are of leading order $\lambda \leq \lambda_0$ must be detained and terms not satisfying this condition are ignored.

   The order-of-magnitude method gives the Euler and Navier-Stokes-Fourier equations at zeroth and first order, respectively, and hence agrees with the classical Chapmann-Enskog method in the lower orders. At second order this approach yields the well known 13-moment equations of Grad [(Grad 1949)] and at third order it gives a "regularization" of the Grad moment equations, the so-called R13 moment equations. These R13 moment equations were first derived in [(Struchtrup & Torrilhon 2003; Torrilhon & Struchtrup 2004)] by combining two closure-methods, namely, Grad and Chapmann-Enskog.

## 7.3 14-Moment Equations for a Granular Gas

As discussed in Chapter 2, the state of the granular gas is described by a set of moments of the single-particle distribution function $f(\mathbf{r}, \mathbf{v}, t)$. In general, the moment of the distribution function is defined as

$$\langle \phi \rangle = \int \phi \, f \, \mathrm{d}\mathbf{v}. \tag{7.2}$$

where $\phi$ is a polynomial of the particle velocity $\boldsymbol{v}$. To obtain the well-known 13-moment theory of Grad [Grad (1949)] one has to take $\phi = m\{1, v_i, \frac{1}{3}C^2, C_{\langle i}C_{j\rangle}, \frac{1}{2}C^2\,C_i\}$. So the variables under consideration in Grad's 13-moment system are the moments $\rho, \rho\,u_i, p, \sigma_{ij}, q_i$. In order to obtain the 14-moment system, an extra moment, namely, the contracted fourth-order moment,

$$R = \langle m\,C^4\rangle = \int m\,C^4\,f\,\mathrm{d}\mathbf{v}, \tag{7.3}$$

is added. It is convenient to use a dimensionless non-equilibrium part of $R$, denoted by $\Delta$, and is defined by

$$\Delta = \frac{1}{15\,\rho\,\theta^2}(R - R^{eq}) = \frac{1}{15\,\rho\,\theta^2}\int m\,C^4\,(f - f^{eq})\,\mathrm{d}\mathbf{v}, \tag{7.4}$$

where

$$f^{eq} = \frac{n}{(2\pi\theta)^{\frac{3}{2}}}e^{-\frac{C^2}{2\theta}} \tag{7.5}$$

is the equilibrium distribution function. At equilibrium the contracted fourth order moment $R^{eq}$ is given by

$$R^{eq} = \int m\,C^4\,f^{eq}\,\mathrm{d}\mathbf{v} = 15\,\rho\,\theta^2, \tag{7.6}$$

where $\rho$ and $\theta$ are the density and temperature, respectively.

As discussed in Chapter 2, the basic equations for the 14-moment system $(\rho, \rho\,u_i, \theta, \sigma_{ij}, q_i, \Delta)$ of a dilute granular gas read as

$$\frac{\partial\rho}{\partial t} + \frac{\partial\,(\rho\,u_i)}{\partial x_i} = 0, \tag{7.7}$$

$$\frac{\partial\,(\rho\,u_i)}{\partial t} + \frac{\partial\,(\rho\,u_i\,u_j)}{\partial x_j} + \frac{\partial p}{\partial x_i} + \frac{\partial\sigma_{ij}}{\partial x_j} = 0, \tag{7.8}$$

$$\rho\left(\frac{\partial\theta}{\partial t} + u_i\,\frac{\partial\theta}{\partial x_i}\right) + \frac{2}{3}\left(\rho\,\theta\,\frac{\partial u_i}{\partial x_i} + \sigma_{ij}\frac{\partial u_i}{\partial x_j} + \frac{\partial q_i}{\partial x_i}\right) = -\mathcal{D}, \tag{7.9}$$

$$\frac{\partial\sigma_{ij}}{\partial t} + \frac{\partial(\sigma_{ij}\,u_k)}{\partial x_k} + \frac{4}{5}\frac{\partial q_{\langle i}}{\partial x_{j\rangle}} + \frac{\partial\mathcal{Q}_{ijk}}{\partial x_k} + 2\,p\,\frac{\partial u_{\langle i}}{\partial x_{j\rangle}} + 2\,\sigma_{k\langle i}\frac{\partial u_{j\rangle}}{\partial x_k} = \sigma^s_{ij}, \tag{7.10}$$

$$\begin{aligned}&\frac{\partial q_i}{\partial t} + \frac{\partial(q_i\,u_j)}{\partial x_j} + \frac{1}{2}\frac{\partial\mathcal{R}_{ij}}{\partial x_j} + \frac{1}{6}\frac{\partial R}{\partial x_i} - \frac{5}{2}\,\theta\left(\rho\,\frac{\partial\theta}{\partial x_i} + \theta\,\frac{\partial\rho}{\partial x_i} + \frac{\partial\sigma_{ij}}{\partial x_j}\right)\\ &- \frac{\sigma_{ij}}{\rho}\left(\rho\,\frac{\partial\theta}{\partial x_j} + \theta\,\frac{\partial\rho}{\partial x_j} + \frac{\partial\sigma_{jk}}{\partial x_k}\right) + \frac{7}{5}\,q_j\frac{\partial u_i}{\partial x_j} + \frac{2}{5}\,q_i\frac{\partial u_j}{\partial x_j} + \frac{2}{5}\,q_k\frac{\partial u_k}{\partial x_i} + \mathcal{Q}_{ijk}\frac{\partial u_j}{\partial x_k} = q^s_i,\end{aligned} \tag{7.11}$$

$$\begin{aligned}&15\,\rho\,\theta^2\left(\frac{\partial\Delta}{\partial t} + u_i\,\frac{\partial\Delta}{\partial x_i}\right) - 20\,(1+\Delta)\,\theta\left(\frac{\partial q_i}{\partial x_i} + \sigma_{ij}\frac{\partial u_i}{\partial x_j}\right) + \frac{\partial S_i}{\partial x_i} + 4\,\mathcal{R}_{ij}\,\frac{\partial u_i}{\partial x_j}\\ &\qquad - 8\,q_i\,\frac{\partial\theta}{\partial x_i} - \frac{8}{\rho}\,q_i\left(\frac{\partial\sigma_{ij}}{\partial x_j} + \theta\,\frac{\partial\rho}{\partial x_i}\right) = \Delta^s,\end{aligned} \tag{7.12}$$

where the angular brackets over subscripts denote deviatoric part of respective tensors. In the above equations, for notational convenience, the higher-order moments $Q_{\langle ijk\rangle}$ and $R_{\langle ij\rangle}$ are replaced with $\mathcal{Q}_{ijk}$ and $\mathcal{R}_{ij}$, respectively. So the definitions of higher-order moments which

appear in the above transport equations are given as

$$\mathcal{Q}_{ijk} = \int m\, C_{\langle i} C_j C_{k\rangle} f \mathrm{d}\mathbf{v}, \tag{7.13}$$

$$\mathcal{R}_{ij} = \int m\, C^2 C_{\langle i} C_{j\rangle} f \mathrm{d}\mathbf{v}, \tag{7.14}$$

$$S_i = \int m\, C^2 C^2 C_i f \mathrm{d}\mathbf{v}, \tag{7.15}$$

and the source terms are given by

$$\mathcal{D} = \frac{m\, d^2\,(1-\,\alpha^2\,)}{12} \int_{\boldsymbol{g}\cdot\boldsymbol{k}>0} (\boldsymbol{g}\cdot\boldsymbol{k})^3\, f_1\, f\, \mathrm{d}\boldsymbol{k}\mathrm{d}\mathbf{v}_1\mathrm{d}\mathbf{v} \tag{7.16}$$

$$\sigma^s_{ij} = \frac{1}{2}\int_{(\boldsymbol{g}\cdot\boldsymbol{k})>0} m\,(\,\acute{C}_{\langle i}\acute{C}_{j\rangle} + \acute{C}_{1\langle i}\acute{C}_{1j\rangle} - C_{\langle i}C_{j\rangle} - C_{1\langle i}C_{1j\rangle}\,) f_1\, f\, d^2\,(\boldsymbol{g}\cdot\boldsymbol{k})\,\mathrm{d}\boldsymbol{k}\mathrm{d}\mathbf{v}_1\mathrm{d}\mathbf{v} \tag{7.17}$$

$$q^s_i = \frac{1}{2}\int_{(\boldsymbol{g}\cdot\boldsymbol{k})>0} \frac{m}{2}(\,\acute{C}^2\acute{C}_i + \acute{C}_1{}^2\acute{C}_{1_i} - C^2\,C_i - C_1^2\,C_{1_i}\,)\, f_1\, f\, d^2\,(\boldsymbol{g}\cdot\boldsymbol{k})\,\mathrm{d}\boldsymbol{k}\mathrm{d}\mathbf{v}_1\mathrm{d}\mathbf{v}, \tag{7.18}$$

$$\Delta^s = R^s + 30\,(1+\Delta)\,\mathcal{D}\,\theta, \tag{7.19}$$

$$R^s = \frac{1}{2}\int m\,[\,\acute{C}^4 + \acute{C}_1{}^4 - C^4 - C_1^4\,]\, f_1\, f\, d^2\,(\boldsymbol{g}\cdot\boldsymbol{k})\,\mathrm{d}\boldsymbol{k}\mathrm{d}\mathbf{v}_1\mathrm{d}\mathbf{v}. \tag{7.20}$$

The first two equations (7.7) and (7.8) represent the conservation laws for mass and momentum, respectively, while Eqs. (7.9), (7.10), (7.11) and (7.12) represent the balance laws for the energy, the deviatoric part of the pressure tensor, the heat flux vector and the dimensionless non-equilibrium part of fourth-order contracted moment, respectively. Equations (7.10), (7.11) and (7.12) do not form a closed set of equations as they contains additional moments, $\mathcal{Q}_{ijk}, \mathcal{R}_{ij}$, and $S_i$ of higher order as defined in Eqs. (7.13), (7.14) and (7.15). These additional terms must be related to the variables under consideration via the distribution function. The variables under consideration in 14-moment system, the Grad's non-equilibrium distribution function [Kremer & Marques Jr (2011)] reads

$$f|_{14} = f^M\left(1 + \frac{\sigma_{ij}}{2\rho\theta^2}C_iC_j + \frac{q_i}{5\rho\theta^3}\Big(C^2 - 5\theta\Big)C_i + \Big(\frac{C^4 - 10C^2\theta + 15\theta^2}{8\theta^2}\Big)\Delta\right). \tag{7.21}$$

Using the above distribution function one can compute the constitutive equations for the additional moments of the distribution function. Using the distribution function (7.21) one can express the higher-order moments in terms of lower-order moments as

$$\mathcal{Q}_{ijk|14} = 0, \qquad \mathcal{R}_{ij|14} = 7\,\theta\,\sigma_{ij}, \qquad S_{i|14} = 28\,\theta\,q_i, \tag{7.22}$$

and similarly one can evaluate the collisional source terms. To evaluate the collisional source terms $\mathcal{D}$ and $R^s$, only linear terms in $\Delta$ are retained but to determine $\sigma^s_{ij}$ and $q^s_i$ the products of $\Delta$ with $\sigma_{ij}$ and $q_i$, in addition to the linear terms, are retained [Kremer & Marques Jr (2011)].

$$
\begin{aligned}
\mathcal{D} &= \frac{4}{3\,\tau_r}\,(1-\alpha^2)\left[1+\frac{3\,\Delta}{16}\right]\rho\,\theta,\\
\sigma_{ij}^s &= -\frac{4}{5\,\tau_r}\,(1+\alpha)\,(3-\alpha)\left[1-\frac{\Delta}{32}\right]\sigma_{ij},\\
q_i^s &= -\frac{1}{15\,\tau_r}\,(1+\alpha)\left[49-33\,\alpha+(19-3\,\alpha)\,\frac{\Delta}{32}\right]q_i,\\
R^s &= -\frac{4}{\tau_r}\,(1+\alpha)\left[(2\,\alpha^2+9)\,(1-\alpha)+(30\,\alpha^2\,(1-\alpha)+271-207\,\alpha)\,\frac{\Delta}{16}\right]\rho\,\theta^2\\
\Delta^s &= \frac{4}{\tau_r}\,(1+\alpha)\left[(1-\alpha)\,(1-2\,\alpha^2)-(30\,\alpha^2\,(1-\alpha)-17\,\alpha+81)\,\frac{\Delta}{16}\right]\rho^2\,\theta^2.
\end{aligned}
\tag{7.23}
$$

In the above equations we have introduced a relaxation time, $\tau_r$, which is given by

$$
\tau_r = \frac{m}{\rho\,d^2\,\sqrt{\pi\,\theta}}. \tag{7.24}
$$

Insertion of the expressions for additional moments given in (7.22) and the collisional source terms given in (7.23) into Eqs. (7.7) - (7.12) yields the Grad-type 14-moment system for a dilute granular gas. Like, the well-known Grad's 13-moment system, the present 14-moment system is symmetric hyperbolic [Müller & Ruggeri (2013); Weiss (1995)] and develops discontinuous stationary shocks for the Mach numbers above 1.763. The main difference between 13-moment and 14-moment systems when applied to stationary shock wave problem is that the critical Mach number is increased from $\mathrm{Ma}_{cr|_{13}} = 1.65$ to $\mathrm{Ma}_{cr|_{14}} = 1.763$ - we have analysed this issue in §5.4.

The primary goal of this Chapter is to derive a set of 14-moment equations which admit continuous shock solutions at any Mach number. Towards this goal, we follow the order-of-magnitude method of Struchtrup (2004). It is shown §7.4.1 that the resulting equations have additional higher-order gradient terms that regularize the 14-moment theory [Eq. (7.7) - (7.12)].

## 7.4 Regularization of 14-Moment Equations

To regularize the 14-moment system, Eq. (7.7) - Eq. (7.12), we introduce the deviations of $\mathcal{Q}_{ijk}, \mathcal{R}_{ij}$, and $S_i$ from their values obtained from the 14-moment distribution function (7.21) as

$$
\begin{aligned}
\tilde{\mathcal{Q}}_{ijk} &= \mathcal{Q}_{ijk} - \mathcal{Q}_{ijk|_{14}} = \mathcal{Q}_{ijk},\\
\tilde{\mathcal{R}}_{ij} &= \mathcal{R}_{ij} - \mathcal{R}_{ij|_{14}} = \mathcal{R}_{ij} - 7\,\theta\,\sigma_{ij},\\
\tilde{S}_i &= S_i - S_{i|_{14}} = S_i - 28\,\theta\,q_i.
\end{aligned}
\tag{7.25}
$$

It is clear from the above that for the fourteen moment closure $\tilde{\mathcal{Q}}_{ijk} = \tilde{\mathcal{R}}_{ij} = \tilde{S}_i = 0$. In order to compute non-zero approximations for these deviation quantities, one has to consider the evolution equations for $\mathcal{Q}_{ijk}, \mathcal{R}_{ij}$, and $S_i$. The moment transport equations for $\mathcal{Q}_{ijk}, \mathcal{R}_{ij}$,

and $S_i$ are given by

$$\frac{\partial \mathcal{Q}_{ijk}}{\partial t} + \frac{\partial \left(\mathcal{Q}_{ijk}\, u_l\right)}{\partial x_l} + \frac{\partial \mathcal{R}_{ijkl}}{\partial x_l} + \frac{3}{7}\frac{\partial \mathcal{R}_{\langle ij}}{\partial x_{k\rangle}} - \frac{3}{\rho}\sigma_{\langle ij}\frac{\partial p}{\partial x_{k\rangle}} - \frac{3}{\rho}\sigma_{\langle ij}\frac{\partial \sigma_{k\rangle l}}{\partial x_l}$$
$$+ 3\,\mathcal{Q}_{l\langle ij}\frac{\partial u_{k\rangle}}{\partial x_l} + \frac{12}{5}\,q_{\langle i}\frac{\partial u_{k\rangle}}{\partial x_j} = \mathcal{Q}^s_{ijk}, \tag{7.26}$$

$$\frac{\partial \mathcal{R}_{ij}}{\partial t} + \frac{\partial \left(\mathcal{R}_{ij}\, u_k\right)}{\partial x_k} + \frac{\partial \mathcal{N}_{ijk}}{\partial x_k} + \frac{2}{5}\frac{\partial S_{\langle i}}{\partial x_{j\rangle}} + 2\,\mathcal{R}_{ijkl}\frac{\partial u_l}{\partial x_k} + \frac{14}{15}\,R\frac{\partial u_{\langle i}}{\partial x_{j\rangle}} + 2\,\mathcal{R}_{k\langle i}\frac{\partial u_{j\rangle}}{\partial x_k}$$
$$+ \frac{4}{5}\mathcal{R}_{k\langle i}\frac{\partial u_k}{\partial x_{j\rangle}} + \frac{6}{7}\mathcal{R}_{\langle ij}\frac{\partial u_{k\rangle}}{\partial x_k} - \frac{2}{\rho}\mathcal{Q}_{ijk}\frac{\partial p_{kl}}{\partial x_l} - \frac{28}{5\,\rho}\,q_{\langle i}\frac{\partial p_{j\rangle k}}{\partial x_k} = \mathcal{R}^s_{ij}, \tag{7.27}$$

$$\frac{\partial S_i}{\partial t} + \frac{\partial \left(S_i\, u_j\right)}{\partial x_j} + \frac{\partial \mathcal{M}^{(6)}_{ij}}{\partial x_j} + 4\,\mathcal{N}_{ijk}\frac{\partial u_k}{\partial x_j} - \frac{4}{\rho}\mathcal{R}_{ij}\frac{\partial p_{jk}}{\partial x_k} - \frac{7}{3}\frac{R}{\rho}\frac{\partial p_{ij}}{\partial x_j}$$
$$+ \frac{4}{5}\left(S_i\frac{\partial u_j}{\partial x_j} + S_j\frac{\partial u_j}{\partial x_i}\right) + \frac{9}{5}\,S_j\frac{\partial u_i}{\partial x_j} = S^s_i, \tag{7.28}$$

where the source terms are defined as

$$\mathcal{Q}^s_{ijk} = \frac{1}{2}\int_{(\boldsymbol{g}\cdot\boldsymbol{k})>0} m\left(\acute{C}_{\langle i}\acute{C}_{j}\acute{C}_{k\rangle} + \acute{C}_{1\langle i}\acute{C}_{1j}\acute{C}_{1k\rangle} - C_{\langle i}C_{j}C_{k\rangle} - C_{1\langle i}C_{1j}C_{1k\rangle}\right) f_1\, f\, d^2\left(\boldsymbol{g}\cdot\boldsymbol{k}\right)\mathrm{d}\boldsymbol{k}\mathrm{d}\mathbf{v}_1\mathrm{d}\mathbf{v}, \tag{7.29}$$

$$\mathcal{R}^s_{ij} = \frac{1}{2}\int_{(\boldsymbol{g}\cdot\boldsymbol{k})>0} m\left(\acute{C}^2\acute{C}_{\langle i}\acute{C}_{j\rangle} + \acute{C}_1^2\acute{C}_{1\langle i}\acute{C}_{1j\rangle} - C^2C_{\langle i}C_{j\rangle} - C_1^2C_{1\langle i}C_{1j\rangle}\right) f_1\, f\, d^2\left(\boldsymbol{g}\cdot\boldsymbol{k}\right)\mathrm{d}\boldsymbol{k}\mathrm{d}\mathbf{v}_1\mathrm{d}\mathbf{v}, \tag{7.30}$$

$$S^s_i = \frac{1}{2}\int_{(\boldsymbol{g}\cdot\boldsymbol{k})>0} m\left(\acute{C}^2\acute{C}^2\acute{C}_i + \acute{C}_1{}^2\acute{C}_1{}^2\acute{C}_{1_i} - C^2\,C^2\,C_i - C_1^2C_1^2\,C_{1_i}\right) f_1\, f\, d^2\left(\boldsymbol{g}\cdot\boldsymbol{k}\right)\mathrm{d}\boldsymbol{k}\mathrm{d}\mathbf{v}_1\mathrm{d}\mathbf{v}. \tag{7.31}$$

Note that the equations (7.26 - 7.28) have been derived by following the same procedure as discussed in §2.3 of Chapter 2. Further the higher order moments involved in equations (7.26 - 7.28) are defined as

$$\mathcal{R}_{ijkl} = \int m\, C_{\langle i}C_jC_kC_{l\rangle} f\mathrm{d}\mathbf{v}, \tag{7.32}$$

$$\mathcal{N}_{ijk} = \int m\, C^2C_{\langle i}C_jC_{k\rangle} f\mathrm{d}\mathbf{v}, \tag{7.33}$$

$$\mathcal{M}^{(6)}_{ij} = \int m\, C^2C^2C_iC_j f\mathrm{d}\mathbf{v}. \tag{7.34}$$

### 7.4.1 Procedure to calculate regularized terms

Our aim is to find the non-zero contributions of $\tilde{\mathcal{Q}}_{ijk}, \tilde{\mathcal{R}}_{ij}$ and $\tilde{S}_i$ [see Eq. (7.25)] and hence one has to consider linear contributions in terms of $\tilde{\mathcal{Q}}_{ijk}, \tilde{\mathcal{R}}_{ij}$ and $\tilde{S}_i$ when evaluating the above source terms. To determine the constitutive relations for source terms, one must consider the fifth-order approximation for the non-equilibrium distribution function which also contains the moments under consideration for the regularization process. Hence one has to consider the

following fifth-order approximation for the distribution function [Gu & Emerson (2009)]

$$f = f^M\Bigg(1 + \frac{\sigma_{ij}}{2\,\rho\,\theta^2}\,C_i\,C_j + \frac{q_i}{5\,\rho\,\theta^3}\,(C^2 - 5\,\theta)\,C_i + \left(\frac{C^4 - 10\,C^2\,\theta + 15\,\theta^2}{8\,\theta^2}\right)\Delta + \underline{\frac{\mathcal{Q}_{ijk}}{6\,\rho\,\theta^3}\,C_i\,C_j\,C_k} \\ + \underline{\frac{(\mathcal{R}_{ij} - 7\,\theta\,\sigma_{ij})}{28\,\rho\,\theta^4}\,(C^2 - 7\,\theta)\,C_i\,C_j + \frac{(S_i - 28\,\theta\,q_i)}{280\,\rho\,\theta^5}\,(C^4 - 14\,C^2\theta + 35\,\theta^2)\,C_i}\Bigg), \tag{7.35}$$

where the underlined terms are new in comparison to the distribution function (7.21) that holds for a 14-moment system. In fact, Eq. (7.35) generates a system of 29-moment equations.

Using (7.35), the source terms (7.29), (7.30), and (7.31) have been evaluated which are linear in $\tilde{\mathcal{Q}}_{ijk}, \tilde{\mathcal{R}}_{ij}$, and $\tilde{S}_i$, respectively, and are given by

$$\mathcal{Q}^s_{ijk} = -\frac{6}{5\,\tau_r}\,(1+\alpha)\,(3-\alpha)\,\tilde{\mathcal{Q}}_{ijk}, \tag{7.36}$$

$$\mathcal{R}^s_{ij} = -\frac{1}{105\,\tau_r}\,(1+\alpha)\,[499 - 6\,\alpha\,(48 + \alpha(5\,\alpha - 11))]\,\tilde{\mathcal{R}}_{ij}, \tag{7.37}$$

$$S^s_i = -\frac{1}{3360\,\tau_r}\,(1+\alpha)\,\left[20551 - 13947\,\alpha + 5217\,\alpha^2 - 3093\,\alpha^3\right]\,\tilde{S}_i. \tag{7.38}$$

Now we outline the procedure of obtaining non-zero values for the deviation quantities $\tilde{\mathcal{Q}}_{ijk}, \tilde{\mathcal{R}}_{ij}$, and $\tilde{S}_i$, using the transport equations of $\mathcal{Q}_{ijk}$ [Eq.(7.26)], $\mathcal{R}_{ij}$ [Eq.(7.27)], and $S_i$ [Eq.(7.28)], respectively. Firstly we insert the deviation quantities $\tilde{\mathcal{Q}}_{ijk}, \tilde{\mathcal{R}}_{ij}$, and $\tilde{S}_i$ [(7.25)] into the transport equations of $\mathcal{Q}_{ijk}$, $\mathcal{R}_{ij}$, $S_i$ and all the time derivatives of the fourteen field variable $(\rho, \rho\,u_i, \theta, \sigma_{ij}, q_i, \Delta)$ are eliminated using their corresponding transport equations (7.7 - 7.12). After some simple algebra and with the help of the source terms (7.36 - 7.38), one obtains the following set of evolution equations

$$\frac{\partial\tilde{\mathcal{Q}}_{ijk}}{\partial t} + \frac{\partial\left(\tilde{\mathcal{Q}}_{ijk}\,u_l\right)}{\partial x_l} + \frac{\partial\mathcal{R}_{ijkl}}{\partial x_l} + \frac{3}{7}\,\frac{\partial\tilde{\mathcal{R}}_{\langle ij}}{\partial x_{k\rangle}} + 3\,\frac{\partial\left(\theta\,\sigma_{\langle ij}\right)}{\partial x_{k\rangle}} - \frac{3}{\rho}\,\sigma_{\langle ij}\,\frac{\partial p}{\partial x_{k\rangle}} \\ - \frac{3}{\rho}\,\sigma_{\langle ij}\,\frac{\partial\sigma_{k\rangle l}}{\partial x_l} + 3\,\tilde{\mathcal{Q}}_{l\langle ij}\,\frac{\partial u_{k\rangle}}{\partial x_l} + \frac{12}{5}\,q_{\langle i}\,\frac{\partial u_{k\rangle}}{\partial x_j} = -\frac{A_1}{\tau_r}\,\tilde{\mathcal{Q}}_{ijk}, \tag{7.39}$$

$$\frac{\partial\tilde{\mathcal{R}}_{ij}}{\partial t} + \frac{\partial\left(\tilde{\mathcal{R}}_{ij}\,u_k\right)}{\partial x_k} - 7\,\sigma_{ij}\left\{\frac{\mathcal{D}}{\rho} + u_k\,\frac{\partial\theta}{\partial x_k} + \frac{2}{3\,\rho}\left(\rho\,\theta\,\frac{\partial u_k}{\partial x_k} + \sigma_{kl}\frac{\partial u_k}{\partial x_l} + \frac{\partial q_k}{\partial x_k}\right)\right\} \\ + 7\,\theta\left\{\sigma^s_{\langle ij\rangle} - \frac{\partial(\sigma_{ij}\,u_k)}{\partial x_k} - \frac{4}{5}\frac{\partial q_{\langle i}}{\partial x_{j\rangle}} - \frac{\partial\tilde{\mathcal{Q}}_{ijk}}{\partial x_k} - 2\,p\,\frac{\partial u_{\langle i}}{\partial x_{j\rangle}} - 2\,\sigma_{k\langle i}\frac{\partial u_{j\rangle}}{\partial x_k}\right\} \\ + 7\frac{\partial\left(\theta\,\sigma_{ij}\,u_k\right)}{\partial x_k} + \frac{\partial\mathcal{N}_{ijk}}{\partial x_k} + \frac{2}{5}\frac{\partial\tilde{S}_{\langle i}}{\partial x_{j\rangle}} + \frac{56}{5}\frac{\partial\left(\theta\,q_{\langle i}\right)}{\partial x_{j\rangle}} + 2\,\mathcal{R}_{ijkl}\,\frac{\partial u_l}{\partial x_k} + 14\,\rho\,\theta^2\,\frac{\partial u_{\langle i}}{\partial x_{j\rangle}} \\ + 14\,\rho\,\theta^2\,\Delta\,\frac{\partial u_{\langle i}}{\partial x_{j\rangle}} + 2\,\tilde{\mathcal{R}}_{k\langle i}\,\frac{\partial u_{j\rangle}}{\partial x_k} + 14\,\theta\,\sigma_{k\langle i}\frac{\partial u_{j\rangle}}{\partial x_k} + \frac{4}{5}\tilde{\mathcal{R}}_{k\langle i}\,\frac{\partial u_k}{\partial x_{j\rangle}} + \frac{28}{5}\,\theta\,\sigma_{k\langle i}\,\frac{\partial u_k}{\partial x_{j\rangle}} \\ + \frac{6}{7}\tilde{\mathcal{R}}_{\langle ij}\,\frac{\partial u_{k\rangle}}{\partial x_k} + 6\,\theta\,\sigma_{\langle ij}\,\frac{\partial u_{k\rangle}}{\partial x_k} - \frac{2}{\rho}\,\tilde{\mathcal{Q}}_{ijk}\,\frac{\partial p_{kl}}{\partial x_l} - \frac{28}{5\,\rho}\,q_{\langle i}\,\frac{\partial p_{j\rangle k}}{\partial x_k} = -\frac{A_2}{\tau_r}\,\tilde{\mathcal{R}}_{ij}, \tag{7.40}$$

$$
\begin{aligned}
&\frac{\partial \tilde{S}_i}{\partial t} + \frac{\partial\left(\tilde{S}_i\, u_j\right)}{\partial x_j} - 28\, q_i \left\{\frac{\mathcal{D}}{\rho} + u_j \frac{\partial \theta}{\partial x_j} + \frac{2}{3\,\rho}\left(\rho\,\theta \frac{\partial u_j}{\partial x_j} + \sigma_{jk}\frac{\partial u_j}{\partial x_k} + \frac{\partial q_j}{\partial x_j}\right)\right\} \\
&- 28\,\theta\Bigg\{ - q_i^s + \frac{\partial\left(q_i\, u_j\right)}{\partial x_j} + \frac{1}{2}\frac{\partial \tilde{\mathcal{R}}_{ij}}{\partial x_j} + \frac{7}{2}\frac{\partial\left(\theta\,\sigma_{ij}\right)}{\partial x_j} + \frac{5}{2}\frac{\partial\left(\rho\,\theta^2\,(1+\delta)\right)}{\partial x_i} \\
&- \frac{5}{2}\,\theta\left(\rho\frac{\partial \theta}{\partial x_i} + \theta\frac{\partial \rho}{\partial x_i} + \frac{\partial \sigma_{ij}}{\partial x_j}\right) - \frac{\sigma_{ij}}{\rho}\left(\rho\frac{\partial \theta}{\partial x_j} + \theta\frac{\partial \rho}{\partial x_j} + \frac{\partial \sigma_{jk}}{\partial x_k}\right) + \frac{7}{5}\,q_j\frac{\partial u_i}{\partial x_j} \\
&+ \frac{2}{5}\,q_i\frac{\partial u_j}{\partial x_j} + \frac{2}{5}\,q_k\frac{\partial u_k}{\partial x_i} + \tilde{\mathcal{Q}}_{ijk}\frac{\partial u_j}{\partial x_k}\Bigg\} + 28\,\frac{\partial\left(\theta\, q_i\, u_j\right)}{\partial x_j} + \frac{\partial \mathcal{M}_{ij}^{(6)}}{\partial x_j} + 4\,\mathcal{N}_{ijk}\frac{\partial u_k}{\partial x_j} \\
&- \frac{4}{\rho}\tilde{\mathcal{R}}_{ij}\frac{\partial p_{jk}}{\partial x_k} - \frac{28}{\rho}\theta\,\sigma_{ij}\frac{\partial p_{jk}}{\partial x_k} - 35\,\theta^2\,(1+\Delta)\frac{\partial p_{ij}}{\partial x_j} + \frac{4}{5}\left(\tilde{S}_i\frac{\partial u_j}{\partial x_j} + \tilde{S}_j\frac{\partial u_j}{\partial x_i}\right) \\
&+ \frac{9}{5}\,\tilde{S}_j\frac{\partial u_i}{\partial x_j} + \frac{112}{5}\,\theta\left(q_i\frac{\partial u_j}{\partial x_j} + q_j\left(\frac{\partial u_i}{\partial x_j} + \frac{\partial u_j}{\partial x_i}\right)\right) + 28\,\theta\, q_j\frac{\partial u_i}{\partial x_j} = -\frac{A_3}{\tau_r}\,\tilde{S}_i,
\end{aligned}
\tag{7.41}
$$

where

$$
A_1 = \frac{6}{5}\,(1+\alpha)\,(3-\alpha), \tag{7.42}
$$

$$
A_2 = \frac{1}{105}\,(1+\alpha)\,\left[499 - 6\,\alpha\,(48 + \alpha(5\,\alpha - 11))\right], \tag{7.43}
$$

$$
A_3 = \frac{1}{3360}\,(1+\alpha)\,\left[20551 - 13947\,\alpha + 5217\,\alpha^2 - 3093\,\alpha^3\right]. \tag{7.44}
$$

Following the arguments of Struchtrup & Torrilhon (2003) [see also, Struchtrup & Torrilhon (2013)], we assume that the non-equilibrium moments of the 14-moment system, i.e., $\sigma_{ij}, q_i$ and $\Delta$, change on the time scale defined by $\tau_r$, while all other non-equilibrium moments $\mathcal{Q}_{ijk}, \mathcal{R}_{ij}$, and $S_i$ change on a faster time scale $\varepsilon\,\tau_r$ where $\varepsilon$ is a small parameter. [Indeed, we will set this small parameter $\varepsilon$ equal to unity at the end]. Using the above argument, Eqs. (7.39) -(7.41) are changed slightly on the right hand side which contains the small parameter $\varepsilon$, and are given by

$$
\begin{aligned}
&\frac{\partial \tilde{\mathcal{Q}}_{ijk}}{\partial t} + \frac{\partial\left(\tilde{\mathcal{Q}}_{ijk}\, u_l\right)}{\partial x_l} + \frac{\partial \mathcal{R}_{ijkl}}{\partial x_l} + \frac{3}{7}\frac{\partial \tilde{\mathcal{R}}_{\langle ij}}{\partial x_{k\rangle}} + 3\,\frac{\partial\left(\theta\,\sigma_{\langle ij}\right)}{\partial x_{k\rangle}} - \frac{3}{\rho}\,\sigma_{\langle ij}\frac{\partial p}{\partial x_{k\rangle}} \\
&- \frac{3}{\rho}\,\sigma_{\langle ij}\frac{\partial \sigma_{k\rangle l}}{\partial x_l} + 3\,\tilde{\mathcal{Q}}_{l\langle ij}\frac{\partial u_{k\rangle}}{\partial x_l} + \frac{12}{5}\,q_{\langle i}\frac{\partial u_{k\rangle}}{\partial x_j} = -\frac{1}{\varepsilon}\,\frac{A_1}{\tau_r}\,\tilde{\mathcal{Q}}_{ijk},
\end{aligned}
\tag{7.45}
$$

$$
\begin{aligned}
&\frac{\partial \tilde{\mathcal{R}}_{ij}}{\partial t} + \frac{\partial\left(\tilde{\mathcal{R}}_{ij}\, u_k\right)}{\partial x_k} - 7\,\sigma_{ij}\left\{\frac{\mathcal{D}}{\rho} + u_k\frac{\partial \theta}{\partial x_k} + \frac{2}{3\,\rho}\left(\rho\,\theta\frac{\partial u_k}{\partial x_k} + \sigma_{kl}\frac{\partial u_k}{\partial x_l} + \frac{\partial q_k}{\partial x_k}\right)\right\} \\
&+ 7\,\theta\left\{\sigma_{\langle ij\rangle}^s - \frac{\partial(\sigma_{ij}\,u_k)}{\partial x_k} - \frac{4}{5}\frac{\partial q_{\langle i}}{\partial x_{j\rangle}} - \frac{\partial \tilde{\mathcal{Q}}_{ijk}}{\partial x_k} - 2\,p\,\frac{\partial u_{\langle i}}{\partial x_{j\rangle}} - 2\,\sigma_{k\langle i}\frac{\partial u_{j\rangle}}{\partial x_k}\right\} \\
&+ 7\frac{\partial\left(\theta\,\sigma_{ij}\,u_k\right)}{\partial x_k} + \frac{\partial \mathcal{N}_{ijk}}{\partial x_k} + \frac{2}{5}\frac{\partial \tilde{S}_{\langle i}}{\partial x_{j\rangle}} + \frac{56}{5}\frac{\partial\left(\theta\, q_{\langle i}\right)}{\partial x_{j\rangle}} + 2\,\mathcal{R}_{ijkl}\frac{\partial u_l}{\partial x_k} + 14\,\rho\,\theta^2\frac{\partial u_{\langle i}}{\partial x_{j\rangle}} \\
&+ 14\,\rho\,\theta^2\,\Delta\frac{\partial u_{\langle i}}{\partial x_{j\rangle}} + 2\,\tilde{\mathcal{R}}_{k\langle i}\frac{\partial u_{j\rangle}}{\partial x_k} + 14\,\theta\,\sigma_{k\langle i}\frac{\partial u_{j\rangle}}{\partial x_k} + \frac{4}{5}\tilde{\mathcal{R}}_{k\langle i}\frac{\partial u_k}{\partial x_{j\rangle}} + \frac{28}{5}\,\theta\,\sigma_{k\langle i}\frac{\partial u_k}{\partial x_{j\rangle}} \\
&+ \frac{6}{7}\tilde{\mathcal{R}}_{\langle ij}\frac{\partial u_{k\rangle}}{\partial x_k} + 6\,\theta\,\sigma_{\langle ij}\frac{\partial u_{k\rangle}}{\partial x_k} - \frac{2}{\rho}\,\tilde{\mathcal{Q}}_{ijk}\frac{\partial p_{kl}}{\partial x_l} - \frac{28}{5\,\rho}\,q_{\langle i}\frac{\partial p_{j\rangle k}}{\partial x_k} = -\frac{1}{\varepsilon}\,\frac{A_2}{\tau_r}\,\tilde{\mathcal{R}}_{ij},
\end{aligned}
\tag{7.46}
$$

$$
\begin{aligned}
&\frac{\partial \tilde{S}_i}{\partial t} + \frac{\partial\left(\tilde{S}_i\, u_j\right)}{\partial x_j} - 28\, q_i \left\{ \frac{\mathcal{D}}{\rho} + u_j \frac{\partial \theta}{\partial x_j} + \frac{2}{3\,\rho}\left(\rho\,\theta \frac{\partial u_j}{\partial x_j} + \sigma_{jk}\frac{\partial u_j}{\partial x_k} + \frac{\partial q_j}{\partial x_j}\right)\right\} \\
&- 28\,\theta\Bigg\{ - q_i^s + \frac{\partial\left(q_i\, u_j\right)}{\partial x_j} + \frac{1}{2}\frac{\partial \tilde{\mathcal{R}}_{ij}}{\partial x_j} + \frac{7}{2}\frac{\partial\left(\theta\,\sigma_{ij}\right)}{\partial x_j} + \frac{5}{2}\frac{\partial\left(\rho\,\theta^2\,(1+\delta)\right)}{\partial x_i} \\
&- \frac{5}{2}\,\theta\left(\rho\frac{\partial \theta}{\partial x_i} + \theta\frac{\partial \rho}{\partial x_i} + \frac{\partial \sigma_{ij}}{\partial x_j}\right) - \frac{\sigma_{ij}}{\rho}\left(\rho\frac{\partial \theta}{\partial x_j} + \theta\frac{\partial \rho}{\partial x_j} + \frac{\partial \sigma_{jk}}{\partial x_k}\right) + \frac{7}{5}\,q_j\frac{\partial u_i}{\partial x_j} \\
&+ \frac{2}{5}\,q_i\frac{\partial u_j}{\partial x_j} + \frac{2}{5}\,q_k\frac{\partial u_k}{\partial x_i} + \tilde{\mathcal{Q}}_{ijk}\frac{\partial u_j}{\partial x_k}\Bigg\} + 28\,\frac{\partial\left(\theta\, q_i\, u_j\right)}{\partial x_j} + \frac{\partial \mathcal{M}_{ij}^{(6)}}{\partial x_j} + 4\,\mathcal{N}_{ijk}\frac{\partial u_k}{\partial x_j} \\
&- \frac{4}{\rho}\tilde{\mathcal{R}}_{ij}\frac{\partial p_{jk}}{\partial x_k} - \frac{28}{\rho}\theta\,\sigma_{ij}\frac{\partial p_{jk}}{\partial x_k} - 35\,\theta^2\,(1+\Delta)\frac{\partial p_{ij}}{\partial x_j} + \frac{4}{5}\left(\tilde{S}_i\frac{\partial u_j}{\partial x_j} + \tilde{S}_j\frac{\partial u_j}{\partial x_i}\right) \\
&+ \frac{9}{5}\,\tilde{S}_j\frac{\partial u_i}{\partial x_j} + \frac{112}{5}\,\theta\left(q_i\frac{\partial u_j}{\partial x_j} + q_j\left(\frac{\partial u_i}{\partial x_j} + \frac{\partial u_j}{\partial x_i}\right)\right) + 28\,\theta\, q_j\frac{\partial u_i}{\partial x_j} = -\frac{1}{\varepsilon}\frac{A_3}{\tau_r}\,\tilde{S}_i.
\end{aligned}
\tag{7.47}
$$

The above Eqs. (7.45) -(7.47) are now expanded in terms of the small parameter $\varepsilon$ via

$$
\begin{aligned}
\tilde{\mathcal{Q}}_{ijk} &= \tilde{\mathcal{Q}}_{ijk}^{(0)} + \varepsilon\,\tilde{\mathcal{Q}}_{ijk}^{(1)} + \cdots, \\
\tilde{\mathcal{R}}_{ij} &= \tilde{\mathcal{R}}_{ij}^{(0)} + \varepsilon\,\tilde{\mathcal{R}}_{ij}^{(1)} + \cdots, \\
\tilde{S}_i &= \tilde{S}_i^{(0)} + \varepsilon\,\tilde{S}_i^{(1)} + \cdots.
\end{aligned}
\tag{7.48}
$$

Here we account for terms up to first order in $\varepsilon$. The above expansion is a Chapman-Enskog-like expansion, with $\varepsilon$ being the small parameter. For a detailed discussion, we refer to Struchtrup & Torrilhon (2003), Struchtrup (2004) and Struchtrup & Torrilhon (2013).

Now inserting the ansatz (7.48) into the balance laws for $\tilde{\mathcal{Q}}_{ijk}$, $\tilde{\mathcal{R}}_{ij}$, and $\tilde{S}_i$, i.e., Eqs. (7.45) - (7.47), we compare the terms of the same order in $\varepsilon$. It is straightforward to verify that the zeroth-order approximations of $\tilde{\mathcal{Q}}_{ijk}$, $\tilde{\mathcal{R}}_{ij}$, and $\tilde{S}_i$ resulting from balancing terms of order $\varepsilon^{-1}$, gives

$$
\tilde{\mathcal{Q}}_{ijk}^{(0)} = \tilde{\mathcal{R}}_{ij}^{(0)} = \tilde{S}_i^{(0)} = 0. \tag{7.49}
$$

Hence the zeroth-order approximation gives the original 14-moment system as discussed in §7.3 (also in chapter 2).

The first-order approximations of $\tilde{\mathcal{Q}}_{ijk}$, $\tilde{\mathcal{R}}_{ij}$, and $\tilde{S}_i$, resulting from balancing terms of order $\varepsilon^0$, can be written as

$$
\begin{aligned}
&\Bigg[\frac{\partial \tilde{\mathcal{Q}}_{ijk}}{\partial t} + \frac{\partial\left(\tilde{\mathcal{Q}}_{ijk}\, u_l\right)}{\partial x_l} + \frac{\partial \mathcal{R}_{ijkl}}{\partial x_l} + \frac{3}{7}\frac{\partial \tilde{\mathcal{R}}_{\langle ij}}{\partial x_{k\rangle}} + 3\,\frac{\partial\left(\theta\,\sigma_{\langle ij}\right)}{\partial x_{k\rangle}} - \frac{3}{\rho}\,\sigma_{\langle ij}\frac{\partial p}{\partial x_{k\rangle}} \\
&- \frac{3}{\rho}\,\sigma_{\langle ij}\frac{\partial \sigma_{k\rangle l}}{\partial x_l} + 3\,\tilde{\mathcal{Q}}_{l\langle ij}\frac{\partial u_{k\rangle}}{\partial x_l} + \frac{12}{5}\,q_{\langle i}\frac{\partial u_{k\rangle}}{\partial x_j}\Bigg]_{|_{f_{14}}} = -\frac{A_1}{\tau_r}\,\tilde{\mathcal{Q}}_{ijk}^{(1)},
\end{aligned}
\tag{7.50}
$$

$$\left[\frac{\partial\tilde{\mathcal{R}}_{ij}}{\partial t}+\frac{\partial\left(\tilde{\mathcal{R}}_{ij}\,u_k\right)}{\partial x_k}-7\,\sigma_{ij}\left\{\frac{\mathcal{D}}{\rho}+u_k\,\frac{\partial\theta}{\partial x_k}+\frac{2}{3\,\rho}\left(\rho\,\theta\,\frac{\partial u_k}{\partial x_k}+\sigma_{kl}\frac{\partial u_k}{\partial x_l}+\frac{\partial q_k}{\partial x_k}\right)\right\}\right.$$
$$+7\,\theta\left\{\sigma^s_{\langle ij\rangle}-\frac{\partial(\sigma_{ij}\,u_k)}{\partial x_k}-\frac{4}{5}\frac{\partial q_{\langle i}}{\partial x_{j\rangle}}-\frac{\partial\tilde{\mathcal{Q}}_{ijk}}{\partial x_k}-2\,p\,\frac{\partial u_{\langle i}}{\partial x_{j\rangle}}-2\,\sigma_{k\langle i}\frac{\partial u_{j\rangle}}{\partial x_k}\right\}$$
$$+7\frac{\partial\left(\theta\,\sigma_{ij}\,u_k\right)}{\partial x_k}+\frac{\partial\mathcal{N}_{ijk}}{\partial x_k}+\frac{2}{5}\frac{\partial\tilde{S}_{\langle i}}{\partial x_{j\rangle}}+\frac{56}{5}\frac{\partial\left(\theta\,q_{\langle i}\right)}{\partial x_{j\rangle}}+2\,\mathcal{R}_{ijkl}\,\frac{\partial u_l}{\partial x_k}+14\,\rho\,\theta^2\,\frac{\partial u_{\langle i}}{\partial x_{j\rangle}}$$
$$+14\,\rho\,\theta^2\,\Delta\,\frac{\partial u_{\langle i}}{\partial x_{j\rangle}}+2\,\tilde{\mathcal{R}}_{k\langle i}\,\frac{\partial u_{j\rangle}}{\partial x_k}+14\,\theta\,\sigma_{k\langle i}\frac{\partial u_{j\rangle}}{\partial x_k}+\frac{4}{5}\tilde{\mathcal{R}}_{k\langle i}\,\frac{\partial u_k}{\partial x_{j\rangle}}+\frac{28}{5}\,\theta\,\sigma_{k\langle i}\,\frac{\partial u_k}{\partial x_{j\rangle}}$$
$$\left.+\frac{6}{7}\tilde{\mathcal{R}}_{\langle ij}\,\frac{\partial u_{k\rangle}}{\partial x_k}+6\,\theta\,\sigma_{\langle ij}\,\frac{\partial u_{k\rangle}}{\partial x_k}-\frac{2}{\rho}\,\tilde{\mathcal{Q}}_{ijk}\,\frac{\partial p_{kl}}{\partial x_l}-\frac{28}{5\,\rho}\,q_{\langle i}\,\frac{\partial p_{j\rangle k}}{\partial x_k}\right]_{|_{f_{14}}}=-\frac{A_2}{\tau_r}\,\tilde{\mathcal{R}}^{(1)}_{ij},\qquad(7.51)$$

$$\left[\frac{\partial\tilde{S}_i}{\partial t}+\frac{\partial\left(\tilde{S}_i\,u_j\right)}{\partial x_j}-28\,q_i\left\{\frac{\mathcal{D}}{\rho}+u_j\,\frac{\partial\theta}{\partial x_j}+\frac{2}{3\,\rho}\left(\rho\,\theta\,\frac{\partial u_j}{\partial x_j}+\sigma_{jk}\frac{\partial u_j}{\partial x_k}+\frac{\partial q_j}{\partial x_j}\right)\right\}\right.$$
$$-28\,\theta\left\{-q^s_i+\frac{\partial\left(q_i\,u_j\right)}{\partial x_j}+\frac{1}{2}\frac{\partial\tilde{\mathcal{R}}_{ij}}{\partial x_j}+\frac{7}{2}\frac{\partial\left(\theta\,\sigma_{ij}\right)}{\partial x_j}+\frac{5}{2}\frac{\partial\left(\rho\,\theta^2\,(1+\delta)\right)}{\partial x_i}\right.$$
$$-\frac{5}{2}\,\theta\left(\rho\,\frac{\partial\theta}{\partial x_i}+\theta\,\frac{\partial\rho}{\partial x_i}+\frac{\partial\sigma_{ij}}{\partial x_j}\right)-\frac{\sigma_{ij}}{\rho}\left(\rho\,\frac{\partial\theta}{\partial x_j}+\theta\,\frac{\partial\rho}{\partial x_j}+\frac{\partial\sigma_{jk}}{\partial x_k}\right)+\frac{7}{5}\,q_j\frac{\partial u_i}{\partial x_j}$$
$$\left.+\frac{2}{5}\,q_i\frac{\partial u_j}{\partial x_j}+\frac{2}{5}\,q_k\frac{\partial u_k}{\partial x_i}+\tilde{\mathcal{Q}}_{ijk}\frac{\partial u_j}{\partial x_k}\right\}+28\,\frac{\partial\left(\theta\,q_i\,u_j\right)}{\partial x_j}+\frac{\partial\mathcal{M}^{(6)}_{ij}}{\partial x_j}+4\,\mathcal{N}_{ijk}\,\frac{\partial u_k}{\partial x_j}$$
$$-\frac{4}{\rho}\tilde{\mathcal{R}}_{ij}\,\frac{\partial p_{jk}}{\partial x_k}-\frac{28}{\rho}\theta\,\sigma_{ij}\,\frac{\partial p_{jk}}{\partial x_k}-35\,\theta^2\,(1+\Delta)\,\frac{\partial p_{ij}}{\partial x_j}+\frac{4}{5}\left(\tilde{S}_i\,\frac{\partial u_j}{\partial x_j}+\tilde{S}_j\,\frac{\partial u_j}{\partial x_i}\right)$$
$$\left.+\frac{9}{5}\,\tilde{S}_j\,\frac{\partial u_i}{\partial x_j}+\frac{112}{5}\,\theta\left(q_i\,\frac{\partial u_j}{\partial x_j}+q_j\left(\frac{\partial u_i}{\partial x_j}+\frac{\partial u_j}{\partial x_i}\right)\right)+28\,\theta\,q_j\,\frac{\partial u_i}{\partial x_j}\right]_{|_{f_{14}}}=-\frac{A_3}{\tau_r}\,\tilde{S}^{(1)}_i,\qquad(7.52)$$

where the notation $\left[\cdot\right]_{|_{f_{14}}}$ indicates that all moments inside the square brackets must be evaluated with the fourteen-field phase density $f_{14}$, which is given by (7.21). The constitutive relations for higher-order moments using the fourteen-field density distribution function are given by

$$\mathcal{R}_{ijkl|14}=\mathcal{N}_{ijk|14}=0,\quad \mathcal{M}^{(6)}_{ij}=35\,\rho\,\theta^3\,(1\,+\,3\,\Delta)\,\delta_{ij}\,+\,63\,\theta^2\,\sigma_{ij},$$
$$\text{and}\quad \tilde{\mathcal{Q}}_{ijk|14}=\tilde{\mathcal{R}}_{ij|14}=\tilde{S}_{i|14}=0.\qquad(7.53)$$

Finally the corrections to 14-moment equations are obtained as follows after setting $\varepsilon=1$.

$$\tilde{\mathcal{Q}}_{ijk}=\tilde{\mathcal{Q}}^{(1)}_{ijk}=-\frac{3\,\tau_r}{A_1}\left[\theta\,\frac{\partial\sigma_{\langle ij}}{\partial x_{k\rangle}}-\theta\,\sigma_{\langle ij}\,\frac{\partial\ln\rho}{\partial x_{k\rangle}}-\frac{\sigma_{\langle ij}}{\rho}\,\frac{\partial\sigma_{k\rangle l}}{\partial x_l}+\frac{4}{5}\,q_{\langle i}\,\frac{\partial u_{k\rangle}}{\partial x_j}\right],\qquad(7.54)$$

$$\tilde{\mathcal{R}}_{ij} = \tilde{\mathcal{R}}_{ij}^{(1)} = -\frac{\tau_r}{A_2}\Bigg[7\,\theta\,\sigma_{ij}^s - \frac{7}{\rho}\sigma_{ij}\,\mathcal{D} + \frac{28}{5}\,\theta\,\frac{\partial q_{\langle i}}{\partial x_{j\rangle}} + \frac{28}{5}\,q_{\langle i}\,\frac{\partial \theta}{\partial x_{j\rangle}} - \frac{28}{5}\,\theta\,q_{\langle i}\,\frac{\partial \ln\rho}{\partial x_{j\rangle}} - \frac{28}{5\,\rho}\,q_{\langle i}\,\frac{\partial \sigma_{j\rangle k}}{\partial x_k} + 4\,\theta\,\sigma_{k\langle i}\frac{\partial u_{j\rangle}}{\partial x_k} + 4\,\theta\,\sigma_{k\langle i}\,\frac{\partial u_k}{\partial x_{j\rangle}} - \frac{8}{3}\,\theta\,\sigma_{ij}\frac{\partial u_k}{\partial x_k} - \frac{14}{3\,\rho}\,\sigma_{ij}\,\sigma_{kl}\,\frac{\partial u_k}{\partial x_l} - \frac{14}{3\,\rho}\,\sigma_{ij}\,\frac{\partial q_k}{\partial x_k} + 14\,\rho\,\theta^2\,\Delta\,\frac{\partial u_{\langle i}}{\partial x_{j\rangle}}\Bigg], \tag{7.55}$$

$$\tilde{S}_i = \tilde{S}_i^{(1)} = -\frac{\tau_r}{A_3}\Bigg[28\,\theta\,q_i^s - \frac{28}{\rho}\,q_i\,\mathcal{D} + 140\,\rho\,\theta^2\,\Delta\,\frac{\partial \theta}{\partial x_i} + 28\,\theta\,\sigma_{ij}\,\frac{\partial \theta}{\partial x_j} + 35\,\rho\,\theta^3\,\frac{\partial \Delta}{\partial x_i} - 35\,\theta^2\,\Delta\,\frac{\partial \sigma_{ij}}{\partial x_j} - \frac{56}{3}\left(\frac{q_i}{\rho}\,\frac{\partial q_j}{\partial x_j} + \theta\,q_i\,\frac{\partial u_j}{\partial x_j} + \frac{q_i}{\rho}\,\sigma_{jk}\,\frac{\partial u_j}{\partial x_k}\right) + \frac{56}{5}\,\theta\left(q_i\,\frac{\partial u_j}{\partial x_j} + q_j\frac{\partial u_i}{\partial x_j} + q_j\,\frac{\partial u_j}{\partial x_i}\right)\Bigg]. \tag{7.56}$$

### 7.4.2 Regularized 14-moment equations

The above corrections, Eqs. (7.161 - 7.56), must be inserted into the equations for stress tensor, heat flux vector and the fourth order contracted moment which read

$$\frac{\partial \sigma_{ij}}{\partial t} + \frac{\partial(\sigma_{ij}\,u_k)}{\partial x_k} + \frac{4}{5}\frac{\partial q_{\langle i}}{\partial x_{j\rangle}} + 2\,p\,\frac{\partial u_{\langle i}}{\partial x_{j\rangle}} + 2\,\sigma_{k\langle i}\frac{\partial u_{j\rangle}}{\partial x_k} + \underline{\frac{\partial \tilde{\mathcal{Q}}_{ijk}}{\partial x_k}} = \sigma_{ij}^s, \tag{7.57}$$

$$\frac{\partial q_i}{\partial t} + \frac{\partial(q_i\,u_j)}{\partial x_j} + \frac{5}{2}\,\sigma_{ij}\,\frac{\partial \theta}{\partial x_j} + \frac{5}{2}\,\rho\,\theta\,\frac{\partial \theta}{\partial x_i} + \theta\,\frac{\partial \sigma_{ij}}{\partial x_j} - \frac{\sigma_{ij}}{\rho}\,\frac{\partial \sigma_{jk}}{\partial x_k} - \sigma_{ij}\,\theta\,\frac{\partial \ln\rho}{\partial x_j} + \frac{5}{2}\,\frac{\partial\left(\rho\,\theta^2\,\Delta\right)}{\partial x_i} + \frac{7}{5}\,q_j\frac{\partial u_i}{\partial x_j} + \frac{2}{5}\,q_i\frac{\partial u_j}{\partial x_j} + \frac{2}{5}\,q_k\frac{\partial u_k}{\partial x_i} + \underline{\frac{1}{2}\frac{\partial \tilde{\mathcal{R}}_{ij}}{\partial x_j} + \tilde{\mathcal{Q}}_{ijk}\,\frac{\partial u_j}{\partial x_k}} = q_i^s, \tag{7.58}$$

$$15\,\rho\,\theta^2\left(\frac{\partial \Delta}{\partial t} + u_i\,\frac{\partial \Delta}{\partial x_i}\right) + 4\,(2 + 5\,\Delta)\,\theta\left(\frac{\partial q_i}{\partial x_i} + \sigma_{ij}\frac{\partial u_i}{\partial x_j}\right) + 20\,q_i\,\frac{\partial \theta}{\partial x_i} - \frac{8}{\rho}\,q_i\left(\frac{\partial \sigma_{ij}}{\partial x_j} + \theta\,\frac{\partial \rho}{\partial x_i}\right) + \underline{\frac{\partial \tilde{S}_i}{\partial x_i} + 4\,\tilde{\mathcal{R}}_{ij}\,\frac{\partial u_i}{\partial x_j}} = \Delta^s. \tag{7.59}$$

Note that the underlined terms in Eqs. (7.57 - 7.59) are of higher-order and are dubbed "regularization" terms which are absent in the original 14-moment theory [see Eqs. (7.7 - 7.12)].

Hence, we have derived the complete set of regularized equations for the 14-field variables $\rho, u_i, \theta, \sigma_{ij}, q_i, \Delta$ that consists of Eqs. (7.7) - (7.9) and (7.57) - (7.59) with higher-order terms given by (7.161) - (7.56). From now onwards we refer to these equations as the R14 equations, where "R" stands for "regularized", and 14 denotes the number of field variables.

### 7.4.3 R14 Equations in One-Dimension

The R14-moment model is reduced to a system of six equations for the plane shock wave problem. The one-dimensional field equations for R14-moment system, which involves six field variables namely, the density ($\rho(x,t)$), the velocity ($u(x,t)$), the scalar temperature ($\theta(x,t)$), the longitudinal stress ($\sigma(x,t)$), the heat flux $q(x,t)$, and the dimensionless non-equilibrium part of the full contracted fourth-order moment $\Delta$. The one-dimensional equations for the R14 extended hydrodynamic model are

$$\frac{\partial \rho}{\partial t} + \frac{\partial}{\partial x}\Big(\rho\, u\Big) = 0, \tag{7.60}$$

$$\frac{\partial}{\partial t}\Big(\rho\, u\Big) + \frac{\partial}{\partial x}\Big(\rho\, u^2 + \rho\,\theta + \sigma\Big) = 0, \tag{7.61}$$

$$\frac{\partial}{\partial t}\Big(\rho\, u^2 + 3\,\rho\,\theta\Big) + \frac{\partial}{\partial x}\Big(\rho\, u^3 + 5\,\rho\,\theta\, u + 2\,\sigma\, u + 2\, q\Big) = -3\,\mathcal{D}, \tag{7.62}$$

$$\frac{\partial}{\partial t}\Big(\frac{2}{3}\,\rho\, u^2 + \sigma\Big) + \frac{\partial}{\partial x}\Big(\frac{2}{3}\,\rho\, u^3 + \frac{4}{3}\,\rho\,\theta\, u + \frac{7}{3}\,\sigma\, u + \frac{8}{15}\, q + \underline{\mathcal{Q}}\Big) = \sigma^s, \tag{7.63}$$

$$\begin{aligned}\frac{\partial}{\partial t}\Big(\frac{1}{2}\,\rho\, u^3 + \frac{5}{2}\,\rho\,\theta\, u + \sigma\, u + q\Big) + \frac{\partial}{\partial x}\Big(\frac{1}{2}\,\rho\, u^4 + 4\,\rho\,\theta\, u^2 + \frac{5}{2}\,\sigma\, u^2 + \frac{16}{5}\, q\, u \\ + \frac{7}{2}\,\sigma\,\theta + \frac{5}{2}\,\rho\,\theta^2\,(1+\Delta) + \underline{\mathcal{Q}\, u + \frac{1}{2}\mathcal{R}}\Big) = q^s + \sigma^s\, u - \frac{5}{2}\mathcal{D}\, u,\end{aligned} \tag{7.64}$$

$$\begin{aligned}&\frac{\partial}{\partial t}\Big(\rho\, u^4 + 10\,\rho\,\theta\, u^2 + 4\,\sigma\, u^2 + 8\, q\, u + 15\,\rho\,\theta^2\,(1+\Delta)\Big) + \frac{\partial}{\partial x}\Big(\rho\, u^5 + 14\,\rho\,\theta\, u^3 \\ &+ 8\,\sigma\, u^3 + \frac{84}{5}\, q\, u^2 + 35\,\rho\,\theta^2\,(1+\Delta)\, u + 28\,\sigma\,\theta\, u + 28\,\theta\, q + \underline{4\,\mathcal{Q}\, u^2 + 4\,\mathcal{R}\, u + \mathcal{S}}\Big) \\ &= R^s + 8\, q^s\, u + 4\,\sigma^s\, u^2 - 10\,\mathcal{D}\, u^2,\end{aligned} \tag{7.65}$$

where $\mathcal{Q}$, $\mathcal{R}$ and $\mathcal{S}$ are non-zero terms which are arising from the regularization and these terms are underlined in (7.63) - (7.65). The expressions for these non-zero terms and the source terms $\mathcal{D}$,$\sigma^s$, $q^s$, and $R^s$ are given by:

$$\mathcal{Q} = \tilde{\mathcal{Q}}_{xxx} = -\frac{3\,\tau_r}{A_1}\left[\frac{3}{5}\,\theta\,\frac{\partial \sigma}{\partial x} - \frac{3}{5}\,\theta\,\sigma\,\frac{\partial \ln \rho}{\partial x} - \frac{3}{5}\,\frac{\sigma}{\rho}\,\frac{\partial \sigma}{\partial x} + \frac{8}{25}\, q\,\frac{\partial u}{\partial x}\right], \tag{7.66}$$

$$\begin{aligned}\mathcal{R} = \tilde{\mathcal{R}}_{xx} = -\frac{\tau_r}{A_2}\Bigg[&7\,\theta\,\sigma^s - 7\,\frac{\sigma}{\rho}\,\mathcal{D} + \frac{14}{3}\left(\frac{4}{5}\,\theta - \frac{\sigma}{\rho}\right)\frac{\partial q}{\partial x} + \frac{56}{15}\, q\left(\frac{\partial \theta}{\partial x} - \frac{1}{\rho}\,\frac{\partial \sigma}{\partial x}\right) \\ &- \frac{56}{15}\,\theta\, q\,\frac{\partial \ln \rho}{\partial x} + \left(\frac{8}{3}\,\theta\,\sigma - \frac{14}{3}\,\frac{\sigma^2}{\rho} + \frac{28}{3}\,\rho\,\theta^2\,\Delta\right)\frac{\partial u}{\partial x}\Bigg],\end{aligned} \tag{7.67}$$

$$\begin{aligned}\mathcal{S} = \tilde{S}_x = -\frac{\tau_r}{A_3}\Bigg[&28\,\theta\, q^s - 28\,\frac{q}{\rho}\,\mathcal{D} + \big(140\,\rho\,\theta^2\,\Delta + 28\,\theta\,\sigma\big)\,\frac{\partial \theta}{\partial x} - 35\,\theta^2\,\Delta\,\frac{\partial \sigma}{\partial x} \\ &+ 35\,\rho\,\theta^3\,\frac{\partial \Delta}{\partial x} - \frac{56}{3}\,\frac{q}{\rho}\,\frac{\partial q}{\partial x} + \frac{56}{3}\, q\left(\frac{4}{5}\,\theta - \frac{\sigma}{\rho}\right)\frac{\partial u}{\partial x}\Bigg],\end{aligned} \tag{7.68}$$

$$\mathcal{D} = \frac{4}{3}\frac{d^2}{m}\sqrt{\pi}\,(1-\alpha^2)\left[1 + \frac{3\,\Delta}{16}\right]\rho^2\,\theta^{\frac{3}{2}}, \tag{7.69}$$

$$\sigma^s = -\frac{4}{5}\frac{d^2}{m}\sqrt{\pi\,\theta}\,(1+\alpha)\,(3-\alpha)\left[1 - \frac{\Delta}{32}\right]\rho\,\sigma, \tag{7.70}$$

$$q^s = -\frac{1}{15}\frac{d^2}{m}\sqrt{\pi\,\theta}\,(1+\alpha)\left[49 - 33\,\alpha + (19 - 3\,\alpha)\,\frac{\Delta}{32}\right]\rho\,q, \tag{7.71}$$

$$R^s = -4\,\frac{d^2}{m}\,\sqrt{\pi\,\theta}\,(1+\alpha)\left[(2\,\alpha^2 + 9)\,(1 - \alpha) + (30\,\alpha^2\,(1 - \alpha) + 271 - 207\,\alpha)\,\frac{\Delta}{16}\right]\rho^2\,\theta^2. \tag{7.72}$$

The numerical solution of the plane shock waves using R14-equations is left to a future work. However, we will show some preliminary numerical results on shock waves using R10-equations in Section 7.6.

## 7.5 Euler Equations and Their Regularized Forms

In this section we intend to show that the same idea [Struchtrup & Torrilhon (2003)] that resulted in the R14 equations can be used to derive the equations of Navier-Stokes and Fourier. These familiar equations can be obtained as the regularization of the 5-moment equations, better known as Euler equations. In the following we shall show that the resulting NSF-equations differ slightly if we start from (i) the 13-moment equations [§7.5.1], or, from (ii) the 14-moment theory [§7.5.2].

### 7.5.1 Navier-Stokes-Fourier equations from 13-moment theory

The basic equations of gas dynamics, namely, the Euler equations, are obtained by taking $\phi = m\{1, v_i, \frac{1}{3}C^2\}$, so the variables under consideration are the moments $\rho, \rho\,u_i, p = \rho\,\theta$ and the relevant moment equations are the mass conservation law (7.7), momentum conservation law (7.8)and the energy equation (7.9).These five equations for five field variables $\rho, u_i, \theta$ do not form a closed set due to the presence of the pressure deviator $\sigma_{ij}$ and the heat flux vector $q_i$ in these equations. It follows from (7.21) and (7.35) that the corresponding distribution function for this closure is the Maxwellian distribution, $f|_5 = f^M$. The Maxwellian closure yields

$$\sigma_{ij|5} = 0, \qquad q_{i|5} = 0, \qquad \Delta = 0, \tag{7.73}$$

and the resulting equations are the Euler equations.

It is well-known that the Euler equations are hyperbolic in nature and produces discontinuous shocks in super-sonic flows [Courant & Friedrichs (1948)]. For the regularization of these equations we follow the same procudure adopted in the previous section. First consider the

transport equations for $\sigma_{ij}$ and $q_i$,

$$\frac{\partial \sigma_{ij}}{\partial t} + \frac{\partial(\sigma_{ij}\,u_k)}{\partial x_k} + \frac{4}{5}\frac{\partial q_{\langle i}}{\partial x_{j\rangle}} + \frac{\partial \mathcal{Q}_{ijk}}{\partial x_k} + 2\,p\,\frac{\partial u_{\langle i}}{\partial x_{j\rangle}} + 2\,\sigma_{k\langle i}\frac{\partial u_{j\rangle}}{\partial x_k} = -\frac{A_4}{\tau_r}\,\sigma_{ij}, \tag{7.74}$$

$$\frac{\partial q_i}{\partial t} + \frac{\partial(q_i\,u_j)}{\partial x_j} + \frac{1}{2}\frac{\partial \mathcal{R}_{ij}}{\partial x_j} + \frac{1}{6}\frac{\partial R}{\partial x_i} - \frac{5}{2}\,\theta\left(\rho\,\frac{\partial \theta}{\partial x_i} + \theta\,\frac{\partial \rho}{\partial x_i} + \frac{\partial \sigma_{ij}}{\partial x_j}\right)$$
$$-\frac{\sigma_{ij}}{\rho}\left(\rho\,\frac{\partial \theta}{\partial x_j} + \theta\,\frac{\partial \rho}{\partial x_j} + \frac{\partial \sigma_{jk}}{\partial x_k}\right) + \frac{7}{5}\,q_j\frac{\partial u_i}{\partial x_j} + \frac{2}{5}\,q_i\frac{\partial u_j}{\partial x_j} + \frac{2}{5}\,q_k\frac{\partial u_k}{\partial x_i} + \mathcal{Q}_{ijk}\frac{\partial u_j}{\partial x_k} = -\frac{A_5}{\tau_r}\,q_i, \tag{7.75}$$

where

$$A_4 = \frac{4}{5}\,(1+\alpha)\,(3-\alpha), \tag{7.76}$$

$$A_5 = \frac{1}{15}\,(1+\alpha)\,(49\,-33\,\alpha). \tag{7.77}$$

Note that Eqs. (7.7 - 7.9) and Eqs. (7.74 - 7.75) form the 13-moment theory of Grad. We introduce a small parameter $\varepsilon$ in the right-hand sides of balance equations for $\sigma_{ij}$ and $q_i$, which then read

$$\frac{\partial \sigma_{ij}}{\partial t} + \frac{\partial(\sigma_{ij}\,u_k)}{\partial x_k} + \frac{4}{5}\frac{\partial q_{\langle i}}{\partial x_{j\rangle}} + \frac{\partial \mathcal{Q}_{ijk}}{\partial x_k} + 2\,p\,\frac{\partial u_{\langle i}}{\partial x_{j\rangle}} + 2\,\sigma_{k\langle i}\frac{\partial u_{j\rangle}}{\partial x_k} = -\frac{1}{\varepsilon}\,\frac{A_4}{\tau_r}\,\sigma_{ij}, \tag{7.78}$$

$$\frac{\partial q_i}{\partial t} + \frac{\partial(q_i\,u_j)}{\partial x_j} + \frac{1}{2}\frac{\partial \mathcal{R}_{ij}}{\partial x_j} + \frac{1}{6}\frac{\partial R}{\partial x_i} - \frac{5}{2}\,\theta\left(\rho\,\frac{\partial \theta}{\partial x_i} + \theta\,\frac{\partial \rho}{\partial x_i} + \frac{\partial \sigma_{ij}}{\partial x_j}\right)$$
$$-\frac{\sigma_{ij}}{\rho}\left(\rho\,\frac{\partial \theta}{\partial x_j} + \theta\,\frac{\partial \rho}{\partial x_j} + \frac{\partial \sigma_{jk}}{\partial x_k}\right) + \frac{7}{5}\,q_j\frac{\partial u_i}{\partial x_j} + \frac{2}{5}\,q_i\frac{\partial u_j}{\partial x_j} + \frac{2}{5}\,q_k\frac{\partial u_k}{\partial x_i} + \mathcal{Q}_{ijk}\frac{\partial u_j}{\partial x_k} = -\frac{1}{\varepsilon}\,\frac{A_5}{\tau_r}\,q_i. \tag{7.79}$$

Next, we make the following ansatz [Struchtrup & Torrilhon (2003)],

$$\sigma_{ij} = \sigma_{ij}^{(0)} + \varepsilon\,\sigma_{ij}^{(1)}, \qquad q_i = q_i^{(0)} + \varepsilon\,q_i^{(1)}, \tag{7.80}$$

and compare the same order terms in $\varepsilon$. As expected we find the zeroth-order approximation to be

$$\sigma_{ij}^{(0)} = 0, \qquad q_i^{(0)} = 0, \tag{7.81}$$

which results in the Euler equations.

The first-order approximation yields

$$\left[\frac{\partial \sigma_{ij}}{\partial t} + \frac{\partial(\sigma_{ij}\,u_k)}{\partial x_k} + \frac{4}{5}\frac{\partial q_{\langle i}}{\partial x_{j\rangle}} + \frac{\partial \mathcal{Q}_{ijk}}{\partial x_k} + 2\,p\,\frac{\partial u_{\langle i}}{\partial x_{j\rangle}} + 2\,\sigma_{k\langle i}\frac{\partial u_{j\rangle}}{\partial x_k}\right]_{|_{f_5}} = -\frac{A_4}{\tau_r}\,\sigma_{ij}^{(1)}, \tag{7.82}$$

$$\left[\frac{\partial q_i}{\partial t}+\frac{\partial(q_i\,u_j)}{\partial x_j}+\frac{1}{2}\frac{\partial \mathcal{R}_{ij}}{\partial x_j}+\frac{1}{6}\frac{\partial R}{\partial x_i}-\frac{5}{2}\theta\left(\rho\frac{\partial \theta}{\partial x_i}+\theta\frac{\partial \rho}{\partial x_i}+\frac{\partial \sigma_{ij}}{\partial x_j}\right)\right.$$
$$\left.-\frac{\sigma_{ij}}{\rho}\left(\rho\frac{\partial \theta}{\partial x_j}+\theta\frac{\partial \rho}{\partial x_j}+\frac{\partial \sigma_{jk}}{\partial x_k}\right)+\frac{7}{5}q_j\frac{\partial u_i}{\partial x_j}+\frac{2}{5}q_i\frac{\partial u_j}{\partial x_j}+\frac{2}{5}q_k\frac{\partial u_k}{\partial x_i}+\mathcal{Q}_{ijk}\frac{\partial u_j}{\partial x_k}\right]_{|f_5}=-\frac{A_5}{\tau_r}q_i^{(1)}, \tag{7.83}$$

where all moments inside the notation $\left[\,\cdot\,\right]_{|f_5}$ must be replaced by their values evaluated with the Maxwellian phase density $f_5 = f^M$. The constitutive relations for higher-order moments using the Maxwellian phase density distribution function are given by

$$\sigma_{ij|5}=q_{i|5}=\mathcal{Q}_{ijk|5}=\mathcal{R}_{ij|5}=0 \quad \text{and} \quad R=15\,\rho\,\theta^2. \tag{7.84}$$

From the above constitutive relations, Eq. (7.82) and Eq. (7.83) reduce to Navier-Stokes law for the stress tensor and the Fourier law for the heat flux, respectively, and are given by

$$\sigma_{ij}=\sigma_{ij}^{(1)}=-2\mu\frac{\partial u_{\langle i}}{\partial x_{j\rangle}}, \tag{7.85}$$

$$q_i=q_i^{(1)}=-\kappa\frac{\partial \theta}{\partial x_i}. \tag{7.86}$$

Here, $\mu$ and $\kappa$ denote shear viscosity and thermal conductivity, respectively, and are given as

$$\mu=\frac{5}{4}\frac{m}{d^2}\sqrt{\frac{\theta}{\pi}}\frac{1}{(1+\alpha)(3-\alpha)}, \tag{7.87}$$

$$\kappa=\frac{75}{2}\frac{m}{d^2}\sqrt{\frac{\theta}{\pi}}\frac{1}{(1+\alpha)\,(49-33\alpha)}. \tag{7.88}$$

The above expressions for the transport coefficients of shear viscosity and thermal conductivity coincides with the expressions of Jenkins & Richman (1985*b*) for the hard-sphere gas molecules. Here it is noteworthy to say that the heat flux vector is only proportional to the temperature gradient if we consider up to 13-moment theory.

It may be recalled that Navier-Stokes-Fourier (NSF) equations are parabolic in nature and do not allow discontinuous shock solutions– in contrast, the Euler equations are hyperbolic and admit discontinuous shock solutions. Thus, Navier-Stokes-Fourier (NSF) equations can be considered as the "regularized" version of Euler equations, or, simply the R5-moment equations (i.e. regularized five-field moment theory).

### 7.5.2 NSF equations from 14-moment theory

Here we show that Navier-Stokes-Fourier equations can be obtained from the 14-moment theory. In §7.5.1, we found that the heat flux (7.86) follows the standard Fourier law. It is well-known that the heat flux for a granular gas depends on gradient of density too [(Goldhirsch 2003)]. To obtain this gradient term in the Fourier law, we have to regularize the five-field theory by considering fourteen-field variables as we show below. In this regard, we consider the transport

equations for $\sigma_{ij}$, $q_i$ and $\Delta$,

$$\frac{\partial \sigma_{ij}}{\partial t} + \frac{\partial(\sigma_{ij}\,u_k)}{\partial x_k} + \frac{4}{5}\frac{\partial q_{\langle i}}{\partial x_{j\rangle}} + \frac{\partial \mathcal{Q}_{ijk}}{\partial x_k} + 2\,p\,\frac{\partial u_{\langle i}}{\partial x_{j\rangle}} + 2\,\sigma_{k\langle i}\frac{\partial u_{j\rangle}}{\partial x_k} = -\frac{A_6}{\tau_r}\,\sigma_{ij}, \tag{7.89}$$

$$\frac{\partial q_i}{\partial t} + \frac{\partial(q_i\,u_j)}{\partial x_j} - \frac{5}{2}\,\theta\left(\rho\,\frac{\partial \theta}{\partial x_i} + \theta\,\frac{\partial \rho}{\partial x_i} + \frac{\partial \sigma_{ij}}{\partial x_j}\right) - \frac{\sigma_{ij}}{\rho}\left(\rho\,\frac{\partial \theta}{\partial x_j} + \theta\,\frac{\partial \rho}{\partial x_j} + \frac{\partial \sigma_{jk}}{\partial x_k}\right)$$
$$+ \frac{1}{2}\frac{\partial \mathcal{R}_{ij}}{\partial x_j} + \frac{1}{6}\frac{\partial R}{\partial x_i} + \frac{7}{5}\,q_j\frac{\partial u_i}{\partial x_j} + \frac{2}{5}\,q_i\frac{\partial u_j}{\partial x_j} + \frac{2}{5}\,q_k\frac{\partial u_k}{\partial x_i} + \mathcal{Q}_{ijk}\frac{\partial u_j}{\partial x_k} = -\frac{A_7}{\tau_r}\,q_i, \tag{7.90}$$

$$15\,\rho\,\theta^2\left(\frac{\partial \Delta}{\partial t} + u_i\,\frac{\partial \Delta}{\partial x_i}\right) - 20\,(1+\Delta)\,\theta\left(\frac{\partial q_i}{\partial x_i} + \sigma_{ij}\frac{\partial u_i}{\partial x_j}\right) + \frac{\partial S_i}{\partial x_i} + 4\,\mathcal{R}_{ij}\,\frac{\partial u_i}{\partial x_j}$$
$$- 8\,q_i\,\frac{\partial \theta}{\partial x_i} - \frac{8}{\rho}\,q_i\left(\frac{\partial \sigma_{ij}}{\partial x_j} + \theta\,\frac{\partial \rho}{\partial x_i}\right) = -\frac{A_8}{\tau_r}\,[A_9\,\Delta - A_{10}]\,\rho^2\,\theta^2, \tag{7.91}$$

where

$$A_6 = \frac{4}{5}\,(1+\alpha)\,(3-\alpha)\left[1 - \frac{\Delta}{32}\right], \tag{7.92}$$

$$A_7 = \frac{1}{15}\,(1+\alpha)\left[49 - 33\,\alpha + (19 - 3\,\alpha)\,\frac{\Delta}{32}\right], \tag{7.93}$$

$$A_8 = 4\,(1+\alpha), \tag{7.94}$$

$$A_9 = \frac{1}{16}\left(30\,\alpha^2\,(1-\alpha) - 17\,\alpha + 81\right), \tag{7.95}$$

$$A_{10} = (1-\alpha)\,(1-2\,\alpha^2). \tag{7.96}$$

As a first step in regularization, we introduce the small parameter $\varepsilon$ in the right-hand sides of transport equations for $\sigma_{ij}$, $q_i$ and $\Delta$, which are then read as

$$\frac{\partial \sigma_{ij}}{\partial t} + \frac{\partial(\sigma_{ij}\,u_k)}{\partial x_k} + \frac{4}{5}\frac{\partial q_{\langle i}}{\partial x_{j\rangle}} + \frac{\partial \mathcal{Q}_{ijk}}{\partial x_k} + 2\,p\,\frac{\partial u_{\langle i}}{\partial x_{j\rangle}} + 2\,\sigma_{k\langle i}\frac{\partial u_{j\rangle}}{\partial x_k} = -\frac{1}{\varepsilon}\,\frac{A_6}{\tau_r}\,\sigma_{ij}, \tag{7.97}$$

$$\frac{\partial q_i}{\partial t} + \frac{\partial(q_i\,u_j)}{\partial x_j} - \frac{5}{2}\,\theta\left(\rho\,\frac{\partial \theta}{\partial x_i} + \theta\,\frac{\partial \rho}{\partial x_i} + \frac{\partial \sigma_{ij}}{\partial x_j}\right) - \frac{\sigma_{ij}}{\rho}\left(\rho\,\frac{\partial \theta}{\partial x_j} + \theta\,\frac{\partial \rho}{\partial x_j} + \frac{\partial \sigma_{jk}}{\partial x_k}\right)$$
$$+ \frac{1}{2}\frac{\partial \mathcal{R}_{ij}}{\partial x_j} + \frac{1}{6}\frac{\partial R}{\partial x_i} + \frac{7}{5}\,q_j\frac{\partial u_i}{\partial x_j} + \frac{2}{5}\,q_i\frac{\partial u_j}{\partial x_j} + \frac{2}{5}\,q_k\frac{\partial u_k}{\partial x_i} + \mathcal{Q}_{ijk}\frac{\partial u_j}{\partial x_k} = -\frac{1}{\varepsilon}\,\frac{A_7}{\tau_r}\,q_i, \tag{7.98}$$

$$15\,\rho\,\theta^2\left(\frac{\partial \Delta}{\partial t} + u_i\,\frac{\partial \Delta}{\partial x_i}\right) - 20\,(1+\Delta)\,\theta\left(\frac{\partial q_i}{\partial x_i} + \sigma_{ij}\frac{\partial u_i}{\partial x_j}\right) + \frac{\partial S_i}{\partial x_i} + 4\,\mathcal{R}_{ij}\,\frac{\partial u_i}{\partial x_j}$$
$$- 8\,q_i\,\frac{\partial \theta}{\partial x_i} - \frac{8}{\rho}\,q_i\left(\frac{\partial \sigma_{ij}}{\partial x_j} + \theta\,\frac{\partial \rho}{\partial x_i}\right) = -\frac{1}{\varepsilon}\,\frac{A_8}{\tau_r}\,[A_9\,\Delta - A_{10}]\,\rho^2\,\theta^2, \tag{7.99}$$

Secondly, we make the following ansatz [Struchtrup & Torrilhon (2003, 2013)],

$$\sigma_{ij} = \sigma_{ij}^{(0)} + \varepsilon\,\sigma_{ij}^{(1)}, \qquad q_i = q_i^{(0)} + \varepsilon\,q_i^{(1)}, \qquad \Delta = \Delta^{(0)} + \varepsilon\,\Delta^{(1)}. \tag{7.100}$$

Substituting the above ansatz into equations (7.97)-(7.99) and compare the same order terms in $\varepsilon$. It is easy to verify that the zeroth-order approximation for $\sigma_{ij}$, $q_i$ and $\Delta$, which results from balancing the terms of order $\varepsilon^{-1}$, gives

$$\sigma_{ij}^{(0)} = 0, \qquad q_i^{(0)} = 0, \qquad \text{and} \qquad \Delta^{(0)} = 0. \tag{7.101}$$

Hence the zeroth-order approximation again results in the Euler equations.

Now, balancing the terms of order $\varepsilon^0$ we arrive at the first-order approximation, which yields

$$\left[\frac{\partial \sigma_{ij}}{\partial t} + \frac{\partial(\sigma_{ij}\,u_k)}{\partial x_k} + \frac{4}{5}\frac{\partial q_{\langle i}}{\partial x_{j\rangle}} + \frac{\partial \mathcal{Q}_{ijk}}{\partial x_k} + 2\,p\,\frac{\partial u_{\langle i}}{\partial x_{j\rangle}} + 2\,\sigma_{k\langle i}\frac{\partial u_{j\rangle}}{\partial x_k}\right]_{|_{f_{14}}} = -\frac{1}{\varepsilon}\,\frac{A_6}{\tau_r}\,\sigma_{ij}^{(1)}, \tag{7.102}$$

$$\left[\frac{\partial q_i}{\partial t} + \frac{\partial(q_i\,u_j)}{\partial x_j} - \frac{5}{2}\,\theta\left(\rho\,\frac{\partial \theta}{\partial x_i} + \theta\,\frac{\partial \rho}{\partial x_i} + \frac{\partial \sigma_{ij}}{\partial x_j}\right) - \frac{\sigma_{ij}}{\rho}\left(\rho\,\frac{\partial \theta}{\partial x_j} + \theta\,\frac{\partial \rho}{\partial x_j} + \frac{\partial \sigma_{jk}}{\partial x_k}\right)\right.$$
$$\left. + \frac{1}{2}\frac{\partial \mathcal{R}_{ij}}{\partial x_j} + \frac{1}{6}\,\frac{\partial R}{\partial x_i} + \frac{7}{5}\,q_j\frac{\partial u_i}{\partial x_j} + \frac{2}{5}\,q_i\frac{\partial u_j}{\partial x_j} + \frac{2}{5}\,q_k\frac{\partial u_k}{\partial x_i} + \mathcal{Q}_{ijk}\frac{\partial u_j}{\partial x_k}\right]_{|_{f_{14}}} = -\frac{1}{\varepsilon}\,\frac{A_7}{\tau_r}\,q_i^{(1)}, \tag{7.103}$$

$$\left[15\,\rho\,\theta^2\left(\frac{\partial \Delta}{\partial t} + u_i\,\frac{\partial \Delta}{\partial x_i}\right) - 20\,(1+\Delta)\,\theta\left(\frac{\partial q_i}{\partial x_i} + \sigma_{ij}\frac{\partial u_i}{\partial x_j}\right) + \frac{\partial S_i}{\partial x_i} + 4\,\mathcal{R}_{ij}\,\frac{\partial u_i}{\partial x_j}\right.$$
$$\left. - 8\,q_i\,\frac{\partial \theta}{\partial x_i} - \frac{8}{\rho}\,q_i\left(\frac{\partial \sigma_{ij}}{\partial x_j} + \theta\,\frac{\partial \rho}{\partial x_i}\right)\right]_{|_{f_{14}}} = -\frac{1}{\varepsilon}\,\frac{A_8}{\tau_r}\,\left[A_9\,\Delta^{(1)} - A_{10}\right]\,\rho^2\,\theta^2, \tag{7.104}$$

where all moments inside the notation $\left[\cdot\right]_{|_{f_{14}}}$ must be replaced by their values evaluated with the 14-moment phase density $f_{14}$ which is given by (7.21). The constitutive relations for higher-order moments using the 14-moment phase density distribution function are given by

$$\mathcal{Q}_{ijk|14} = 0, \qquad \mathcal{R}_{ij|14} = 7\,\theta\,\sigma_{ij}, \qquad S_{i|14} = 28\,\theta\,q_i, \qquad R = 15\,\rho\,\theta^2(1+\Delta). \tag{7.105}$$

By substituting the constitutive relations (7.105) into equations (7.102) -(7.104) and balancing the terms of order $\varepsilon^0$, equations (7.102) -(7.104) reduces to the following.

$$\sigma_{ij}^{(1)} = -\frac{2\,p\,\tau_r}{A_6}\,\frac{\partial u_{\langle i}}{\partial x_{j\rangle}}, \tag{7.106}$$

$$q_i^{(1)} = -\frac{5\,\tau_r}{2\,A_7}\left[\rho\,\theta\,\frac{\partial \theta}{\partial x_i} + 2\,\rho\,\theta\,\Delta^{(1)}\,\frac{\partial \theta}{\partial x_i} + \theta^2\,\Delta^{(1)}\,\frac{\partial \rho}{\partial x_i} + \rho\,\theta^2\,\frac{\partial \Delta^{(1)}}{\partial x_i}\right], \tag{7.107}$$

$$\Delta^{(1)} = \frac{A_{10}}{A_9} = \frac{16\,(1-\alpha)\,(1-2\,\alpha^2)}{\left(30\,\alpha^2\,(1-\alpha) - 17\,\alpha + 81\right)} = \Delta. \tag{7.108}$$

Finally substituting (7.108) into equations (7.106) and (7.107) we arrive at Navier-Stokes law and the Fourier law, respectively, and are given by

$$\sigma_{ij} = \sigma_{ij}^{(1)} = -2\,\mu\,\frac{\partial u_{\langle i}}{\partial x_{j\rangle}}, \tag{7.109}$$

$$q_i = q_i^{(1)} = -\kappa\,\frac{\partial \theta}{\partial x_i} - \kappa_h\,\frac{\partial \rho}{\partial x_i}. \tag{7.110}$$

Here, $\mu$, $\kappa$ and $\kappa_h$ denote shear viscosity, thermal conductivity and higher-order thermal con-

ductivity, respectively, and are given

$$\mu = \frac{5}{4}\frac{m}{d^2}\sqrt{\frac{\theta}{\pi}}\frac{1}{(1+\alpha)(3-\alpha)\left[1-\frac{\Delta}{32}\right]}, \tag{7.111}$$

$$\kappa = \frac{75}{2}\frac{m}{d^2}\sqrt{\frac{\theta}{\pi}}\frac{1+2\Delta}{(1+\alpha)\left[49-33\alpha+(19-3\alpha)\frac{\Delta}{32}\right]}, \tag{7.112}$$

$$\kappa_h = \frac{75}{2\rho}\frac{m}{d^2}\theta\sqrt{\frac{\theta}{\pi}}\frac{\Delta}{(1+\alpha)\left[49-33\alpha+(19-3\alpha)\frac{\Delta}{32}\right]}. \tag{7.113}$$

The above expressions for the shear viscosity $\mu$, thermal conductivity $\kappa$ and the higher-order thermal conductivity $\kappa_h$ are coincide with the expressions of (Garzó *et al.* 2007) and (Kremer & Marques Jr 2011) and by neglecting $\Delta$ these expressions coincide with the expressions of Jenkins & Richman (1985*b*).

It is noteworthy that the heat flux vector, Eq. (7.110), is proportional to the temperature gradient and also to the density gradient. The latter "non-Fourier" term is the main difference between Navier-Stokes-Fourier equations obtained here and in §7.5.1. Of course, the transport co-efficients obtained here [Eq. (7.111) - (7.113)] differ slightly from those in §7.5.1 [Eq. (7.87) - (7.88)] due to the non-zero value of the fourth-order contracted moment ($\Delta$).

## 7.6 Planar Steady Shock: Smooth Solution from R10 Equations

Our analysis in §5.4 of Chapter 5 for steady plane shock waves using 10-moment model resulted into a single ODE for the density field $\rho(x)$:

$$\frac{\mathrm{d}\rho}{\mathrm{d}x} = \frac{\rho^3}{3(\gamma \mathrm{Ma}_1^2+1)C_1\,\rho_1\,\theta_1}\left[\frac{\mathcal{D}-\sigma^s}{\rho-\rho_c}\right], \tag{7.114}$$

where

$$\rho_c = \frac{4\gamma \mathrm{Ma}_1^2}{3(\gamma \mathrm{Ma}_1^2+1)}\rho_1 \tag{7.115}$$

Clearly, the density gradient blows up when $\rho \geq \rho_c$, or, when $\mathrm{Ma} > \mathrm{Ma}_{cr} = 3/\sqrt{5}$. We reanalyse this problem in §7.6.2 using R10 equations as derived in §7.6.1.

### 7.6.1 R10 equations: derivation

Consider the 10-moment equations for a dilute granular gas.The variables under consideration in the 10-moment system are the moments $\rho, \rho\,u_i, p, \sigma_{ij}$. Hence the basic transport equations

for the this system $(\rho, \rho\, u_i, \theta, \sigma_{ij})$ of dilute granular gas read as

$$\frac{\partial \rho}{\partial t} + \frac{\partial\,(\rho\, u_i)}{\partial x_i} = 0, \tag{7.116}$$

$$\frac{\partial\,(\rho\, u_i)}{\partial t} + \frac{\partial\,(\rho\, u_i\, u_j)}{\partial x_j} + \frac{\partial p}{\partial x_i} + \frac{\partial \sigma_{ij}}{\partial x_j} = 0, \tag{7.117}$$

$$\rho\left(\frac{\partial \theta}{\partial t} + u_i \frac{\partial \theta}{\partial x_i}\right) + \frac{2}{3}\left(\rho\,\theta \frac{\partial u_i}{\partial x_i} + \sigma_{ij}\frac{\partial u_i}{\partial x_j} + \underline{\frac{\partial q_i}{\partial x_i}}\right) = -\mathcal{D}, \tag{7.118}$$

$$\frac{\partial \sigma_{ij}}{\partial t} + \frac{\partial(\sigma_{ij}\, u_k)}{\partial x_k} + \underline{\frac{4}{5}\frac{\partial q_{\langle i}}{\partial x_{j\rangle}} + \frac{\partial \mathcal{Q}_{ijk}}{\partial x_k}} + 2\,p\frac{\partial u_{\langle i}}{\partial x_{j\rangle}} + 2\,\sigma_{k\langle i}\frac{\partial u_{j\rangle}}{\partial x_k} = \sigma^s_{ij}, \tag{7.119}$$

where the angular brackets over subscripts denote deviatoric part of respective terms. The first two equations (7.116) and (7.117) represent the conservation laws for mass and momentum, respectively, while Eqs. (7.118) and (7.119) represent the balance laws for the energy and the deviatoric part of the pressure tensor, respectively. Equations (7.118) and (7.119) do not form a closed set of equations as they contains additional moments, $q_i$ and $\mathcal{Q}_{ijk}$ of higher order. These additional terms must be related to the variables under consideration via the distribution function. The variables under consideration in 10-moment system, the Grad's non-equilibrium distribution function [Kremer & Marques Jr (2011)] reads

$$f|_{10} = f^M\left(1 + \frac{\sigma_{ij}}{2\rho\theta^2} C_i C_j\right). \tag{7.120}$$

With the help of the distribution function (7.120) one can obtain the higher-order moments presented in equations (7.118) and (7.119) to be

$$q_{i|10} = 0, \qquad \mathcal{Q}_{ijk|10} = 0, \tag{7.121}$$

and the collisional source terms $\mathcal{D}$ and $\sigma^s_{ij}$ are given in (7.23) with $\Delta$ to be zero. Therefore, the 10-moment system consists of Eqs. (7.116 - 7.119) in the absence of underlined terms.

In order to regularize the 10-moment system, one has to consider the moment equations for $q_i$ and $\mathcal{Q}_{ijk}$. The moment transport equations for $q_i$ and $\mathcal{Q}_{ijk}$ are given by

$$\begin{aligned}
&\frac{\partial q_i}{\partial t} + \frac{\partial(q_i\, u_j)}{\partial x_j} + \frac{1}{2}\frac{\partial \mathcal{R}_{ij}}{\partial x_j} + \frac{1}{6}\frac{\partial R}{\partial x_i} - \frac{5}{2}\theta\left(\rho\frac{\partial \theta}{\partial x_i} + \theta\frac{\partial \rho}{\partial x_i} + \frac{\partial \sigma_{ij}}{\partial x_j}\right)\\
&- \frac{\sigma_{ij}}{\rho}\left(\rho\frac{\partial \theta}{\partial x_j} + \theta\frac{\partial \rho}{\partial x_j} + \frac{\partial \sigma_{jk}}{\partial x_k}\right) + \frac{7}{5}q_j\frac{\partial u_i}{\partial x_j} + \frac{2}{5}q_i\frac{\partial u_j}{\partial x_j} + \frac{2}{5}q_k\frac{\partial u_k}{\partial x_i} + \mathcal{Q}_{ijk}\frac{\partial u_j}{\partial x_k} = q^s_i,
\end{aligned} \tag{7.122}$$

$$\begin{aligned}
&\frac{\partial \mathcal{Q}_{ijk}}{\partial t} + \frac{\partial\,(\mathcal{Q}_{ijk}\, u_l)}{\partial x_l} + \frac{\partial \mathcal{R}_{ijkl}}{\partial x_l} + \frac{3}{7}\frac{\partial \mathcal{R}_{\langle ij}}{\partial x_{k\rangle}} - \frac{3}{\rho}\sigma_{\langle ij}\frac{\partial p}{\partial x_{k\rangle}} - \frac{3}{\rho}\sigma_{\langle ij}\frac{\partial \sigma_{k\rangle l}}{\partial x_l}\\
&\qquad + 3\,\mathcal{Q}_{l\langle ij}\frac{\partial u_{k\rangle}}{\partial x_l} + \frac{12}{5}q_{\langle i}\frac{\partial u_{k\rangle}}{\partial x_j} = \mathcal{Q}^s_{ijk}.
\end{aligned} \tag{7.123}$$

The higher-order moments involved in the above equations are evaluated with the distribution function $f|_{10}$, which is given in (7.120) and are given by

$$R = 15\,\rho\,\theta^2, \qquad \mathcal{R}_{ij|10} = 7\,\theta\,\sigma_{ij}, \qquad \mathcal{R}_{ijkl|10} = 0. \tag{7.124}$$

The source terms $q_i^s$ and $\mathcal{Q}_{ijk}^s$ are given by

$$q_i^s = -\frac{A_5}{\tau_r}\, q_i, \qquad \mathcal{Q}_{ijk}^s = -\frac{A_1}{\tau_r}\, \mathcal{Q}_{ijk}. \tag{7.125}$$

As discussed in Sec.7.3 and 7.4, we assume that the non-equilibrium moments of the 10-moment system, i.e., $\sigma_{ij}$, change on the time scale defined by $\tau_r$, while the remaining higher-order non-equilibrium moments $q_i$ and $\mathcal{Q}_{ijk}$ change on a faster time scale $\varepsilon\,\tau_r$, where $\varepsilon$ is a small parameter. Using these argument, equations (7.122) and (7.123) are changed slightly on the right hand side which contains the small parameter $\varepsilon$:

$$\begin{aligned}
&\frac{\partial q_i}{\partial t} + \frac{\partial (q_i\, u_j)}{\partial x_j} + \frac{1}{2}\frac{\partial \mathcal{R}_{ij}}{\partial x_j} + \frac{1}{6}\frac{\partial R}{\partial x_i} - \frac{5}{2}\,\theta\left(\rho\,\frac{\partial \theta}{\partial x_i} + \theta\,\frac{\partial \rho}{\partial x_i} + \frac{\partial \sigma_{ij}}{\partial x_j}\right)\\
&- \frac{\sigma_{ij}}{\rho}\left(\rho\,\frac{\partial \theta}{\partial x_j} + \theta\,\frac{\partial \rho}{\partial x_j} + \frac{\partial \sigma_{jk}}{\partial x_k}\right) + \frac{7}{5}\,q_j\frac{\partial u_i}{\partial x_j} + \frac{2}{5}\,q_i\frac{\partial u_j}{\partial x_j} + \frac{2}{5}\,q_k\frac{\partial u_k}{\partial x_i} + \mathcal{Q}_{ijk}\frac{\partial u_j}{\partial x_k} = -\frac{1}{\varepsilon}\,\frac{A_5}{\tau_r}\,q_i,,
\end{aligned} \tag{7.126}$$

$$\begin{aligned}
&\frac{\partial \mathcal{Q}_{ijk}}{\partial t} + \frac{\partial\,(\mathcal{Q}_{ijk}\,u_l)}{\partial x_l} + \frac{\partial \mathcal{R}_{ijkl}}{\partial x_l} + \frac{3}{7}\,\frac{\partial \mathcal{R}_{\langle ij}}{\partial x_{k\rangle}} - \frac{3}{\rho}\,\sigma_{\langle ij}\,\frac{\partial p}{\partial x_{k\rangle}} - \frac{3}{\rho}\,\sigma_{\langle ij}\,\frac{\partial \sigma_{k\rangle l}}{\partial x_l}\\
&\qquad + 3\,\mathcal{Q}_{l\langle ij}\,\frac{\partial u_{k\rangle}}{\partial x_l} + \frac{12}{5}\,q_{\langle i}\,\frac{\partial u_{k\rangle}}{\partial x_j} = -\frac{1}{\varepsilon}\,\frac{A_1}{\tau_r}\,\mathcal{Q}_{ijk}.
\end{aligned} \tag{7.127}$$

As before inserting the following ansatz

$$q_i = q_i^{(0)} + \varepsilon\, q_i^{(1)} + \cdots, \tag{7.128}$$

$$\mathcal{Q}_{ijk} = \mathcal{Q}_{ijk}^{(0)} + \varepsilon\, \mathcal{Q}_{ijk}^{(1)} + \cdots, \tag{7.129}$$

into equations (7.126) and (7.127), and comparing the terms of the same order in $\varepsilon$, it is straightforward to verify that the zeroth-order approximations of $q_i$ and $\mathcal{Q}_{ijk}$ resulting from balancing terms of order $\varepsilon^{-1}$, gives

$$q_i^{(0)} = 0, \qquad \mathcal{Q}_{ijk}^{(0)} = 0. \tag{7.130}$$

Hence the zeroth-order approximation gives the original 10-moment system. The first-order approximations of $q_i$ and $\mathcal{Q}_{ijk}$, resulting from balancing terms of order $\varepsilon^0$, can be written as

$$\begin{aligned}
&\left[\frac{\partial q_i}{\partial t} + \frac{\partial (q_i\, u_j)}{\partial x_j} + \frac{1}{2}\frac{\partial \mathcal{R}_{ij}}{\partial x_j} + \frac{1}{6}\frac{\partial R}{\partial x_i} - \frac{5}{2}\,\theta\left(\rho\,\frac{\partial \theta}{\partial x_i} + \theta\,\frac{\partial \rho}{\partial x_i} + \frac{\partial \sigma_{ij}}{\partial x_j}\right)\right.\\
&\left.- \frac{\sigma_{ij}}{\rho}\left(\rho\,\frac{\partial \theta}{\partial x_j} + \theta\,\frac{\partial \rho}{\partial x_j} + \frac{\partial \sigma_{jk}}{\partial x_k}\right) + \frac{7}{5}\,q_j\frac{\partial u_i}{\partial x_j} + \frac{2}{5}\,q_i\frac{\partial u_j}{\partial x_j} + \frac{2}{5}\,q_k\frac{\partial u_k}{\partial x_i} + \mathcal{Q}_{ijk}\frac{\partial u_j}{\partial x_k}\right]_{|f_{10}} = -\frac{A_5}{\tau_r}\,q_i^{(1)},
\end{aligned} \tag{7.131}$$

$$\begin{aligned}
&\left[\frac{\partial \mathcal{Q}_{ijk}}{\partial t} + \frac{\partial\,(\mathcal{Q}_{ijk}\,u_l)}{\partial x_l} + \frac{\partial \mathcal{R}_{ijkl}}{\partial x_l} + \frac{3}{7}\,\frac{\partial \mathcal{R}_{\langle ij}}{\partial x_{k\rangle}} - \frac{3}{\rho}\,\sigma_{\langle ij}\,\frac{\partial p}{\partial x_{k\rangle}} - \frac{3}{\rho}\,\sigma_{\langle ij}\,\frac{\partial \sigma_{k\rangle l}}{\partial x_l}\right.\\
&\qquad \left. + 3\,\mathcal{Q}_{l\langle ij}\,\frac{\partial u_{k\rangle}}{\partial x_l} + \frac{12}{5}\,q_{\langle i}\,\frac{\partial u_{k\rangle}}{\partial x_j}\right]_{|f_{10}} = -\frac{A_1}{\tau_r}\,\mathcal{Q}_{ijk}^{(1)},
\end{aligned} \tag{7.132}$$

where the notation $\Big[\cdot\Big]_{|_{f_{10}}}$ indicates that all moments inside the square brackets must be evaluated with the ten field phase density $f_{10}$, which is given in (7.120). The corrections to 10-moment equations are obtained as

$$q_i = q_i^{(1)} = -\frac{\tau_r}{A_5}\left[\frac{5}{2}\rho\,\theta\,\frac{\partial\theta}{\partial x_i} + \frac{5}{2}\sigma_{ij}\,\frac{\partial\theta}{\partial x_j} + \theta\,\frac{\partial\sigma_{ij}}{\partial x_j} - \theta\,\sigma_{ij}\,\frac{\partial\ln\rho}{\partial x_j} - \frac{\sigma_{ij}}{\rho}\,\frac{\partial\sigma_{jk}}{\partial x_k}\right], \tag{7.133}$$

$$\mathcal{Q}_{ijk} = \mathcal{Q}_{ijk}^{(1)} = -\frac{3\,\tau_r}{A_1}\left[\theta\,\frac{\partial\sigma_{\langle ij}}{\partial x_{k\rangle}} - \theta\,\sigma_{\langle ij}\,\frac{\partial\ln\rho}{\partial x_{k\rangle}} - \frac{\sigma_{\langle ij}}{\rho}\,\frac{\partial\sigma_{k\rangle l}}{\partial x_l}\right], \tag{7.134}$$

The above corrections must be inserted into the energy equation (7.118) and the stress tensor equation (7.119) to get the complete set of regularized equations for the 10-field variables $\rho, u_i, \theta, \sigma_{ij}$ that consists of Eqs. (7.116) - (7.119) with higher-order terms given by (7.133) - (7.134). We refer to these equations as the R10 equations from now onwards, where "R" stands for "regularized", and 10 denotes the number of field variables.

### 7.6.2 One-dimensional conservation form of R10 equations

The R10-moment model is reduced to a system of four equations for the plane shock wave problem. The one-dimensional field equations for R10-moment system, which involves four field variables namely, the density $(\rho(x,t))$, the velocity $(u(x,t))$, the scalar temperature $(\theta(x,t))$, and the longitudinal stress $(\sigma(x,t))$. The one-dimensional equations for the R10-moment model are

$$\frac{\partial\rho}{\partial t} + \frac{\partial}{\partial x}\Big(\rho\,u\Big) = 0, \tag{7.135}$$

$$\frac{\partial}{\partial t}\Big(\rho\,u\Big) + \frac{\partial}{\partial x}\Big(\rho\,u^2 + \rho\,\theta + \sigma\Big) = 0, \tag{7.136}$$

$$\frac{\partial}{\partial t}\Big(\rho\,u^2 + 3\,\rho\,\theta\Big) + \frac{\partial}{\partial x}\Big(\rho\,u^3 + 5\,\rho\,\theta\,u + 2\,\sigma\,u + \underline{2\,q}\Big) = -3\,\mathcal{D}, \tag{7.137}$$

$$\frac{\partial}{\partial t}\Big(\frac{2}{3}\,\rho\,u^2 + \sigma\Big) + \frac{\partial}{\partial x}\Big(\frac{2}{3}\,\rho\,u^3 + \frac{4}{3}\,\rho\,\theta\,u + \frac{7}{3}\,\sigma\,u + \underline{\frac{8}{15}\,q + \mathcal{Q}}\Big) = \sigma^s, \tag{7.138}$$

where $q$ and $\mathcal{Q}$ are non-zero terms which are arising from the regularization and these terms are underlined in (7.137) and (7.138). The expressions for these non-zero terms and the source terms $\mathcal{D}$ and $\sigma^s$ are given by:

$$q = q_x = -\frac{\tau_r}{A_5}\left[\frac{5}{2}\,(\rho\,\theta + \sigma)\,\frac{\partial\theta}{\partial x} + \left(\theta - \frac{\sigma}{\rho}\right)\frac{\partial\sigma}{\partial x} - \theta\,\sigma\,\frac{\partial\ln\rho}{\partial x}\right], \tag{7.139}$$

$$\mathcal{Q} = \tilde{\mathcal{Q}}_{xxx} = -\frac{9\,\tau_r}{5\,A_1}\left[\theta\,\frac{\partial\sigma}{\partial x} - \theta\,\sigma\,\frac{\partial\ln\rho}{\partial x} - \frac{\sigma}{\rho}\,\frac{\partial\sigma}{\partial x}\right], \tag{7.140}$$

$$\mathcal{D} = \frac{4}{3}\frac{d^2}{m}\sqrt{\pi}\,(1-\alpha^2)\,\rho^2\,\theta^{\frac{3}{2}}, \tag{7.141}$$

$$\sigma^s = -\frac{4}{5}\frac{d^2}{m}\sqrt{\pi\,\theta}\,(1+\alpha)\,(3-\alpha)\,\rho\,\sigma. \tag{7.142}$$

Now, we focus on the R10-moment system for a planar shock moving at a constant speed, i.e. the shock is stationary in a reference frame which is moving with the shock speed and hence the time derivatives vanish. For a planar stationary shock, the R10-moment equations for a dilute granular gas boil down to:

$$\frac{\mathrm{d}}{\mathrm{d}x}\Big(\rho u\Big) = 0, \tag{7.143}$$

$$\frac{\mathrm{d}}{\mathrm{d}x}\Big(\rho u^2 + \rho\theta + \sigma\Big) = 0, \tag{7.144}$$

$$\frac{\mathrm{d}}{\mathrm{d}x}\Big(\rho u^3 + 5\rho\theta u + 2\sigma u\Big) = -3\,\mathcal{D} \,-\, 2\,\frac{\mathrm{d}q}{\mathrm{d}x}, \tag{7.145}$$

$$\frac{\mathrm{d}}{\mathrm{d}x}\Big(\frac{2}{3}\rho u^3 + \frac{4}{3}\rho\theta u + \frac{7}{3}\sigma u\Big) = \sigma^s \,-\, \frac{8}{15}\,\frac{\mathrm{d}q}{\mathrm{d}x} \,-\, \frac{\mathrm{d}\mathcal{Q}}{\mathrm{d}x}. \tag{7.146}$$

The boundary conditions for the above system of ODEs are supplied by the RH relations and $\theta_{s1} = 0 = \theta_{s2}$. Solving the first two equations of (7.143 - 7.152) and using the boundary conditions, we get:

$$\begin{aligned} C_1 &= \rho u \,=\, \rho_1 u_1, \\ C_2 &= \rho u^2 + \rho\theta + \sigma \;=\; (\gamma \mathrm{Ma}_1^2 + 1)\rho_1\theta_1. \end{aligned} \tag{7.147}$$

Recall that $\sigma = 0$ at both upstream and downstream ends. Using the relations (7.147), the system of ODEs (7.143 - 7.152) can be combined to get following coupled ODEs for $\rho(x)$ and $\theta(x)$,

$$\frac{\mathrm{d}\rho}{\mathrm{d}x} = \frac{\rho^3}{3(\gamma \mathrm{Ma}_1^2 + 1)C_1\,\rho_1\,\theta_1}\left[\frac{\mathcal{D} \,-\, \sigma^s \,+\, \frac{6}{5}\,\frac{\mathrm{d}q}{\mathrm{d}x} \,+\, \frac{\mathrm{d}\mathcal{Q}}{\mathrm{d}x}}{\rho - \rho_c}\right], \tag{7.148}$$

$$\frac{\mathrm{d}\theta}{\mathrm{d}x} = \frac{1}{3\,C_1}\left(-2\,\mathcal{D} \,-\, \sigma^s \,-\, \frac{4}{5}\,\frac{\mathrm{d}q}{\mathrm{d}x} \,+\, \frac{\mathrm{d}\mathcal{Q}}{\mathrm{d}x}\right) + \left(\frac{2\,C_1^2 \,-\, \rho\,C_2}{3\,\rho^3}\right)\frac{\mathrm{d}\rho}{\mathrm{d}x}, \tag{7.149}$$

$$\tag{7.150}$$

along with two algebraic equations

$$u = \frac{C_1}{\rho}, \qquad \sigma = C_2 \,-\, \frac{C_1^2}{\rho} \,-\, \rho\,\theta, \tag{7.151}$$

where

$$\rho_c = \frac{4\gamma \mathrm{Ma}_1^2}{3(\gamma \mathrm{Ma}_1^2 + 1)}\rho_1, \tag{7.152}$$

and the expressions for $q$, $\mathcal{Q}$, $\mathcal{D}$ and $\sigma^s$ are given in (7.139) - (7.142), respectively. The presence of $\frac{\mathrm{d}q}{\mathrm{d}x}$ and $\frac{\mathrm{d}\mathcal{Q}}{\mathrm{d}x}$ results in second-order gradient terms $[\frac{\mathrm{d}^2\rho}{\mathrm{d}x^2}, \frac{\mathrm{d}^2\theta}{\mathrm{d}x^2}]$ in (7.148) which smoothens discontinuous solutions as demonstrated in §7.7.

## 7.7 Comparison Between 10-M and R10-M Models for Plane Shock Waves: Numerical Results

Here we analyze the Riemann problem of planar shock waves for a molecular gas as well as for a granular gas by solving the R10-moment equations and the results are compared with those obtained from the 10-moment equations. The upstream boundary conditions for this plane shock wave problem are taken as

$$\rho_1 = 1, \quad u_1 = \mathrm{Ma}_1 \sqrt{\gamma}, \quad \theta_1 = 1, \quad \sigma_1 = 0, \tag{7.153}$$

while the downstream boundary conditions are provided by RH jump conditions (3.11) which are given by

$$\begin{aligned} \rho_2 &= \frac{(\gamma+1)\mathrm{Ma}_1^2}{2+(\gamma-1)\mathrm{Ma}_1^2}\,\rho_1, \\ u_2 &= \frac{2+(\gamma-1)\mathrm{Ma}_1^2}{(\gamma+1)\mathrm{Ma}_1^2}\,u_1, \\ \theta_2 &= \frac{(2\gamma\mathrm{Ma}_1^2-(\gamma-1))((\gamma-1)\mathrm{Ma}_1^2+2)}{(\gamma+1)^2\mathrm{Ma}_1^2}\,\theta_1, \\ \sigma_2 &= 0. \end{aligned} \tag{7.154}$$

### 7.7.1 Comparison for a molecular gas

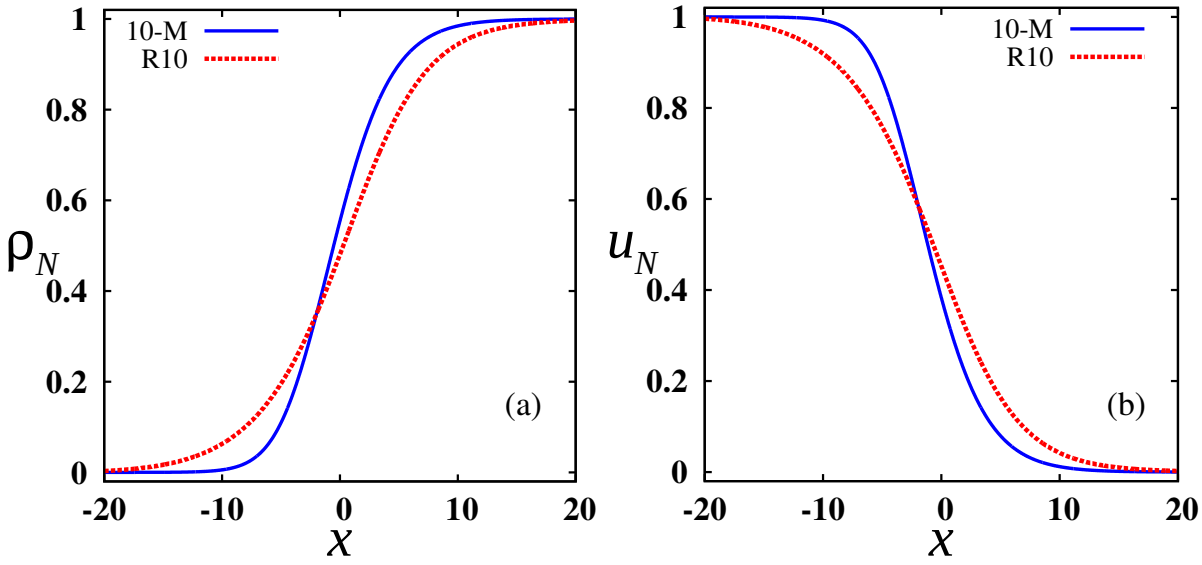


Figure 7.1: Molecular shock wave profiles as predicted by R10 and 10-moment model for an upstream Mach number $\mathrm{Ma}_1 = 1.2$: (a) density and (b) velocity.

First, we perform numerical simulations of shock waves in a molecular gas using the numerical scheme of Delis & Katsaounis (2003), which is described in the §3.5.2. We have done plane shock wave numerical experiments by considering an one-dimensional domain of length 50 covering $(-25, 25)$ with 2000 grid points, until a time of 100 with $\Delta t = \mathcal{C} \cdot \Delta x / max(a_i)$ and placing

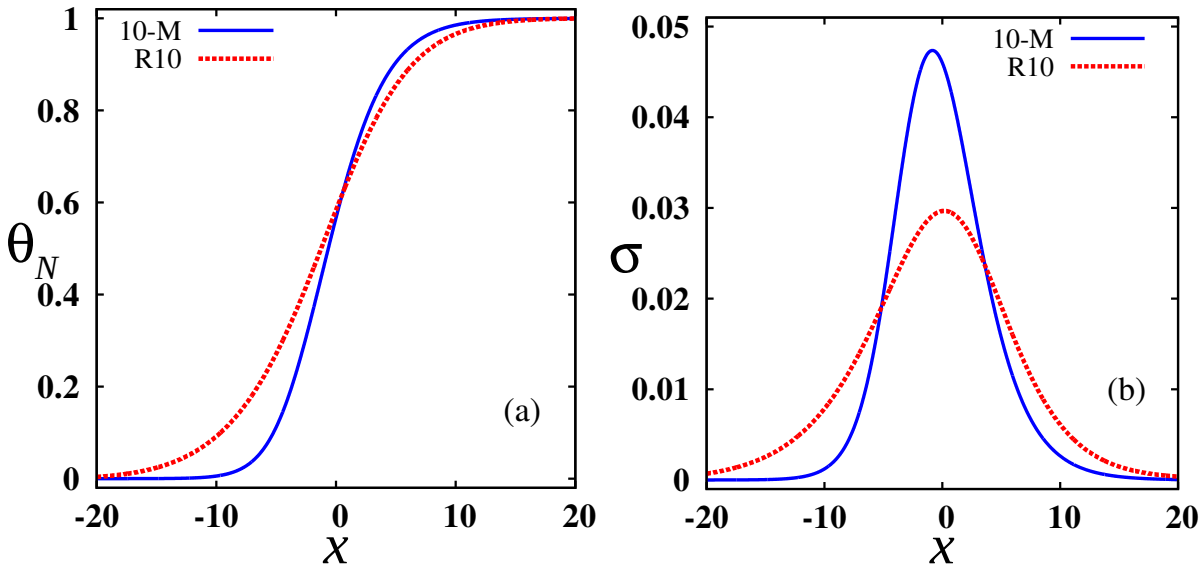


Figure 7.2: Molecular shock wave profiles as predicted by R10 and 10-moment model for an upstream Mach number $\mathrm{Ma}_1 = 1.2$: (a) temperature and (b) longitudinal stress.

the initial discontinuity at $x = 0$. In all numerical experiments we take the relaxation rate $\epsilon$ in (3.40) to be $10^{-8}$ as this gives converged results for both molecular and granular gases. We have pointed out in §6.2 that the CFL number should be very small for Navier-Stokes model which is treated as R5 model. This true in the case of R10-moment model also. So for present computations of shocks in a molecular gas, we take the CFL($\mathcal{C}$) number as 0.01, which gives the stable solution.

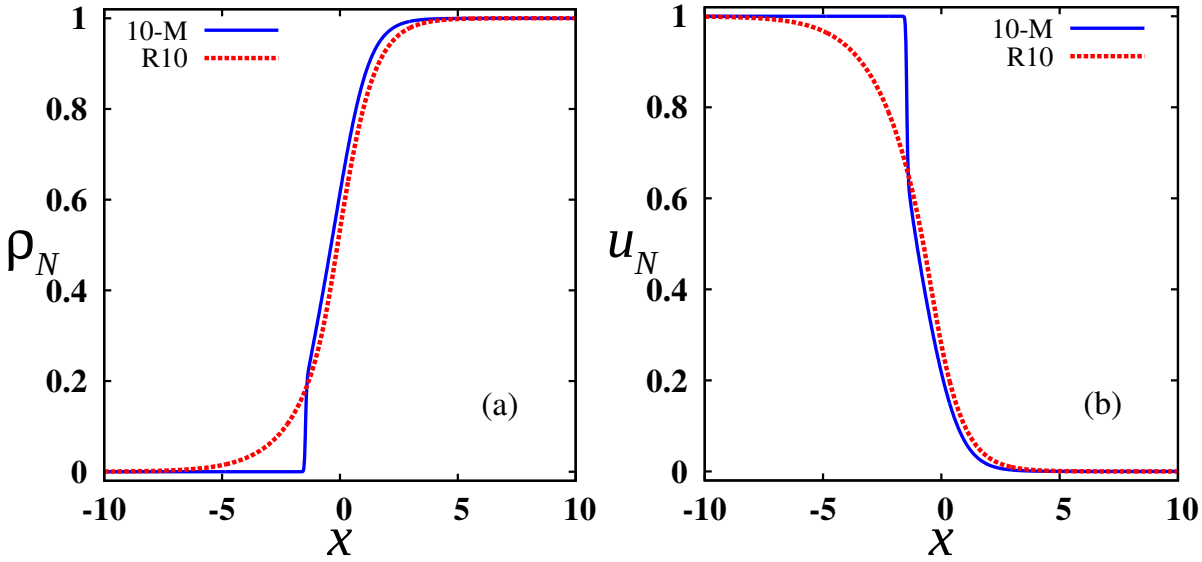


Figure 7.3: Molecular shock wave profiles as predicted by R10 and 10-moment model for an upstream Mach number $\mathrm{Ma}_1 = 2$: (a) density and (b) velocity.

As we know from §5.4 that the critical Mach number for 10-moment model is $\mathrm{Ma}_{cr|_{10}} = 1.34$. To show the clear-cut advantage of the R10-moment model over the 10-moment model, we present the results by choosing two different Mach numbers, in which one is less than $\mathrm{Ma}_{cr|_{10}}$ and

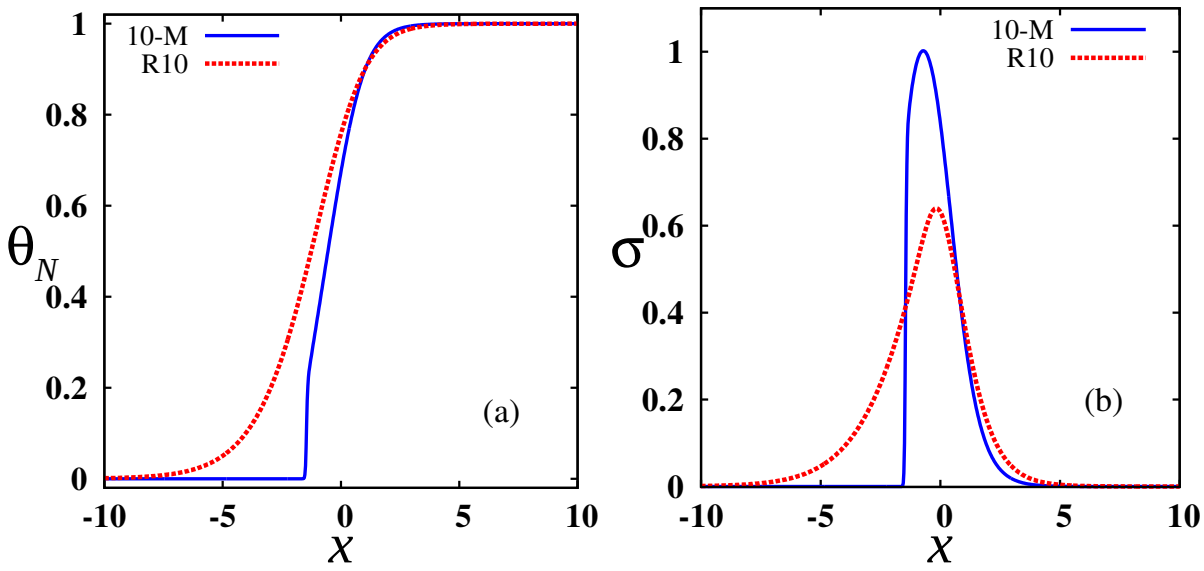


Figure 7.4: Molecular shock wave profiles as predicted by R10 and 10-moment model for an upstream Mach number $\mathrm{Ma}_1 = 2$: (a) temperature and (b) longitudinal stress.

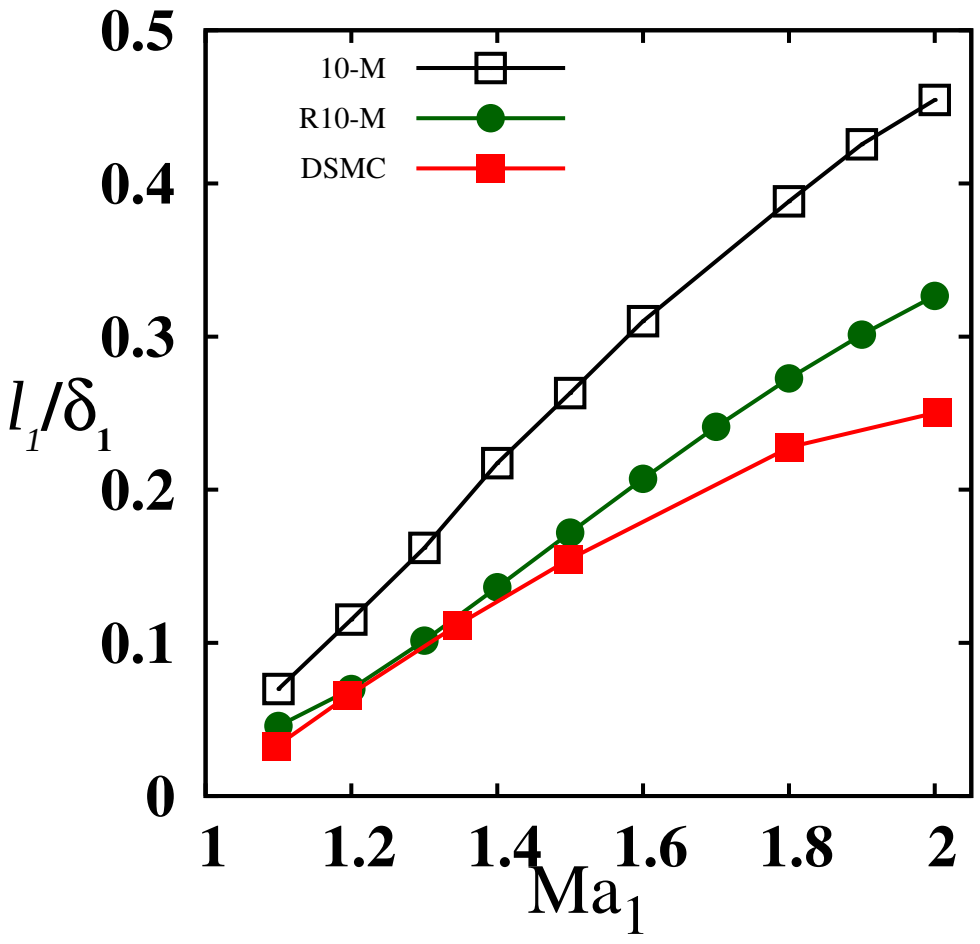


Figure 7.5: Inverse shock width vs Mach number for a molecular gas. 10-moment and DSMC results on inverse shock width are same as in Fig. 6.18, but upto a Mach number of 2.

other is greater than $\mathrm{Ma}_{cr|_{10}}$. The density, velocity and the temperature profiles are normalized via (6.11) and (6.12), respectively, for a molecular case comparison. For a Mach number $\mathrm{Ma}_1 = 1.2$, the density and velocity profiles are presented in Fig. 7.1 (a), (b), and the temperature and longitudinal stress profiles are shown in Fig. 7.2 (a), (b). At this upstream Mach number both models produce continuous shock structure but a qualitative and quantitative difference can be seen in all profiles [see Figs. 7.1 & 7.2]. By comparing the density, velocity, temperature and the longitudinal stress from Fig. reffig:7f1 and 7.2, we comment that all profiles predicted by R10-moment model are more diffusive on both upstream and downstream sides, where as the 10-moment profiles look some what steeper on the upstream part than the downstream one. Recall that the R10-moment model, is capable of modelling heat-transfer effects like Navier-Stokes model, whereas the 10-moment model does not incorporate these effects.

Figure 7.3 shows the density and velocity profiles as predicted by 10-moment and R10-moment models for an upstream Mach number $\mathrm{Ma}_1 = 2$, and Fig. 7.4 presents the temperature and longitudinal stress profiles for the same upstream Mach number. A noticeable feature of results at this upstream Mach number is that the 10-moment model produce discontinuous shock structure whereas the R10-moment model produces continuous shock structure [see Figs. 7.3 & 7.4]. One can see that all profiles predicted by 10-moment model are steepened into a discontinuity on the upstream part of the shock but this unwanted feature is not seen in the case of R10-moment model profiles. Overall, R10-moment model predicts the smooth shock profiles unlike the 10-moment model. Observing the profiles predicted by the R10-moment model for both upstream Mach numbers $\mathrm{Ma}_1 = 1.2$ and $\mathrm{Ma}_1 = 2$, we point out that the profiles are less diffusive at the downstream end than the upstream end.

Finally, we compare an important parameter, namely, the shock thickness (width) which is defined in §6.2.3 [see (6.14) and (6.15)], between R10-moment and 10-moment models. The shock width results from these two models are compared with the shock width results calculated from DSMC data (which are obtained from Gilbarg & Paolucci (1953); Pham-Van-Diep *et al.* (1991); Torrilhon & Struchtrup (2004)) and are presented in Fig. 7.5. From this figure one can notice that the results from 10-moment model are not in good agreement with the DSMC data whereas the results from R10-moment model have an better agreement upto an upstream Mach number of $\mathrm{Ma}_1 \approx 1.5$. Overall, Fig. 7.5 confirms the advantage of regularized moment models over original moment models and the classical hydrodynamic models.

### 7.7.2 Comparison for a granular gas

Here we present results of one-dimensional Riemann problem in a dilute granular gas using 10-moment and R10-moment models. We show the comparison of shock wave structure among these two models at time $t = 10$. So to study shock wave structures in a dilute granular gas, we consider a one-dimensional domain of length $L = 100$ covering $(-50, 50)$, filled with a dilute granular gas of two different homogeneous cooling states at left and right, namely, upstream and downstream, respectively. The upstream boundary conditions for a dilute granular gas are given as in (7.154) and the downstream boundary conditions are provided by RH relations (3.11). The shock is being positioned at $x = 0$ initially and propagates to the right(towards downstream)

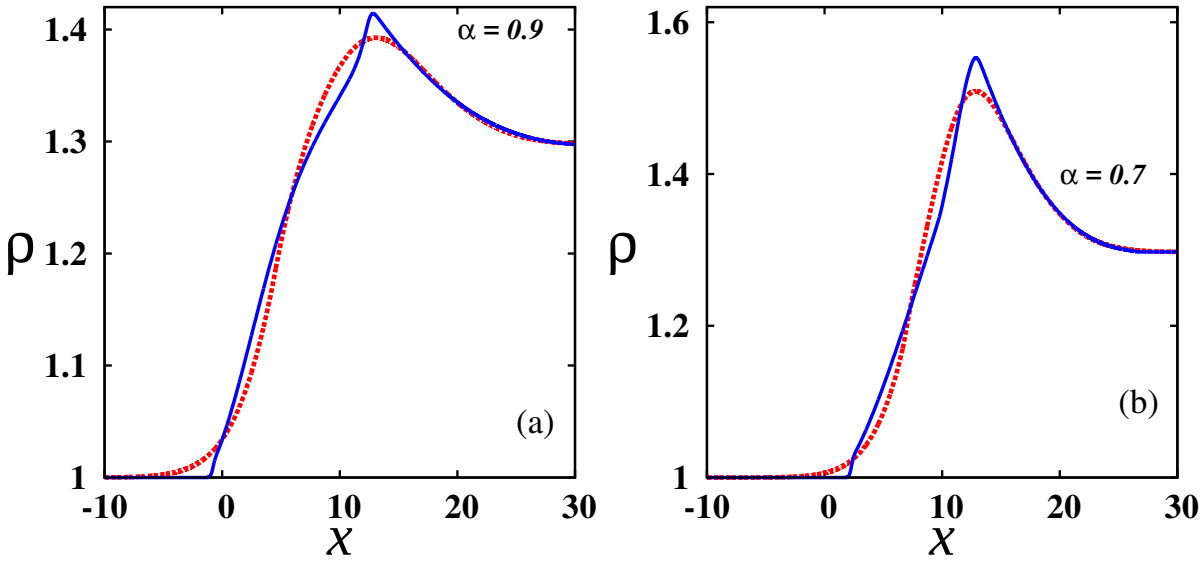


Figure 7.6: Granular density profiles predicted by R10 (red dashed curve) and 10-moment model (blue curve) for an upstream Mach number $\mathrm{Ma}_1 = 1.2$: at time $t = 10$ (a) for a restitution coefficient of $\alpha = 0.9$ and (b) for $\alpha = 0.7$.

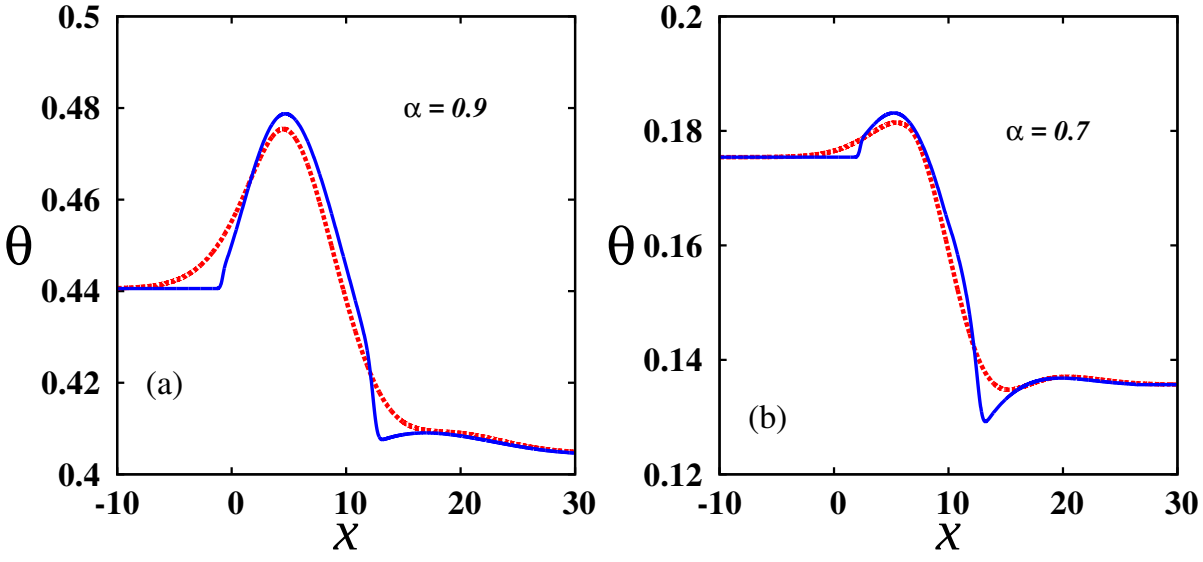


Figure 7.7: Granular temperature profiles predicted by R10 (red dashed curve) and 10-moment model (blue curve) for an upstream Mach number $\mathrm{Ma}_1 = 1.2$: at time $t = 10$ (a) for a restitution coefficient of $\alpha = 0.9$ and (b) for $\alpha = 0.7$.

as time progresses. The numerical computations are performed using the numerical scheme of Delis & Katsaounis (2003), which is discussed in the §3.5.2 and by taking 10000 grid points, with a CFL number($\mathcal{C}$) of 0.005 for both models discussed here.

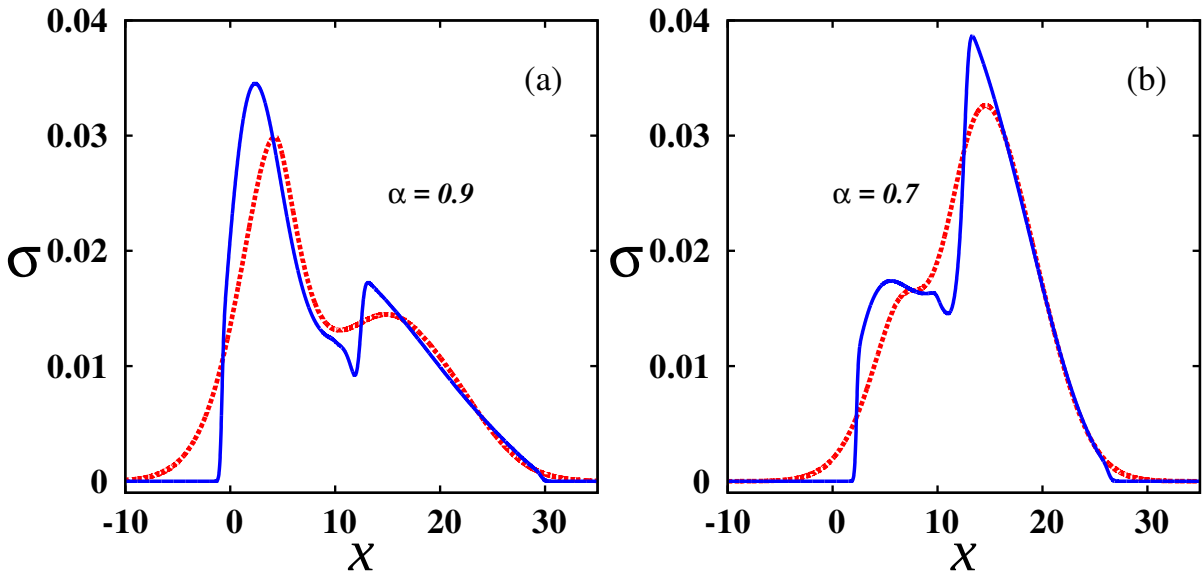


Figure 7.8: Granular longitudinal stress profiles predicted by R10 (red dashed curve) and 10-moment model (blue curve) for an upstream Mach number $\mathrm{Ma}_1 = 1.2$: at time $t = 10$ (a) for a restitution coefficient of $\alpha = 0.9$ and (b) for $\alpha = 0.7$.

We present the results on granular shock waves for two values of the upstream Mach number $\mathrm{Ma}_1 = 1.2$ and $\mathrm{Ma}_1 = 1.5$, and two values of restitution coefficient $\alpha = 0.9$ and $\alpha = 0.7$. Fig. 7.6 and Fig. 7.9 show the predictions of 10-moment (blue curve) and R10-moment (red dashed curve) models for density at time $t = 10$ for the upstream Mach number $\mathrm{Ma}_1 = 1.2$ and $\mathrm{Ma}_1 = 1.5$, respectively. In each figure, panel (a) and panel (b) represent the results for a restitution coefficient of $\alpha = 0.9$ and $\alpha = 0.7$, respectively. Comparing Fig. 7.6 and Fig. 7.9, we can make following observations:

- the density profiles predicted by R10-moment model are smoother and more diffusive on the upstream side than 10-moment model,
- both 10-moment and R10-moment models predict a non-zero density overshoot ($\triangle\rho \equiv (\rho_{\max} - \rho_2)$) within the shock-layer, which is a novel feature of shock waves in a granular gas [Reddy & Alam (2015)],
- R10-moment model predict a lesser magnitude of the density overshoot ($\triangle\rho$) compared to 10-moment model, and
- the density maximum ($\rho_{max}$) increases with increasing Mach number ($\mathrm{Ma}_1 \uparrow$) and the dissipation ($\alpha < 1$) for both models.

Fig. 7.7 shows the granular temperature profiles as predicted by 10-moment (blue curve) and R10-moment (red dashed curve) models for an upstream Mach number of $\mathrm{Ma}_1 = 1.2$, and Fig.

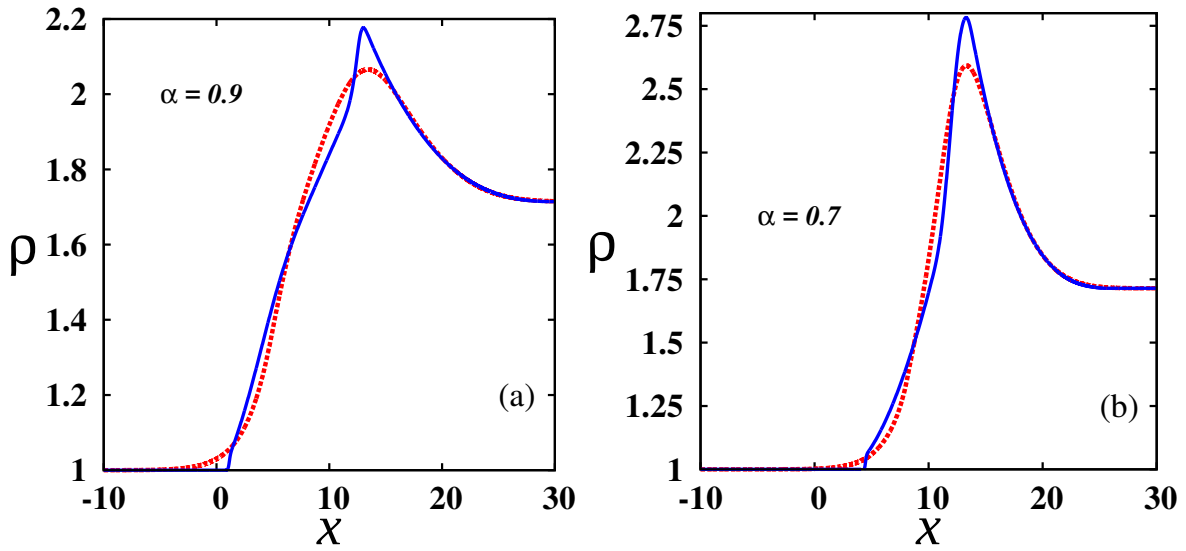


Figure 7.9: Granular density profiles predicted by R10 (red dashed curve) and 10-moment model (blue curve) for an upstream Mach number $\mathrm{Ma}_1 = 1.5$: at time $t = 10$ (a) for a restitution coefficient of $\alpha = 0.9$ and (b) for $\alpha = 0.7$.

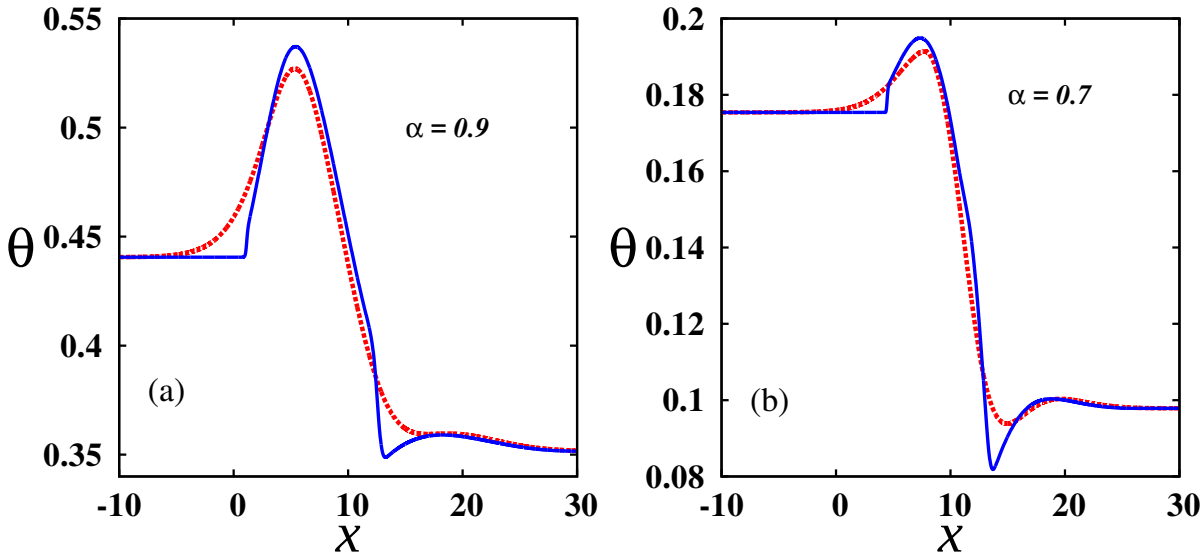


Figure 7.10: Granular temperature profiles predicted by R10 (red dashed curve) and 10-moment model (blue curve) for an upstream Mach number $\mathrm{Ma}_1 = 1.5$: at time $t = 10$ (a) for a restitution coefficient of $\alpha = 0.9$ and (b) for $\alpha = 0.7$.

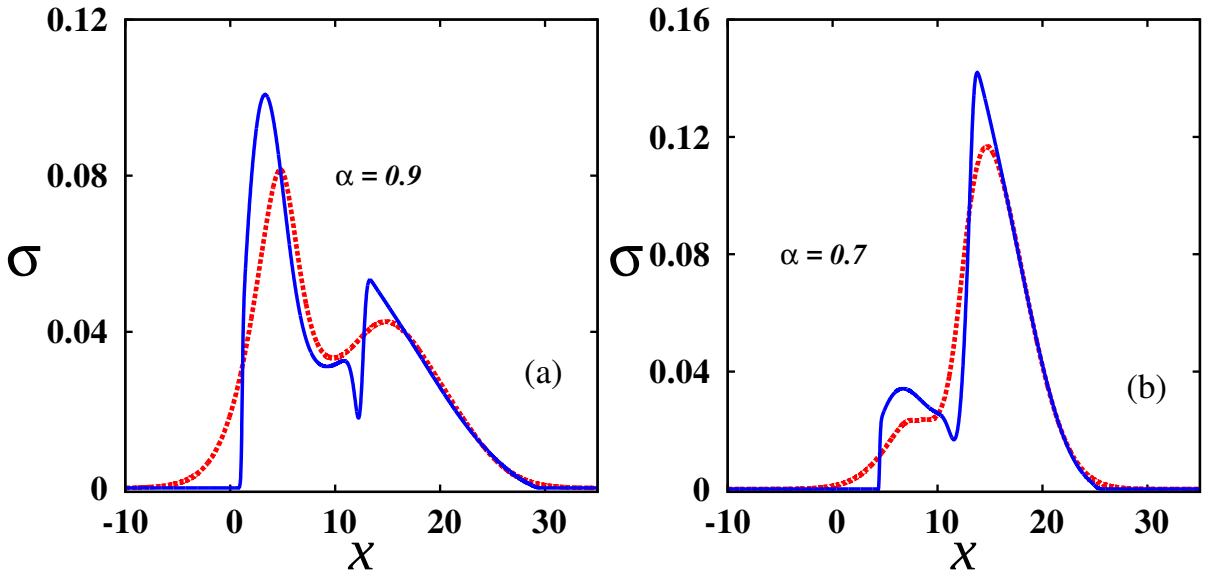


Figure 7.11: Granular longitudinal stress profiles predicted by R10 (red dashed curve) and 10-moment model (blue curve) for an upstream Mach number $\mathrm{Ma}_1 = 1.5$: at time $t = 10$ (a) for a restitution coefficient of $\alpha = 0.9$ and (b) for $\alpha = 0.7$.

7.10 present the same but for an upstream Mach number of $\mathrm{Ma}_1 = 1.5$ at time $t = 10$. As in the density case, panel (a) and panel (b) in each figure indicate the results for a restitution coefficient of $\alpha = 0.9$ and $\alpha = 0.7$, respectively. By comparing Fig. 7.7 and Fig. 7.10, one can conclude the following:

- granular temperature profiles predicted by R10 model are smoother at both Mach numbers, whereas steepend discontinuity at the upstream side of the shock can be seen in temperature profiles predicted by 10-moment model for an upstream Mach number of $\mathrm{Ma}_1 = 1.5$,
- both models predict the temperature maximum $\theta_{max}$ and temperature minimum $\theta_{min}$ within the shock layer, and
- R10 model predicts a lesser value for the temperature maximum ($\theta_{max}$) and the higher value for the temperature minimum ($\theta_{min}$), which can be clearly seen from panel (b) of Fig. 7.7 and Fig. 7.10.

Fig. 7.8 shows the granular longitudinal stress profiles as predicted by 10-moment (blue curve) and R10-moment (red dashed curve) models for an upstream Mach number of $\mathrm{Ma}_1 = 1.2$, and Fig. 7.11 shows for an upstream Mach number of $\mathrm{Ma}_1 = 1.5$ at time $t = 10$. panel (a) and panel (b) in each figure correspond to a restitution coefficient of $\alpha = 0.9$ and $\alpha = 0.7$, respectively. By comparing Fig. 7.8 and Fig. 7.11, we can conclude the following:

- longitudinal stress profiles predicted by R10-moment model are smoother like density and temperature profiles,
- like in temperature maximum ($\theta_{max}$), R10 model predicts a lesser value for the maximum of longitudinal stress ($\sigma_{max}$), and

- an interesting feature of two-peak structure can be observed from the longitudinal stress profiles for both models.

In overall, from the comparison of results for granular shock waves, we can say that the R10-moment model predicts smooth shock profiles beyond $\mathrm{Ma}_{cr|_{10}}$, unlike the standard 10-moment model. Both models predict the density overshoot, temperature maximum within the shock layer; in particular, the R10-moment model predicts smaller values for the above said quantities.

## 7.8 Summary

A detailed derivation of the "regularized" version of 14-moment equations (dubbed "R14" moment equations) for a dilute granular gas is presented following the Chapman-Enskog-like "order-of-magnitude" method of Struchtrup (2004)– these equations contain additional higher-order gradient terms that help to produce 'continuous/smooth' shock solutions at all Mach numbers studied. Subsequently, Navier-Stokes-Fourier (NSF) equations are obtained via the regularization of Euler equations (which admit 'discontinuous' shock solutions) by implementing the Maxwell-iteration procedure on (i) 13-field variables, and (ii) 14-field variables. It is shown that there is a difference between NSF equations obtained from these two approaches: while the heat flux vector is proportional only to the temperature gradient in the first approach (i.e. the well-known Fourier law), in the second approach the heat flux is found to be proportional to the temperature gradient as well as to the density gradient, leading to the generic "non-Fourier" law (Goldhirsch 2003) in a granular gas.

In the later part of this Chapter (§7.6 and §7.7) the regularized 10-moment (R10) equations are derived, and in order to clarify the advantage of regularized moment equations, the R10 equations have been employed to solve the Riemann problem for both molecular and granular gases. Based on a comparison of results between the 10-moment and R10-moment models, it is found that (i) while the 10-moment model fails to produce continuous shock structures beyond an upstream Mach number of $\mathrm{Ma}_1 = 1.34$, the R10-moment model predicts continuous and smooth shocks even beyond the upstream Mach number of $\mathrm{Ma}_1 = 1.34$, (iii) all profiles predicted by 10-moment model are steepened into a discontinuity (for $\mathrm{Ma}_1 > 1.34$) on the upstream part of the shock but this unwanted feature is not seen in the case of R10-moment model profiles, (iv) the profiles predicted by R10-moment model are less diffusive at the downstream end than the upstream end and, lastly for a granular gas, (v) both R10 and 10-moment models predict asymmetric density and temperature profiles, with the maxima of both density and temperature occurring within the shock-layer, and the profiles are found to be smooth for the regularized model for all Ma. Overall, from this chapter, it is concluded that the regularized moment equations produce continuous shock structures beyond the critical Mach number of respective moment equations and the shock profiles appear more realistic since they compare well with DSMC results. The regularized version of extended hydrodynamic equations seems to be suitable for shock calculations in both molecular and granular gases.

## Appendix 7A. R14 equations for a dilute granular gas

The complete set of regularized moment equations at 14-field variables $\rho, u_i, \theta, \sigma_{ij}, q_i, \Delta$ is given by

$$\frac{\partial \rho}{\partial t} + \frac{\partial (\rho\, u_i)}{\partial x_i} = 0, \tag{7.155}$$

$$\frac{\partial (\rho\, u_i)}{\partial t} + \frac{\partial (\rho\, u_i\, u_j)}{\partial x_j} + \frac{\partial p}{\partial x_i} + \frac{\partial \sigma_{ij}}{\partial x_j} = 0, \tag{7.156}$$

$$\rho \left( \frac{\partial \theta}{\partial t} + u_i \frac{\partial \theta}{\partial x_i} \right) + \frac{2}{3} \left( \rho\, \theta \frac{\partial u_i}{\partial x_i} + \sigma_{ij} \frac{\partial u_i}{\partial x_j} + \frac{\partial q_i}{\partial x_i} \right) = -\mathcal{D}, \tag{7.157}$$

$$\frac{\partial \sigma_{ij}}{\partial t} + \frac{\partial (\sigma_{ij}\, u_k)}{\partial x_k} + \frac{4}{5} \frac{\partial q_{\langle i}}{\partial x_{j\rangle}} + 2\, p \frac{\partial u_{\langle i}}{\partial x_{j\rangle}} + 2\, \sigma_{k\langle i} \frac{\partial u_{j\rangle}}{\partial x_k} + \underline{\frac{\partial \tilde{\mathcal{Q}}_{ijk}}{\partial x_k}} = \sigma^s_{ij}, \tag{7.158}$$

$$\begin{aligned} &\frac{\partial q_i}{\partial t} + \frac{\partial (q_i\, u_j)}{\partial x_j} + \frac{5}{2} \sigma_{ij} \frac{\partial \theta}{\partial x_j} + \frac{5}{2} \rho\, \theta \frac{\partial \theta}{\partial x_i} + \theta \frac{\partial \sigma_{ij}}{\partial x_j} - \frac{\sigma_{ij}}{\rho} \frac{\partial \sigma_{jk}}{\partial x_k} - \sigma_{ij}\, \theta \frac{\partial \ln \rho}{\partial x_j} \\ &+ \frac{5}{2} \frac{\partial \left( \rho\, \theta^2\, \Delta \right)}{\partial x_i} + \frac{7}{5} q_j \frac{\partial u_i}{\partial x_j} + \frac{2}{5} q_i \frac{\partial u_j}{\partial x_j} + \frac{2}{5} q_k \frac{\partial u_k}{\partial x_i} + \underline{\frac{1}{2} \frac{\partial \tilde{\mathcal{R}}_{ij}}{\partial x_j} + \tilde{\mathcal{Q}}_{ijk} \frac{\partial u_j}{\partial x_k}} = q^s_i, \end{aligned} \tag{7.159}$$

$$\begin{aligned} &15\, \rho\, \theta^2 \left( \frac{\partial \Delta}{\partial t} + u_i \frac{\partial \Delta}{\partial x_i} \right) + 4\, (2 + 5\, \Delta)\, \theta \left( \frac{\partial q_i}{\partial x_i} + \sigma_{ij} \frac{\partial u_i}{\partial x_j} \right) + 20\, q_i \frac{\partial \theta}{\partial x_i} \\ &\qquad - \frac{8}{\rho} q_i \left( \frac{\partial \sigma_{ij}}{\partial x_j} + \theta \frac{\partial \rho}{\partial x_i} \right) + \underline{\frac{\partial \tilde{S}_i}{\partial x_i} + 4\, \tilde{\mathcal{R}}_{ij} \frac{\partial u_i}{\partial x_j}} = \Delta^s. \end{aligned} \tag{7.160}$$

with higher-order terms

$$\tilde{\mathcal{Q}}_{ijk} = -\frac{3\, \tau_r}{A_1} \left[ \theta \frac{\partial \sigma_{\langle ij}}{\partial x_{k\rangle}} - \theta\, \sigma_{\langle ij} \frac{\partial \ln \rho}{\partial x_{k\rangle}} - \frac{\sigma_{\langle ij}}{\rho} \frac{\partial \sigma_{k\rangle l}}{\partial x_l} + \frac{4}{5} q_{\langle i} \frac{\partial u_{k\rangle}}{\partial x_j} \right], \tag{7.161}$$

$$\begin{aligned} \tilde{\mathcal{R}}_{ij} = -\frac{\tau_r}{A_2} \Bigg[ &7\, \theta\, \sigma^s_{ij} - \frac{7}{\rho} \sigma_{ij}\, \mathcal{D} + \frac{28}{5} \theta \frac{\partial q_{\langle i}}{\partial x_{j\rangle}} + \frac{28}{5} q_{\langle i} \frac{\partial \theta}{\partial x_{j\rangle}} - \frac{28}{5} \theta\, q_{\langle i} \frac{\partial \ln \rho}{\partial x_{j\rangle}} \\ &- \frac{28}{5\, \rho} q_{\langle i} \frac{\partial \sigma_{j\rangle k}}{\partial x_k} + 4\, \theta\, \sigma_{k\langle i} \frac{\partial u_{j\rangle}}{\partial x_k} + 4\, \theta\, \sigma_{k\langle i} \frac{\partial u_k}{\partial x_{j\rangle}} - \frac{8}{3} \theta\, \sigma_{ij} \frac{\partial u_k}{\partial x_k} \\ &- \frac{14}{3\, \rho} \sigma_{ij}\, \sigma_{kl} \frac{\partial u_k}{\partial x_l} - \frac{14}{3\, \rho} \sigma_{ij} \frac{\partial q_k}{\partial x_k} + 14\, \rho\, \theta^2\, \Delta \frac{\partial u_{\langle i}}{\partial x_{j\rangle}} \Bigg], \end{aligned} \tag{7.162}$$

$$\begin{aligned} \tilde{S}_i = -\frac{\tau_r}{A_3} \Bigg[ &28\, \theta\, q^s_i - \frac{28}{\rho} q_i\, \mathcal{D} + 140\, \rho\, \theta^2\, \Delta \frac{\partial \theta}{\partial x_i} + 28\, \theta\, \sigma_{ij} \frac{\partial \theta}{\partial x_j} + 35\, \rho\, \theta^3 \frac{\partial \Delta}{\partial x_i} \\ &- 35\, \theta^2\, \Delta \frac{\partial \sigma_{ij}}{\partial x_j} - \frac{56}{3} \left( \frac{q_i}{\rho} \frac{\partial q_j}{\partial x_j} + \theta\, q_i \frac{\partial u_j}{\partial x_j} + \frac{q_i}{\rho} \sigma_{jk} \frac{\partial u_j}{\partial x_k} \right) \\ &+ \frac{56}{5} \theta \left( q_i \frac{\partial u_j}{\partial x_j} + q_j \frac{\partial u_i}{\partial x_j} + q_j \frac{\partial u_j}{\partial x_i} \right) \Bigg]. \end{aligned} \tag{7.163}$$

## Appendix 7B. R10 equations for a dilute granular gas

The complete set of regularized moment equations at 10-field variables $\rho, u_i, \theta, \sigma_{ij}$ is given by

$$\frac{\partial \rho}{\partial t} + \frac{\partial (\rho\, u_i)}{\partial x_i} = 0, \tag{7.164}$$

$$\frac{\partial (\rho\, u_i)}{\partial t} + \frac{\partial (\rho\, u_i\, u_j)}{\partial x_j} + \frac{\partial p}{\partial x_i} + \frac{\partial \sigma_{ij}}{\partial x_j} = 0, \tag{7.165}$$

$$\rho \left( \frac{\partial \theta}{\partial t} + u_i \frac{\partial \theta}{\partial x_i} \right) + \frac{2}{3} \left( \rho\, \theta \frac{\partial u_i}{\partial x_i} + \sigma_{ij} \frac{\partial u_i}{\partial x_j} + \underline{\frac{\partial q_i}{\partial x_i}} \right) = -\mathcal{D}, \tag{7.166}$$

$$\frac{\partial \sigma_{ij}}{\partial t} + \frac{\partial (\sigma_{ij}\, u_k)}{\partial x_k} + \underline{\frac{4}{5} \frac{\partial q_{\langle i}}{\partial x_{j\rangle}} + \frac{\partial \mathcal{Q}_{ijk}}{\partial x_k}} + 2\, p \frac{\partial u_{\langle i}}{\partial x_{j\rangle}} + 2\, \sigma_{k\langle i} \frac{\partial u_{j\rangle}}{\partial x_k} = \sigma_{ij}^{s}, \tag{7.167}$$

with higher-order terms

$$q_i = -\frac{\tau_r}{A_5} \left[ \frac{5}{2} \rho\, \theta \frac{\partial \theta}{\partial x_i} + \frac{5}{2} \sigma_{ij} \frac{\partial \theta}{\partial x_j} + \theta \frac{\partial \sigma_{ij}}{\partial x_j} - \theta\, \sigma_{ij} \frac{\partial \ln \rho}{\partial x_j} - \frac{\sigma_{ij}}{\rho} \frac{\partial \sigma_{jk}}{\partial x_k} \right], \tag{7.168}$$

$$\mathcal{Q}_{ijk} = -\frac{3\, \tau_r}{A_1} \left[ \theta \frac{\partial \sigma_{\langle ij}}{\partial x_{k\rangle}} - \theta\, \sigma_{\langle ij} \frac{\partial \ln \rho}{\partial x_{k\rangle}} - \frac{\sigma_{\langle ij}}{\rho} \frac{\partial \sigma_{k\rangle l}}{\partial x_l} \right]. \tag{7.169}$$

# Chapter 8

# Summary and Conclusions

In this Chapter a summary of research work done, with conclusions drawn from the present research work, is presented. A brief discussion on the future work that can be taken up as a consequence of the present work is presented at the end.

As stated in §1.4 of Chapter 1, the primary goals of this thesis were to (i) study the well-known Riemann problem of plane shock waves propagating in a granular gas using hydrodynamic-like equations (Chapters 3 and 4), (ii) develop numerical schemes to solve the related inhomogeneous PDEs (Chapter 3), (iii) analyse and identify the unique characteristics of granular shock-waves in comparison to their molecular counterparts (Chapter 4), (iv) a comparative analysis between the predictions of the Euler- and Navier-Stokes-order hydrodynamic equations and the "extended" (beyond Navier-Stokes-order) hydrodynamic models (Chapter 6), (v) analyse the characteristics and the well-posedness of extended granular hydrodynamic models (Chapter 5) and finally (vi) suggest ways to 'regularize' the extended moment models for a granular gas (Chapter 7) so as to obtain smooth solutions at any Mach number.

## 8.1 Summary

A brief introduction about granular materials and their importance in the world were discussed in Chapter 1. This Chapter also presented the background literature on shock waves in both molecular and granular gases. It also presented the objective and motivation of present research work.

Chapter 2 was devoted to the kinetic theory of dilute granular gas. We started with the derivation of basic inelastic Boltzmann equation and discussed the properties of the inelastic collision integral $\boldsymbol{\Omega}(f, f)$. Later we derived the moment transfer equation and also discuss about the closure problem. In the next section of this Chapter we discussed about different moment closure methods: (i) the Chapman-Enskog method, (ii) the Grad's moment method and (iii) the maximum entropy method. The Grad's moment method was used to obtain the extended sets of hydrodynamic equations namely 10-moment, 13-moment and 14-moment equations for dilute granular gas and the constitutive relations were taken from the model of Kremer & Marques Jr (2011).

In Chapter 3, we formulated Euler and Navier-Stokes hydrodynamics equations for one-dimensional planar shock waves and the theory of normal shocks in molecular/granular gas. Plane shock wave problem via Navier-Stokes hydrodynamic equations is solved by relaxation-type numerical scheme using two different methods: (i) PDE-splitting technique following Jin & Xin (1995) [§3.5.1] and (ii) the numerical scheme of Delis & Katsaounis (2003) [§3.5.2]. A comparison of shock width results obtained from the present schemes with the data of Torrilhon

& Struchtrup (2004), using a different numerical method, confirmed the accuracy of our numerical schemes. Moreover from Fig. 3.6, it was confirmed that both numerical schemes used here predict the shock profiles accurately but they differ in the execution time.

Chapter 4 was devoted to the analysis of the Riemann problem of granular shock waves by solving the granular hydrodynamic equations, namely, Euler equations and Navier-Stokes equations, numerically. It was shown that the Rankine-Hugoniot relations are identical for both molecular and dilute granular gases at Euler and Navier-Stokes order hydrodynamics. In §4.3, the grid convergence of the two numerical schemes discussed in §3.5 was demonstrated for the granular shock waves via Navier-Stokes model. The Euler and Navier-Stokes predictions about the shock structures in granular gases were presented in §4.3.1 for different Mach numbers (Ma) and restitution coefficients ($\alpha$). Two important features, which make granular shock waves different from the molecular case, were found to be (i) the density overshoot and (ii) its steady propagation speed as discussed in §4.3.2. Section 4.3.3 revealed that the maximum temperature within the shock layer follows the Haff's law for initial times and deviations occurred there after. A scaling relation (4.22) was uncovered that expresses the critical time (at which the maximum temperature deviates from Haff's law) as a function of Mach number and inelasticity. The long time behaviour of granular shock structures, leading to the continual build-up of density inside the shock, was discussed in §4.3.4. A simple regularization procedure to arrest the maximum density was proposed in §4.3.5.

Chapter 5 discussed the "extended" hydrodynamic equations when applied to plane shock wave problem. The one-dimensional reduced equations for planar shock wave problem obtained from the extended hydrodynamic models, namely, 10-moment, 13-moment, and 14-moment models, were presented in §5.2. For one-dimensional field equations for planar shock wave problem, the 10-moment model was reduced to a system of four coupled PDE's which involves four physical field variables, namely, the density $\rho(x,t)$, the velocity $u(x,t)$, the scalar temperature $\theta(x,t)$ and the longitudinal stress $\sigma(x,t)$; the 13-moment model was reduced to a system of five coupled PDE's which involves an additional physical field variable namely heat flux $q(x,t)$ in addition to the 10-moment field variables, and the 14-moment model was reduced to a system of six coupled PDE's with an extra field variable, namely, the dimensionless non-equilibrium part of the full-contracted fourth-order moment $\Delta$ apart from the field variables of 13-moment model. In §5.3 we presented a detailed analysis on the characteristics of extended hydrodynamic models and this analysis confirmed that the largest characteristic speed in extended hydrodynamic equations depends on the number of moments (hydrodynamic fields) in extended hydrodynamic equations. Moreover, the largest characteristic speed increased when the number of moments was increased in extended hydrodynamics: $s_{\max} = \sqrt{3\theta}$, $\sqrt{4.54\theta}$ and $\sqrt{5.18\theta}$ for 10, 13 and 14-moment models, respectively. It was found that 14-moment equations still form a hyperbolic system even in the presence of small finite stresses and heat flux.

We carried out the critical Mach-number analysis in §5.4, which confirmed that the critical Mach number and the critical density are not influenced by the restitution coefficient ($\alpha$), and the critical Mach number for 10-moment, 13-moment and 14-moment models are $1.34, 1.65$ and $1.763$, respectively. This analysis also confirmed that the critical Mach number increases with increasing the number of moments retained in extended hydrodynamic models. For planar

stationary shock problem in a molecular gas, the 10-moment system boiled down to a single ODE for density (5.62). We found an excellent agreement between the solution of this ODE (5.62) with that of the solution of the system of PDE's obtained via the numerical schemes discussed in §3.5. In §5.6, we derived spatially homogeneous solution and Haff's law from the 14-moment model.

Chapter 6 was devoted to the numerical solutions of plane shock waves in a molecular gas as well as in a dilute granular gas with the extended hydrodynamic equations (10-moment, 13-moment, 14-moment equations). For both molecular and granular shock waves, the results on the density, the temperature, the skew temperature, the heat flux and the fourth moment were compared among these moment models and Navier-Stokes model. The extended hydrodynamic equations yield steady smooth shock solutions up to a critical Mach number ($\mathrm{Ma}_{cr}$) as elaborated in Chapter 5 (§5.3). For shock wave results in a molecular gas, the agreement for the shock solutions of the moment equations (13-moment and 14-moment equations) was found to be better than those predicted by Navier-Stokes equations. These results showed reliable qualitative and quantitative agreement with DSMC simulations for Mach numbers up to $\mathrm{Ma} \approx 2.0$ [see Fig. 6.18]. It was noted that for Mach numbers $\mathrm{Ma} \leq 1.3$, the shock width described by Navier-Stokes, the 13-moment and 14-moment equations are within the DSMC computational scatter, whereas the shock width described by the 10-moment equations is in poor agreement with DSMC data. For Mach numbers $\mathrm{Ma} > 1.3$, the 13-moment and 14-moment predictions are more accurate than the NS-model. For shock waves in a granular gas, we observed a density overshoot which is not present in the case of a molecular gas, and every extended-hydrodynamic model predicted this feature. Among all models presented here, the 14-moment model predicted a lesser density overshoot [Eq. (6.19)]. We also found that at sufficiently late times the density peaks travels with a steady constant speed. It was shown that the maximum temperature within the shock-layer follows the Haff's law up to a critical time (for weak shocks only) and decays much slower for $t > t_c$.

Appendix-A has been added as a supplement to Chapter-6 in which the numerical results for blast waves are presented using four variants of hydrodynamic equations: Euler, 10-moment, NSF and 14-moment models. Blast waves are a special class of shock waves that are caused by the rapid and localized release of a large amount of energy in a medium. The results on the density, granular temperature, skew temperature, heat flux and the contracted fourth moment are compared among all models and it is found that the shock profiles are smoother for the NSF and 14-moment model compared to those predicted by the Euler equations and 10-moment equations; a shock-splitting phenomenon is observed in the skew temperature profiles for blast waves in both molecular and granular gases.

In Chapter 7, we presented a detailed derivation of "regularized" 14-moment equations for a dilute granular gas and also showed that Navier-Stokes-Fourier equations can be obtained in two different ways: the regularization of Euler equations via (i) the 13-field theory and (ii) the 14-field theory. The main difference between NSF equations obtained from these two approaches was that the heat flux vector is proportional to only the temperature gradient from the first approach whereas the heat flux vector is proportional to the temperature gradient and also to the density gradient. In §7.6 we presented a derivation of regularized 10-moment equations.

To show the advantage of R10-moment equations over the 10-moment equations, we applied these models to the Riemann problem of shock waves in a molecular gas as well as in a granular gas and the results were compared between these two models. The 10-moment model fails to produce continuous shock structures beyond an upstream Mach number of $\mathrm{Ma}_1 = 1.34$ whereas the R10-moment model was found to predict continuous and smooth structure as compared to 10-moment model beyond an upstream Mach number of $\mathrm{Ma}_1 = 1.34$.

## 8.2 Conclusions

Based on results presented in Chapters 3 to 7, the conclusions of the present work are summarized below.

From the two relaxation-type numerical schemes discussed in Chapter 3 [(i) PDE-splitting technique using Jin & Xin (1995) and (ii) the numerical scheme of Delis & Katsaounis (2003)], we conclude that the both numerical schemes to produce the same shock profiles accurately which is evident from Fig. 3.6. The shock thickness results extracted from the present numerical schemes were compared with the data of Torrilhon & Struchtrup (2004) [who used a different numerical method] which further confirmed the accuracy of both numerical schemes. Furthermore, it was demonstrated that the numerical scheme of Delis & Katsaounis is slower than the PDE-splitting technique even though both predict the shock profiles accurately.

In chapter 4, the Riemann problem of granular shock waves was analysed by numerically solving the Euler and Navier-Stokes hydrodynamic equations. The density and temperature profiles were found to be "asymmetric", with the maxima of both density and temperature occurring within the shock layer which constitute two distinguishing features of the "granular" Riemann problem (compared to that for ideal gases). The fundamental difference of the granular shock problem from its ideal-gas counterpart can be tied to 'inelastic dissipation' since this makes the upstream and downstream states of a granular shock to live in non-equilibrium 'decaying' states (similar to HCS), which, in turn, is responsible for the non-trivial shock structures uncovered here. Inside the shock too, the Haff's law was found to hold for the maximum temperature, but for weak shocks ($Ma_1 \sim 1$) only, and deviations occurred for strong shocks. The origin of asymmetric density profiles, leading to the continual build-up of density inside the shock, seems to be tied to a pressure instability in granular gases. It is shown that the granular energy equation must be regularized in order to arrest the maximum density within the shock-layer.

The detailed analysis done in §5.3 on the characteristics of extended hydrodynamic models confirmed that the largest characteristic speed in extended hydrodynamic equations depends on the number of moments retained and the largest characteristic speed increases with increasing moments: $s_{\max} = \sqrt{3\theta}$, $\sqrt{4.54\theta}$ and $\sqrt{5.18\theta}$ for 10-, 13- and 14-moment models, respectively. The analysis carried out in §5.4 confirmed that the critical Mach number and the critical density are not influenced by the restitution coefficient ($\alpha$), and the critical Mach number for 10-, 13- and 14-moment models are found to be $1.34, 1.65$ and $1.763$, respectively. This analysis also clarified that the critical Mach number increases with the number of moments retained in extended hydrodynamic models.

For shock wave results in a molecular gas, the agreement for the shock solutions of the 13- and 14-moment equations, is better than those predicted by Navier-Stokes equations. The results showed reliable qualitative and quantitative agreement with DSMC simulations for Mach numbers up to Ma $\approx 2.0$ [see Fig. 6.18]. For Mach numbers Ma $\leq 1.3$ the shock width described by Navier-Stokes, the 13-moment and 14-moment equations are within the DSMC computational scatter, whereas the shock width described by the 10-moment equations is in poor agreement with DSMC data. For Mach numbers Ma $> 1.3$, the 13-moment and 14-moment predictions are more accurate than the NS-model. For shock waves in a granular gas, we observed a density overshoot which is not present in the case of a molecular gas, and every extended hydrodynamic model predicts this feature too. Among all models presented here, the 14-moment model yields a lesser density overshoot [Eq. (6.19)]. The predictions on granular shock-waves are found to be similar to those predicted by the NS-model as discussed in Chapter 4. Different moment models do not seem to have noticeable effect on the magnitude of the critical time for given control parameters.

The "regularized" 14-moment equations for a dilute granular gas was derived in Chapter 7 by applying the order-of-magnitude method of Struchtrup (2004). We conclude that Navier-Stokes-Fourier equations obtained from (i) the 13-moment theory and (ii) the 14-moment theory are different. In particular they differ in the constitutive relation for the heat flux vector $q_i$; the heat flux is proportional to both temperature gradient and density gradient when the NSF equations are derived from the 14-field variables while it is proportional to the temperature gradient when the NSF equations are obtained from the 13-field variables. Based on a comparison of results for the Riemann problem of shock waves in molecular and granular gases using the 10-moment and R10-moment models, we conclude that the regularized moment equations produce continuous shock structures beyond the critical Mach numbers of respective moment equations and the results appear more realistic since they compare well with DSMC results [Fig. 7.5]. Therefore it is recommended to use the "regularized" moment equations to solve shock-wave problems for both molecular and granular gases.

## 8.3 Future work

As pointed out in the introduction of this thesis, this research work was focused primarily on plane shock wave propagation in a dilute granular gas via different sets of hydrodynamic equations. We used extended hydrodynamic models along with the classical Euler and Navier-Stokes hydrodynamic models to study the shock propagation in molecular and granular gases. The following issues may be investigated in a future work.

- ⋆ This work can be extended to study the propagation of shock waves in a "dense" granular gas as well as in a visco-elastic granular gas to understand the dense gas effects and the visco-elastic effects on shock structures.
- ⋆ A detailed investigations on the regularization of the energy equation in order to arrest the maximum density [§4.3.5] in a dilute granular gas for Navier-Stokes model have to be carried out in future.

- ⋆ Large time behaviour ($t \to \infty$) of granular shock structures needs to be investigated via moment models, since most results presented in §6.3 pertain to $t \leq 10$. This analysis is likely to show whether the energy equation requires "additional" regularization as found for Navier-Stokes model [see §4.3.5 in Chapter 4].

- ⋆ A detailed numerical analysis of the plane shock wave problem using the R10 and R14 models can be carried out in future. These continuum predictions should be compared with particle-level simulations via DSMC or MD simulations.

  Performing DSMC simulations for this plane shock wave problem in a granular gas is not as simple as in a molecular gas because of temperature decaying initial conditions. This can be taken up in a future work.

- ⋆ The spatio-temporal stability analyses of the HCS (homogeneous cooling state) using R10 and R14 models need to be carried out. Such linear stability analysis is required to address the "well-posedness" of the "regularized" moment models. This is also likely to shed light on possible instabilities associated with higher-order fields which, in turn, may influence the dynamics of granular shock waves.

- ⋆ The boundary conditions for the higher-order fields of "regularized" granular hydrodynamic equations should be derived in future. These are required to solve any practical problem, such as the channel flow, vibrated bed, the flow over obstacles, etc..

  In simulations of rarefied gas flows boundary conditions pose major difficulties. To solve confined flows such as channel flow, complete set of wall boundary conditions are required for moment equations. The macroscopic boundary conditions for higher moments should be obtained from the microscopic boundary conditions for the Boltzmann equation through averaging, since the macroscopic moment equations were obtained by averaging from the Boltzmann equation. In future, we plan to derive the boundary conditions for R10 and R14 moment models by following the works of Struchtrup (2005*b*); Gu & Emerson (2007); Torrilhon & Struchtrup (2008) and Rana & Struchtrup (2016).

# Appendix A

# Planar Blast Waves in a Granular Gas[†].

## A.1 Introduction

Blast waves are a special class of shock waves that occur in compressible gases in a natural way [(Blandford & McKee 1976; Smoller 1983)]. They are caused by the rapid and localized release of a large amount of energy in a medium[(Taylor 1950*a*,*b*; Ostriker & McKee 1988; Courant & Friedrichs 1948)]. Shocks and blasts waves are also generated in granular flows, irrespective of the flow being dense or dilute [(Boudet *et al.* 2009; Boudet & Kellay 2013; Barbier *et al.* 2015)]. Figure A.1 shows a graphic example of a spherical blast wave formed in the first nuclear detonation named the "Trinity" explosion (1945) in which the atomic explosive was fired 100 ft above the ground. The dynamics of the growth of the hole [(Boudet *et al.* 2009)] generated by impacting a thin, dilute, and fast flowing granular layer with steel spheres, which is found to mimic spherical blast shocks, is depicted in Fig. A.2.

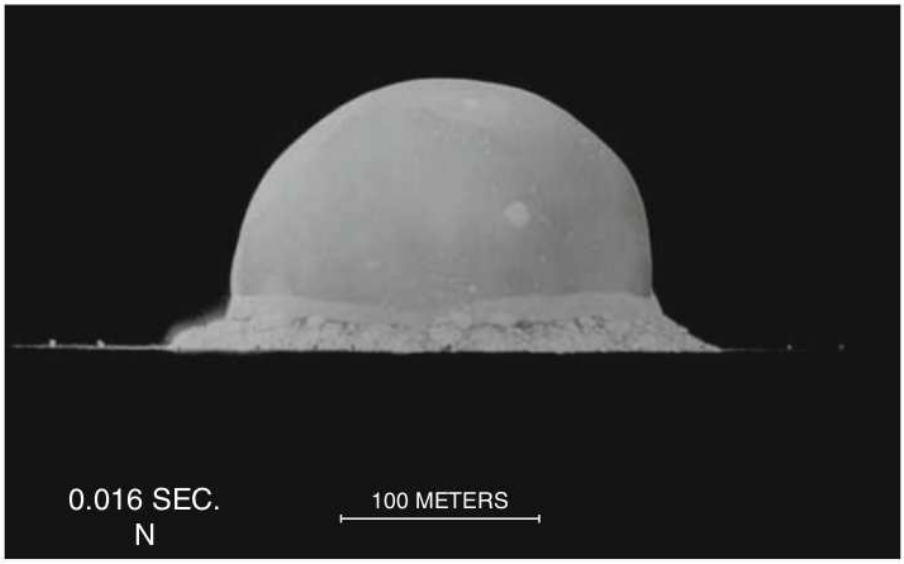


Figure A.1: Photograph of the Trinity detonation at a time of 16 msec taken from http://www.atomicheritage.org/history/trinity-test-1945

Here we present the study of one-dimensional analog of spherical blast shocks in a dilute granular gas which is modelled using four variants of hydrodynamic equations: Euler, 10-moment,

[†]Part of this chapter has been published in Proceedings of the $29^{th}$ International Symposium on Rarefied Gas Dynamics, AIP Publishing (Reddy, Ansumali & Alam, Vol. 1628, pp. 480-487, 2014)

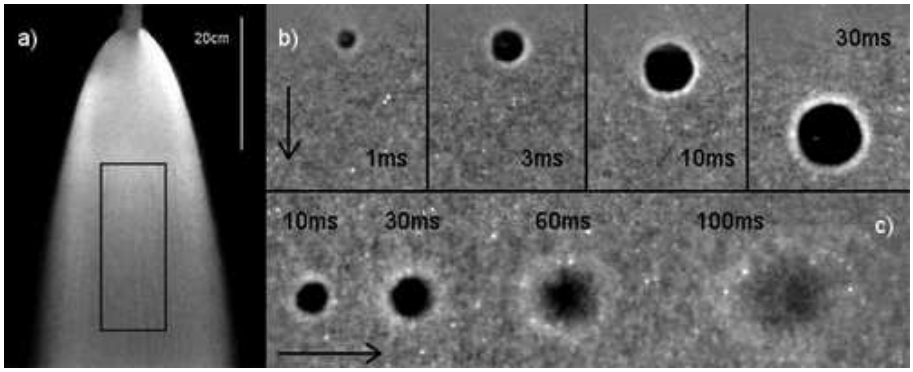


Figure A.2: Images of the expanding hole right after the impact of a steel sphere. (a) An image of the flow produced from a funnel of 2.4 mm in diameter. (b) impact of a 16 mm diameter steel sphere. (c) impact of a 2 mm diameter steel sphere. This figure is adopted from Boudet *et al.* (2009)

Navier-Stokes and 14-moment models (which are discussed in chapter 2). The one-dimensional blast-wave problem is formulated and the resulting equations are solved numerically using a relaxation-type scheme (which was discussed in §3.5). The results on the density, the granular temperature, the skew temperature, the heat flux and the fourth moment are compared among all models. Like in chapter 6, we find that the shock profiles are smoother for Navier-Stokes and 14-moment model compared to those predicted by the standard Euler equations and 10-moment equations. A shock-splitting phenomenon is observed in the skew temperature profiles for blast waves in a granular gas as well as in a molecular gas.

## A.2 Planar Blast Wave Experiments: Initial Data

In the absence of gravity the one-dimensional blast waves are generated when evolving in time by taking the left state of a Riemann problem as a supersonic granular gas, with the right state being at rest. The one-dimensional shock-wave problem is formulated in a similar way as in Chapter 4 and the resulting equations are then solved numerically using a relaxation-type scheme which is discussed in Chapter 3. We choose the initial data in such a way that it generates a shock-contact-shock structure [(Serna & Marquina 2005)]. We have conducted numerical experiments with four values of the restitution coefficient $\alpha = 1$, 0.95 , 0.9, and $\alpha = 0.75$, using the following initial data [Reddy *et al.* (2014)]:

$$\begin{bmatrix} \rho_1 \\ u_1 \\ \theta_1 \\ \sigma_1 \\ q_1 \end{bmatrix} = \begin{bmatrix} 1.0 \\ 2.0 \\ 1.0 \\ 0.0 \\ 0.0 \end{bmatrix}, \quad \begin{bmatrix} \rho_2 \\ u_2 \\ \theta_2 \\ \sigma_2 \\ q_2 \end{bmatrix} = \begin{bmatrix} 1.5 \\ 0.0 \\ 0.014 \\ 0.0 \\ 0.0 \end{bmatrix}, \tag{A.1}$$

and

$$\Delta_1 = \frac{16(1-\alpha)(1-2\alpha^2)}{30\alpha^2(1-\alpha)+81-17\alpha} = \Delta_2. \tag{A.2}$$

The computations are carried out by considering a one-dimensional domain of length 50 covering $[-25, 25]$ with 5000 grid points, until a time $t = 10$, with a Courant-Friedrichs-Lewy (CFL) number of 0.01 for Navier-Stokes model and 0.1 for all other models. The initial discontinuity is located at $x = 0$.

## A.3 Effects of Inelasticity on Time Evolution of Blast Waves

Firstly we present the results corresponding to a restitution coefficient ($\alpha$) equal to unity via four different models at time $t = 10$. This means that the particles are perfectly elastic and the results resemble the blast waves in a molecular gas. Elastic blast wave results for the density, scalar temperature and velocity profiles are depicted in Fig. A.3 and the skew-temperature, heat-flux and the fourth order moment ($\Delta$) profiles are depicted in Fig. A.4. From Fig. A.3, we

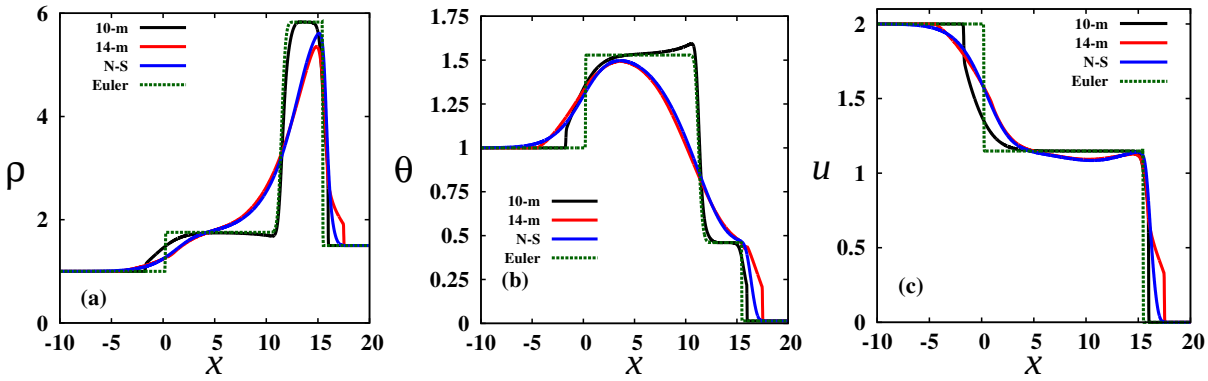


Figure A.3: Predictions of Euler, 10-moment, Navier-Stokes and 14-moment models for elastic blast wave profiles at time $t = 10$. (a) Density, (b) temperature, (c) velocity profiles.

see that Navier-Stokes and 14-moment model profiles are much smoother comparative to those of 10-moment profiles and the 10-moment model profiles are smoother comparative to the Euler model, which is expected because Navier-Stokes and 14-moment models incorporate heat and shear stress effects and the 10-moment model can predict only shear stress effects whereas the Euler model fails to predict any of these effects. Further note that the skew-temperature which is arising from the normal stress effects vanishes for the Euler model. An interesting feature, a two peak structure, is observed on the skew-temperature profiles which was not found in "shock wave" skew-temperature profiles, which is presented in Fig. A.4 (a).

For a granular gas with restitution coefficient of $\alpha = 0.9$, the time evolution of the density profile is displayed in Fig. A.5 for the 10-moment model (a), Navier-Stokes model (b) and 14-moment model (c). For all cases the density build-up is observed around the contact wave. i.e., the clustering of a granular gas is seen to occur around the contact when evolving in time. Comparing the density profiles at time $t = 10$, we find that the density maximum is $\rho_{max} \approx 18$, 10 and 8.5 for the 10-moment model, Navier-Stokes model and 14-moment model, respectively. Considering Navier-Stokes model as a reference, we conclude that the density maximum predicted by the 14-moment model is 0.15 times less than the density maximum in Navier-Stokes model whereas the density maximum predicted by the 10-moment model is 1.8 times. In contrast, for the elastic case, the density maximum approaches steady state value of

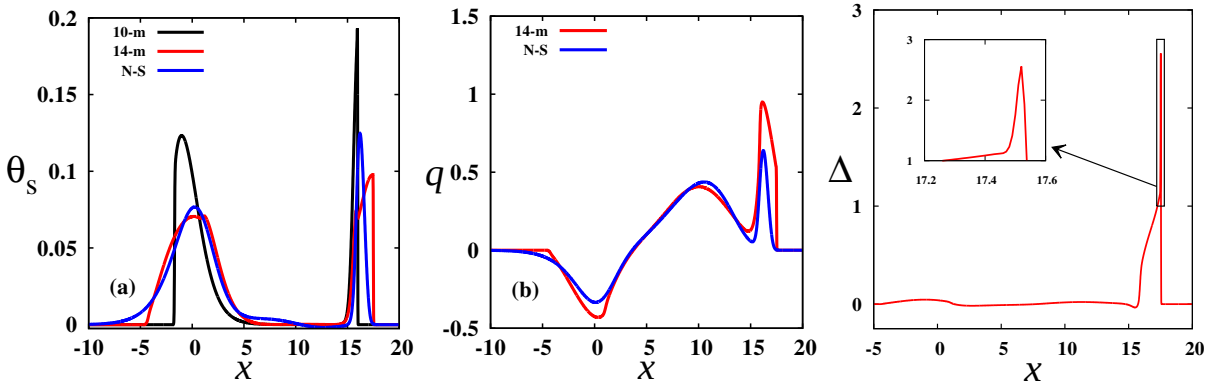


Figure A.4: Predictions of 10-moment, Navier-Stokes and 14-moment models for elastic blast wave profiles at time $t = 10$. (a) Skew temperature, (b) heat-flux, (c) contracted fourth-order moment ($\Delta$) profiles.

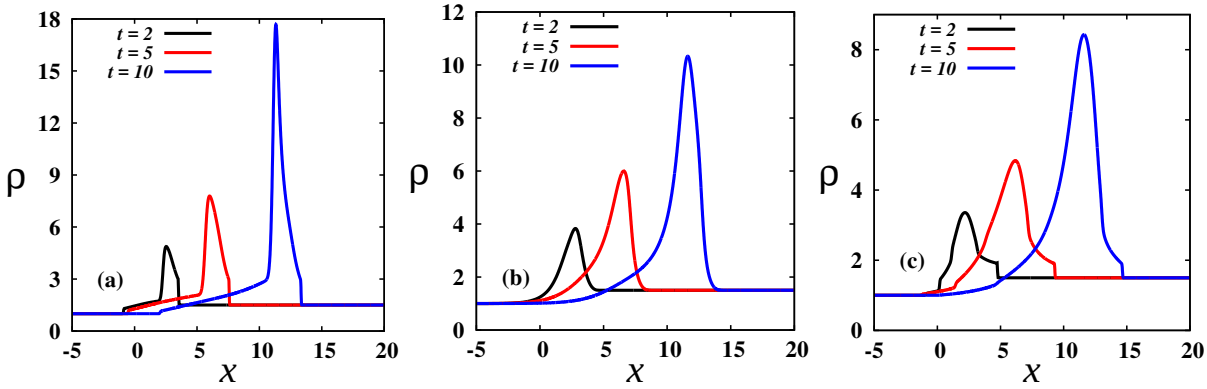


Figure A.5: Temporal evolution of blast wave density for $\alpha = 0.9$. (a) 10-moment model, (b) Navier-Stokes model, (c) 14-moment model.

$\rho_{max} \approx 5.8$ (see Fig. A.3). Comparing with the density plots for $\alpha = 0.75$ (see Fig. A.6), we find that the particle clustering occurs faster with decreasing restitution coefficient whereas for an elastic gas there is no clustering.

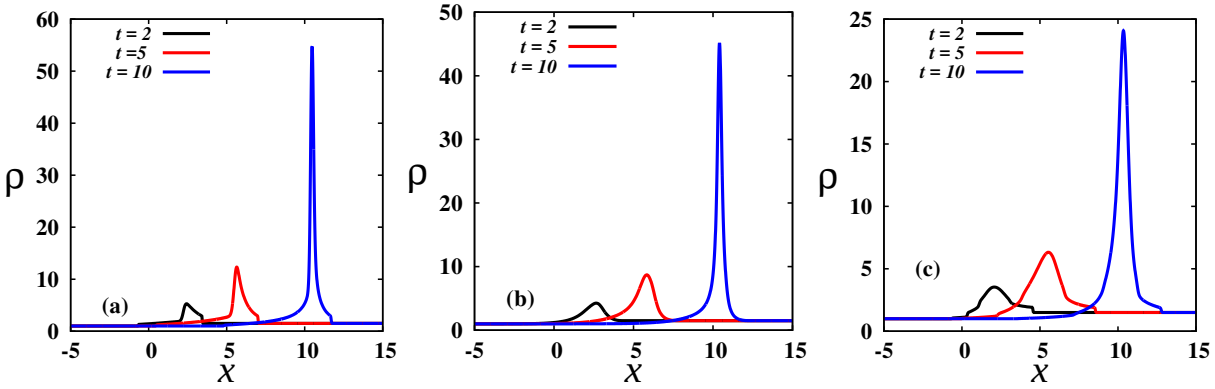


Figure A.6: Temporal evolution of blast wave density for $\alpha = 0.75$. (a) 10-moment model, (b) Navier-Stokes model, (c) 14-moment model.

The temporal evolution of density maximum as predicted by the Euler, Navier-Stokes, 10-moment and 14-moment models are presented in the main panels of Fig. A.7 (a), (b), and (c) for restitution coefficients of 0.95, 0.9 and 0.75, respectively and the insets show the location of the density maximum with time. From Fig. A.7 (main panels), we conclude that the value of density maximum increases with time. It is seen that $(\rho_{max})_{10,14,NS} < (\rho_{max})_{Euler}$ from the very beginning and moreover the 14-moment model predicts a lower density maximum compared to any model discussed here. From the main panels of Fig. A.7, we also remark that the value of density maximum increases with increasing dissipation and time. Overall, in the absence of gravity, the blast waves in granular gases produce a continuous build-up of density around the contact wave which may approach to close-packed limit in a finite time irrespective of the system being dilute or dense.

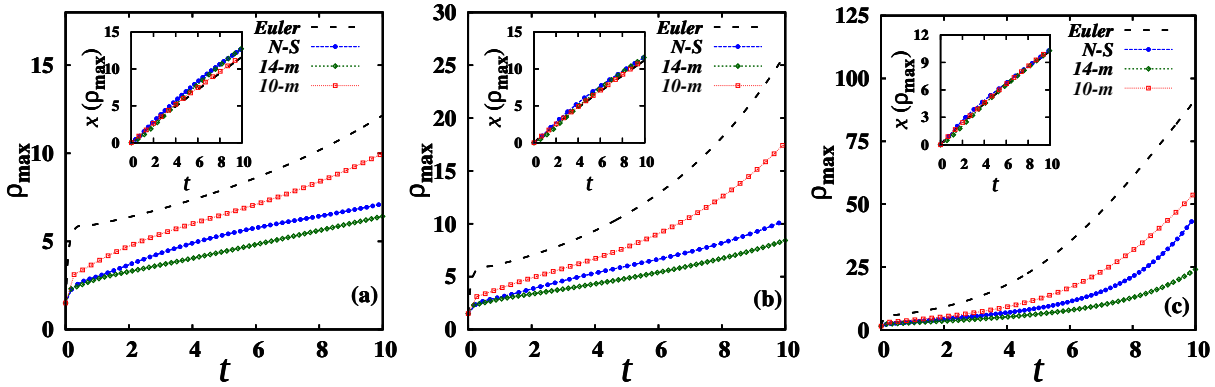


Figure A.7: Temporal evolution of density maximum (main panel) and the variation of spacial location of $\rho_{max}$ with time (inset). (a) $\alpha = 0.95$, (b) $\alpha = 0.9$, (c) $\alpha = 0.75$.

The insets of Fig. A.7 show that the spatial position of $\rho_{max}$ shifts to the right with time, from which a speed of propagation of the density maximum can be estimated. The speed of

propagation of density maximum is defined as $v_s = x(\rho_{max})/t$, and its temporal evolutions are displayed in the Fig. A.8 (a), (b), and (c) for the restitution coefficient of 0.95, 0.9 and 0.75, respectively. It is seen that the speed of the density maximum (peak) attains a steady state value after a long time. This result for blast-waves is similar to that found for granular shock waves as discussed in Chapters 4 and 6.

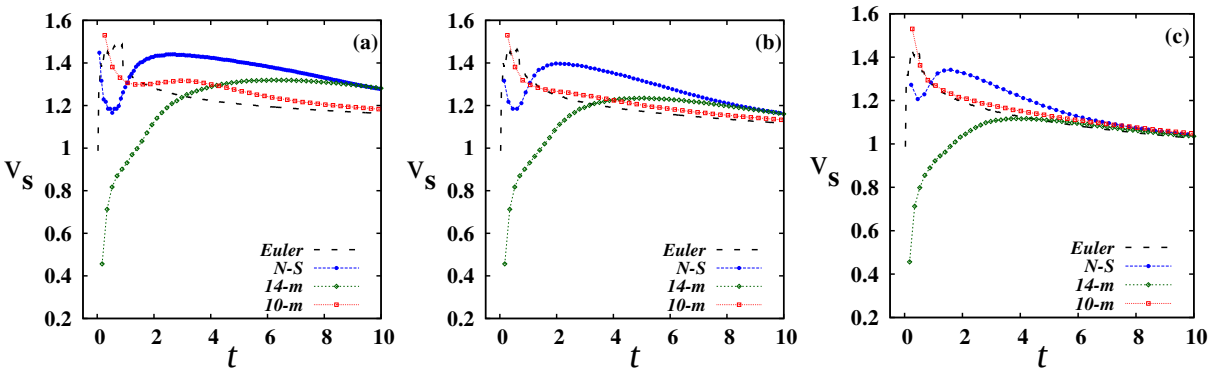


Figure A.8: Temporal evolution of the speed of density maximum ($v_s$)profiles. (a) $\alpha = 0.95$, (b) $\alpha = 0.9$, (c) $\alpha = 0.75$.

The time evolution of the granular temperature profiles using (a) 10-moment, (b) Navier-Stokes and (c) 14-moment models corresponding to restitution coefficients of $\alpha = 0.9$ and $\alpha = 0.75$ are displayed in Fig. A.9 and Fig. A.10, respectively. We notice that there is a jump in

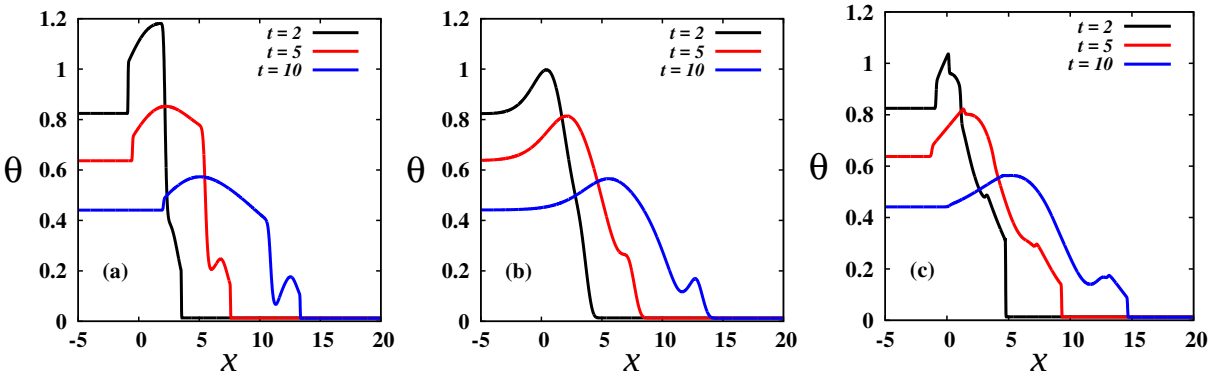


Figure A.9: Temporal evolution of blast wave granular temperature for $\alpha = 0.9$. (a) 10-moment model, (b) Navier-Stokes model, (c) 14-moment model.

granular temperature at the blast wave front and it decreases nearly to zero near the contact, again increases in fluidized region (to the right of contact wave) and then decreases, as dictated by the physics of the inelastic granular gas. The main reason is that the gas becomes less compressible near the contact wave. By comparing the granular temperature profiles at time $t = 10$ in Fig. A.9 and Fig. A.10, it is noted that Navier-Stokes granular temperature profiles are smoother than the 10- and 14-moment models.

In Fig. A.11, we present the time evolution of skew temperature profiles which are obtained from the 10-moment (a), Navier-Stokes (b) and 14-moment (c) models for $\alpha = 0.9$. An interesting feature of a *two peak* structure is seen to be developed on the skew-temperature profile

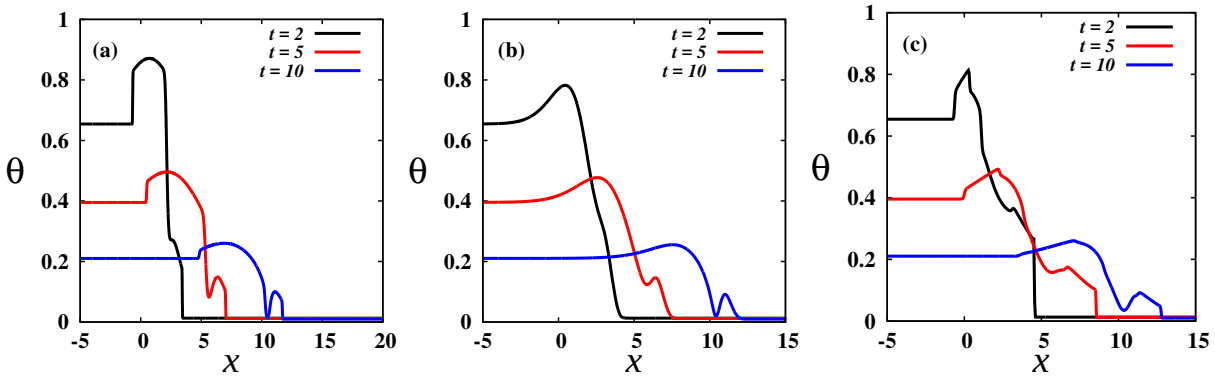


Figure A.10: Temporal evolution of blast wave granular temperature for $\alpha = 0.75$.(a) 10-moment model, (b) Navier-Stokes model, (c) 14-moment model.

in each case at a short time. It is noteworthy that these two peaks propagate downstream at

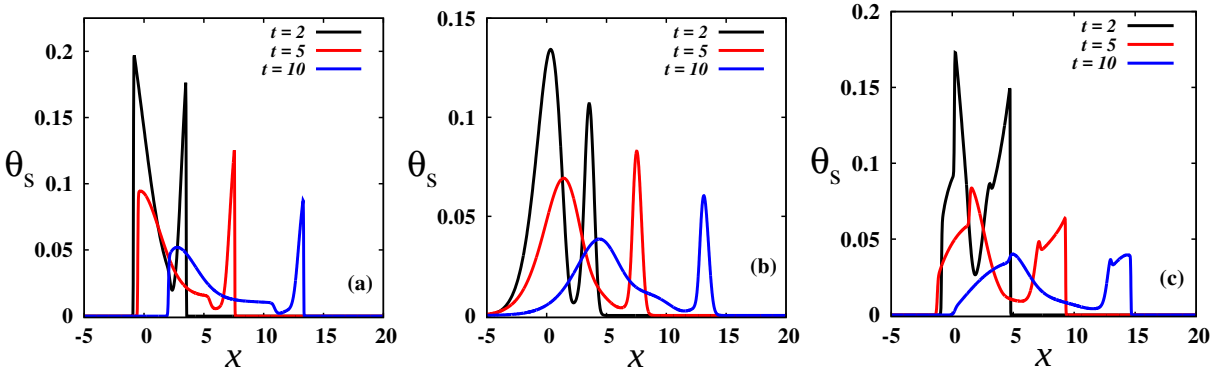


Figure A.11: Temporal evolution of blast wave skew-temperature for $\alpha = 0.9$. (a) 10-moment model, (b) Navier-Stokes model, (c) 14-moment model.

different speeds, thereby splitting away from each other with time: the downstream peak travels at a faster rate than its upstream cousin. We also remark that, initially the magnitude of the upstream peak is higher than the magnitude of the downstream peak and as time progress the magnitude of downstream peak becomes higher compared to its upstream peak. As in the case of scalar temperatures, the skew temperature profiles are smoother in the case of Navier-Stokes model. From the skew temperature profiles for a restitution coefficient of $\alpha = 0.75$, which are displayed in Fig. A.12, we find that the magnitude of skew temperature decreases with the increase of inelasticity.

In Fig. A.13, we display the temporal evolution of "blast-wave" heat-flux profiles for the restitution coefficient of $\alpha = 0.9$ using Navier- Stokes model (a) and 14-moment model (b). A comparison of heat flux profiles at time $t = 10$ is displayed in Fig. A.13 (c) for $\alpha = 0.9$ marked by the black dashed line and $\alpha = 0.75$ marked by the red dash double dotted line, respectively, with the main panel showing the results from Navier-Stokes model and the inset showing the results from 14-moment model. Recall that the heat flux is zero in the Euler and 10-moment models. It is seen that the heat flux profiles have a multiple-peak structure and these structural features of heat-flux $q$ are directly correlated with the corresponding scalar temperature profiles in Fig.

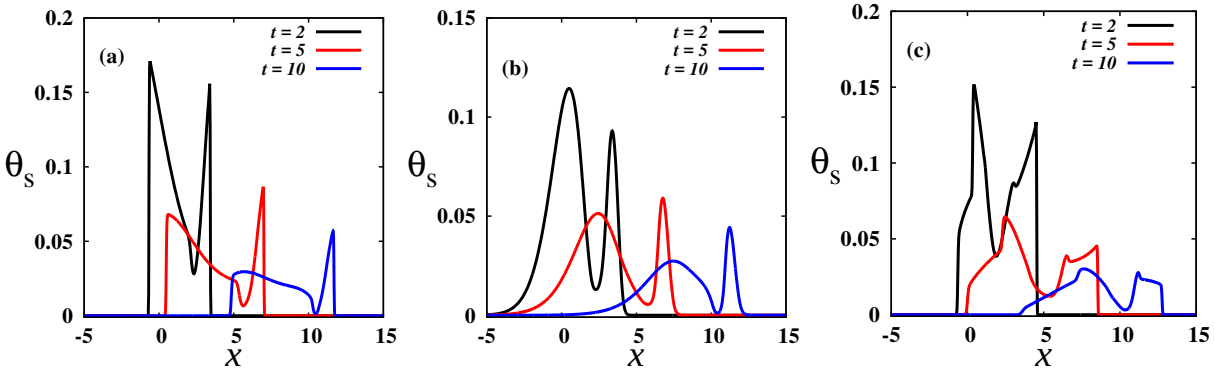


Figure A.12: Temporal evolution of blast wave skew-temperature for $\alpha = 0.75$. (a) 10-moment model, (b) Navier-Stokes model, (c) 14-moment model.

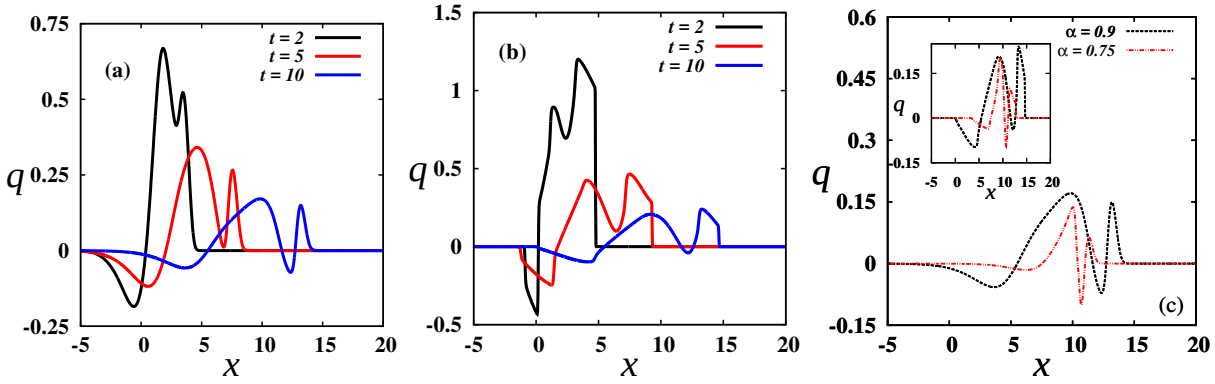


Figure A.13: (a) Temporal evolution of blast wave heat flux for $\alpha = 0.9$ using Navier-Stokes model, (b) Temporal evolution of blast wave heat flux for $\alpha = 0.9$ using 14-moment model, (c) Comparison of heat flux profiles at time $t = 10$ for the restitution coefficients 0.9 and 0.75, with the main panel showing Navier-Stokes solution and the inset shows the same for 14-moment solution.

A.9 and Fig. A.10 that can be understood by analyzing the constitutive relation of heat flux for a granular gas. Considering the nearly elastic case ($\alpha = 0.9$) for which the density-gradient term in the Fourier law for a granular gas can be neglected and hence Fourier law: $q \propto -\partial\theta/\partial x$, we see that the granular temperature in Fig. A.9 (b) has a two-hump structure: it increases at the blast wave-front, decreases near the contact wave, again increases to the right of contact wave and later decreases; hence the heat flux profiles in Fig. A.13 have to follow the opposite pattern as dictated by the Fourier law. From heat flux profiles at time $t = 10$, we see that the overall blast wave width is approximately same for the N-S and 14-moment models and it decreases from $\approx 15$ for $\alpha = 0.9$ to $\approx 8$ for $\alpha = 0.75$.

Lastly, we present the time evolution of the fourth order moment ($\Delta$) in Fig. A.14 for the restitution coefficient of (a) $\alpha = 0.9$, (b) $\alpha = 0.75$. From Fig. A.14 (a) and (b), we remark that the magnitude of the fourth order moment decreases with time. Figure A.14 (c) shows a comparison of fourth order moment profiles at time $t = 10$ for $\alpha = 0.9$ marked by the black dashed line and $\alpha = 0.75$ marked by the red dash double dotted line. From Fig. A.14 (c), one can conclude that the magnitude of the fourth order moment ($\Delta$) increases as you go towards the elastic limit. In other words, the magnitude of the fourth order moment decreases with decrease of the restitution coefficient.

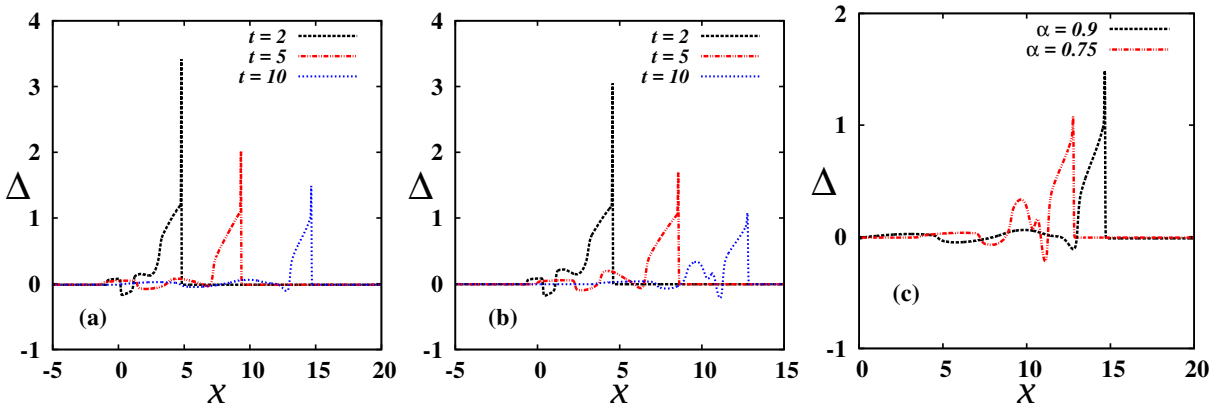


Figure A.14: Temporal evolution of blast wave fourth order moment ($\Delta$) using 14-moment model. (a) $\alpha = 0.9$, (b) $\alpha = 0.75$, (c) Comparison of fourth order moment ($\Delta$) profiles at time $t = 10$ for the restitution coefficients 0.9 and 0.75.

# References


Alam, M. & Luding, S. 2003 First normal stress difference and crystallization in a dense sheared granular fluid. *Phys. Fluids* **15** (8), 2298–2312.

Alam, M. & Luding, S. 2005 Non-newtonian granular fluids: Simulation and theory. *Powders and Grains (Editors: R.Garcia, H. Herrmann and S. McNamara)* pp. 1141–1144.

Alam, M. & Nott, P. R. 1997 The influence of friction on the stability of unbounded granular shear flow. *Journal of Fluid Mechanics* **343**, 267–301.

Alam, M. & Nott, P. R. 1998 Stability of plane couette flow of a granular material. *Journal of Fluid Mechanics* **377**, 99–136.

Alam, M., Shukla, P. & Luding, S. 2008 Universality of shear-banding instability and crystallization in sheared granular fluid. *Journal of Fluid Mechanics* **615**, 293–321.

Alam, M., Willits, J. T., Arnarson, B. Ö. & Luding, S. 2002 Kinetic theory of a binary mixture of nearly elastic disks with size and mass disparity. *Physics of Fluids (1994-present)* **14** (11), 4085–4087.

Amarouchene, Y. & Kellay, H. 2006 Speed of sound from shock fronts in granular flows. *Physics of Fluids (1994-present)* **18** (3), 031707.

Aranson, I. S. & Tsimring, L. S. 2006 Patterns and collective behavior in granular media: Theoretical concepts. *Reviews of Modern Physics* **78** (2), 641.

Barbier, M., Villamaina, D. & Trizac, E. 2015 Blast dynamics in a dissipative gas. *Physical Review Letters* **115** (21), 214301.

Bird, G. A. 1994 *Molecular Gas Dynamics and the Direct Simulation of Gas Flows*. Oxford Univ Press.

Blandford, R. & McKee, C. 1976 Fluid dynamics of relativistic blast waves. *Phys. Fluids* **19** (8), 1130–1138.

Boltzmann, L. 1878 Zur theorie der elastischen nachwirkung. *Annalen der Physik* **241** (11), 430–432.

Boudet, J.-F., Amarouchene, Y. & Kellay, H. 2008 Shock front width and structure in supersonic granular flows. *Physical Review Letters* **101** (25), 254503.

Boudet, J.-F., Cassagne, J. & Kellay, H. 2009 Blast shocks in quasi-two-dimensional supersonic granular flows. *Physical Review Letters* **103** (22), 224501.

Boudet, J.-F. & Kellay, H. 2013 Unstable blast shocks in dilute granular flows. *Physical Review E* **87** (5), 052202.

Bougie, J., Moon, S. J., Swift, J. & Swinney, H. L. 2002 Shocks in vertically oscillated granular layers. *Physical Review E* **66** (5), 051301.

Breu, A., Ensner, H.-M., Kruelle, C. A. & Rehberg, I. 2003 Reversing the brazil-nut effect: competition between percolation and condensation. *Physical Review Letters* **90** (1), 014302.

Brey, J. J., Dufty, J. W., Kim, C. S. & Santos, A. 1998 Hydrodynamics for granular flow at low density. *Physical Review E* **58** (4), 4638.

Brey, J. J., Dufty, J. W. & Santos, A. 1997 Dissipative dynamics for hard spheres. *Journal of Statistical Physics* **87** (5-6), 1051–1066.

Brey, J. J., Dufty, J. W. & Santos, A. 1999 Kinetic models for granular flow. *Journal of Statistical Physics* **97** (1-2), 281–322.

Brilliantov, N. & Pöschel, T. 2003 Hydrodynamics and transport coefficients for dilute granular gases. *Physical Review E* **67** (6), 061304.

Brilliantov, N. & Pöschel, T. 2004 *Kinetic Theory of Granular Gases*. Oxford Univ Press.

Buchholtz, V. & Pöschel, T. 1998 Interaction of a granular stream with an obstacle. *Granular matter* **1** (1), 33–41.

Burgers, J. M. 1948 A mathematical model illustrating the theory of turbulence. *Adv. in Appl. Mech.* **1**, 171–199.

Burnett, D. 1935 The distribution of velocities in a slightly non-uniform gas. *Proceedings of the London Mathematical Society* **2** (1), 385–430.

Callen, H. B. 2006 *Thermodynamics & an Intro. to Thermostatistics*. John Wiley & Sons.

Campbell, C. S. 1990 Rapid granular flows. *Annual Review of Fluid Mechanics* **22** (1), 57–90.

Carrillo, J. A., Poeschel, T. & Saluena, C. 2008 Granular hydrodynamics and pattern formation in vertically oscillated granular disk layers. *Journal of Fluid Mechanics* **597**, 119–144.

Cercignani, C. 1975 *Theory and application of the Boltzmann equation*. Scottish Academic Press.

Chapman, S. 1918 On the kinetic theory of a gas. part ii: a composite monatomic gas: diffusion, viscosity, and thermal conduction. *Philosophical Transactions of the Royal Society of London. Series A, Containing Papers of a Mathematical or Physical Character* **217**, 115–197.

Chapman, S. & Cowling, T. G. 1970 *The Mathematical Theory of Non-uniform Gases: An Account of the Kinetic Theory of Viscosity, Thermal Conduction and Diffusion in Gases*. Cambridge university press.

Courant, R. & Friedrichs, K. 1948 Supersonic Flow and Shock Waves. *New York: Interscience* .

Cui, X. & Gray, J. 2013 Gravity-driven granular free-surface flow around a circular cylinder. *Journal of Fluid Mechanics* **720**, 314–337.

Delis, A. & Katsaounis, T. 2003 Relaxation schemes for the shallow water equations. *International journal for numerical methods in fluids* **41** (7), 695–719.

Delis, A. I. & Katsaounis, T. 2005 Numerical solution of the two-dimensional shallow water equations by the application of relaxation methods. *Applied Mathematical Modelling* **29** (8), 754–783.

Enskog, D. 1917 Theorie der Vorgänge in Massing Verdumten Gasen. PhD thesis, Ph. D thesis, University of Uppsala, Sweden.

Enskog, D. 1923 Zur quantentheorie des dampfdruckes und der dissoziation. *Annalen der Physik* **377** (21), 321–344.

Esipov, S. E. & Pöschel, T. 1997 The granular phase diagram. *Journal of Statistical Physics* **86** (5-6), 1385–1395.

Evje, S. & Fjelde, K. 2002 Relaxation schemes for the calculation of two-phase flow in pipes. *Mathematical and Computer Modelling* **36** (4), 535–567.

Forterre, Y. & Pouliquen, O. 2008 Flows of dense granular media. *Annu. Rev. Fluid Mech.* **40**, 1–24.

Garzó, V. 2013 Grad's moment method for a granular fluid at moderate densities: Navier-stokes transport coefficients. *Physics of Fluids (1994-present)* **25** (4), 043301.

Garzó, V. & Dufty, J. 1999 Dense fluid transport for inelastic hard spheres. *Physical Review E* **59** (5), 5895.

Garzó, V., Santos, A. & Montanero, J. M. 2007 Modified sonine approximation for the navier–stokes transport coefficients of a granular gas. *Physica A: Statistical Mechanics and its Applications* **376**, 94–107.

Gayen, B. & Alam, M. 2006 Algebraic and exponential instabilities in a sheared micropolar granular fluid. *Journal of Fluid Mechanics* **567**, 195–233.

Gilbarg, D. & Paolucci, D. 1953 The structure of shock waves in the continuum theory of fluids. *Journal of Rational Mechanics and Analysis* **2** (5), 617–642.

Goldhirsch, I. 2003 Rapid granular flows. *Annual Review of Fluid Mechanics* **35** (1), 267–293.

Goldhirsch, I. & Zanetti, G. 1993 Clustering instability in dissipative gases. *Physical Review Letters* **70** (11), 1619.

Goldreich, P. & Tremaine, S. 1978 The velocity dispersion in saturn's rings. *Icarus* **34** (2), 227–239.

Goldshtein, A. & Shapiro, M. 1995 Mechanics of collisional motion of granular materials. part 1. general hydrodynamic equations. *Journal of Fluid Mechanics* **282**, 75–114.

Goldshtein, A., Shapiro, M. & Gutfinger, C. 1996*a* Mechanics of collisional motion of granular materials. part 3. self-similar shock wave propagation. *Journal of Fluid Mechanics* **316**, 29–51.

Goldshtein, A., Shapiro, M. & Gutfinger, C. 1996*b* Mechanics of collisional motion of granular materials. part 4. expansion wave. *Journal of Fluid Mechanics* **327**, 117–138.

Goldshtein, A., Shapiro, M., Moldavsky, L. & Fichman, M. 1995 Mechanics of collisional motion of granular materials. part 2. wave propagation through vibrofluidized granular layers. *Journal of Fluid Mechanics* **287**, 349–382.

Gonzalez, S., Thornton, A. & Luding, S. 2014 Free cooling phase-diagram of hard-spheres with short-and long-range interactions. *The European Physical Journal Special Topics* **223** (11), 2205–2225.

Gorban, A. N. & Karlin, I. V. 1994 General approach to constructing models of the boltzmann equation. *Physica A: Statistical Mechanics and its Applications* **206** (3), 401–420.

Grad, H. 1949 On the kinetic theory of rarefied gases. *Communications on Pure and Applied Mathematics* **2** (4), 331–407.

Grad, H. 1952 The profile of a steady plane shock wave. *Communications on Pure and Applied Mathematics* **5** (3), 257–300.

Grad, H. 1958 Principles of the kinetic theory of gases. In *Thermodynamik der Gase/Thermodynamics of Gases*, pp. 205–294. Springer.

Gray, J. & Cui, X. 2007 Weak, strong and detached oblique shocks in gravity-driven granular free-surface flows. *Journal of Fluid Mechanics* **579**, 113–136.

Gray, J., Tai, Y.-C. & Noelle, S. 2003 Shock waves, dead zones and particle-free regions in rapid granular free-surface flows. *Journal of Fluid Mechanics* **491**, 161–181.

Gray, J. & Thornton, A. 2005 A theory for particle size segregation in shallow granular free-surface flows. In *Proceedings of the Royal Society of London A: Mathematical, Physical and Engineering Sciences*, , vol. 461, pp. 1447–1473. The Royal Society.

Greenshields, C. J. & Reese, J. M. 2007 The structure of shock waves as a test of brenner's modifications to the navier–stokes equations. *Journal of Fluid Mechanics* **580**, 407–429.

Groth, C. P. & McDonald, J. G. 2009 Towards physically realizable and hyperbolic moment closures for kinetic theory. *Continuum Mechanics and Thermodynamics* **21** (6), 467–493.

Gu, X. & Emerson, D. 2007 A computational strategy for the regularized 13 moment equations with enhanced wall-boundary conditions. *Journal of computational physics* **225** (1), 263–283.

Gu, X.-j. & Emerson, D. R. 2009 A high-order moment approach for capturing non-equilibrium phenomena in the transition regime. *Journal of Fluid Mechanics* **636**, 177–216.

Haff, P. 1983 Grain flow as a fluid-mechanical phenomenon. *Journal of Fluid Mechanics* **134**, 401–430.

Herminghaus, S. 2005 Dynamics of wet granular matter. *Advances in Physics* **54** (3), 221–261.

Holway Jr, L. H. 1966 New statistical models for kinetic theory: methods of construction. *Physics of Fluids (1958-1988)* **9** (9), 1658–1673.

Hutter, K. & Savage, S. 1988 Avalanche dynamics: the motion of a finite mass of gravel down a mountain side. In *Proceedings of the 5th International Symposium on Landslides, July*, pp. 7–9.

Ikenberry, E. & Truesdell, C. 1956 On the pressures and flux of energy in a gas according to Maxwell's kinetic theory. *J. Rat. Mech. Anal.* **5**.

Jaeger, H. M., Nagel, S. R. & Behringer, R. P. 1996 Granular solids, liquids, and gases. *Reviews of Modern Physics* **68** (4), 1259.

Jaeger, H. M., Nagel, S. R. *et al.* 1992 Physics of the granular state. *Science* **255** (5051), 1523–1531.

Jaynes, E. T. 1957*a* Information theory and statistical mechanics. *Physical Review* **106** (4), 620.

Jaynes, E. T. 1957*b* Information theory and statistical mechanics. ii. *Physical Review* **108** (2), 171.

Jenkins, i. J. & Richman, M. W. 1988 Plane simple shear of smooth inelastic circular disks: the anisotropy of the second moment in the dilute and dense limits. *Journal of Fluid Mechanics* **192**, 313–328.

Jenkins, J. & Richman, M. 1985*a* Kinetic theory for plane flows of a dense gas of identical, rough, inelastic, circular disks. *Physics of Fluids (1958-1988)* **28** (12), 3485–3494.

Jenkins, J. & Savage, S. 1983 A theory for the rapid flow of identical, smooth, nearly elastic, spherical particles. *Journal of Fluid Mechanics* **130**, 187–202.

Jenkins, J. T. & Richman, M. W. 1985*b* Grad's 13-moment system for a dense gas of inelastic spheres. *Archive for Rational Mechanics and Analysis* **87** (4), 355–377.

Jin, S. & Xin, Z. 1995 The relaxation schemes for systems of conservation laws in arbitrary space dimensions. *Communications on Pure and Applied Mathematics* **48** (3), 235–276.

Johnson, C. & Gray, J. 2011 Granular jets and hydraulic jumps on an inclined plane. *Journal of Fluid Mechanics* **675**, 87–116.

Kamenetsky, V., Goldshtein, A., Shapiro, M. & Degani, D. 2000 Evolution of a shock wave in a granular gas. *Physics of Fluids (1994-present)* **12** (11), 3036–3049.

Kremer, G. M. 2010 *An Introduction to the Boltzmann Equation and Transport Processes in Gases*. Springer Science & Business Media.

Kremer, G. M. & Marques Jr, W. 2011 Fourteen moment theory for granular gases. *Kinet. Relat. Models* **4**, 317.

Lam, C. 2011 Application of Gaussian Moment Closure Methods to Three-dimensional Micro-scale Flows. PhD thesis, University of Toronto.

Lattanzio, C. & Serre, D. 2001 Convergence of a relaxation scheme for hyperbolic systems of conservation laws. *Numerische Mathematik* **88** (1), 121–134.

LeVeque, R. J. 1992 *Numerical methods for conservation laws*, , vol. 132. Springer.

LeVeque, R. J. 2002 *Finite Volume Methods for Hyperbolic Problems*, , vol. 31. Cambridge university press.

Levermore, C. D. 1996 Moment closure hierarchies for kinetic theories. *Journal of Statistical Physics* **83** (5-6), 1021–1065.

Levermore, C. D. & Morokoff, W. J. 1998 The gaussian moment closure for gas dynamics. *SIAM Journal on Applied Mathematics* **59** (1), 72–96.

Li, X.-G., Yu, X.-J. & Chen, G.-N. 2002 The third-order relaxation schemes for hyperbolic conservation laws. *Journal of Computational and Applied Mathematics* **138** (1), 93–108.

Liepmann, H. W. & Roshko, A. 1957 *Elements of Gas Dynamics*. Courier Corporation.

Liu, X.-D. & Osher, S. 1996 Nonoscillatory high order accurate self-similar maximum principle satisfying shock capturing schemes i. *SIAM Journal on Numerical Analysis* **33** (2), 760–779.

Luding, S. & Goldshtein, A. 2003 Collisional cooling with multi-particle interactions. *Granular Matter* **5** (3), 159–163.

Luding, S. & Herrmann, H. 1999 Cluster-growth in freely cooling granular media. *Chaos: An Interdisciplinary Journal of Nonlinear Science* **9** (3), 673–681.

Mackenzie, N. S. 2006 Stability of the Beagle 2 Mars Explorer. PhD thesis, University of Melbourne.

Matsuo, K. & Aoki, T. 1992 Wave problems in high-speed railway tunnels. In *Shock Waves*, pp. 95–102. Springer.

McDonald, J. & Torrilhon, M. 2013 Affordable robust moment closures for cfd based on the maximum-entropy hierarchy. *Journal of Computational Physics* **251**, 500–523.

McDonald, J. G. & Groth, C. P. 2013 Towards realizable hyperbolic moment closures for viscous heat-conducting gas flows based on a maximum-entropy distribution. *Continuum Mechanics and Thermodynamics* **25** (5), 573–603.

Mitarai, N. & Nori, F. 2006 Wet granular materials. *Advances in Physics* **55** (1-2), 1–45.

Müller, I., Reitebuch, D. & Weiss, W. 2003 Extended thermodynamics–consistent in order of magnitude. *Continuum Mechanics and Thermodynamics* **15** (2), 113–146.

Müller, I. & Ruggeri, T. 1993*a* Extended Thermodynamics. *Springer Tracts in Natural Philosophy* **37**.

Müller, I. & Ruggeri, T. 1993*b* Extended thermodynamics of mon-atomic gases. In *Extended Thermodynamics*, pp. 17–39. Springer.

Müller, I. & Ruggeri, T. 2013 *Rational Extended Thermodynamics*, , vol. 37. Springer Science & Business Media.

Narasimha, R. & Das, P. 1990 A spectral solution of the Boltzmann equation for the infinitely strong shock. *Philosophical Transactions of the Royal Society of London A: Mathematical, Physical and Engineering Sciences* **330** (1611), 217–252.

Nott, P. R. 2011 Boundary conditions at a rigid wall for rough granular gases. *Journal of Fluid Mechanics* **678**, 179–202.

Ostriker, J. P. & McKee, C. F. 1988 Astrophysical blastwaves. *Reviews of Modern Physics* **60** (1), 1.

Ottino, J. & Khakhar, D. 2000 Mixing and segregation of granular materials. *Annual Review of Fluid Mechanics* **32** (1), 55–91.

Pham-Van-Diep, G. C., Erwin, D. A. & Muntz, E. P. 1991 Testing continuum descriptions of low-mach-number shock structures. *Journal of Fluid Mechanics* **232**, 403–413.

Pöschel, T. & Brilliantov, N. V. 2003 *Granular Gas Dynamics*, , vol. 624. Springer Science & Business Media.

Pöschel, T. & Luding, S. 2001 *Granular Gases*. Springer Science & Business Media.

Prasad, P. 2001 *Nonlinear Hyperbolic Waves in Multidimensions*. CRC Press.

Rana, A. S. & Struchtrup, H. 2016 Thermodynamically admissible boundary conditions for the regularized 13 moment equations. *Physics of Fluids (1994-present)* **28** (2), 027105.

Rao, K. K. & Nott, P. R. 2008 *An Introduction to Granular Flow*. Cambridge University Press, New York.

Razis, D., Edwards, A., Gray, J. & van der Weele, K. 2014 Arrested coarsening of granular roll waves. *Physics of Fluids (1994-present)* **26** (12), 123305.

Reddy, M. L. & Alam, M. 2015 Plane shock waves and haff's law in a granular gas. *Journal of Fluid Mechanics* **779**, R2.

Reddy, M. L., Ansumali, S. & Alam, M. 2014 Shock waves in a dilute granular gas. In *PROCEEDINGS OF THE 29TH INTERNATIONAL SYMPOSIUM ON RAREFIED GAS DYNAMICS*, , vol. 1628, pp. 480–487. AIP Publishing.

Reese, J., Woods, L., Thivet, F. & Candel, S. 1995 A second-order description of shock structure. *Journal of Computational Physics* **117** (2), 240–250.

Rericha, E. C., Bizon, C., Shattuck, M. D. & Swinney, H. L. 2001 Shocks in supersonic sand. *Physical Review Letters* **88** (1), 014302.

Ruggeri, T. 1993 Breakdown of shock-wave-structure solutions. *Physical Review E* **47** (6), 4135.

Saha, S. & Alam, M. 2014 Non-newtonian stress, collisional dissipation and heat flux in the shear flow of inelastic disks: a reduction via grad's moment method. *Journal of Fluid Mechanics* **757**, 251–296.

Saha, S. & Alam, M. 2016 Normal stress differences, their origin and constitutive relations for a sheared granular fluid. *Journal of Fluid Mechanics* **795**, 549–580.

Samadani, A. & Kudrolli, A. 2000 Segregation transitions in wet granular matter. *Physical Review Letters* **85** (24), 5102.

Savage, S. B. & Hutter, K. 1989 The motion of a finite mass of granular material down a rough incline. *Journal of fluid mechanics* **199**, 177–215.

Sela, N. & Goldhirsch, I. 1998 Hydrodynamic equations for rapid flows of smooth inelastic spheres, to burnett order. *Journal of Fluid Mechanics* **361**, 41–74.

Serna, S. & Marquina, A. 2005 Capturing shock waves in inelastic granular gases. *Journal of Computational Physics* **209** (2), 787–795.

Shu, C.-W. & Osher, S. 1988 Efficient implementation of essentially non-oscillatory shock-capturing schemes. *Journal of Computational Physics* **77** (2), 439–471.

Shukla, P., Ansari, I. H., van der Meer, D., Lohse, D. & Alam, M. 2014 Nonlinear instability and convection in a vertically vibrated granular bed. *Journal of Fluid Mechanics* **761**, 123–167.

Sirmas, N. & Radulescu, M. 2014 Evolution of shock instability in granular gases with viscoelastic collisions. *arXiv preprint arXiv:1407.4202* .

Smoller, J. 1983 *Shock Waves and Reaction-Diffusion Equations*. Springer-Verlag, New York.

Sone, Y. & Aoki, K. 1987 Steady gas flows past bodies at small knudsen numbers: Boltzmann and hydrodynamic systems. *Transport Theory and Statistical Physics* **16** (2-3), 189–199.

Sone, Y., Takata, S. & Golse, F. 2001 Notes on the boundary conditions for fluid-dynamic equations on the interface of a gas and its condensed phase. *Physics of Fluids (1994-present)* **13** (1), 324–334.

Struchtrup, H. 2004 Stable transport equations for rarefied gases at high orders in the knudsen number. *Physics of Fluids (1994-present)* **16** (11), 3921–3934.

Struchtrup, H. 2005*a* Derivation of 13 moment equations for rarefied gas flow to second order accuracy for arbitrary interaction potentials. *Multiscale Modeling & Simulation* **3** (1), 221–243.

Struchtrup, H. 2005*b* *Macroscopic Transport Equations for Rarefied Gas Flows*. Springer.

Struchtrup, H. & Torrilhon, M. 2003 Regularization of grad's 13 moment equations: derivation and linear analysis. *Physics of Fluids (1994-present)* **15** (9), 2668–2680.

Struchtrup, H. & Torrilhon, M. 2013 Regularized 13 moment equations for hard sphere molecules: linear bulk equations. *Physics of Fluids (1994-present)* **25** (5), 052001.

Taylor, G. 1950*a* The formation of a blast wave by a very intense explosion. i. theoretical discussion. *Proceedings of the Royal Society of London. Series A, Mathematical and Physical Sciences* pp. 159–174.

Taylor, G. 1950*b* The formation of a blast wave by a very intense explosion. ii. the atomic explosion of 1945. In *Proceedings of the Royal Society of London A: Mathematical, Physical and Engineering Sciences*, , vol. 201, pp. 175–186. The Royal Society.

Torrilhon, M. 2000 Characteristic waves and dissipation in the 13-moment-case. *Continuum Mechanics and Thermodynamics* **12** (5), 289–301.

Torrilhon, M. 2010 Hyperbolic moment equations in kinetic gas theory based on multivariate pearson-iv-distributions. *Communications in Computational Physics* **7** (4), 639.

Torrilhon, M. & Struchtrup, H. 2004 Regularized 13-moment equations: shock structure calculations and comparison to burnett models. *Journal of Fluid Mechanics* **513**, 171–198.

Torrilhon, M. & Struchtrup, H. 2008 Boundary conditions for regularized 13-moment-equations for micro-channel-flows. *Journal of Computational Physics* **227** (3), 1982–2011.

Truesdell, C. & Muncaster, R. 1980 Fundamentals of Maxwell's Kinetic Theory of a Simple Monatomic Gas. *Academic, New York* .

Umbanhowar, P. 2003 Granular materials: Shaken sand - a granular fluid? *Nature* **424** (6951), 886–887.

Van der Weele, K. 2008 Granular gas dynamics: how Maxwell's demon rules in a non-equilibrium system. *Contemporary Physics* **49** (3), 157–178.

Weiss, W. 1995 Continuous shock structure in extended thermodynamics. *Physical Review E* **52** (6), R5760.

Whitham, G. 1974 Linear andnonlinear waves. *John Wiley&Sons, NewYork* .

Xu, K. 2002 A well-balanced gas-kinetic scheme for the shallow-water equations with source terms. *Journal of Computational Physics* **178** (2), 533–562.

Xu, K. & Huang, J.-C. 2010 A unified gas-kinetic scheme for continuum and rarefied flows. *Journal of Computational Physics* **229** (20), 7747–7764.

Xu, K. & Josyula, E. 2006 Continuum formulation for non-equilibrium shock structure calculation. *Communications in Computational Physics* **1** (3), 425–448.

Yee, H. C., Klopfer, G. H. & Montagne, J.-L. 1990 High-resolution shock-capturing schemes for inviscid and viscous hypersonic flows. *Journal of Computational Physics* **88** (1), 31–61.

# Publications

### Journal Publication

1. Plane shock waves and Haff's law in a granular gas,
   **M. H. Lakshminarayana Reddy** & Meheboob Alam,
   *Journal of Fluid Mechanics* **779**, **R2**, 2015. [Chapter 4]

2. Analysis of shock structures via extended hydrodynamic equations,
   **M. H. Lakshminarayana Reddy**, Santosh Ansumali & Meheboob Alam,
   In preparation (2016). [Chapter 6]

3. Regularized moment equations for a granular gas and plane shock waves,
   **M. H. Lakshminarayana Reddy** & Meheboob Alam,
   In preparation (2016). [Chapter 7]

4. Characteristics of one-dimensional blast waves in granular gas,
   **M. H. Lakshminarayana Reddy**,
   In preparation (2016). [Appendix A]

### Conference Publication

1. Shock waves in a dilute granular gas,
   **M. H. Lakshminarayana Reddy**, Santosh Ansumali & Meheboob Alam,
   *Proceedings of the 29th international Symposium on Rarefied Gas Dynamics*,
   *AIP Conf. Proc.*, **1628**, p. 480-487, 2014.
   (13-18 July 2014, Xi'an, China).